



## City Research Online

### City, University of London Institutional Repository

---

**Citation:** Anwar, N. (2005). Computer modelling of electro-optic modulators. (Unpublished Doctoral thesis, City, University of London)

This is the accepted version of the paper.

This version of the publication may differ from the final published version.

---

**Permanent repository link:** <https://openaccess.city.ac.uk/id/eprint/30252/>

**Link to published version:**

**Copyright:** City Research Online aims to make research outputs of City, University of London available to a wider audience. Copyright and Moral Rights remain with the author(s) and/or copyright holders. URLs from City Research Online may be freely distributed and linked to.

**Reuse:** Copies of full items can be used for personal research or study, educational, or not-for-profit purposes without prior permission or charge. Provided that the authors, title and full bibliographic details are credited, a hyperlink and/or URL is given for the original metadata page and the content is not changed in any way.

# **COMPUTER MODELLING OF ELECTRO-OPTIC MODULATORS**

by

**Najm Anwar**

PhD Electronic Engineering

A thesis submitted to  
City University  
in fulfilment of the requirement  
for the Degree of Doctor of Philosophy

**CITY UNIVERSITY**

Measurement and Instrumentation Centre  
Department of Electrical, Electronic and Information Engineering  
Northampton Square, London EC1V 0HB

August 2005

*Sometimes our light burns bright,  
Sometimes 'tis but a dull flame;  
Who will rekindle this light?  
Tis to whom we owe our deepest thanks.*

(adapted from Albert Schweitzer)

*To my parents  
for always being there  
and  
to all those  
who have always believed in me*

# *Table of Contents*

Table of Contents .....	iv
List of Tables .....	viii
List of Figures .....	x
Acknowledgements .....	xvi
Declaration .....	xvii
Abstract .....	xviii
Symbols and Abbreviations .....	xix

## **1 Introduction ..... 1**

1.1 Aims of the Thesis .....	1
1.2 Structure of the Thesis .....	3
1.3 Photonics: an historical perspective .....	7
1.3.1 Developments in Optical Fibres .....	8
1.3.2 Developments in Lasers .....	10
1.3.3 Developments in Photodetectors .....	12
1.3.4 Developments in Modulators .....	14
1.3.4.1 Early Modulators .....	14
1.3.4.1.1 Integrated Optics .....	17
1.3.4.1.2 LiNbO <sub>3</sub> Waveguide Modulators .....	17
1.3.4.1.3 Direct Modulation .....	20
1.3.4.1.4 Semiconductor Modulators .....	20
1.3.4.1.5 Types of Modulator .....	22
1.3.4.2 Present Day Device Characteristics .....	24
1.3.4.3 Future Predictions for Modulators .....	27
1.3.5 Optoelectronics: Requirements & Usage .....	29
1.4 Numerical Modelling of Waveguide Devices .....	30
1.4.1 Optical Waveguides .....	30
1.4.2 Maxwell's Equations .....	33
1.4.2.1 Boundary Conditions .....	34
1.4.3 Analytical Methods .....	35
1.4.4 Numerical Methods .....	36
1.4.4.1 Methods Based On Series Expansion .....	37
1.4.4.2 Global and Related Methods .....	38
1.4.4.3 Other Methods .....	42
1.4.5 The Method of Choice .....	44
1.5 Summary .....	46

## **2 The Finite Element Method ..... 47**

2.1 Introduction .....	47
2.1.1 History .....	48
2.2 Variational Formulations .....	50
2.2.1 Scalar Formulations .....	51
2.2.2 Vector Formulations .....	52
2.2.3 Natural and Forced Boundary Conditions .....	56
2.3 The Finite Element Methodology .....	57
2.4 The Elements and their Shape Functions .....	58

2.5	Spurious Modes .....	64
2.6	Assembly of the Global Matrices .....	65
2.6.1	Sparsity .....	68
2.7	Infinite elements .....	69
2.8	Boundary Values .....	71
2.9	Summary .....	72

### **3 An Introduction to Electro-Optic Waveguide Modulators 75**

3.1	Introduction .....	75
3.2	The Fabrication of Electro-Optic Devices .....	79
3.2.1	Ti:LiNbO <sub>3</sub> Waveguide Modulator .....	80
3.2.1.1	Waveguide Fabrication .....	80
3.2.1.2	Electrode Fabrication .....	82
3.2.2	GaAs/Al <sub>x</sub> Ga <sub>1-x</sub> As Waveguide Modulator .....	84
3.3	The Device Design Issues .....	85
3.3.1	Diffusion Process in the Formation of Ti:LiNbO <sub>3</sub> Waveguides .....	85
3.3.2	Insertion Loss .....	87
3.3.2.1	The Beam Propagation Method .....	88
3.3.2.2	The Perturbation Technique .....	91
3.3.3	Electrode Design .....	94
3.3.4	Other Features Involved .....	97
3.4	Summary .....	98

### **4 Electro-Optic Directional Coupler Modulators.....99**

4.1	Introduction .....	99
4.2	Theory of Directional Coupler Modulators .....	101
4.3	Diffused Anisotropic Ti:LiNbO <sub>3</sub> Guides for Directional Couplers .....	104
4.3.1	Structure of the Directional Coupler .....	107
4.4	The Electro-Optic Effect on Ti:LiNbO <sub>3</sub> Directional Couplers .....	112
4.5	Effects of Diffusion Parameters on Device Performance .....	119
4.6	Fabrication Effects on Drive Voltage .....	126
4.7	Optical Loss due to Metal Electrodes .....	130
4.8	Power Transfer .....	132
4.8.1	LSBR .....	132
4.8.2	Power Transfer Theory .....	136
4.9	Summary .....	145

### **5 Ti:LiNbO<sub>3</sub> Interferometric Modulators ..... 147**

5.1	Introduction .....	147
5.2	Theory of Interferometric Modulators .....	149
5.3	The Comparison Between An Unetched Channel Waveguide And An Etched Ridge Waveguide .....	154
5.3.1	Structure for a Single Guide .....	155
5.3.1.1	Calculation of the Refractive Index Profile .....	157
5.3.2	The Optical Characteristics of the Waveguides .....	160
5.3.3	Comparison of Optical Bends using Channel and Etched Ridge Waveguides .....	167

5.4	The Comparison between an Unetched Channel Waveguide and an Etched Ridge Waveguide Interferometer.....	176
5.4.1	Structure of the Interferometric-based Modulator .....	176
5.4.2	Electrooptic Characteristics .....	181
5.4.2.1	The Nature of the Electric Field.....	182
5.4.2.2	The Linear Electrooptic Effect.....	184
5.5	The Effect of Fabrication Parameters on the Operation of the Etched Ridge Waveguide Modulator .....	188
5.6	Electrode Design .....	192
5.6.1	Optical Loss due to the Metal Electrodes.....	192
5.6.2	Electrode Design for Impedance and Velocity Matching .....	193
5.7	Uses of Mach-Zehnder Interferometers for Sensing Devices .....	196
5.8	Summary.....	206

## **6 GaAs/Al<sub>x</sub>Ga<sub>1-x</sub>As Electrooptic Waveguide Modulator .....209**

6.1	Introduction .....	209
6.2	Structure of the Electro-optic GaAs/ Al <sub>x</sub> Ga <sub>1-x</sub> As MZI modulator .....	212
6.2.1	Introduction.....	212
6.2.2	Calculation of the Refractive Indices.....	215
6.2.3	Structure of the Rib Waveguide.....	215
6.3	Electro-Optical Characteristics of the GaAs/Al <sub>x</sub> Ga <sub>1-x</sub> As MZI Modulator ..	221
6.3.1	Calculation of the Electric Field.....	222
6.3.2	Calculation of the Refractive Index Profile under the Influence of an Applied Field .....	225
6.3.3	Calculation and Relevance of the Spot Size Area of the Optical Field .....	231
6.4	Changes in Characteristics with Fabrication Parameters.....	232
6.4.1	Rib Height.....	232
6.4.2	Slant Angle .....	234
6.4.3	Other Fabrication Parameters.....	235
6.5	Summary.....	238

## **7 Discussion and Suggestions for further work .....241**

7.1	General Conclusions .....	241
7.2	Suggestions for future work.....	247

<b>Appendix A1:</b>	Maxwell's Equations .....	249
<b>Appendix A2:</b>	Modal Solutions for Symmetric Domains .....	251
<b>Appendix A3:</b>	Assembly of Element Matrices.....	259
<b>Appendix A4:</b>	The calculation of $\epsilon^{-1}$ .....	266

<b>Appendix B:</b>	Calculation of the General Solution of the Problem of Optical Propagation in a Crystal in the Presence of an External Field along an Arbitrary Direction .....	267
--------------------	--	-----

<b>Appendix C:</b>	Miller Indices.....	276
--------------------	---------------------	-----

<b>Appendix D:</b>	List of Publications by the Author Relevant to the Thesis .....	279
--------------------	---	-----

<b>References</b>	.....	281
-------------------	-------	-----

# List of Tables

- Table 1.1:** Comparison of early LiNbO<sub>3</sub> and semiconductor modulators.
- Table 1.2:** Comparison of device types, using both Ti:LiNbO<sub>3</sub> and semiconductor materials
- Table 1.3:** A comparison between various waveguide modulators (Walker, 1987).  
\*\*\*\*\*
- Table 4.1:** A comparison of  $L_{c0}$ ,  $V_{\pi}$  and  $L_{c0}V_{\pi}$  for three different titanium layer thicknesses for a guide separation,  $s$ , of 7.5 $\mu\text{m}$ .
- Table 4.2:** A comparison of  $L_{c0}$ ,  $V_{\pi}$  and  $L_{c0}V_{\pi}$  for three different diffusion times for a guide separation,  $s$ , of 7.5 $\mu\text{m}$ .
- Table 4.3:** A comparison of  $L_{c0}$ ,  $V_{\pi}$  and  $L_{c0}V_{\pi}$  for three different diffusion temperatures for a guide separation,  $s$ , of 7.5 $\mu\text{m}$ .
- Table 4.4:** A comparison of  $L_{c0}$ ,  $V_{\pi}$  and  $L_{c0}V_{\pi}$  for four different titanium layer widths for a guide separation,  $s$ , of 7.5 $\mu\text{m}$ .
- Table 4.5:** A comparison of  $L_{c0}$ ,  $V_{\pi}$  and  $L_{c0}V_{\pi}$  for three different titanium thicknesses for four guide separations.  
\*\*\*\*\*
- Table 5.1:**  $\beta$  values for optical modes in guide 1 and 2 of the etched ridge waveguide interferometric modulator and the resulting effective index vs mesh size.
- Table 5.2:** A table showing variation in  $V_{\pi}L$  with a number of fabrication parameters.  
\*\*\*\*\*
- Table 6.1:**  $\beta$  values for four different modes in two planar waveguides of thickness  $t_2$  and  $t_1$ , as well as those for a vertical rib waveguide and a slanted rib waveguide structure with similar dimensions.
- Table 6.2:** The change in spot size ( $H_y^{11}$  mode) with applied voltage.
- Table 6.3:** Variation in spot size area and  $V_{\pi}$  with height of AlGaAs rib.
- Table 6.4:** Variation in spot size area and  $V_{\pi}$  with height of AlGaAs rib for the two scenarios given above.
- Table 6.5:** Variation in spot size area and  $V_{\pi}$  with slant angle of the AlGaAs rib.

- Table 6.6:** Variation in spot size area and  $V_\pi$  with thickness of the GaAs guiding layer,  $d_g$ .
- Table 6.7:** Variation in spot size area and  $V_\pi$  with the thickness of the upper  $\text{Al}_x\text{Ga}_{1-x}\text{As}$  layer,  $t_2$ .
- Table 6.8:** Variation in spot size area and  $V_\pi$  with the width of the rib,  $w_r$ .
- Table 6.9:** Variation in spot size area and  $V_\pi$  with percentage of Al in the  $\text{Al}_x\text{Ga}_{1-x}\text{As}$  layers,  $x$ .

# List of Figures

- Figure 1.1:** A basic optical communications system (Gowar, 1984).
- Figure 1.2:** The paths of the light propagating through a slab waveguide, based on the laws of refraction and reflection.
- Figure 1.3:** The refractive index profile for (a) a multilayer planar waveguide and (b) a cylindrical waveguide.
- Figure 1.4:** The boundary at an abrupt interface. The two different media have refractive indices of  $n_1$  and  $n_2$ , respectively, and  $\hat{\mathbf{n}}$  is the unit vector normal to the interface.

\*\*\*\*\*

- Figure 2.1:** An arbitrary shaped optical waveguide, with an arbitrary number of subdomains, each with a different type of material.
- Figure 2.2:** A rectangular dielectric waveguide discretised into linear, triangular, orthodox finite elements. A node and element when using such a linear triangular element have been shown.
- Figure 2.3:** (a) Linear and (b) second order triangular elements (with labelled nodes).
- Figure 2.4:** Pascal's triangle for complete polynomials.
- Figure 2.5:** A linear triangular element with labelled nodes and co-ordinates for this element.
- Figure 2.6:** A simple structure discretised into eight elements. The circled numbers denote the element numbers.
- Figure 2.7:** Part of a rectangular dielectric waveguide (with two-fold symmetry) discretised into finite and infinite elements.

\*\*\*\*\*

- Figure 3.1:** A Y-Branch Modulator.

\*\*\*\*\*

- Figure 4.1:** Layout of the uniform electrode directional coupler.
- Figure 4.2:** Cross-section of uniform electrode  $\Delta\beta$  DC modulator.
- Figure 4.3:** 2-d profile of the permittivity  $\epsilon_e(x,y)$  of the Ti-diffused structure shown in Fig. 4.5.
- Figure 4.4:**  $n_e(x,y)$  at a depth of  $0.676\mu\text{m}$  into the  $\text{LiNbO}_3$  substrate.

- Figure 4.5:** The even supermode profile for a structure with  $t=6$ hours,  $\tau=1000\text{\AA}$  and  $T=1050^\circ\text{C}$ .
- Figure 4.6:** The odd supermode profile for a structure with  $t=6$ hours,  $\tau=1000\text{\AA}$  and  $T=1050^\circ\text{C}$ .
- Figure 4.7:** Coupling length,  $L_{c0}$ , vs no. of elements with  $V=0$ .
- Figure.4.8:** Plots of the  $E_y$  field for symmetric coplanar electrodes at (a)  $y = -0.32\mu\text{m}$ , (b)  $y = -1.03\mu\text{m}$ , (c)  $y = -1.75\mu\text{m}$ , for an applied voltage of 7V.
- Figure 4.9:** A contour plot of the change in the extraordinary refractive index,  $\Delta n_e$ , for an applied field,  $E_y$ .
- Figure 4.10:** Coupling length,  $L_c$ , vs applied voltage for the two directional coupler waveguide separations,  $s$ , of  $7.5\mu\text{m}$  and  $5\mu\text{m}$ .
- Figure 4.11:** The (a) even supermode and (b) odd supermode contour plots of the  $H_x$  field for 7V.
- Figure 4.12:** The odd supermode profile for an increase in diffusion temperature,  $T$ , to  $1075^\circ\text{C}$ .
- Figure 4.13:** The odd supermode profile showing the change with an increase in  $\tau$  to  $1200\text{\AA}$ .
- Figure 4.14:** The odd supermode profile showing the change with a decrease in  $t$  to 4 hours.
- Figure 4.15:** The odd supermode profile showing the change with an increase in  $w$  to  $9.5\mu\text{m}$ .
- Figure 4.16:** The variation of  $L_{c0}$  with  $w$ .
- Figure 4.17:** The variation in mean mode size with  $w$ .
- Figure 4.18:** Coupling length,  $L_{c0}$ , switching voltage,  $V_\pi$ , and the product of coupling length and switching voltage,  $L_{c0} V_\pi$ , vs waveguide separation,  $s$ .
- Figure 4.19:** Coupling length,  $L_{c0}$ , switching voltage,  $V_\pi$ , and the product of coupling length and switching voltage,  $L_{c0} V_\pi$ , vs buffer layer thickness,  $d$ .
- Figure 4.20:** (a) The applied field,  $E_y$ , with variation in electrode spacing,  $e$ , and (b) The variation of switching voltage,  $V_\pi$ , with electrode separation,  $e$ .
- Figure 4.21:** The optical loss (for a quasi-TM mode) due to the electrodes,  $\alpha$ , vs buffer thickness,  $d$ , for the gold and aluminium electrodes of thickness,  $t_e=0.15\mu\text{m}$ .

- Figure 4.22:** The optical loss due to gold electrodes vs buffer layer thickness,  $d$ , for both TE and TM polarised light for  $t_e=0.15\mu\text{m}$ .
- Figure 4.23:** An isolated guide butt-coupled (section I) to the directional coupler (section II).
- Figure 4.24:** Supermode coefficients indicating the amplitude of the even and odd modes,  $b_1$  and  $b_2$ , respectively, in guide 2.
- Figure 4.25:** The variation in power in guide 1,  $P_1$ , and in guide 2,  $P_2$ , with  $z$ , for no applied voltage and an applied voltage of  $V_\pi$  ( $z$  is varied from 0 to  $L_{c0}$ ).
- Figure 4.26:** Mode profile for the Ti:LiNbO<sub>3</sub> directional coupler modulator for no applied voltage at (a)  $z=0$ , (b)  $z=L_{c0}$ , (c)  $z=2L_{c0}$ .
- Figure 4.27:** Mode profile for the Ti:LiNbO<sub>3</sub> uniform electrode  $\Delta\beta$  directional coupler modulator for an applied voltage of  $V_\pi$  at (a)  $z=0$ , (b)  $z=L_c=L_{c0}/2$ , (c)  $z=2L_c=L_{c0}$ .
- Figure 4.28:** Maximum power transfer from guide 2 to guide 1 of the  $\Delta\beta$  directional coupler, and the output power in guide 1 for a waveguide separation of  $7.5\mu\text{m}$ .
- Figure 4.29:** The variation in power in guide 1,  $P_1$ , and in guide 2,  $P_2$ , with  $z$  for an applied voltage of 12.1V ( $z$  is varied from 0 to  $L_{c0}$ ).
- Figure 4.30:** Mode profile for the Ti:LiNbO<sub>3</sub> uniform electrode  $\Delta\beta$  directional coupler modulator for an applied voltage of 12.1V at (a)  $z=0$ , (b)  $z=L_c=L_{c0}/3$ , (c)  $z=2L_c=2L_{c0}/3$ , (d)  $z=3L_c=L_{c0}$ .

\*\*\*\*\*

- Figure 5.1:** Structure for a Y Branch Modulator.
- Figure 5.2:** The structure of the unetched Ti:LiNbO<sub>3</sub> channel waveguide.
- Figure 5.3:**  $\beta$  vs no. of elements, for the cases when only  $n_x$  is changed (with  $n_y$  held constant), when only  $n_y$  is changed (with  $n_x$  held constant) and when both  $n_x$  and  $n_y$  are varied.
- Figure 5.4:** The diffusion profile of the single Ti:LiNbO<sub>3</sub> diffused channel waveguide.
- Figure 5.5:** Optical mode for the channel Ti:LiNbO<sub>3</sub> waveguide.
- Figure 5.6:** The structure of the etched Ti:LiNbO<sub>3</sub> ridge waveguide.
- Figure 5.7:** The diffusion profile of the etched ridge waveguide
- Figure 5.8:** Optical mode for the etched ridge Ti:LiNbO<sub>3</sub> waveguide.

- Figure 5.9:** The resulting instability in radiation loss along the  $90^\circ$  circular bend when BPM parameter  $\theta$  is taken to have a value of 0.5.
- Figure 5.10** The change in radiation loss,  $\Delta\alpha_r$ , with increasing BPM parameter  $\theta$ .
- Figure 5.11:** The variation in radiation loss with a decreasing reflection coefficient,  $R$ , at the interface between the computational domain and the PML for three bends of differing radii,  $r$ .
- Figure 5.12:** The variations in  $\beta$  and the variation in radiation loss with the number of elements of the mesh for a  $90^\circ$  circular bend with a 10mm radius.
- Figure 5.13:** The optical field at the output of a  $90^\circ$  circular bend for a 7mm radius for the unetched waveguide MZI modulator.
- Figure 5.14:** The optical field (a)  $\frac{1}{4}$ , (b) halfway, (c)  $\frac{3}{4}$  along and (d) at the output of a  $90^\circ$  circular bend for a 7mm radius for the etched ridge waveguide MZI modulator of etch depth  $4.5 \mu\text{m}$ .
- Figure 5.15:** Radiation loss vs  $\vartheta$  for the unetched MZI modulator, and the etched ridge waveguide MZI modulator for ridge height of  $3.5\mu\text{m}$  and  $4.5\mu\text{m}$ , all of which have a bending radius of 7mm.
- Figure 5.16:** Radiation loss for a  $90^\circ$  circular bend vs the radius of the bend for an unetched MZI modulator and etched MZI modulators with etch depths of  $3.5\mu\text{m}$  and  $4.5\mu\text{m}$ .
- Figure 5.17:** The layout of both the unetched and etched Mach-Zehnder interferometric (MZI) modulators.
- Figure 5.18:** The cross-section of the unetched MZI modulator.
- Figure 5.19:** The cross-section of the etched MZI modulator with etch depth,  $h$ .
- Figure 5.20:** The diffusion profile of the Ti:LiNbO<sub>3</sub> channel waveguide interferometric modulator.
- Figure 5.21:** Quasi-TM fundamental near-degenerate optical modes for the two guides of the Ti:LiNbO<sub>3</sub> channel waveguide interferometric-based modulator.
- Figure 5.22:** Diffusion profile of the Ti:LiNbO<sub>3</sub> etched ridge waveguide interferometric-based modulator.
- Figure 5.23:** Quasi-TM fundamental near-degenerate optical modes for the two guides of the Ti:LiNbO<sub>3</sub> etched ridge waveguide interferometric-based modulator.

- Figure 5.24:** The  $E_y$  component of the modulating electric field  $\mathbf{E}$  for the unetched MZI modulator for an applied voltage of 5V.
- Figure 5.25:** The  $E_y$  component of the modulating electric field  $\mathbf{E}$  for the etched MZI modulator with ridge height of  $3.5\mu\text{m}$  for an applied voltage of 5V.
- Figure 5.26:** The change in refractive index due to an applied electric field,  $\Delta n_e(x,y)$ , for an applied voltage of 5V for the unetched MZI modulator.
- Figure 5.27:** The change in refractive index due to an applied electric field,  $\Delta n_e(x,y)$ , for an applied voltage of 5V for the etched MZI modulator with ridge height of  $3.5\mu\text{m}$ .
- Figure 5.28:**  $V_\pi L$  vs ridge height,  $h$ , for the etched MZI modulator, showing the optimum  $h$  for such a structure.
- Figure 5.29:** Optical loss due to metal electrodes vs buffer layer thickness for 3 electrode thicknesses of  $0.15\mu\text{m}$ ,  $1.0\mu\text{m}$  and  $10\mu\text{m}$  and  $V_\pi L$  vs buffer layer thickness, for the etched MZI modulator with a  $4.5\mu\text{m}$  ridge height.
- Figure 5.30:** The microwave effective index,  $n_m$ , and characteristic impedance of the electrodes,  $Z_c$ , vs buffer layer thickness,  $d$ .
- Figure 5.31:** The conductor loss,  $\alpha_c$  vs buffer layer thickness,  $d$ , for a number of electrode thicknesses,  $t_e$ , and ridge heights,  $h$ .
- Figure 5.32:** Schematic of the Mach-Zehnder interferometer considered: (a) layout and (b) cross-section.
- Figure 5.33:** Diffusion profile for the Mach-Zehnder interferometer shown in Fig. 5.32.
- Figure 5.34:** Degenerate quasi-TE fundamental optical modes at  $V=0$ .
- Figure 5.35:** Degenerate quasi-TE fundamental optical modes at  $V=V_\pi$ .
- Figure 5.36:** Variation of  $\Delta\phi$  and  $L_\pi$  with sensing voltage,  $V$ .
- Figure 5.37:** Variation of the sensing field,  $E_x$ , along the waveguide centre, for an applied voltage of 10V.
- Figure 5.38:** The spatial profile of the refractive index change,  $\Delta n$ , for a given applied voltage,  $V=10\text{V}$  when: (a)  $w=16\mu\text{m}$  and (b)  $w=6\mu\text{m}$ .
- Figure 5.39:** Variation of  $\Delta\phi$  with different electrode gaps,  $e$ .

\*\*\*\*\*

- Figure 6.1:** (a) The layout and (b) a single arm of the Mach-Zehnder Interferometer structure.

- Figure 6.2:** Cross-section of a (a) vertical rib waveguide (b) slanted rib waveguide.
- Figure 6.3:**  $\beta$  vs mesh size for both the fundamental quasi-TE and TM modes at  $V=0$  for the vertical rib waveguide.
- Figure 6.4:** Optical field profile of the fundamental  $H_y^{II}$  mode at  $V=0$  for a vertical rib waveguide.
- Figure 6.5:** Optical field profile of the fundamental  $H_y^{II}$  mode at  $V=0$  for a slanted rib waveguide.
- Figure 6.6:** A 3-d plot of the magnitude of the  $E_y$  component of the applied electric field across the device at 10V.
- Figure 6.7:** A view of the magnitude of the  $E_x$  component of the applied electric field across the device at 10V.
- Figure 6.8:** A view of the magnitude of the  $E_y$  component of the applied electric field at two cross-sections in the device.
- Figure 6.9:** The contour profile  $\Delta n(x,y)$  for an applied voltage of 10V for the slanted rib device.
- Figure 6.10:** The variation of  $\Delta\beta$  with the applied voltage.
- Figure 6.11:** The fundamental quasi-TE optical mode for an applied voltage of 10V for the slanted rib device.
- Figure 6.12:** The fundamental quasi-TE optical mode for an applied voltage of 10V for the vertical rib device.

# *Acknowledgements*

I would like to express my deepest gratitude to my two supervisors, Professors B.M.A. Rahman and K.T.V. Grattan, for their assistance, guidance and support throughout the project and the writing up process of this thesis.

I am also grateful to the EPSRC for funding this project.

My thanks are also due to my family for their support and constant encouragement, and my many colleagues for creating an enjoyable and work-conducive atmosphere. Also, many thanks to the secretarial and technical staff of the Electrical, Electronic and Information Engineering Department, who have always been extremely helpful.

## *Declaration*

I grant powers of discretion to the University Librarian to allow this thesis to be copied in whole or in part without further reference to the author. The permission covers only single copies made for study purposes, subject to normal conditions of acknowledgement.

# *Abstract*

An electro-optic modulator is an essential part of an optical communications system. An ideal modulator would have low drive voltage, large bandwidth, small size, low insertion loss, a very high extinction ratio, very low chirp and low power consumption. However, there is a trade-off between some of these characteristics, and consequently the modulator is designed with a compromise. It is due to these complex devices that computer modelling has become a necessary and integral part of device design, which is made easier and more economically acceptable by the larger capacities of today's computers.

In this work, a finite element method-based approach is used to design and develop computer programs in order to simulate the major characteristics of electro-optic modulators (i.e. low drive voltage, a large bandwidth, small size, low insertion loss) and fabrication variables and combine these separate computer programs into one complete suite to model electro-optic waveguide modulators for a good and complete design process for these devices. The devices examined in this work are the Ti:LiNbO<sub>3</sub> directional coupler-based modulator, the Ti:LiNbO<sub>3</sub> Mach-Zehnder interferometric modulator and a GaAs/AlGaAs interferometric-based electro-optic modulator.

These computer programs give the optical mode for each of the devices examined in this work both before and after application of an electric field, giving exact values for the refractive and any change in refractive index with applied electric field. In this way it is the drive voltage and size of the device that can be adjusted and examined in order to obtain an optimum design. The electrode design is important to modulators particularly bandwidth but is also essential for decreasing optical loss without increasing the drive voltage. A program was designed and developed using a perturbational approach in order to model this optical loss. For the Ti:LiNbO<sub>3</sub> directional coupler based modulator, the light coupling process between the two adjacent waveguides as well as the power transfer efficiency were also modelled using a FEM LSBR-based approach. However, the directional coupler based devices are slower than their MZI-based counterparts. A Ti:LiNbO<sub>3</sub> MZI-based modulator was also studied with both channel and ridge waveguides. It was found that a ridge waveguide is optimally beneficial only if the FWHM (width and height) of the mode fit into the ridge. The bending waveguides at the input and output of the Ti:LiNbO<sub>3</sub> MZI-based modulator were modelled using a FEM BPM-based approach. This approach yields accurate results for structures where the cross-section of the device is changing. A computer program was also developed to incorporate the RF characteristics of the device in order to find the bandwidth of the device for perfect velocity and impedance matching conditions. Furthermore, smaller studies were undertaken for a Ti:LiNbO<sub>3</sub> MZI-based modulator for electrical sensing applications as well as for a GaAs/AlGaAs interferometric-based modulator.

The main work of this thesis was to improve these device structures in order to provide optimal results. The suite of computer programs yielded results very close and similar to that examined in the literature.

Most importantly, the computer modelling approach to device design yields accurate results for both simple and more complex devices structures and is a cheaper long-term approach to device design.

# *Symbols and Abbreviations*

2-d	Two-dimensional
III-V	Bonding of semiconductor materials from Groups III and V in the Periodic Table
APE	Annealed Proton Exchanged
BPM	Beam Propagation Method
CMT	Coupled Mode Theory
CPU	Central Processing Unit
CPW	Coplanar Waveguide
cw	continuous wave
dc	direct current
DC	Directional Coupler
DBR	Distributed Bragg reflector
DFB	Distributed Feedback
DOS	Digital Optical Switch
DWDM	Dense Wavelength Division Multiplexing
EA	Electroabsorption
EAM	Electroabsorption Modulator
ECR	Electron Cyclotron Resonance
EO	Electro-optic
FEM	Finite Element Method
FKE	Franz-Keldysh Effect
FSK	Frequency Shift Keying
FWHM	Full Width Half Maximum
HFEM	vector H-field Finite Element Method
ITU	International Telecommunication Unit
I/O	Input/Output
LED	Light Emitting Diode
LSBR	least squares boundary residual
MQW	Multiple Quantum Well
MMI	Multimode Interference
MZI	Mach-Zehnder Interferometer

ODE	Ordinary Differential Equation
PDE	Partial Differential Equation
PML	Perfectly Matched Layers
QEO	Quadratic Electro-optic
QW	Quantum Well
RF	radio frequency
SOA	Semiconductor Optical Amplifier
SVFEBPM	Semi-Vectorial Finite Element Beam Propagation Method
TE	Transverse Electric
TEM	Transverse Electromagnetic
TIR	Total Internal Reflection
TM	Transverse Magnetic
TW	Travelling Wave
WDM	Wavelength Division Multiplexing
Al	Aluminium
BaTiO <sub>3</sub>	Barium Titanate
Fe	Iron
GaAs	Gallium Arsenide
AlGaAs	Aluminium Gallium Arsenide
GaAs/AlGaAs (or GaAs/Al <sub>x</sub> Ga <sub>1-x</sub> As)	Gallium Arsenide/ Aluminium Gallium Arsenide
GaAs/[(InAs)(GaAs)]	Gallium Arsenide/superlattices of Indium Arsenide and Gallium Arsenide
GaN/InGaN	Gallium Nitride/ Indium Gallium Nitride
GaP	Gallium Phosphide
Ge	Germanium
HeNe	Helium Neon
InGaAlAs/InAlAs	Indium Gallium Aluminium Arsenide/ Indium Aluminium Arsenide
InGaAs/InAlAs	Indium Gallium Arsenide/ Indium Aluminium Arsenide
InP	Indium Phosphide
InP/InGaAs	Indium Phosphide/ Indium Gallium Arsenide

InP/InGaAlAs	Indium Phosphide/ Indium Gallium Aluminium Arsenide
InP/InGaAsP	Indium Phosphide/ Indium Gallium Arsenide Phosphide
KDP	Potassium Dihydrogen Phosphate
LiNbO <sub>3</sub>	Lithium Niobate
Li <sub>2</sub> O	Lithium Oxide
LiTaO <sub>3</sub>	Lithium Tantalate
Si	Silicon
SiO <sub>2</sub>	Silicon Dioxide
Ti	Titanium
Ti:LiNbO <sub>3</sub>	Titanium (diffused) Lithium Niobate
$b_{1,2}$	coefficients of the transmitted even and odd supermodes (LSBR)
$C_l$	capacitance from sensor to high voltage line
$C_g$	capacitance from the sensor to ground
$d_g$	thickness of the GaAs guiding layer
$d_{x,y}$	the diffusion length along the $x,y$ axes given by $2\sqrt{D_{x,y}t}$
$D_o$	diffusion constants along the $x,y$ axes, and depend on the crystal cut
$e$	electrode separation
$E_o$	activation energies in the $x, y$ directions
$\mathbf{E}$	full vector electric field ( $E_x, E_y, E_z$ )
$\mathbf{E}_t$	transverse components of the $\mathbf{E}$ field ( $E_x, E_y$ ) – $z$ being the direction of propagation
$E$	electric field
$E_{x,y}(x,y)$	profile of the $x,y$ components of the applied electric field
$E_{x,y}$	$x,y$ components of the applied electric field
$E_z$	electric field along $Z$ in terms of the crystal axes
$\Delta f$	bandwidth
$h$	height of rib for an etched ridge waveguide (device)
$\mathbf{H}$	full vector magnetic field ( $H_x, H_y, H_z$ )
$\mathbf{H}_t$	transverse components of the $\mathbf{H}$ field ( $H_x, H_y$ ) – $z$ being the direction of propagation

H	magnetic field
$H_x^{pq}$	general symbolic representation of a quasi-TM mode
$H_y^{11}$	symbolic representation of a fundamental quasi-TE mode
$k$	wavenumber
$k_0$	free space wavenumber and is given by $\omega\sqrt{\epsilon_0\mu_0}$
$L$	interaction length (or length of electrodes)
$L_c$	coupling length
$L_{c0}$	original coupling length (when $V=0$ )
$L_\pi$	length of electrode in order to obtain $V_\pi$
$n$	refractive index
$n(x,y)$	refractive index profile
$n_e$	extraordinary index
$n_e(x,y)$	extraordinary index profile
$\Delta n(x,y)$	change in the refractive index profile
$\Delta n_e$	change in the extraordinary index
$\Delta n_o$	change in the ordinary index
$n_{X,Y,Z}$	refractive indices along the principal dielectric axes (of the crystal)
$\hat{\mathbf{n}}$	unit normal vector
$\mathbf{N}$ or $[\mathbf{N}]$	shape function matrix
$n_{eff}$	optical effective index of waveguide
$n_{ele}$	total number of elements
$n_m$	microwave effective index of waveguide
$n_p$	total number of nodes
p-n (or p-i-n)	p-n (or p-i-n) junction modulator – for clearer definition see Chapter 3
$P_{1,2}(z)$	power fraction in guide 1 or 2, respectively
$P_{max}$	maximum power transferable from guide 2 to guide 1
$P_o$	the power output at the end of guide 1
$r_{ij}$	the electro-optic tensor (or components of the electro-optic tensor) of a dielectric material
$R$	theoretical reflection coefficient at the interface between the computational domain and the PML

$s$	the gap between the two guides of the directional coupler (edge-to-edge)
$t$	diffusion time in hours
$T$	diffusion temperature in Kelvin
$t_{1,2}$	see Fig 6.2 for definition
$t_e$	electrode thickness
$t_{tot}$	total thickness of epilayer between electrodes
$V$	applied voltage
$V_\pi$	half wave (or drive) voltage
$V_\pi L$	figure of merit for modulators (half wave voltage length product)
$w$	width of the titanium layer or the effective width of the guide
$w_b$	width of the base of the rib for a slanted etched ridge waveguide (device)
$w_r$	width of rib for an etched ridge waveguide (device) or upper width of rib for a slanted etched ridge waveguide (device)
$w_{x,y}$	1/e intensity full width along $x$ and $y$ , respectively
$Z_c$	characteristic impedance of the electrode
$Z_o$	the characteristic impedance of the device/ waveguide
$\Delta z$	propagation step size
$\alpha$	attenuation constant
$\alpha$	optical loss due to the metal electrodes
$\alpha_t$	penalty coefficient
$\alpha_c$	conductor loss of the electrodes of the optical waveguide device
$\alpha_{ch}$	chirp parameter
$\alpha_r$	radiation loss for a circular bend
$\alpha_{wf}$	weighting factor used in LSBR
$\beta$	propagation constant (for lossless medium)
$\beta_{e,o}$	propagation constant for the even and odd modes, respectively
$\beta_{1,2}$	propagation constant in individual waveguides 1 and 2, respectively
$\Delta\beta$	change in propagation constant
$\gamma = \alpha + j\beta$	propagation constant (for lossy medium)
$\Gamma$	overlap of the optical and electric fields

$\hat{\epsilon}$	permittivity tensor
$\epsilon$	permittivity of the material given by $\epsilon_r \epsilon_0$
$\epsilon_r$	dielectric constant of the material
$\epsilon_g$	dielectric constant of the core of the optical waveguide
$\epsilon_0$	dielectric constant in free space
$\epsilon_{xx}, \epsilon_{yy}, \epsilon_{zz}$	diagonal non-zero components of the permittivity tensor, $\hat{\epsilon}$
$\Delta\phi$	phase difference between the two waveguides (or arms) of the interferometer
$\kappa$	coupling coefficient which describes the strength of the interguide coupling
$\lambda$	wavelength
$\lambda_g$	guide wavelength ( $=\lambda/n_{eff}$ )
$\hat{\mu}$	permeability tensor
$\mu$	permeability of the material given by $\mu_r \mu_0$
$\mu_0$	permeability constant in free space
$\theta$	propagation step parameter (where $\theta \geq 0.5$ )
$\vartheta$	distance in degrees around the circular optical bend
$\theta_r$	slant angle of rib
$\rho$	resultant charge due to applied voltage
$\tau$	thickness of the titanium layer
$\omega$	angular frequency
$\omega^2$ (or $\lambda$ )	eigenvalue
$\Omega$	domain over which integration to be carried out – which for this thesis is waveguide cross-section
$\psi$	scalar potential of device

# 1

## *Introduction*

---

---

### **1.1 Aims of the Thesis**

From the background work given in this thesis, it should be clear that directional coupler devices and Mach-Zehnder interferometric based devices (single arm or push-pull fashion) are amongst the most commonly used for optical devices. Also, that LiNbO<sub>3</sub> devices are still among the best modulator devices with present estimates at 75GHz bandwidths. However, due to there not being any possibility of integration of LiNbO<sub>3</sub> devices with semiconductor devices (i.e. source and detector), there has been interest in GaAs electro-optic modulators, with bandwidths expected to be in excess of 40GHz. Moreover, from the numerical modelling methods available it is quite clear that the **H**-field vector formulation finite element method (HFEM) is one of the most powerful and versatile methods with the availability to involve an arbitrary shape of waveguide device or any arbitrary refractive index profile in the modelling technique.

So the primary aims of the work in this thesis are:

1. To investigate established work on Ti:LiNbO<sub>3</sub> devices and determine which are the best device and material configurations for electro-optic modulators.

Moreover, in the light of this, to determine the best method with which to model these devices.

2. To take an existing **H**-field full vectorial finite element method modal solver package for isotropic waveguides and develop it for an anisotropic, inhomogeneous (e.g. Ti:LiNbO<sub>3</sub>) electro-optic modulator. The package could then be extended to include other modulator device types (e.g. Mach-Zehnder interferometric based devices) and other material configurations (e.g. GaAs/AlGaAs).
3. To develop a scalar finite element based Laplace solver to find the two-dimensional electric field profile in the cross-section of the device (which is uniform in the active region), and to ensure that this solver can also be extended to include other electro-optic modulators and anisotropic materials.
4. To develop a program to model the change in the refractive index due to the linear electro-optic effect in an anisotropic inhomogeneous material and ensure that this can be extended for use in all electro-optic modulating devices and material configurations.
5. To examine any changes in the device characteristics with changes in the fabrication parameters, and note any significance in these changes.
6. To determine the benefit of using electro-optic semiconductor (GaAs/Al<sub>x</sub>Ga<sub>1-x</sub>As) materials compared with Ti:LiNbO<sub>3</sub>.
7. To include as many features as possible as are important to the fabrication and characterisation of these devices:
  - Power transfer efficiency of two-dimensional directional couplers.  
This would be calculated using an existing LSBR approach.
  - Optical loss due to metal electrodes  
This would be calculated by developing an existing **H**-field finite element method package for optical waveguides, which uses a perturbational approach to incorporate loss, to include directional coupler based and Mach-Zehnder interferometric based electro-optic modulators.
  - Calculation of radiation loss in the input and output waveguide bends of directional coupler and Mach-Zehnder interferometric based electro-optic modulators

This would be achieved by developing an existing semi-vectorial beam propagation method approach, using perfectly matched layers, to include diffused anisotropic refractive index waveguides.

- Calculation of RF properties of the electrodes

This would be achieved for the Ti:LiNbO<sub>3</sub> Mach-Zehnder interferometric-based modulator device using an extension of the above-mentioned Laplace solver, and to model electrode properties.

All these aspects have been included into the model of an electro-optic modulator with the aim of obtaining as complete a model for these devices as possible. This is the aim for any package with which to model devices. Although many aspects may have been covered for different types of devices, to the author's knowledge this is the first time that all these major features have been included in the model of an electro-optic modulator. There are other more minor features of an electro-optic modulator which can also be added, but these have been left for further work for a new member of the group to undertake.

## 1.2 Structure of the Thesis

This thesis covers the work produced by the author. The finite element method was used in conjunction with the least squares boundary residual (LSBR) method and the beam propagation method (BPM) as well as a perturbation technique to find the characteristics of various electro-optic modulators. A review of the contents of the work presented in this entire thesis, including this introductory chapter is given below:

*Chapter 1*, the Introduction, contains a brief history of lightwave technology with respect to the components of a basic optical communications system, with a simple review/ history of the optical fibre, laser and photodetector. The prevalence of optoelectronics is also noted. This is followed by an introduction to optical waveguide theory including Maxwell's equations and the associated boundary conditions, and it is shown how these are rearranged to form the wave equation. A review of a number of

analytical and numerical methods available to model these waveguides with their associated advantages and disadvantages has also been given. The Chapter ends with the aims of the project and this section on the structure of the thesis.

**Chapter 2** contains a detailed picture of the finite element method for 2-dimensional waveguide devices, starting with a brief history of this method. The variational formulations for the vector and scalar **H**-field wave equations are also examined and a comparison of several other formulations for these wave equations has been made. The different types of elements available through this method have also been mentioned, and it is then suggested that the first-order triangular element approach is a better choice for the devices which are to be studied in later chapters. The assembly of the matrices for individual elements is detailed and it is shown how the area co-ordinates and the shape functions of these elements are important to the numerical procedure.

It has also been shown that the occurrence of spurious modes in vector formulations can be substantially reduced (if not totally removed) by the penalty method. This, as well as the modelling of the open space of the waveguide, as the waveguide is essentially an unbounded electromagnetic problem, is one of the most important considerations when choosing a numerical method. The finite element method can be used to model the open space in the form of the infinite element, which has an exponentially decaying function.

The assembly of the global matrix leads to a sparse matrix, which can then be manipulated into a one-dimensional array which contains only the non-zero elements of the matrix. This leads to a faster matrix solution with the use of intelligent matrix solvers.

The approach towards the whole chapter is to show the true versatility of the finite element method.

In **Chapter 3**, the important aspects of the device fabrication have been given in more detail in the first section, with emphasis placed on the channel Ti:LiNbO<sub>3</sub> waveguide fabrication, the etching processes involved in the making of the Ti:LiNbO<sub>3</sub> ridge waveguide, as well as electrode fabrication, together with an initial section detailing the

advantages and disadvantages of LiNbO<sub>3</sub>. Note that the terms ‘ridge waveguide’ and ‘rib waveguide’ mean the same and are interchangeable.

The aspects and methods of modelling the Ti indiffusion process into the LiNbO<sub>3</sub> crystal have then been given followed by a description of the numerical methods used to calculate the insertion loss of the waveguide. The importance of electrode design to the drive voltage and both electrical and optical 3dB bandwidth is discussed in a subsequent section, and calculation of these bandwidths has been given for the optimum case of an impedance and velocity-matched Ti:LiNbO<sub>3</sub> electro-optic modulator.

**Chapter 4** first contains a review of the types of directional coupler modulator available, as well as a theoretical analysis of uniform  $\Delta\beta$  directional coupler modulators. This is followed by a detailed calculation of the refractive indices for the Ti indiffused LiNbO<sub>3</sub> waveguides and the two-dimensional diffusion profile of the permittivity, refractive index profile at a certain depth in the LiNbO<sub>3</sub> crystal. The odd and even supermodes for this structure are also given, where the term supermode is associated with the optical modes of the coupled waveguide system. A calibration exercise involving the coupling length and mesh size is also given to show that the mesh used for the FEM throughout the chapter should give stable results. The effect of the applied electric field on the change in refractive index is given in the next section; and how this affects the mode profiles of the light through the device, as well as the coupling length are also given.

The importance of the diffusion process is shown by observing the variation in the coupling length for no applied voltage,  $L_{c0}$ , and a drive voltage or half wave voltage,  $V_{\pi}$ , with variation in the diffusion parameters. This is followed by a study of the variation in the figure of merit for modulators,  $V_{\pi} L_{c0}$ , with the fabrication parameters. Next, the nature of the loss due to the metal electrodes is shown. Lastly, the theory supporting the transfer of the light from one waveguide to the other for strongly coupled devices, such as the one studied in this chapter, is given followed by results showing both the propagation of the optical (super)modes through the device and the power transferred from one waveguide to the other along the length of the device.

The theory of Y-branch interferometric modulators is given in **Chapter 5**, together with a review of the variations between these and other interferometric based devices or other

types of 3dB couplers typically used with this type of device. In this chapter a comparison is made between the channel waveguide Ti:LiNbO<sub>3</sub> modulator and the etched ridge Ti:LiNbO<sub>3</sub> waveguide modulator. This is preceded by a more detailed description than given in Chapter 4 of the several methods which have been used to calculate the refractive indices of these waveguides in the available literature. This is followed by a calibration type exercise to find the optimum mesh size (for the FEM) to be used in this study. A comparison of the diffusion profiles and optical modes in a single waveguide was given for both the channel and ridge Ti:LiNbO<sub>3</sub> waveguides. Next is a detailed study comparing the radiation loss from both channel waveguide and ridge waveguide 90° optical bends using the BPM. Included in this study is the observation of the optimum value of the key BPM parameters used to calculate radiation loss.

The 2-d refractive index profile, the quasi-TM modes for the interferometric modulator and the difference in the layout of the applied electric field for both types of waveguide modulator are given. A detailed section on the theory of the linear electro-optic effect has also been given, and the difference in the change in refractive index with applied electric field has been shown for both modulators. This is followed by a study of the way in which the fabrication parameters affect the device performance. The electrode design affects both the bandwidth as well as the electrode loss and  $V_{\pi}$ . The effect of variation of electrode parameters with  $V_{\pi}$  was given, followed by the variation of optical loss due to the electrodes with changes in electrode thickness and buffer layer thickness. For travelling wave modulators, the electrodes resemble transmission lines. The impedance and phase (or velocity) matching conditions are studied here to find the optimum electrode design for the modulator.

There is wide use of interferometric devices for optical sensors, and the last section of the chapter examines the use of an  $X$ -cut Ti:LiNbO<sub>3</sub> device for the purpose of electrical sensing. The  $X$ -cut substrate is used because it is reported to be much more stable than the  $Z$ -cut LiNbO<sub>3</sub> substrate which is more prone to bias drift due to mainly pyroelectric effects, and stability is essential for sensing devices.

In **Chapter 6** an electro-optic GaAs/Al<sub>x</sub>Ga<sub>1-x</sub>As interferometric modulator is studied. The material, although semiconductor, can be very similar to a dielectric material if it is

unintentionally doped. Again, as for previous studies, the refractive indices for the material are calculated, and the phase propagation constant,  $\beta$ , was studied with the mesh size to determine a stable mesh size in order to obtain more reliable results. The optical mode for a vertical rib and slanted rib device were then compared and the spot sizes of these shallow rib waveguides examined. This was followed by a study of the nature of the applied electric field and the subsequent change in refractive indices. The relationship of the spot size with applied voltage was then examined, as was that of the half wave voltage,  $V_{\pi}$ , and the spot size with changes made to the rib height or the slant angle of the rib.

**Chapter 7** contains the final conclusions of the work, and suggestions for further work.

### 1.3 Photonics: an historical perspective

Light has been used as a form of communication from the time of the most primitive civilisations, to send information over long distances by reflected sunlight or smoke signals during the day or fire beacons from mountain top to mountain top at night (Gowar, 1984). This continued over the intervening centuries until Claude Chappe, in the 1790s, came up with the idea of an ‘optical’ telegraph (Hecht, 1999a), which used the concept of semaphores. By the 1800s the use of the electric telegraph overtook all land-based communications, while signalling from shuttered lamps was still used at sea. This would later be replaced by wireless telegraphy and the telephone. It was the dawning of the age of electrical communications. These electrical systems were much superior to any optical techniques used for communications and this trend would continue for the next century or so.

An interesting development for optical communication that occurred in the 1880s was the ‘photophone’, designed and patented by Alexander Graham Bell four years after the telephone. This operated on the principle that the speech (signal) modulated the sunlight (carrier) by a reflecting mirror/diaphragm. The signal was then transmitted over a distance of about 200m (through air) where a selenium photocell (detector) converted the modulated sunlight back to an electrical signal which was then converted back to

sound via a loudspeaker (demodulation). From Fig. 1.1, the photophone is recognisable as a basic optical communications system, where air is the transmission medium.

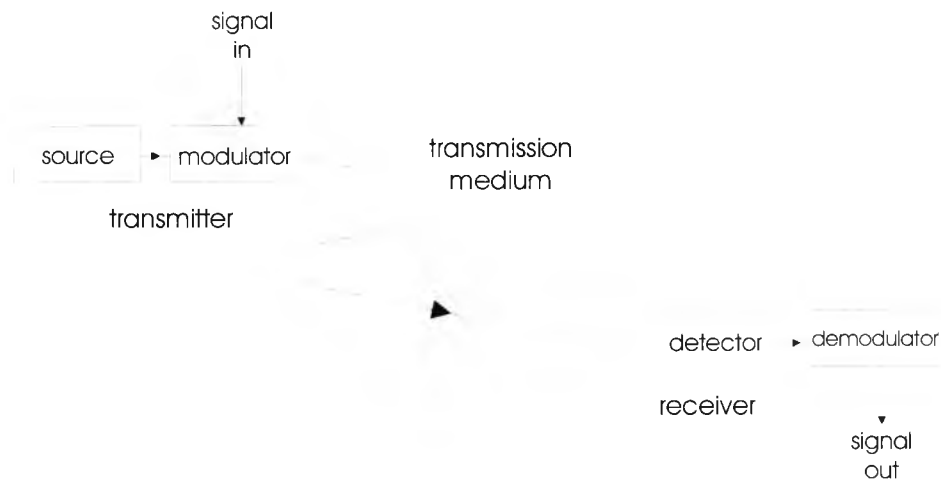


**Fig. 1.1** A basic optical communications system (Gowar, 1984).

However, there were associated limitations with atmospheric optical communications, and these are as much true today as then (Johnson, 2001). Briefly, these are weather conditions (e.g. at times thick fog, rain or snow may be severe enough to block the light path and interrupt communications), need for clear line of sight paths between transmitter and receiver and the positioning of the receiver so that the sun's rays do not diminish the signal to noise ratio for the detector. Hence, there was need for a medium other than air, that was not so dependent on external effects, for fast long distance optical communications.

Although this project is involved with electro-optical modulation of light, each component of the basic optical communications system shown in Fig. 1.1 is in itself equally important, and so a little background information on these will be given at this stage.

### 1.3.1 Developments in Optical Fibres

From the mid-nineteenth century it had been found by a number of inventors that glass rods could guide light (Hecht, 1999b), although it is thought that the Greeks were the first to discover that glass could guide light (Mickelson, 1993). It was, however, John Tyndall who in 1854 revealed the light guiding mechanism of total internal reflection

(TIR) in these rods (Lucent Technologies, 2000). Towards the end of the 19<sup>th</sup> century two Austrian medical scientists found that curved glass rods were useful for illuminating body cavities. This launched the field of medical optics. However, at this stage the glass rods only relied on the air-glass interface to act as the surface at which TIR took place. In 1954, a scientist, van Heel, from the Delft Technical University in Holland, first proposed the idea clad glass fibres of in *Nature* (van Heel, 1954), where the cladding material had a refractive index lower than the inner 'core' material, such that guiding could occur. However, the attenuation loss in these fibres, even by 1960, was still too high, at 1000dB/km, to use for optical communications - although fine for medical endoscopy (Kapany, 1967). In 1966, Kao and Hockham (1966) proposed that through the use of single mode fibres the attenuation losses would soon be down to 10-20dB/km, based on the experimental findings of the group. This was not achieved till 1970 when Corning made single mode fibres that had an attenuation loss of 17dB/km, using a 633nm HeNe laser source (Hecht, 1999a). This major breakthrough for optical communications was achieved by using fused silica, a material which can be made extremely pure, instead of the compound glasses used in standard optics, which had previously been used to make optical fibres. There were several subsequent developments in optical fibres (Hecht, 1999a) over the next decade, including the use of graded index fibres, the discovery of the two optical communication 'windows' at 1.3 $\mu$ m and 1.55 $\mu$ m at which there is negligible dispersion and very low loss ( $\sim$ 0.2dB/km), respectively, in the optical fibre. This allowed loss-limited spans of 100km or more to be achieved and the result of this was that the span length between regenerators could be 40km or more using conventional fibre (Brinkman *et al.*, 2000).

Apart from the continual improvement of this transmission media over the intervening years, such that the ability to send terabits per second through a single optical fibre, which was achieved at Fujitsu, NTT and Bell Labs (Hecht, 1999b) consecutively, one of the other most significant development in the field of fibre optics in the 1990s was that of erbium-doped fibre amplifiers. The outcome of this was that it became practical to cascade amplified spans to provide for unregenerated transmission over dispersion-limited distances of 600km and more in conventional fibre, at 1.55 $\mu$ m. However, it has been found that these distances can be somewhat increased with the use of soliton transmission.

Recent theoretical calculations regarding maximum capacity of single mode fibres (Mitra and Stark, 2001) have shown that it is possible to send up to 100 terabits of information simultaneously per strand of fibre, without excessive noise or interference.

### 1.3.2 Developments in Lasers

Up to 1960, glass rods were mainly for imaging so it was sufficient for a lamp to be used for the source in such applications. The first laser, a ruby laser, was demonstrated by Theodore Maiman of Hughes Labs in 1960. This was a coherent, narrow linewidth source brought about by stimulated light emission. However, the laser could only be used in pulsed mode. The next year Ali Javan of Bell Labs realised the first continuous wave (cw) laser: a helium neon (HeNe) laser. The problem with both these lasers was that the light output could not be directly modulated (Walker, 1991) (see Section 3.2.2 for a description of direct modulation) since the analogue or digital signal could not be directly applied to the lasers (Wilson and Hawkes, 1989). However, there have been examples of resonant modulators (Uchida, 1965) where the modulator is placed inside the cavity of a gas laser, although over time it has been proved that such schemes have not been effective. Semiconductor lasers can be easily directly modulated using frequency shift keying (FSK) systems (Walker, 1991), among other schemes.

The semiconductor laser was invented by four groups simultaneously (Hall *et al.*, 1962; Nathan *et al.*, 1962; Holonyak and Bevacqua, 1962; Quist *et al.*, 1962). For three out of the four groups this was a forward biased gallium arsenide (GaAs) p-n junction with polished ends to form a resonant cavity. The guiding occurred in the active or gain region of the device, between the p-doped and n-doped layers, where population inversion occurred. The refractive index of the guiding region was not very much higher than the surrounding p and n regions and so light was lost to these areas. The two most important issues leading to the creation of these lasers was the demonstration of a silicon (Si) p-n junction by Russell Oh in 1940 and all subsequent work, as well as the fact that by 1952 it was possible to grow III-V semiconductor material of reasonable quality. The operation of these lasers was much below room temperature (77K) with very short pulses (Casey and Panish, 1978). The room temperature threshold current

density was very high at about  $5 \times 10^4 \text{ A/cm}^2$  or more, an intrinsic property of homojunction lasers.

By the spring of 1970 Hayashi and Panish (Casey and Panish, 1978) had found that multilayers of GaAs and Aluminium Gallium Arsenide ( $\text{Al}_x\text{Ga}_{1-x}\text{As}$ ) heterostructures, with the AlGaAs layer lattice-matched to the GaAs layer, improved the room temperature threshold current density to  $1.6 \times 10^3 \text{ A/cm}^2$  and with appropriate heatsinking cw lasing was achieved with the heatsink temperature at 311K. Over the intervening years (till now) a vast number of developments have occurred in the field of lasers (Brinkman *et al.*, 2000) including the creation of DFB (distributed feedback) and DBR (distributed Bragg reflector) lasers, the introduction of MQW (multiple quantum well) layers in the intrinsic region of the device, with strained MQW layers improving the situation further (Dagli, 1999). Vertical cavity surface emitting lasers (VCSELs) have proven to be practical at wavelengths of  $0.85 \mu\text{m}$  and are becoming increasingly common in short distance data links using multimode fibre (Schnitzer *et al.*, 1999). Also, semiconductor photonic integrated circuits (PICs), in which, for example, both lasers and electroabsorption (EA) modulators, which have design features very similar to that of the laser, are simultaneously fabricated on the same indium phosphide (InP) substrate (for  $1.55 \mu\text{m}$  applications), have promised reduction in cost, power consumption and size compared with lithium niobate ( $\text{LiNbO}_3$ ) solutions. The p-i-n junction of the laser is forward biased while that of the modulator is reverse biased. When introduced, these devices were routinely providing 2.5Gbit/s bandwidth with peak wavelength excursions of 0.01nm which resulted in a small frequency modulation compared with the bandwidth of the digital signal (Johnson *et al.*, 1994) and hence such a source could transmit over optically amplified distances of 600km or more in a conventional single mode fibre.

The laser in such a module can be either a DFB or a DBR laser, both of which are of great interest for present-day WDM and DWDM applications because of their ability to work over a range of wavelengths, although both lasers work on different principles (Brinkman *et al.*, 2000). Currently, it is possible with EA modulator-DFB laser modules to achieve 80 channels at 50GHz spacing (Individual optical channels consist of a band centred on one of the standard optical frequencies specified by the ITU Grid for WDM and DWDM applications (Fiber-Optics Info, 2003)). Each channel can support a single

optical wavelength, which can carry an individual data stream, for example a 10Gb/s stream. The spacing between the channels determines optical performance.). However, with an EA modulator – DBR laser module a wavelength coverage of only 8nm is achievable (providing 20 channels of 50GHz spacing).

Although there has been work on other materials in the field of semiconductor lasers, for example the GaN/InGaN blue and violet laser, the biggest push forward is still expected to be for the EA modulator – laser modules, with speeds of 40Gbits/s likely to be the latest bandwidth requirements. Also, regarding the wavelength-selective EA DBR laser modules, it is expected that chip designs or transmitter assemblies will be accessing 80 or more channels in the very near future (Brinkman *et al.*, 2000).

Another promising field of progress with regard to optical waveguide devices is the use of photonic-bandgap microcavities in optical waveguides (Foresi *et al.*, 1997). If a light-emitting cavity is directly coupled into such a waveguide, the light collection from the cavity will be highly efficient, and with the use of several different defect lengths, such a source could be used for future WDM applications.

A much more recent development in the field of lasers is the invention of an ultra broadband laser (Gmachl *et al.*, 2002) which can emit light in the range from 6-8 $\mu$ m. Potential applications can vary from advanced free-space optical communications to (the more commonly known) mid-infrared trace gas sensors. It is believed that the technique which was used to produce the new laser can be used as a basis for future high-performance semiconductor lasers for fibre optics, in addition to applications in other technologies.

### 1.3.3 Developments in Photodetectors

The photodetector is also an essential component of an optical communications system where the optical signal is converted into an electrical signal to be subsequently amplified by the receiver electronics (which consists of an amplifier to amplify the detected photocurrent) and some additional signal processing circuits. The ideal

photodetector would have unity quantum efficiency (Gowar, 1984), low dark current and a number of other requirements such as high speed, small size, low bias which are in common with other optoelectronics components in an optical communications systems (Bandyopadhyay and Deen, 2001).

However, the history of electrical light detection can be traced back 130 years to the selenium photoconductor which consisted of a bulk bar of selenium and was first experimented with by Willoughby Smith (Haegel, 2001). A photoconductor is a device without any p-n junction or contact-based barrier involved, where a bias voltage is applied across two contact regions to collect the photocurrent. If the material is n(or p)-type then both the contacts should be  $n^+$  (or  $p^+$ ) -type in order to realise an ohmic contact. However, these devices suffer from larger minority carrier lifetimes or transit times and so are a much slower option compared with the photodiode.

The p-n junction light detector was found in 1941 because of the photovoltaic effect in a Si p-n junction. This was considered the first rudimentary solar cell (Lucent Technologies, 2000). By 1962, high speed Si p-i-n photodiodes were being introduced. The intrinsic semiconductor has high resistivity which is lowered through doping. So only a few volts of reverse bias are needed to extend the depletion region throughout the whole intrinsic (i-) region and this provides a large sensitive volume for absorption. However, the width of the i-region needs to be optimised to obtain maximum speed and quantum efficiency (Gowar, 1984; Wilson and Hawkes, 1989).

Another type of detector is the high speed avalanche photodiode. These devices operate under high reverse bias such that carriers passing through the depletion region gain enough energy to enable more carriers to be excited across the energy gap by impact excitation. So ionising collisions are taking place, and this phenomenon can be correctly described as the avalanche effect. These devices were developed during 1964-1966 at Bell Labs using Si and germanium (Ge). Although Ge is still used for optical communications systems, Si is no longer used because of the discovery of the low dispersion, low loss windows at the longer wavelengths by the end of the 1970s. By then other materials, such as InP/InGaAsP, were being developed for these longer wavelengths. More recently InP/InGaAs photodiodes with bandwidths of 220GHz have been reported (Ito *et al.*, 1999). A more detailed review of photodetectors for optical

communications systems and their uses can be found in a number of publications, (e.g. Nalwa, 2001; Gowar, 1984 and references therein; Lucent Technologies, 2000), which should also include monolithic integration of optical waveguide circuitry with III-V photodetectors (Deri, 1993).

### 1.3.4. Developments in Modulators

#### 1.3.4.1 Early Modulators

Work on optical modulators came about shortly after the development of the first laser in the 1960s because of the desire to exploit the enormous potential bandwidth offered by optical carrier frequencies. The laser offered the first coherent light source; until then only lamps or sunlight had been used as laboratory light sources. However, the first laser was based on a crystal laser, and so any power supplied to the device, could not be used to modulate the output power. Hence, there was immediately a need for external modulators.

An optical modulator is a device that changes the irradiance (or direction) of the light passing through it. Previous to the development of the laser, optical modulation was carried out with mechanical choppers and shutters (Wilson & Hawkes, 1989), but these were much too slow (rotation rate of approximately 1000 times a second) to modulate light at the required frequencies in the range of MHz-GHz. This was later superceded by magneto-optical modulators (Bloembergen *et al.*, 1960), which had a bandwidth of 200 MHz, and there was no potential to increase the bandwidth of these devices.

The first electro-optic modulators were reported in the early 1960s by a number of groups (Kaminow and Turner, 1966; Chen, 1970), including Bell Labs in 1961 (Lucent Technologies, 2000). These modulators were formed from bulk crystals, typically potassium dihydrogen phosphate (KDP), ammonium dihydrogen phosphate (ADP) and their isomorphs, and the ferroelectrics BaTiO<sub>3</sub>, LiTaO<sub>3</sub> and LiNbO<sub>3</sub>, as well as semiconductors. However, LiNbO<sub>3</sub>, with its very large intrinsic bandwidth, and LiTaO<sub>3</sub>, were found to be superior over other electro-optic materials (Denton *et al.*, 1967; Steier, 1967; White and Chin, 1972; Reinhart, 1968; Kaminow and Turner, 1966), with relative

ease of handling, good electro-optic and acousto-optic properties and greater availability of the crystals. Also, both required less power in device operation to achieve a certain phase modulation due to higher RF dielectric constants and linear electro-optic coefficients and so had generally had cross-sectional dimensions of 0.25mm-0.5mm and lengths of 5-15mm (with this increasing by an order of 1 for KDP and related materials). To obtain the electro-optic modulation meant that a voltage would have to be applied across the width of the crystal. This was achieved by placing metal electrodes on the top and bottom of the crystal. The electrodes were used to apply both the dc bias and the RF signal. Electro-optic modulator devices were understood to work on the principle of linear electro-optic effect, where any change in the refractive index as a consequence of the applied electric field is proportional to the applied electric field. There were various arrangements (involving both the crystal and the electrode structures) proposed for these electro-optic modulators and these will be mentioned in the next few paragraphs.

The electrode design is important to the bandwidth of the device. With simple (lumped) electrodes electro-optic modulator devices achieved bandwidths of typically 200MHz (Kaminow and Turner, 1966) but no higher than 1GHz (Chen, 1970). This bandwidth limitation was a consequence of the mismatch of the phase velocities of the optical and modulating waves. This prompted researchers to look for ways to try to phase match the velocities of both the optical carrier and modulating signal; and so vastly increase the bandwidth.

It should be noted here that the bandwidth mentioned is the modulating bandwidth or the 3dB electrical bandwidth rather than the optical 3dB bandwidth, which is equivalent to 6dB electrical bandwidth (Walker, 1991), and so produces a larger bandwidth figure when quoted.

Out of the many schemes proposed (Rigrod and Kaminow, 1963; Stone, 1964; Kaminow, 1966) travelling wave modulators emerged the most successful (White and Chin, 1972) and are a major share of today's high speed electro-optic modulators, even though at the time these devices were quite long (in order to obtain optimum efficiency) when compared with other schemes. This was because the other schemes had complexities in fabrication. The travelling wave modulators consisted of a bulk crystal with electrodes in the form of microstrip or coplanar waveguides. For present day

travelling wave modulators the electrodes are very similar but the light travels through 2-dimensional waveguides.

Other modulator schemes were also designed to reduce the length of the device and these were structures which were resonant at optical and/or modulating frequencies (Ruscio, 1965; Kaminow, 1963). These electro-optic modulators were designed to have narrow bandwidths. However, there was not much interest in resonant electro-optic modulators and only nonresonant electro-optic modulators are considered in this thesis.

On an historical note, even though the linear electro-optic effect is attributed to Pockels (1906) - because of his more detailed studies regarding the existence of an intrinsic electro-optic effect that was independent of piezoelectrically induced strain - it was Kundt and Röntgen who first noticed this effect in quartz some 20 years after Kerr first observed the quadratic electro-optic (QEO) effect in liquids and gases in 1873 (Kaminow, 1974).

Another type of electro-optic modulator device was a one-dimensional p-n junction waveguide modulators, where the light is confined in only one-dimension, were first realised with reverse-biased GaP (indirect gap material) diodes (Nelson and Reinhart, 1964). The guiding action in these modulators was understood to occur inside the depletion layer because of its higher optical dielectric constant than for the doped n and p-type regions. The linear electro-optic effect was believed to be the predominant cause of modulation for these devices, even at large field strengths. The bandwidth limitation for these devices was typically 7GHz even though lumped electrodes were used since the device dimensions were smaller. It was proposed that bandwidth could be extended by the use of 50-80 $\mu$ m strip-mesas to reduce the diode width (Reinhart, 1968). This would therefore lead to the formation of 2-dimensional waveguides and onto the idea of integrated optics.

### 1.3.4.1.1 Integrated Optics

In his landmark paper in which he introduced the term ‘integrated optics’, Miller (1969) proposed that if an optical waveguide could be built using an electro-optic material such that the diffraction spread of the light beam could be eliminated, the cross-section of the modulator could be reduced to the order of a wavelength, and hence the required modulation power would be reduced. It was these diffraction effects that prohibited making bulk modulators with small lateral dimensions and long interaction lengths needed for low drive power. Such a waveguide (proposed by Miller (1969)) was realised by having a core higher index material totally surrounded by a substrate of lower index material, many examples of which can be found in Fig. 1.1 of Fernández and Lu (1996).

There are many advantages of using 2-dimensional (2-d) waveguides devices over their bulk crystal equivalent (Jaeger & Young, 1989; Kondo, 1993). Modulators and switches in integrated optics perform functions analogous to those of electronic transistors in integrated circuits and thus serve as active components that are able to deliver power to another part of the circuit rather than only consuming power. Interestingly, modulators and switches produced from LiNbO<sub>3</sub>, an insulating crystal, expend energy only when switching states (Korotky and Alferness, 1987). When several integrated optics components are integrated onto the same substrate, then this is known as an integrated optical circuit (IOC), the key elements of which are the waveguides (either for simply guiding the light or when used to form waveguide devices). This technology promised compact, efficient and inexpensive optical devices (Tien, 1971).

### 1.3.4.1.2 LiNbO<sub>3</sub> Waveguide Modulators

Several attempts were made at fabricating waveguides (Channin, 1971; Kaminow and Carruthers, 1973) and waveguide modulators (Kaminow *et al.*, 1973) using these materials, but this did not give any significant confinement of the light. However, there was still a vast improvement in the power-bandwidth product compared with the bulk LiNbO<sub>3</sub> or LiTaO<sub>3</sub> modulator (see Table 1.1). One important fact that had been found in one of the experiments, was that there were fabrication difficulties (Kaminow and Carruthers, 1973) with LiTaO<sub>3</sub> for outdiffusion of Li<sub>2</sub>O at temperatures higher than

600°C (the Curie temperature of LiTaO<sub>3</sub>) and so needed close temperature control to keep temperatures below 600°C (Taylor and Yariv, 1974). This was not the case for LiNbO<sub>3</sub>, which has a Curie temperature of 1154°C (Xu *et al.*, 1994).

However, LiNbO<sub>3</sub> (not without its own disadvantages) is associated with the photorefractive effect (Kaminow and Sharpless, 1967), a term which refers to optical damage due to high power (greater than 100mW (Wooten *et al.*, 2000)) laser light, although this is not so much of a problem at higher infrared wavelengths as at 0.633µm

**Table 1.1** Comparison of early LiNbO<sub>3</sub> and semiconductor modulators.

Typical Values of	Bulk LiNbO <sub>3</sub> <sup>(a)</sup>	Waveguide LiNbO <sub>3</sub> <sup>(b)</sup>	GaP p-n junction <sup>(c)</sup>	GaAs/ AlGaAs p-n junction <sup>(d)</sup>
Power/ bandwidth ratio	~20mW/MHz	0.2mW/MHz	1.5mW/MHz	0.1mW/MHz ( $\lambda=0.9\mu\text{m}$ ) 0.2mW/MHz ( $\lambda=1.15\mu\text{m}$ )
Drive Voltage/ $V_{\pi}$	0.5-1kV	7.7V	48V	10V
Size	(L) 5-15mm (W,D) 0.25-0.5mm	(L) 15mm (W) 5mm- (D) 2mm	(L) 5-15mm (W,D) 0.25-0.5mm	(L) 1mm (W,D) 50µm
Electrode Length	—	0.2mm	—	—

(a) (Chen, 1970), (b) (Kaminow *et al.*, 1973), (c) (Reinhart, 1968), (d) (Reinhart and Miller, 1972).

(i.e. less than 1µm), and although some of the effects of the optical damage recede with time, some effects remain and may be removed by a variety of methods (Chen, 1969; Barry *et al.*, 1999; Korotky and Alferness, 1987; Jackel *et al.*, 1981; Betts *et al.*, 1994). However because the devices studied in this thesis were designed to operate at longer wavelengths (i.e. 1.55µm) these methods are of no interest to this study.

It was not until 1974 that Schmidt and Kaminow (1974) managed to fabricate the first successful 2-d waveguides in LiNbO<sub>3</sub>. The waveguides were formed by diffusing titanium (Ti), nickel (Ni) and Vanadium (V) into separate LiNbO<sub>3</sub> substrates. However, it was found that with Ti, there was a much larger change in refractive index in the guiding region than was obtained with the other two materials, and it is this higher refractive index in the guiding region compared with that in the substrate which

promotes waveguiding. The maximum change in refractive index due to the Ti indiffusion in these waveguides was typically 0.01-0.02. These waveguides were also found to be superior when compared to the outdiffused guides (Kaminow and Carruthers, 1973) fabricated from  $\text{LiNbO}_3$  as it was established that the maximum index change and the effective guide thickness as well as the number of modes were affected, and therefore controlled, by the diffusion parameters. These waveguides were multimode planar structures: however single-mode channel structures were developed the following year (Schmidt and Kaminow, 1975). This was a convenient, relatively simple method of fabricating low loss, strip waveguides in a  $\text{LiNbO}_3$  substrate. Methods of the doping and fabrication of these waveguide devices and the device design issues associated with this will be given in Section 3.2 and 3.3 of this thesis, respectively.

At this time semiconductor waveguide devices suffered from a much higher insertion loss than in titanium lithium niobate ( $\text{Ti:LiNbO}_3$ ) equivalents.

Ion exchange techniques for producing waveguides in  $\text{LiNbO}_3$  were also being investigated (Shah, 1975), but they exhibited large step-like refractive index profiles for the extraordinary refractive index,  $n_e$ , (De Micheli *et al.*, 1983) while the ordinary refractive index,  $n_o$ , changed very little. (Please note:  $\text{LiNbO}_3$  is a birefringent material with a refractive index of  $n_e$  along one axis and  $n_o$  along the remaining two axes). They also suffered from characteristics detrimental to their performance (Becker, 1983; Suhara *et al.*, 1989) and large scattering losses. Although, these were later eliminated (Keys *et al.*, 1990) through annealing the proton-exchanged waveguides, this caused a large reduction in large step-like refractive index profiles for  $n_e$  (Cao *et al.*, 1992). Therefore, if used for modulators these devices would be ineffective and so will not be considered any further.

Another variant of the above technique, but for which both TE and TM modes are supported, are annealed Ti ion implanted waveguides (Ashley *et al.*, 1989). Although it was reported that a higher refractive index change due to the Ti ion implantation is obtained when compared with Ti indiffusion (so allowing smaller waveguide geometries and tighter mode confinement), this method was not as popular as Ti indiffusion for fabricating waveguides. This may be due to scattering losses usually associated with higher doses of ion implantation, which lead to higher losses along the Y-branches than

for those fabricated from Ti indiffusion (0.6dB was reported by Ramaswamy and Divino (1981) compared with 1.1dB by Ashley *et al.* (1989)).

Another technique used to define 2-d channel waveguides is lithography, which is used to delineate a rib in the surface of a slab waveguide sample. Although this technique is typically used for semiconductor waveguides it has recently been used to design ridge Ti:LiNbO<sub>3</sub> waveguide devices (Mitsugi *et al.*, 1998), which have resulted in improved characteristics for Ti:LiNbO<sub>3</sub> electro-optic modulators.

#### 1.3.4.1.3 Direct Modulation

The arrival of the semiconductor lasers led to researchers suggesting direct modulation of the light by varying the drive current with the desired (modulating) signal. However, this method was found to cause chirp for higher bandwidths which in turn broadened the laser linewidth and so led to poor laser performance. The varying modulating current leads to varying carrier density which leads to varying refractive index but this varies over a certain time and this means that any consequent phase delays will also vary with time. Since the phase delay induces a wider spread of frequencies, this means that the frequency also varies over time and this damaging process is known as chirp. Early systems gave speeds of 622Mb/s, but later these were improved to 1GHz (Brinkman *et al.*, 2000). External modulation was still preferable. With further improvements in design fabrication, speeds of 10Gb/s are now achievable (Brinkman *et al.*, 2000). However, although direct modulation is a cost effective option due to the elimination of an external modulator, there is still a trade-off between the bit-rate and the distance over which the signal is sent (Rigby, 2001) due to chirp. For directly modulated lasers, a chirp value of about 5 is obtained, hence the need for external modulators to reduce this chirp or frequency broadening.

#### 1.3.4.1.4 Semiconductor Modulators

Developments in semiconductor lasers also led to improvements for semiconductor modulators. The p-n GaAs-Al<sub>x</sub>Ga<sub>1-x</sub>As (with  $x=0.3$ ) double heterostructure diode was

expected to have a much tighter coupling of the optical field to the junction field than for the p-n GaP diodes (Reinhart and Miller, 1972). Since these devices were made from direct bandgap material, their efficiency also increased. However, they were still thought to be predominantly electro-optic devices. However, it was soon accepted (Reinhart, 1973) that the refractive index change in these devices was also due to electroabsorption (this process is also called the Franz-Keldysh effect which was first observed in 1958) were hence called electroabsorption modulators. Results were further improved by using a p-i-n structure for these diodes (Gowar, 1984), where the intrinsic(i) region was sandwiched by the p- and n-doped regions. Typically the material for the i-region had a higher refractive index (e.g. GaAs) and bandgap material and this was surrounded by a lower refractive index and bandgap material (e.g. p- and n- doped AlGaAs material).

Electroabsorption modulators operate with the concept of the change in the refractive index with applied electric field, and are based on the Franz-Keldysh effect (FKE) for bulk semiconductor modulators and the quantum confined Stark effect (QCSE (Miller *et al.*, 1984)) for quantum well devices. Both these effects work in the region of the bandgap of the material from which the device is made and, essentially, shift the optical absorption edge of a semiconductor to longer wavelengths while under the influence of a strong electric field.

From early theoretical predictions (Aspnes, 1966) to more recent theoretical models it is accepted that the FKE and QEO effect are related, since as both show a quadratic change in refractive index with applied electric field. For this reason, some of the earlier simulation models for semiconductor waveguide modulators (Mendoza-Alvarez *et al.*, 1988; Faist and Reinhart, 1990a; Lee *et al.*, 1991) gave change in the refractive index due to FKE as being dependent only on the QEO coefficient and the applied electric field. However, later, more sophisticated, models (Glingener *et al.*, 1995) used absorption coefficients (obtained from first principles) followed by the Kramers-Kronig relation to calculate the change in refractive index with applied electric field.

### 1.3.4.1.5 Types of Modulator

The phase modulator, with its single waveguide structure, is perhaps the simplest waveguide electro-optic device (Alferness, 1988) and is mainly used with semiconductor materials. These are typically characterised by giving the phase efficiency for such a device in  $^{\circ}/V\cdot\text{mm}$ . Phase modulation is a basic function which is used in nearly every electrooptic device and is fundamental to the operation of directional couplers and interferometric modulators. However, these two devices use the electro-optic induced phase change to modulate the optical intensity. One of the first implementations of a Ti:LiNbO<sub>3</sub> waveguide device was a directional coupler device (Papuchon *et al.*, 1975). This device could be used as a switch or an amplitude modulator. Other types of switches/ modulators being proposed and considered at this time were interferometric bridges (Raganath and Wang, 1977; Ramaswamy *et al.*, 1978), optical modulators and switches based on y-junctions and diffraction gratings (Sasaki and De La Rue, 1976; Chen and Meijer, 1978), waveguide cutoff modulators and electro-optic TE $\leftrightarrow$ TM modulators (Alferness, 1981). However, it was the directional coupler and the interferometric modulators that were more popular (Alferness, 1982), as they offered the possibility of high speed, broadband optical switching, time-division multiplexing/ demultiplexing, and which demonstrated the lowest crosstalk switching states (Alferness, 1981).

However, the efficiency of these devices was dependent on the component of the electro-optic tensor used to obtain the electro-optic induced phase shift (Ramaswamy *et al.*, 1978); early devices used smaller coefficients of this tensor. Table 1.2 compares a number of types of devices fabricated from Ti:LiNbO<sub>3</sub> and GaAs. It is clear from this that travelling wave modulators were superior to those using lumped electrodes in terms of bandwidth,  $\Delta f$ , and the voltage bandwidth ratio. It is also clear that the Ti:LiNbO<sub>3</sub> devices of the time were much superior to their semiconductor counterparts.

The goal in modulator design was to achieve high modulation bandwidth and low drive voltage. The potential modulation bandwidth depends upon the electrode geometry and the substrate dielectric constant. The drive voltage decreases with a longer interaction length, as does the bandwidth. So for these devices it has been found that there is a trade-off between the required drive voltage and bandwidth and hence the reason for

Table 3.4 Comparison of device types, using both Ti:LiNbO<sub>3</sub> and semiconductor materials.

	Phase Modulator		Directional Coupler (DC) Modulator						Y-branch Modulator		Travelling Wave (TW) DC Modulator	TW Y-branch Modulator
	Ti:LiNbO <sub>3</sub> (a)	GaAs (b)	(c)	Ti:LiNbO <sub>3</sub> (d)	(e)	(f)	GaAs (g)	InP (h)	Ti:LiNbO <sub>3</sub> (j)	GaAs (k)	Ti:LiNbO <sub>3</sub> (l)	Ti:LiNbO <sub>3</sub> (m)
$\lambda$				1.06 $\mu\text{m}$	1.3 $\mu\text{m}$				0.647 $\mu\text{m}$	1.15 $\mu\text{m}$	1.32 $\mu\text{m}$	0.633 $\mu\text{m}$
$V_{\pi}$			5V	8V	$\pm 5.5\text{V}$	20-25V	25V	12V	3.8V	14.6V	4V	8.8V
$\Delta f$				2.5GHz	4.2GHz		100MHz		1.1GHz	3GHz (expected)	3.6GHz	11.2GHz
$V/\Delta f$				3.2V/GHz					3.45V/GHz		1.1V/GHz	0.8V/GHz
L			$\sim 1\text{cm}$	0.9cm		$\sim 1\text{cm}$	0.7cm	0.8cm	0.6cm		1.6cm	0.6cm
$V_{\pi}L$	1.1 V.cm	1.1 V.cm										
Extinction ratio/ Crosstalk			-27dB			$\sim -25\text{dB}$	13dB	16dB		17dB		
Insertion Loss					2dB						5.4dB*	3dB @10GHz <sup>†</sup>

(a) (Alferness, 1982), (b) (McKenna and Reinhart, 1976), (c) (Schmidt and Cross, 1978), (d) (Thioulouse *et al.*, 1981), (e) (Auracher *et al.*, 1984), (f) (Alferness, 1981), (g) (Campbell *et al.*, 1975), (h) (Menigaux *et al.*, 1982), (j) (Auracher and Keil, 1980), (k) (Rodgers, 1985), (l) (Kubota *et al.*, 1980), (m) (Sueta and Izutsu, 1981).

\*This can be decreased by careful management of guide geometry and use of an effective buffer layer to 1.5dB @  $\lambda=1.32\mu\text{m}$  (Alferness *et al.*, 1982), but it is difficult as there is a trade-off between achieving efficient modulators with low loss bends and achieving good coupling to optical fibres, since the former requires a small guide geometry and the latter requires a large guide geometry.

<sup>†</sup>Insertion loss (measured directly as  $S_{21} - S$ -parameter tests (Auracher *et al.*, 1984)) is dependent on the frequency of the modulating voltage (Noguchi *et al.*, 1998).

using the drive voltage-bandwidth ratio, as a figure of merit. A device is considered superior if the value of the voltage-bandwidth ratio (VBR) is much smaller when compared with other devices.

**Table 1.3** A comparison between various waveguide modulators (Walker, 1987).

	GaAs Y branch lumped MZ	GaAs/ AlGaAs TW phase modulator	GaAs/ AlGaAs MQW EAM	InGaAsP/ InP bulk waveguide EAM	LiNbO <sub>3</sub> Y branch lumped MZ	LiNbO <sub>3</sub> Y branch TW MZ
VBR (V/GHz)	1.85	1.5	1.7	1.58	1.47	0.415
$\lambda$ ( $\mu\text{m}$ )	1.3	1.3	0.85	1.55	0.85	0.83
$\Delta f$ (GHz)	5	16*	2.95	3.8	2.75	17

\*Although this can be dependent on the nature of the substrate and electrodes., e.g. for a GaAs/ AlGaAs travelling wave (TW) modulator with an  $n^+$  substrate  $\Delta f=4\text{GHz}$  (Lin *et al.*, 1986), whereas with a semi-insulating substrate and coplanar electrodes  $\Delta f=20\text{GHz}$  (Wang *et al.*, 1987).

From Table 1.3, the figure of merit for waveguide TW LiNbO<sub>3</sub> devices is lower, when compared with early electroabsorption modulators (EAM), multiple quantum well (MQW) or bulk semiconductor waveguide devices or III-V travelling wave devices. It can also be seen that the GaAs Y-branch Mach-Zehnder (MZ)-based device has the highest, and therefore the worst, voltage/bandwidth ratio. It is therefore clear that the LiNbO<sub>3</sub> devices of the time had lower voltage/bandwidth ratios compared with similar semiconductor devices and, hence were much superior to their semiconductor counterparts.

#### 1.3.4.2 Present Day Device Characteristics

An ideal modulator would have low drive voltage, a large bandwidth, low insertion loss, a very high extinction ratio, very low chirp, small size, low power consumption - to avoid heating, reasonable angular tolerance, temperature tolerance, linearity over a large bandwidth, a high degree of isolation and the ability to handle large amounts of power, where the first few are more generally desirable characteristics. However, there may be a trade-off between some of these characteristics, for example drive voltage and bandwidth, and consequently the modulator is designed as a less than ideal compromise. When modulators are used as switching devices, the parameters important to device

performance essentially remain within the set given above for modulators with crosstalk (essentially the same as extinction ratio), switching speed, insertion loss and bandwidth becoming the more important parameters. Although the present designs are more than acceptable for today's technology, there is always a need for better and faster devices and these typically follow a logarithmic rate of increase (Alferness *et al.*, 2000).

The highest bandwidth (3dB electrical) to date has been shown for ridge Ti:LiNbO<sub>3</sub> Y-branch devices and is 70GHz (Noguchi *et al.*, 1998). However, this non-packaged device has a length of 2cm and a drive voltage of 5.1V. For a similar device (Noguchi *et al.*, 1995), the insertion loss and the extinction ratio were given as 6dB and 22dB respectively. These are very good results: however, the drive voltage is rather high as is usually the case for electro-optic devices. A bandwidth of 22GHz was reported (Wakita *et al.*, 1990) for an InGaAlAs/InAlAs MQW modulator with an extinction ratio of 25dB and a drive voltage of 6V, with an insertion loss of 18dB. However, the insertion losses in EA modulators are high because of the absorption losses but these can be reduced through detuning (i.e. moving the wavelength of operation away from the band edge of the QW material (Dagli, 1999)). Bandwidths can also be increased by reducing the device capacitance, and by reducing the length of the device. However, for MQW EA modulators, this gives a very small (50-100 $\mu$ m) device which then cannot be packaged easily; but by fabricating waveguides at the input and output of the device (Ido *et al.*, 1995; Ido *et al.*, 1996) 3dB electrical bandwidths as high as 40-60GHz have been reported with low insertion loss (7dB), low drive voltage (2.6V) and a rather low extinction ratio of 10dB. Bandwidths of 40GHz have also been reported for InGaAsP/InP bulk EA TW waveguide modulators (Li *et al.*, 2001). However, a higher insertion loss of 11.3dB and a -0.8V drive voltage were obtained for this device.

The lowest drive voltage for a Ti:LiNbO<sub>3</sub> device has been reported for a fully packaged 3cm device, where a value of  $V_{\pi}$  of 3.5V was reported for a corresponding bandwidth of 30GHz (Noguchi *et al.*, 1998). A smaller device length yielded a higher drive voltage. A similar device was recently reported by Gill *et al.* (2004). Hence, actual advances have been small for LiNbO<sub>3</sub> – based optical modulators in recent years. However, these devices are still expected to remain a major market force for 40Gb/s transmission over the next few years (Schmid, 2003). Much lower drive voltages have been reported for

semiconductor waveguide modulators. For a bias of  $-2\text{V}$ , an extinction ratio of over 10dB was recorded for an InGaAsP/InP EA waveguide modulator with a 10.1dB insertion loss (Koren *et al.*, 1994). However, a drive voltage of 1.2V has been reported for an extinction ratio of 15dB for a strained InGaAs/InAlAs MQW EA waveguide modulator with a 3dB electrical bandwidth of 20GHz (Ido *et al.*, 1994).

The extinction ratio for a modulator device should be as high as possible, and is typically required to be greater than 20dB at dc for digital applications (Wooten *et al.*, 2000). This can be obtained for longer devices (Dagli, 1999), but this is detrimental to both the bandwidth and insertion losses for EA-type devices. However, a very high extinction ratio of 24-32dB was obtained for a bulk InGaAsP/InP waveguide EA modulator, obtained by strategic placement of an InGaAs absorbing layer (Rolland *et al.*, 1992). For Ti:LiNbO<sub>3</sub> devices Dolfi and Raganath (1992) and Kawano *et al.* (1989) reported low insertion losses of  $\sim 3\text{dB}$  and high extinction ratios of greater than 20dB and 25dB, respectively. High extinction ratios of 40dB have been reported for InGaAsP/InP MZI-based MQW modulators (Fetterman *et al.*, 1996), with a voltage length product of 1.8V.mm (much lower than for the Ti:LiNbO<sub>3</sub> modulator device (10.25V.mm) reported in the previous two paragraphs).

As explained above high insertion losses are inherent to EA modulators: however, by using carefully designed short devices (Ido *et al.*, 1996) lower insertion losses can be obtained. An InAlAs/InGaAs MQW modulator has a reported insertion loss of 7dB (Ido *et al.*, 1995), while even lower insertion losses of 4.5dB were obtained for a bulk InGaAsP/InP EA waveguide modulator (Rolland *et al.*, 1991). However, with the use of an integrated semiconductor optical amplifier (SOA), insertion losses of 0dB have been obtained with bandwidths of 40-60GHz, an extinction ratio of 26dB and a 2V voltage swing (Mason *et al.*, 2002). A fibre-to-fibre insertion loss of 5dB for a Ti:LiNbO<sub>3</sub> travelling wave modulator with 5cm long electrodes (Dagli, 1999). This is due to good quality Ti-indiffused waveguides have recently been reported as having a propagation loss of 0.2dB/cm at a wavelength of 1.55 $\mu\text{m}$ .

Although in the near past there has been a concerted effort to obtain zero chirp in communications system, this result is only near achievable for X-cut LiNbO<sub>3</sub>

modulators (Jiang and O'Donnell, 1996; Schmid, 2003), and is not so for Z-cut LiNbO<sub>3</sub> modulators because of an asymmetric electrode structure. Chirp-free operation and low loss has been reported for GaAs/AlGaAs interferometric electrooptic modulators which have been grown on a [100] oriented undoped substrate. Moreover, it has been suggested that the use of an interferometric based device can also produce chirp-free operation (Koyama and Iga, 1988). Nearly chirp-free operation has also been reported for some EA modulators (Hou and Chang, 1995; Pires *et al.*, 2000) but not for those made from more complex materials (Guo *et al.*, 2000).

By the early-mid 1980s the problem of higher insertion losses had been alleviated for semiconductor waveguide devices and GaAs/AlGaAs heterostructure waveguide modulators gave an improved phase efficiency of 56°/V.mm (Alping *et al.*, 1986), which is better than any other past or present modulator.

To date, the best modulation efficiencies obtained are for a GaAs/AlGaAs bulk waveguide EA modulator (96°/Vmm), followed by a MQW EA modulator (Kaneko *et al.*, 1999) with a Ti:LiNbO<sub>3</sub> electro-optic modulators in third place.

#### 1.3.4.3 Future Predictions for Modulators

Although there are a number of advantages associated with semiconductor devices, i.e. their ability to be integrated with other components on the same substrate, LiNbO<sub>3</sub>, though a mature technology, also has a good number of advantages which make it a well cultivated, niche technology rather than an old and outdated one (Wooten *et al.*, 2000; Suchoski and Leonberger, 1999; Schmid, 2003; Arizmendi, 2004).

Presently, LiNbO<sub>3</sub> technology is being used for modulation in cable television (CATV) networks where bandwidths of no more than 10GHz are needed. 70GHz (3dB electrical bandwidth) modulators had been shown in laboratory-based experimental work (Noguchi *et al.*, 1998), however, when packaged these devices have shown bandwidths of no more than 30GHz. This bandwidth has also been demonstrated for electroabsorption modulator (EAM) – laser modules with the hope of even greater rates

(Kawanishi *et al.*, 2001): however, there is no mention of whether the device was packaged.

40Gb/s transmission has now become a standard industry transmission rate (Feng *et al.*, 2002; Prosyk *et al.*, 2002; Schmid, 2003; JGKB, 2004). However, up to now there has been very small use of modulators in 40Gbps communication links (Laser Focus World, 2003). This is expected to rise to 15.5% by the year 2008. The same market study also showed that electro-optical modulators (LiNbO<sub>3</sub> is the most widely used material) still dominate the optical modulator market with over 60% consumption. However, by 2008 electroabsorption modulators may to have a leading share of the market. Nevertheless, polymer electro-optic modulators, which are regarded as a more promising electro-optic technology (Rigby, 2000) have not been taken into account.

It is anticipated that, in the near future, LiNbO<sub>3</sub> will continue to be used with perhaps a move to multifunction devices (Wooten *et al.*, 2000) and/or for devices with wavelength of operation greater than 1.55 $\mu$ m. Using DBR lasers for the EAM-laser modules it is likely that overall device characteristics (e.g. bandwidth, no of channels, etc) will improve (Brinkman *et al.*, 2000) and will become the next wave of this technology.

There has been interest in lower dimensional quantum modulator devices (Schilling *et al.*, 1993; Sahara *et al.*, 1996): however although the growth of these structures is improving (Jiang *et al.*, 2001), there have been no reports regarding working modulator devices using such low-dimensional structures (Tsurumachi *et al.*, 2002).

A newer, more promising technology may exist in the form of polymer electro-optic modulators now that photochemical stability (Dalton, 2003; Luo *et al.*, 2004), losses (Zhang *et al.*, 2001) and thermal stability (Ma *et al.*, 2002) of these devices now seem to have been somewhat addressed. The advantages of these devices are a large bandwidth (at 100MHz (Rigby, 2000) this is higher than for any of other present day electro-optic or electroabsorption devices), a low voltage (at lower than 1V (Rigby, 2000) this is less than for any of other present day electro-optic or electroabsorption devices) and low propagation losses (at 0.2dB/cm (Zhang *et al.*, 2001) these are similar to present day electro-optic or electroabsorption devices). However, there is still much more potential for these materials (Bechtel *et al.*, 2003) and these figures are most likely still being

improved upon. The study of electro-optic modulators is important to present day and future technologies.

### **1.3.5 Optoelectronics: Requirements & Usage**

Although there has been a push towards an all-optical communications network, for the present most sources, in one form or another, follow the basic principles of electrical energy to light energy conversion and similarly all detectors follow the principle of light to electrical energy conversion.

Today optoelectronic technology is prevalent in all areas of our lives from indicators on electrical equipment, lasers with which to read from and write on CDs (compact discs) or DVDs (digital video discs), light sensors in cameras, LED (light emitting diode) displays at bus stops, LCDs (liquid crystal displays) in calculators and laptops, LEDs and photodiodes in remote control systems and also for environmental and structural sensing. Perhaps in the near future, with the development of the “white LED”, there may be a form of lighting that is even cheaper than the electric light bulb or the fluorescent light tube (News (IEE Review), 2004).

For communications, one of the main advantages is the broad bandwidth of the optical fibre. In order to take full advantage of this a spectrum of low-loss, low cost, low drive voltage, high bandwidth devices is required. Photonic integrated circuits have the potential to fulfil such expectations as well as to provide improved functionality and performance. Optics and optoelectronics is ubiquitous, and it would suffice to say that this technology is indeed an important and necessary technology for the way we live today. The modelling of these complex devices before fabricating such devices therefore is prudent.

## 1.4. Numerical Modelling of Waveguide Devices

Electromagnetic theory has, for a long time, been used for microwave devices. The demonstration of discrete propagation modes in optical fibres by Snitzer and Osterberg (1961) led the way to extending these approaches to optical waveguide devices. The further demonstration by Yariv and Leite (1963) of planar dielectric waveguides forming in the depletion layer of GaAs p-n junction showed that the same approaches could be used to describe the characteristics of dielectric waveguides.

With the ever-increasing complexities and demands on today's optical devices, there is a need for some form of modelling before any expensive fabrication process occurs. As the device design becomes more complex, it may not be possible to obtain a solution by analytical methods and hence there is a drive towards numerical methods. An analytical solution is defined as a mathematical expression, which can give values for any unknown quantity/ parameter over all of the domain and; therefore the user would make approximations to the fields or device structures in order to obtain the solution (see Section 1.4.3). However, numerical methods are an approximation to a solution and are known only at a discrete number of points in the domain. Hence, there is the need for these approximate solutions to be as accurate as possible.

### 1.4.1 Optical Waveguides

An optical guide is formed when a material of higher refractive index ( $n_2$ ) is surrounded by a material of lower refractive index ( $n_1, n_3$ ), such that the higher refractive index is 'transparent' to the light (from a narrow linewidth source) to be launched in this region. Typically, the refractive index difference between the cladding and core (or guiding) regions of the waveguide should be reasonably high (of the order 1.35% or higher) in order to achieve low attenuation rates. Fig. 1.2 shows two possible paths along which light can be launched into the waveguide. Path 1 involves launching the light into the core region by refraction from the first cladding region of refractive index  $n_1$ , and here the angles calculated are dependent on Snell's Law of refraction. Most of the light then leaves the core at the second interface to flow into the second cladding region,  $n_3$ . In addition, there is a small amount of light being reflected at each interface

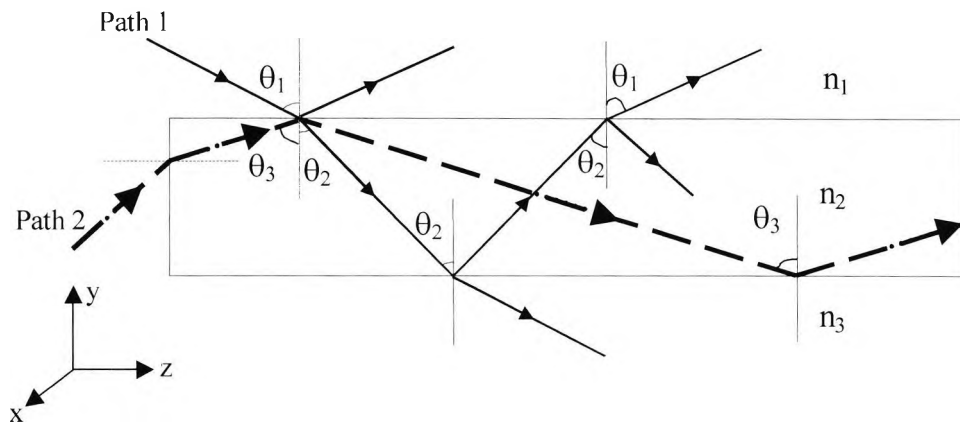


**Fig. 1.2** The paths of the light propagating through a slab waveguide, based on the laws of refraction and reflection.

(where the angles calculated are dependent on the law of reflection). Hence it can be seen that light entering the core region in such a way will have a minimal amount of light remaining in the guiding area. A much better way to retain light in the higher refractive index core is by launching light straight into the core region as for Path 2 in Fig. 1.2, where the light is then guided along the total length of the waveguide by the total internal reflection of the light.

The planar (slab) structure shown in Fig. 1.2 and Fig. 1.3(a), where  $n_2 > n_1, n_3$ , is one of the simplest optical waveguides. In fact, electromagnetic waveguides, of which optical waveguides are a subset, can be classified into a number of categories (Fernández and Lu, 1996): those of interest being multilayer planar waveguides (Fig. 1.3a), cylindrically layered waveguides (Fig. 1.3(b), where  $n_2 > n_1$ ) and the more general, arbitrarily-shaped waveguide with arbitrary properties in the transverse cross-section. The first two can

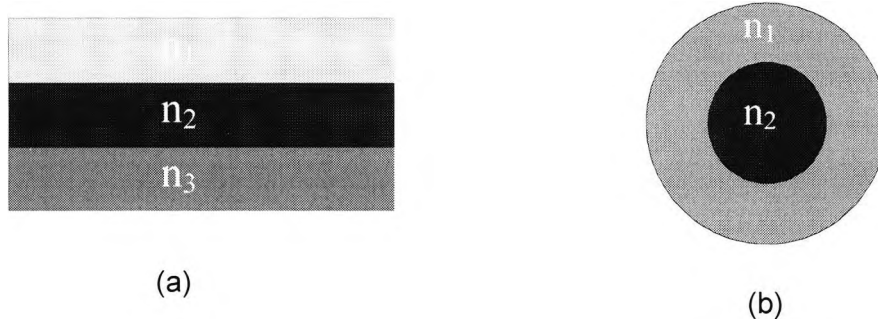


**Fig. 1.3** The refractive index profile for (a) a multilayer planar waveguide and (b) a cylindrical waveguide.

both be treated as one-dimensional problems, for which exact solutions can be found. This is only for a stepped index change: however, exact analytical solutions are also obtainable for some graded index profiles (Kogelnik, 1988). In the case of varying refractive index a 2-d approach is needed, and approximate solutions to the wave equation need to be obtained. An example of such methods is the Wentzel, Kramers, Brillouin (WKB) method (Kogelnik, 1988).

2-d problems, or rather channel dielectric waveguides are used in many active and passive devices in integrated optics. There are also variations of this geometry, such as in diffused, rib, embedded strip and ridge waveguides. Several numerical methods have been used to find the solution to the wave equation for these various types of guides and a review of their strengths, weaknesses and accuracy is given in Section 1.4.4.

Another type of guide that is important for integrated optics is the waveguide bend, typically located at the input and output of devices such as directional couplers and interferometric devices. These are used in directional couplers to further separate the waveguide at the input and output to the device, and so prevent any light from coupling between the two outputs or inputs. These bends can also have different geometries from S-bends to 90° circular bends (Minford, 1982), although S-bends are more commonly used in present day devices.

For the 1-d waveguide in Fig. 1.2 to support light propagation, the core needs to be of a certain thickness: however, if  $n_1=n_3$  and the guide is symmetric, it always supports the lowest mode, the fundamental mode. There is no extinction of the mode, or rather cut-off, even for very small values of thickness,  $t$ . The path of light taken is dependent on several factors including the dimensions of the waveguide, the wavelength of the light and the nature of the material of the guide. Depending on the width of the layer, several different light paths may be possible in layer 2 (Fig. 1.2), the higher refractive index core layer. These different light paths, which have an associated number, are called guided modes. If the light enters into the guiding region from the surrounding layers and then exits again into the surrounding layers, such a mode is known as a radiation mode. In reality the paths of light are two superimposed uniform plane waves with a wave normal which follow the zig-zag path along  $z$  in Fig. 1.2. The wave can either be TE (transverse electric) or TM (transverse magnetic), depending on whether only the

electric field or the magnetic field, respectively, is acting perpendicular to the direction of propagation. For the TE mode, the field components are  $E_x$ ,  $H_y$  and  $H_z$  and for the TM mode the field components are  $E_y$ ,  $H_x$  and  $E_z$ . Each guided mode which the structure supports has an individual propagation constant,  $\beta$ , defined as (Kogelnik, 1988)

$$\beta = \frac{\omega}{v_p} = k_0 n_2 \sin \theta_2 \quad (1.1)$$

where  $\omega$  is the angular velocity,  $v_p$  is the related phase velocity, the wavenumber in free space  $k_0 = 2\pi/\lambda$ , where  $\lambda$  is the wavelength of the light,  $n_2$  is the refractive index of the material in layer 2 and  $\theta_2$  is the angle shown in Fig. 1.2. The effective index of the mode, given by  $\beta/k_0$ , has a value between that of the refractive index of the guiding region and the lower refractive index of the substrate region, where that for the fundamental mode is higher than that for the higher order modes (should they occur). However, it is the cross-sectional **E**- or **H**-field profile of each optical mode supported by a waveguide structure that shows the true nature of the mode. The general terminology for the  $m^{\text{th}}$  confined mode is  $\text{TE}_m$ , where  $m$  is the total number of extrema that appear in the field profile along the  $y$  direction. This is the same for the TM mode, where  $\text{TM}_0$  is the fundamental.

For a 2-d channel waveguide, where confinement is not only in the  $y$  direction as for the slab waveguide but in  $x$  and  $y$ , there are no longer true TE and TM modes but hybrids of these which still resemble, in some way, the TE and TM modes and hence are known as quasi-TE and quasi-TM modes, or  $E_x(H_y)$  and  $E_y(H_x)$  modes, respectively (Chiang, 1994). The general terminology for these modes is  $\text{TE}_{mn}$  or  $\text{TM}_{mn}$ , where  $m$  and  $n$  are the total number of extrema that appear in the field profile in the  $x$  and  $y$  directions, respectively.

#### 1.4.2. Maxwell's Equations

The wave equation used to solve optical waveguide problems is derived from Maxwell's equations (see Appendix A1).

### 1.4.2.1 Boundary Conditions

More importantly for the work in this thesis Maxwell's equations are subject to boundary conditions at the positions where abrupt changes of materials occur. A simple abrupt material change, as shown in Fig. 1.4 where  $\hat{\mathbf{n}}$  is a unit vector normal to the surface, is considered. For the precondition of no surface charges or surface currents, the following boundary conditions apply to this abrupt material change:

$$\hat{\mathbf{n}} \times (\mathbf{E}_1 - \mathbf{E}_2) = 0 \quad (1.2)$$

$$\hat{\mathbf{n}} \times (\mathbf{H}_1 - \mathbf{H}_2) = 0 \quad (1.3)$$

$$\hat{\mathbf{n}} \cdot (\mathbf{D}_1 - \mathbf{D}_2) = 0 \quad (1.4)$$

$$\hat{\mathbf{n}} \cdot (\mathbf{B}_1 - \mathbf{B}_2) = 0 \quad (1.5)$$

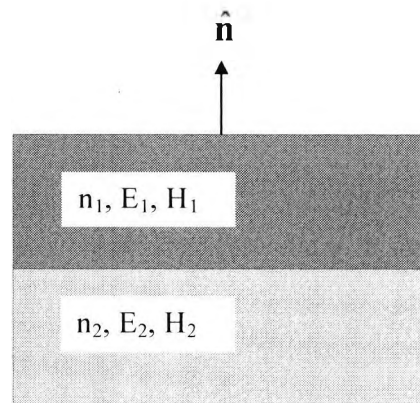


**Fig. 1.4** The boundary at an abrupt interface. The two different media have refractive indices of  $n_1$  and  $n_2$ , respectively, and  $\hat{\mathbf{n}}$  is the unit vector normal to the interface.

Equations (1.2) & (1.3) state that the tangential components of the electric and magnetic field, respectively, must be continuous across the boundary. Equations (1.4) & (1.5) state that the normal components of the electric and magnetic flux density, respectively, must be continuous across the boundary.

Although the tangential components of the fields are always continuous, the normal components are discontinuous across the material surfaces, due to jumps in  $\epsilon$  or  $\mu$ . However, for dielectric materials,  $\mu_r$  is equal to 1 and therefore the normal components of the  $\mathbf{H}$ -field will also be continuous. In fact, not only are the transverse electric fields discontinuous at boundaries, they actually diverge at the corners of

rectangular guides (Sudbø, 1992). Hence, the use of the full- $\mathbf{H}$  equation is more convenient (Chiang, 1994).

In the case of one of the two media becoming a perfect electric conductor, it is then treated as an electric wall boundary, with

$$\hat{\mathbf{n}} \times \mathbf{E} = 0 \quad \text{or} \quad \hat{\mathbf{n}} \cdot \mathbf{H} = 0$$

and so there is a continuation of the electric field, while the magnetic field becomes extinct.

Similarly, in the case of a perfect magnetic conductor, it is then treated as a magnetic wall boundary with

$$\hat{\mathbf{n}} \times \mathbf{H} = 0 \quad \text{or} \quad \hat{\mathbf{n}} \cdot \mathbf{E} = 0$$

and so there is a continuation of the magnetic field, while the electric field vanishes.

This type of boundary can be used along the line of symmetry for a symmetrical optical waveguide, such that only one half of the guide need only be analysed (see Appendix A2).

### 1.4.3 Analytical Methods

For planar waveguides, it has been noted above that analytical techniques are adequate, even for gradual changes in the refractive index (Kogelnik, 1988). For 2-d channel waveguides, the modes are hybrid and should be treated as such for the analysis. However, the analytical solutions treat them as purely TE or TM modes and hence their accuracy deteriorates near the cut-off frequency.

The two main analytical methods are Marcatili's Method (Marcatili, 1969a) and the effective index method (Knox and Toullos, 1970). Both methods use a technique whereby the rectangular core can be approximated to two slab waveguides which are separately obtained, first by extending the height of the rectangular core to infinity and the second time by extending the width of the rectangular core to infinity. The difference between the two methods is that for Marcatili's Method it is assumed that only a negligible amount of optical field lies in certain regions surrounding the core of the

waveguide. This assumption is not made for the effective index method and so this method gives results closer to reality in the region near cutoff.

Moreover, the effective index method has also been used for diffused channel waveguides (Hocker and Burns, 1977) and for other inhomogeneous and arbitrarily shaped waveguides (Chiang, 1986a; Chiang, 1986b; Chiang, 1989).

Both methods were improved by using perturbation correction (Kumar *et al.*, 1983; Chiang, 1992). Other methods for improving the effective index method were also proposed but by far the most accurate for the analysis of rib waveguides was the variational effective index method (Benson *et al.*, 1994). However, it is accepted that numerical methods are generally more accurate for inhomogeneous and arbitrarily shaped waveguides near to cutoff (as in the case of the Ti:LiNbO<sub>3</sub> electro-optic waveguide modulator devices to be studied in Chapters 4 and 5)

#### 1.4.4 Numerical Methods

There are several methods available with which to solve the wave equation for optical guides (Saad, 1985; Chiang, 1994; Itoh, 1989; Vassallo, 1997). However, the method chosen should be appropriate for the structure being characterised. The selection criteria for this is that (Saad, 1985; Chiang, 1994):

- (i) the method should have the ability to deal with more than two homogeneous dielectric layers
- (ii) the method should be accurate in modelling the boundaries between the dielectrics, as well as the open boundaries (at the edge of the device or the area of examination)
- (iii) the accuracy of the method in specific frequency ranges, e.g. near cutoff
- (iv) the accuracy of the method in computing the characteristics of the single modes or near degenerate modes (if these are desired, or expected)
- (v) the ease, accuracy or efficiency with which the method handles inhomogeneous or anisotropic materials

- (vi) how much the method is limited by any built-in restrictions which come of the assumptions made to obtain the solution
- (vii) whether spurious modes are generated by the use of this method and the ways in which to eliminate these non-physical modes
- (viii) the ease with which the method is used, i.e. is there any preprocessing involved?
- (ix) computational efficiency and computer storage requirements
- (x) the ability of the method to deal with bends in the waveguide (which are very important in today's photonic integrated circuits (PICs))

So the best application may not necessarily be the one which can solve the full wave equation for an arbitrary waveguide but that which fits the problem in hand. At one time there would have been a need for choosing the best method that fits the computing facilities of the user; however, with the advances in and falling costs of computing technology, there is no longer such a concern.

The main available methods to solve the wave equation for optical guides can be categorised into 3 groups:

- (i) methods based on series expansion (Chiang, 1994)
- (ii) global methods (Vassallo, 1997)
- (iii) other methods

This last section is used to compare numerical methods that are used for modelling waveguide bends.

#### 1.4.4.1 Methods Based On Series Expansion

These methods involve expanding the field as a series of basis functions, and include the point-matching and Galerkin methods (Chiang, 1994; Davies, 1989) – which are also known as moment methods or weighted residual methods, the boundary-matching method (Wang and Vassallo, 1989), the mode-matching method (Peng and Oliner, 1981) – also known as the equivalent network method (Chiang, 1994) and the spectral-index method (Kendall *et al.*, 1989) – which can be considered a special version of the mode-matching method (Chiang, 1994).

All these methods are sensitive to the waveguide structure, such that a different basis function will be required for a different waveguide structure (Chiang, 1994). It was also found that singularities occur at the corners of dielectric waveguides (Sudbø, 1992) for all these numerical methods which are based on the expansion of the solution in continuous basis function, when the function is discontinuous (i.e. at discontinuities). In Fourier analysis, this is known as the Gibbs phenomena. Hence, although these methods are efficient and easy to implement, they are only useful and satisfactory for isotropic guides.

#### 1.4.4.2 Global and Related Methods

These methods include the variational method, the finite difference method, the finite element method and the boundary element method. When used in conjunction with the variational method the finite difference and finite element methods become much more powerful as does the boundary element method when used in conjunction with the finite element method, and there is no problem with finding an appropriate basis function or trial function for each different structure. Hence there is a need to understand these three methods and study them in more detail in this section of the thesis.

**The variational method** is often an approach where just one parameter provides the required answer (Davies, 1989). The method to obtain a variational expression can be obtained elsewhere (Saad, 1985; Davies, 1989). However, the basic idea, in the example of the scalar wave equation, is to obtain a variational expression for the eigenvalues into which a trial solution of the wave equation is substituted. Then subject to natural, fixed or mixed boundary conditions, the variational expression will remain the same or require an extra expression (Davies, 1989). From this, the eigenvalues for each mode can be obtained. Another option is to substitute a set of basis functions into the minimised variational expression. This called the Rayleigh-Ritz Method (Davies, 1989). However, for this method the accuracy of the method is dependent on the trial function (Goyal *et al.*, 1993), as for the methods based on series expansion.

Although the classical variational method has been used in many areas of physics and engineering, there are a few problems related to boundaries and discontinuities. Since

this method uses trial functions, it would typically not be possible to obtain one function to satisfy all the boundary conditions (Davies, 1980). Also, if there is a discontinuity in the structure and the trial function is continuous throughout that region, the function would again be discontinuous and this may cause problems, discussed in the previous section, regarding singularities at the corners of dielectric waveguides. This can be evaded by using the effective index method, in conjunction with the scalar variational method (Austin, 1984; Benson *et al.*, 1994).

Moreover, since this method makes use of the coupling between points, however distant they are from one another, and even though the coupling may be weak, this leads to the formation of a dense matrix, which means large computer storage requirements would be needed for this method (Davies, 1980).

The variational formulation is sometimes used with the finite difference method and is nearly always used with the finite element method. It is for this reason that there is a similarity between these two methods.

The **finite difference method** is the oldest and most commonly used technique for boundary value problems (Davies, 1972). This method can deal with inhomogeneous media and complicated boundaries for a small enough mesh (Chiang, 1994); however, for discontinuities, the nodes have to be on the boundary and the appropriate changes are made to the difference equations for these nodes. Although this method has the potential for use with anisotropic waveguides, implementations have mainly been restricted to isotropic guides (Chiang, 1994). This method, apart from when solving for scalar equations using a uniform mesh, will result in a very large nonsymmetric matrix (Stern, 1988), but which can be avoided by using iterative techniques for the solution (Galick *et al.*, 1992).

When the finite difference method is used in conjunction with variational method, such that a variational expression is obtained which is then discretised using a finite difference approach, the modelling of discontinuities can be made easier (Chiang, 1994). In this way the finite difference method is very similar to the finite element method when using the first order rectangular elements (Davies, 1972). In fact, when used for isotropic guides with simple boundaries, this method was found to be much

superior to the finite element method (Patrick and Webb, 1992), with smaller and simpler matrices being generated by the finite difference method in comparison with the finite element method (Davies, 1989).

However, when the formulation is based on the variational principle, this method also generates spurious modes for the solution of the vector wave equation, as for the finite element method, and these can be eliminated by the use of the divergence equations, as for the finite element method.

More importantly, since the waveguide is enclosed in a rectangular box with conducting walls, this limits the accuracy of the solution near cutoff. Also, curved or irregular boundaries are harder to model because of the rectangular nature of the finite difference method, whereas the finite element method includes triangular elements, which can more easily fit the curved boundary and these can be extended to include isoparametric elements if the triangular elements are not satisfactory. Moreover, this method (as for the series expansion methods) cannot handle singularities at corners (Vassallo, 1997).

**The finite element method** is a relatively recent method when compared with the finite difference method. It is one of the most powerful and versatile methods for the modelling of optical waveguides. This method has indeed been used for modelling a large variety of waveguides (Rahman *et al.*, 1991). It was found to be superior to the effective index method and the scalar variational method when used for modelling GaAs rib waveguides (Rahman and Davies, 1985).

A formulation of the wave equation can be obtained, based either on a variational or Galerkin approach. However, the variational formulation is preferred because it has a rigorous mathematical basis, in terms of convergence (Strang and Fix, 1973). The Galerkin formulation is usually only used when the variational cannot be used, for example when the differential operator is not positive-definite (Lee, 1994). This approach results in a matrix eigenvalue equation from which unknown values are obtained.

Spurious modes appear when using this method to solve the vector wave equation, and can be eliminated by a number of methods including the correct use of the penalty

method (Rahman & Davies, 1984b), edge elements (Hano, 1984) and a variational  $E_t$ - $H_t$  formulation (Fernández and Lu, 1996), where  $E_t$  and  $H_t$  are the transverse components of the electric and magnetic fields. However, penalty method is easier to use.

Dielectric waveguides are electromagnetically unbound structures and therefore the field can, in theory, extend over all open space (Chiang, 1994). In fact, near cutoff the field does expand out of the core area. There are several methods with which this can be handled, but the infinite element method proposed by Yeh *et al.* (1979), first used with the FEM by Rahman and Davies (1984c) and later optimised by Hayata *et al.* (1988), was found to be the easiest of these methods to implement for vector analysis.

The triangular elements are more adaptable for curved or irregular boundaries. However, if this is not considered accurate enough for a given structure, isoparametric elements can also be used (Rahman, 1995). Moreover adaptive meshing is also possible with this method (Cwik *et al.*, 1997).

Many optical waveguides and waveguide devices have been modelled using this method, and the strength of the method is shown by the diversity of these devices (Buah *et al.*, 1994; Themistos *et al.*, 1995b; Mahmood *et al.*, 1998; Katsriku *et al.*, 1997; Obayya *et al.*, 2000b;).

A more detailed description of the finite element method will be given in Chapter 2.

The **boundary element method** and **integral equation method** are related in the following way:

The wave equation can be transformed into an integral equation using the two-dimensional Green's theorem. Solving this can be in the form of a domain integral equation method (where the core of the waveguide is treated as a perturbation of its surrounding media) (Chiang, 1994) or a surface integral equation method which is based on solving an integral equation that is defined along the core-cladding boundary of the waveguide. This resulting equation is then solved by the point-matching method or the boundary element method (Kishi and Okoshi, 1989). This method in general is known as the **integral equation method**.

The **boundary element method** involves transforming the wave equation into a surface integral equation using the two-dimensional Green's theorem (Itoh, 1989).

However, there is no standard eigenvalue equation as for the case of the finite element method, and so the eigenvalues have to be searched for iteratively (Chiang, 1994). Moreover, the use of special functions in the evaluation of the matrix elements could result in singularities, and as for the methods based on series expansions, different Green's functions are required for different waveguide structures (Chiang, 1994).

By combining the boundary element method with the finite element method it is possible to then also model the boundary between arbitrarily shaped multi-layer (inhomogeneous) waveguides/waveguide devices and this approach has been employed to find the coupling between laser and passive waveguides in a monolithically integrated circuit (Hirayama & Koshiba, 1993), but this is clearly more over complex for modelling standalone waveguide devices (as studied in this thesis)

The **transfer matrix method** can also be used for period structures (Mao and Huang, 1994; Mahmood *et al.*, 1998; Rahman *et al.*, 2000). When used with scalar modes obtained by a variational approach, this method gives poorer results compared with a vector BPM (Mao and Huang, 1994). However, when this method is used with a more rigorous vector **H**-field finite element approach (Mahmood *et al.*, 1998), it should give much more accurate results.

#### 1.4.4.3 Other Methods

Although the method of lines (Pregla and Pascher, 1989) and the beam propagation method (Feit and Fleck, 1980; Yeh *et al.*, 1978) have been used for modelling waveguide devices, in this thesis both methods are of more interest for the modelling of optical waveguide bends.

Although this method is very efficient for straight boundaries and isotropic guides, for curved boundaries or inhomogeneous guides this method is inconvenient. Also, the inaccuracy near cutoff is, as for the finite difference method, caused by the limitations of

the rectangular box. Moreover, as for the finite difference method, this method cannot handle singularities at corners (Vassallo, 1997). Therefore there was more interest in using a beam propagation method based approach for the waveguide bends modelled in this thesis.

The first approach to the **beam propagation method** (BPM) was fast Fourier transform (FFT)- based and employed by Feit and Fleck (1980), and independently by Yeh *et al.* (1978). Other approaches such as the finite difference based BPM, the method of lines based BPM (Gerdes and Pregla, 1991) and the finite element based BPM (Obayya *et al.*, 2000a) are also being used. A review of these and a number of other approaches to optical field propagation techniques has been well documented (Yevick, 1994). However, the finite element based BPM offers several advantages in comparison to other approaches (Selleri *et al.*, 2000)

This method uses discretisation in the transverse plane as well as in the longitudinal axis. In the transverse plane, the two-dimensional discretisation is handled by the finite difference method or the finite element method and a  $\Delta z$  step discretisation is carried out along the longitudinal axis. The latter can also use a finite difference method-type discretisation which involves transforming a correlation function relating the evolved field and the incident field to yield the mode spectrum (Chiang, 1994). The finite element based BPM formulation used to model waveguide bends is given in more detail in Section 3.3.2.1.

For non-uniform waveguides, this is one of the most powerful methods available. However, for uniform waveguides this method is excessive and not as efficient as the two-dimensional methods (Chiang, 1994) because of the three-dimensional discretisation exclusive to BPM. Hence, the BPM has been effectively used for InGaAsP/InP active twin-ridge-waveguide coupler switches (D’Orazio *et al.*, 1997) but for optical fibre couplers (Yu *et al.*, 1994) it was found that coupled-mode methods may be more numerically advantageous for simpler structures.

Moreover, care should also be taken when comparing the BPM with other methods, (as in Bertolotti *et al.* (1994)), because when the comparison is made with the crude

paraxial approximation approach for the BPM rather than the more superior Padé approximation (Obayya *et al.*, 2000a), it is usually considered to be inferior.

### 1.4.5 The Method of Choice

For this particular work, Ti:LiNbO<sub>3</sub> modulator waveguide devices were modelled, as well as GaAs/AlGaAs electro-optic modulators. LiNbO<sub>3</sub> and, therefore, Ti:LiNbO<sub>3</sub> are both anisotropic in nature. However, GaAs, and therefore, AlGaAs are both isotropic in nature until the point at which the material becomes anisotropic under the effect of an electric field. So in both cases this project has dealt with anisotropic waveguides. Further the waveguides produced by Ti indiffusion into LiNbO<sub>3</sub> are also inhomogeneous.

Previously reported modelling techniques for anisotropic inhomogeneous waveguides include:

- *the variational method (Bindal & Sharma, 1992)*  
For this method the accuracy of the results depends on the trial functions (Goyal *et al.*, 1993).
- Modelling the mode profile as a Hermite-Gaussian function and the modulating field using *a moment method (Chang et al., 1999)*. This implies a variational method, although there is no mention in the paper. Even using a moment method to model the modulating electric field can give inaccurate results for anisotropic guides (Saad, 1985). The dielectric tensor of LiNbO<sub>3</sub> at low frequency is anisotropic.
- *the effective index method (Hocker & Burns, 1977)*  
This method is not accurate near the cutoff. The LiNbO<sub>3</sub> devices, which are to be modelled, are single mode and the effective index is very close to the substrate index (Koshiba *et al.*, 1999). This implies that these devices work near cutoff and so for the structures examined in this thesis using this method would not yield accurate results.
- *the equivalent index model (Ashley et al., 1989)*

This method is in a very similar vein to the effective index method (Walpita, 1985). The idea is to replace a waveguide with an equivalent inhomogeneous slab waveguide with an effective index profile that depends on the geometry of the waveguide.

- *the method of lines (Gerdes et al., 1991)*

This method is inaccurate near the cutoff (Chiang, 1994).

- *the beam propagation method (Koai and Liu, 1989a)*

This method is considered not as efficient as 2-d methods (Chiang, 1994) for uniform guides (the devices modelled in this thesis are all taken to have uniform guides)

- *the finite element method - scalar E-field formulation (Strake et al., 1988)*

The full-H equation is considered more convenient as far as the enforcement of the boundary conditions are concerned (Chiang, 1994)

- *the finite element method - type of formulation not given (Noguchi et al., 1995)*

In the literature, there have been reports of waveguide bends or Y-junctions at the input and output of these devices being modelled using:

- mainly the beam propagation method (e.g. (Lee et al., 2000))
- method of lines (Gu et al., 1991)
- the effective index method in conjunction with a conformal mapping technique (Ganguly et al., 1998)
- the conventional beam propagation method in conjunction with a conformal transformation technique (Tavlykaev et al., 1994)

It has been shown that the beam propagation method is one of the most powerful methods when modelling waveguide bends (Rajarajan et al., 2000). However, conformal mapping techniques alone cannot calculate the radiation loss (Heiblum and Harris, 1975).

It is clear from the previous sections in this thesis that the full vector **H**-field formulation for the FEM is superior over all other methods discussed for a standalone waveguide modulator, and it is also clear that a FEM based BPM approach is superior for modelling waveguide bends.

Hence, the choice of method throughout this thesis is the full vector  $\mathbf{H}$ -field formulation for the modal solver for these guides, in conjunction with a scalar formulation for the Laplace equation for finding the modulating field,  $\mathbf{E}(x,y)$ . For modelling the waveguide bends located at the input and output of the device, a semi-vectorial beam propagation method was used. The use of this method is possible for studying the waveguide bends of the devices examined in this thesis, since no hybridisation occurs between the TE and TM modes for any of the structures and so to use a semi-vectorial beam propagation method is beneficial and efficient.

## 1.5 Summary

This chapter started with a section of the aims of the thesis and the structure of each chapter

Next an introduction and history of optical communications, giving the basis for an optical communications system and from there a brief history of the development of the four most basic parts of such a system: the source, the detector, the transmission medium, and most important to this work, the means by which to send a signal over the light source carrier – the modulator.

The Chapter was completed with a detailed account of the theory and different numerical methods behind the analysis of waveguides and waveguide devices was given. A comparison of methods was then given regarding the modelling of  $\text{Ti:LiNbO}_3$  devices, and the reasoning for the methods that have been used in this work have been given.

# 2

## *The Finite Element Method*

---

---

### **2.1 Introduction**

The finite element method (FEM) is a very powerful computational tool, the major application of which began in structural engineering, or more precisely in the aircraft industry, from the early 1960s (Stasa, 1985). However, it is now used for a variety of engineering problems including thermal analysis, fluid mechanics and electromagnetics. It has also been extended for use in medical related areas (Hsia, 1997; Springer and Hendrickson, 2004). The composition of the structures involved can have many different and very diverse forms, and can utilise many different types of materials. Typical problems where the method is widely applicable include stress analysis of bridges, the flow pattern in a coal gasifier, the thermal analysis of an antenna of a satellite in space and the modal solution for an anisotropic, inhomogeneous optical waveguide, as well as many other more complex problems for which a closed form solution cannot be found (even when subject to certain assumptions). These complications may arise because of the use of nonlinear/ anisotropic materials, irregular geometry and mixed boundary conditions. The finite element method can readily handle these and other complexities.

### 2.1.1 History

One of the first uses of numerical solutions was through that of the trial function. The trial function is an assumed mathematical function, usually based on physical intuition, and is applied globally to the region being analysed. The trial function can then be used in various types of integral formulations. Conversely, although trial functions are used in the finite element method (FEM), the main difference between these two methods is that the trial functions for the FEM are applied locally (on an element basis). Hence, a method which just uses trial functions, because it is applied globally, can only be applied to the simplest of problems.

The use of the trial function is neither associated purely with mathematics nor engineering, but has been approached differently in both these subjects. It was first reported in a paper written by Gauss in 1795, in a method now called the method of weighted residuals (Stasa, 1985). However, trial functions were employed in variational methods at a much later date (namely, 1870), by Rayleigh, and this technique was later extended by Ritz to include a number of independent functions, or rather a set of independent basis functions. Hence, the use of the name Rayleigh-Ritz to describe the method for a basis function based variational method (Davies, 1989). In 1915, Galerkin introduced a type of weighted residual method (Davies, 1989), now known as the Galerkin method.

However, all these early uses of the trial function were applied on a global basis. Courant (1943) introduced piecewise continuous trial functions. By using these trial functions on a local (element) basis, where the elements were triangular, this method could now be used for real problems, with irregular geometries and unknown solutions, instead of there being a restriction to simple problems as with the variational method. These first results in the development of the finite element method were in the field of structural engineering. Argyris (1954) developed a matrix theory for structures, using discrete elements, from the point of view of element interpolation functions; and this was then shown to be a particular case of the general continuum. The theory was applied using rectangular elements. Argyris and his colleagues then used this theory to solve complex problems using computational techniques (Davies, 1980). This concept was extended by Turner *et al.* (1956) to include triangular elements and in his paper he

stated that these elements are much better than rectangular elements for a structure of arbitrary shape. However, it was Clough (1960) who first came up with the name ‘finite element method’ in order to show there was a difference between the above mentioned matrix method and the continuum. The finite element method was also later extended to three-dimensional problems (Davies, 1980). One of the first to apply the finite element method to nonstructural problems was Zienkiewicz and Chung (1965) when they used it for general problems described by the Poisson equation, and in the second edition of his book, Zienkiewicz (1971) was the first to include in one book the general applicability of the finite element method, for any problems which could be described by partial differential equations (PDEs) or ordinary differential equations (ODEs) (Stasa, 1985).

Thus it can be seen that the finite element method is an extension of the Rayleigh-Ritz and Galerkin techniques (Zienkiewicz, 2000). In general terms it can be said to be an approximation of the resulting functional of the PDEs, in terms of the nodal value of the elemental domain into which the region has been subdivided.

The interest in the finite element modelling of electromagnetic waveguides started towards the end of the 1960s and this evolved from microwave applications to optical waveguides over the last two to three decades. With the advancement in computing that has occurred over the intervening years from the 1960s, this has meant that the finite element method can easily be used for larger meshes, as well as more intricate guiding structures with arbitrary shapes, material profiles and nonlinearities, as shown in Fig. 2.1.

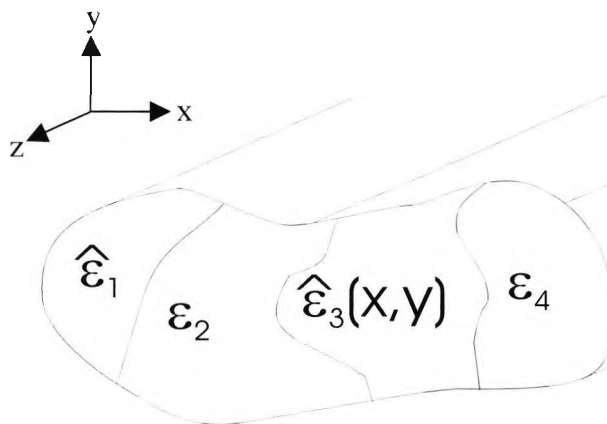


**Fig. 2.1** An arbitrary shaped optical waveguide, with an arbitrary number of subdomains, each with a different type of material.

The finite element method is able to handle any type of material, with the only constraint that the material properties cannot change within an element.

In view of these facts, it is these developments which have led the finite element method to become one of the most powerful numerical methods available to the engineer, particularly with respect to waveguide theory.

## 2.2 Variational Formulations

The electromagnetic fields in a uniform waveguide (assuming time and  $z$  variation is given by  $e^{j\omega t}$  and  $e^{-j\beta z}$ , respectively) have the form,

$$\mathbf{E}(x, y, z, t) = \mathbf{E}(x, y) e^{j(\omega t - \beta z)} \quad (2.1)$$

$$\mathbf{H}(x, y, z, t) = \mathbf{H}(x, y) e^{j(\omega t - \beta z)} \quad (2.2)$$

where  $\omega$  is the angular frequency and  $\beta$  is the propagation constant.

This leads to the vector Helmholtz equations,

$$\nabla^2 \mathbf{E} + \nabla(\mathbf{E} \cdot \nabla \ln \varepsilon) + k^2 \mathbf{E} = 0 \quad (2.3)$$

$$\nabla^2 \mathbf{H} + (\nabla \ln \varepsilon) \times (\nabla \times \mathbf{H}) + k^2 \mathbf{H} = 0 \quad (2.4)$$

for an anisotropic lossless medium (for a lossy medium,  $j\beta$  would be replaced by  $\gamma = \alpha + j\beta$ , where  $\alpha$  is the attenuation constant),

where the wavenumber  $k$  (rad/m) is

$$k = \omega \sqrt{\varepsilon \mu_0} \quad (2.5)$$

since  $\mu = \mu_0$  for a dielectric medium.

If  $\varepsilon = \varepsilon_0$ , then the corresponding wavenumber,  $k_0$ , is called the free space wavenumber and is given by

$$k_0 = \omega \sqrt{\varepsilon_0 \mu_0} \quad (2.6)$$

Throughout this chapter it will be assumed that the guide is anisotropic and 2-dimensional, as a considerable amount of work has been done for planar waveguides (Wongcharoen, 1995).

Finite element formulations are usually established via the variational (or classical) approach, especially when only one global parameter (e.g. the propagation constant,  $\beta$ ) is the required solution, because it has a rigorous mathematical basis, in terms of convergence (Strang and Fix, 1973). However, the Galerkin method (the weighted residual method) is more flexible and can be used in the case of the variational approach not being obtainable (Lee, 1994).

Although there are several variational formulations, they can still be subdivided into the scalar approximations, where only the one dominant field component is considered, or the vector formulation, where at least two of the field components are considered.

However, whichever formulation is used it is usual that this will yield a matrix eigenvalue equation of the form (Rahman & Davies, 1984a):

$$[A]\{\mathbf{x}\} - \lambda[B]\{\mathbf{x}\} = 0 \quad (2.7)$$

where  $[A]$  and  $[B]$  are real symmetric matrices, and  $[B]$  is also positive definite,  $\lambda$  is the eigenvalue and this can be taken as  $k_0^2$  or  $\beta^2$ , depending on the formulation used (Fernández and Lu, 1996). The above equation should have a canonical form in order to achieve an efficient and effective solution.

### 2.2.1 Scalar Formulations

The simplest of this type of formulation requires consideration of the longitudinal components of the TE or TM modes, but only when the fields could be described, with sufficient accuracy, as predominantly TE or TM. This has been applied to a number of problems (Koshiba, 1992) including the analysis of anisotropic waveguides (Koshiba *et al.*, 1982; Koshiba *et al.*, 1984; Strake *et al.*, 1988) and open boundary problems (Chiang, 1985). However, such a formulation is not acceptable for an anisotropic or

truly two-dimensional, inhomogeneous waveguide problem (Fernández and Lu, 1996). Nevertheless quasi-TE and quasi-TM approximations can be sufficiently accurate in a number of cases.

For a waveguide cross-section domain  $\Omega$ , the formulation for quasi-TE modes, for which  $E_x(x,y)$  is the dominant field component can be written as (Mabaya *et al.*, 1981):

$$J(E_x) = \iint_{\Omega} \left[ \left( \frac{\partial E_x}{\partial x} \right)^2 + \left( \frac{\partial E_x}{\partial y} \right)^2 + (\beta^2 - k_0^2 n^2(x,y)) E_x^2 \right] dx dy \quad (2.8)$$

where  $\beta$  is the propagation constant and  $n(x,y)$  is the refractive index profile.

Similarly, for quasi-TM modes, where  $H_x(x,y)$  is the dominant field component, can be written as (Mabaya *et al.*, 1981):

$$J(H_x) = \iint_{\Omega} \frac{1}{n^2(x,y)} \left[ \left( \frac{\partial H_x}{\partial x} \right)^2 + \left( \frac{\partial H_x}{\partial y} \right)^2 + (\beta^2 - k_0^2 n^2(x,y)) H_x^2 \right] dx dy \quad (2.9)$$

Although inadequate for truly anisotropic, inhomogeneous waveguides, the approximate scalar finite element method (FEM) is advantageous compared to the vector FEM, as it has smaller matrix dimensions, less computer time is spent to find the optical field, and there are no spurious solutions.

### 2.2.2 Vector Formulations

So for an anisotropic or purely two-dimensional inhomogeneous optical waveguide, a situation in which hybrid modes are inherent, a vector formulation is required to accurately represent the optical modes of the waveguide, since the scalar formulation can only give an approximation of the situation. However, some of these types of vector formulations are affected by spurious or non-physical solutions, which are obtained alongside with those which are correct for the waveguide.

There are several vector formulations which have been proposed. These include:

1. using longitudinal components of the  $\mathbf{E}$ ,  $E_z$ , and  $\mathbf{H}$ ,  $H_z$ , fields (Mabaya *et al.*, 1981)

2. using the full vector  $\mathbf{E}$  field (English & Young, 1971)
3. using the full vector  $\mathbf{H}$  field (Rahman & Davies, 1984a)
4. using both  $\mathbf{E}$  and  $\mathbf{H}$  fields (Svedin, 1989)
5. using transverse components of the  $\mathbf{E}$  field,  $\mathbf{E}_t$  (Chew & Nasir, 1989)
6. using transverse components of the  $\mathbf{H}$  field,  $\mathbf{H}_t$  (Fernández & Lu, 1991)
7. using transverse components of the  $\mathbf{E}$  and  $\mathbf{H}$  fields (Angkaew *et al.*, 1987)

These FEM formulations of the vector wave equation are based on methods of previously derived vector variational expressions (Berk, 1956; Morishita & Kumagai, 1977; Chen and Lien, 1980), obtained for electromagnetic problems.

The  $E_z$ - $H_z$  formulation was one of the first vector formulations to be applied to microwave and optical waveguides (Ahmed & Daly, 1969; Yeh *et al.*, 1975). However, this formulation cannot be applied to general anisotropic waveguides without the canonical form of equation (2.7) being destroyed, and the enforcing boundary conditions can be quite difficult for waveguides with an arbitrary dielectric distribution. Also, that this formulation is based on the longitudinal components of the vector fields, which are the least important of the six components of  $\mathbf{E}$  and  $\mathbf{H}$ , is of a fundamental disadvantage. Moreover, this type of formulation also suffers from the occurrence of spurious solutions, along with those that are correct for the waveguide, and the techniques to reduce them (Mabaya *et al.*, 1981) significantly complicate the computer programs and increase computer costs.

The full vector  $\mathbf{E}$ -field (English and Young, 1971) and combined 6 component  $\mathbf{E}$  and  $\mathbf{H}$  field formulation (English, 1971) were the next to be derived, and applied to cylindrical waveguides. The  $\mathbf{E}$ -field formulation has also been applied to microstrips (Hano, 1984), optical fibres (Katz, 1982) and anisotropic guides (Koshiba *et al.*, 1985). However, this formulation has the natural boundary condition corresponding to a magnetic wall, and so the electric wall boundary has to be forced by the (boundary) condition  $\hat{\mathbf{n}} \times \mathbf{E} = 0$ . This would mean that irregular shaped structures would be difficult to implement.

The full vector  $\mathbf{H}$ -field formulation has a much greater advantage over the  $\mathbf{E}$ -field formulation in its application to dielectric optical waveguides, since the magnetic field is continuous everywhere, due to a homogeneous permeability, and so there is no need

to ensure continuity of the magnetic field across any dielectric interface. Moreover, it has the natural boundary condition corresponding to an electric wall, which indicates that there are no forced boundary conditions since the magnetic field is continuous everywhere in a dielectric waveguide and so there is no need to ensure the continuity of the magnetic field. For symmetric guides, it is possible to enforce the appropriate boundary conditions along the line of symmetry in order to halve the structure under examination and therefore reduce the size of the matrices of the corresponding eigenvalue equation (2.7) – see Appendix A2. The  $\mathbf{H}$ -field formulation is expressed as (Berk, 1956; Rahman and Davies, 1984a):

$$\omega^2 = \frac{\int (\nabla \times \mathbf{H})^* \cdot \hat{\epsilon}^{-1} \cdot (\nabla \times \mathbf{H}) d\Omega}{\int \mathbf{H}^* \cdot \hat{\mu} \cdot \mathbf{H} d\Omega} \quad (2.10)$$

where  $\omega$  is the angular frequency of each waveguide mode,  $\Omega$  is the waveguide cross-section and,  $\hat{\epsilon}$  and  $\hat{\mu}$  are the permittivity and permeability tensors of the loss-free material, respectively.

Integration is carried out over  $\Omega$ , followed by applying the Rayleigh-Ritz procedure to the formulation in equation (2.10), which leads to the matrix eigenvalue equation (2.7), where  $[A]$  is now a complex Hermitian matrix (which can be reduced to the real symmetric case by using a suitable transformation (Rahman & Davies, 1984c) in the case of a lossless medium),  $[B]$  is a real symmetric and positive definite matrix, and eigenvectors  $\{\mathbf{x}\}$  are the unknown field components at the nodal points of the mesh.  $[A]$  and therefore eigenvector  $\{\mathbf{x}\}$  are different for each mode, with  $\omega^2$  as the corresponding eigenvalue.  $[B]$ , which is only dependent on the structure of the mesh, is the same for every mode. For this type of formulation, the result is given as the frequency of each waveguide mode corresponding to a selected value of the propagation constant (Fernández and Lu, 1996), when it is in fact the propagation constant,  $\beta$ , at a selected frequency (or wavelength) that is of interest to obtain. Hence, in order to obtain the correct mode(s) for a given wavelength,  $\beta$  has to be changed iteratively until the output eigenvalue corresponds to the correct wavelength.

Together with the correct mode(s), spurious solutions are also obtained in this, as well as the vector  $\mathbf{E}$ -field, formulation. The method used to eliminate these non-physical modes is discussed in section 2.5.

Other formulations were found in order to eliminate these spurious modes. This included an approach that used all the six components of  $\mathbf{E}$  and  $\mathbf{H}$  (Svedin, 1989) and where the Galerkin procedure was applied to Maxwell's equations directly. By enabling the enforcement of the correct boundary conditions, the spurious solutions are removed. However, the degrees of freedom also double per node (Rahman, 1995) as all six components of the electric and magnetic fields are being used and so the dimensions of the resultant matrices will be doubled, but if the  $z$ -related off-diagonal elements in the permittivity tensors are equal to zero these can be reduced by one third (Chiang, 1994). The variational approach has also been used with this type of formulation (English, 1971).

A formulation which just uses the transverse components of the  $\mathbf{E}$  or  $\mathbf{H}$  fields or both can also get rid of spurious modes implicitly and can result in maximum efficiency, with a matrix size for the  $\mathbf{H}_t$  formulation being two-thirds the size of that for a full vector  $\mathbf{H}$ -field formulation (Koshiba, 1992), with minimum variables used. Depending on the approach used, the complexity of the matrix can also vary from just some added complication to the loss of sparsity of the matrices, and then there is no possibility of using the sophisticated eigensolvers available for sparse matrices. However, efficient matrix solvers for such cases have been proposed (Fernández *et al.*, 1991).

A variational  $\mathbf{E}_t$ - $\mathbf{H}_t$  formulation was also developed, by Angkaew *et al.* (1987), where any solution which gave complex eigenvalues was treated as a spurious solution and those with real values as a real solution. However, some of the complex solutions may be physically realistic when a general anisotropy is modelled (Mrozowski, 1991).

It is clear from the above that a full vector formulation is much more advantageous to use as the others are fraught with problems. It was also made evident at the start of this section that the full vector  $\mathbf{H}$ -field formulation surpasses the full vector  $\mathbf{E}$ -field formulation because of the ease with which dielectric boundaries are incorporated.

### 2.2.3 Natural and Forced Boundary Conditions

A typical boundary value problem can consist of a two-dimensional region surrounded by an enclosing boundary  $C$ . An optical waveguide fits such a description. In general terms consider that a function  $\phi$ , which satisfies an equation

$$L\phi = f \quad (2.11)$$

where  $\phi = \phi(x,y)$  and  $f = f(x,y)$  and  $L$  is an operator, also satisfies some conditions on the boundary  $C$ . These boundary conditions can take several forms, namely the Dirichlet, Neumann or mixed boundary condition, and can be homogeneous or non-homogeneous (Davies, 1980). The Neumann boundary condition is a direct consequence of the stationarity of the variational expression (Davies, 1989) and is therefore called a natural boundary condition. This condition is usually implied by the variational expression, but it can also be forced (Davies, 1989). However, the trial functions must satisfy the Dirichlet boundary condition, and therefore it is an essential boundary condition (Davies, 1980).

In some cases the natural boundary conditions may be in conflict with the desired boundary conditions. This may be amended by adding a few terms to the variational expression (Davies, 1989), e.g. introducing a surface integral around the boundary  $C$  (Rahman, 1995).

In high frequency electromagnetics, i.e. for optical waveguides, the following boundary conditions are the most likely to occur (Davies, 1989)

$$\phi = 0 \quad (\text{homogeneous Dirichlet}) \quad (2.12)$$

$$\phi = s \quad (\text{inhomogeneous Dirichlet}) \quad (2.13)$$

$$\frac{\partial \phi}{\partial \hat{\mathbf{n}}} = 0 \quad (\text{homogeneous Neumann}) \quad (2.14)$$

where  $\phi$  is either  $\mathbf{E}$  or  $\mathbf{H}$ , the electric or magnetic fields, respectively, and  $\hat{\mathbf{n}}$  is the unit normal vector.

The functionals for the scalar formulation in equations (2.8) and (2.9) have the natural boundary conditions of  $\frac{\partial E_x}{\partial \hat{\mathbf{n}}}$  and  $\frac{1}{n^2} \frac{\partial H_x}{\partial \hat{\mathbf{n}}}$ , respectively, where  $n = n(x,y)$  is the refractive index profile. For the vector  $\mathbf{H}$ -field formulation given in equation (2.10), the

corresponding natural boundary condition is  $\hat{\mathbf{n}} \cdot \mathbf{H} = 0$  (Rahman, 1995). This implies the continuity of the vector  $\mathbf{H}$ -field or the magnetic field across the boundary, whereas for the scalar formulation  $\frac{\partial E_x}{\partial \hat{\mathbf{n}}}$  and  $\frac{1}{n^2} \frac{\partial H_x}{\partial \hat{\mathbf{n}}}$  only implies negligible or zero change in  $E_x$  and  $H_x$ , respectively, across the boundary.

## 2.3 The Finite Element Methodology

The execution of the finite element method requires the discretisation of the domain under investigation. The accuracy of the method depends on the mesh, although a finer mesh across the whole domain may yield accurate results but at the cost of increased computing time. A finer mesh should be used in areas where the field will have a rapid variation and a much coarser mesh in those areas where there is little variation in the field. Elements should not contain physical boundaries, i.e. there should be no abrupt change in property (e.g. refractive index) within the confines of an element, even though the property may change from element to element. Symmetrical domains should have symmetrical meshes as well, although wherever possible it may be better to take advantage of the symmetry in the waveguide by using the appropriate boundary conditions along the line of symmetry (see Appendix A2 for an example of how this is achieved for a rectangular waveguide).

The functional of the wave equation is obtained by considering the Dirichlet and Neumann boundary conditions for the domain that is under examination (Koshiha, 1992). The variational procedure is applied to this functional by the way of the stationary requirement, from which the Euler equation is derived and which corresponds to the wave equation (Koshiha, 1992), and this gives the variational formulation as in equation (2.10) which is then integrated over the domain. The Rayleigh-Ritz approach is applied to this (variational) formulation by using an interpolation function of the elements used to discretise the domain. The polynomial function, which approximates the field, should remain unchanged under a linear (or higher order) transformation from one co-ordinate system to the other.

All the element contributions should then be combined to form a global matrix. The resultant system of (matrix) equations, or rather matrix eigenvalue equation as in equation (2.7), that is obtained should be solved using an appropriate matrix solver, as the matrices are generally sparse.

## 2.4 The Elements and their Shape Functions

The discretisation process involves dividing the domain under investigation into elements. Each element has to be connected to the adjoining elements at each node, as shown by the discretisation of a domain in Fig. 2.2. This example shows triangular elements being used for a two-dimensional problem. However, there are several elements that can be used with the finite element method: the choice available is dependent on the structure under investigation.

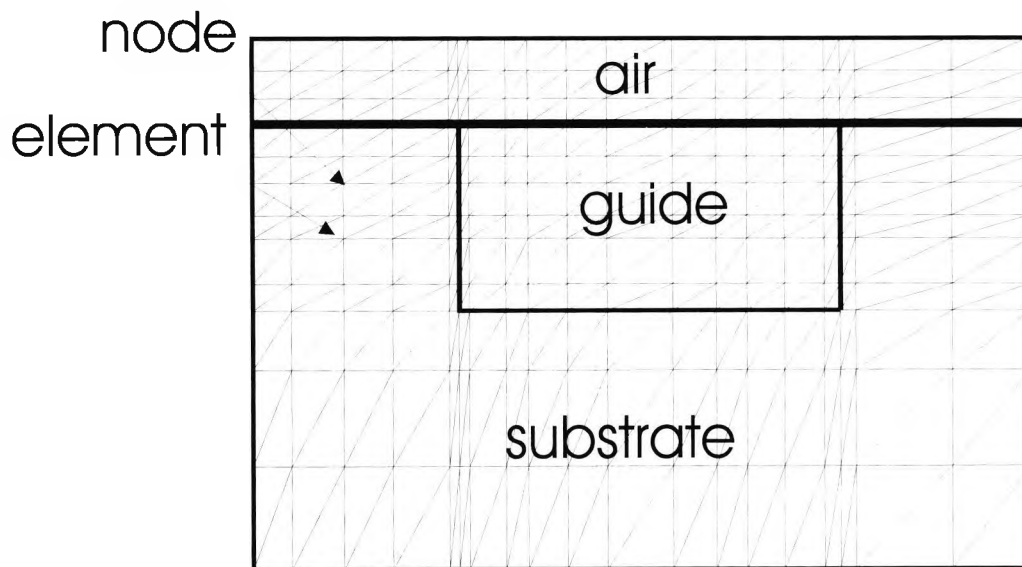


*Fig. 2.2 A rectangular dielectric waveguide discretised into linear, triangular, orthodox finite elements. A node and element when using such a linear triangular element have been shown.*

For one-dimensional problems, the line element can be used. This consists of a line of length,  $l_e$ , which is given by the  $x$ -coordinate of the two points at either end of the element. Although an element can be linear or a higher order element, it is the linear

that is mostly used and interest in the higher order elements only extends to the quadratic elements. For the one-dimensional element this consists of a line with the two nodes at the end of each element (as for the linear) but with another node at the centre of the line.

For two-dimensional problems, the elements can be either rectangular or triangular. However, rectangular elements are not as beneficial to use as triangular elements (Turner *et al.*, 1956), and are generally not used, especially along irregular boundaries of the domain. For those structures that are axisymmetric ring elements can also be used.

For three-dimensional problems, tetrahedral elements are available (Koshiya, 1992), and for axisymmetric three-dimensional problems, triangular ring elements can be used. There are also other special elements called isoparametric elements, which have curved sides and may be used when triangular elements are not considered acceptable for some curved boundary problems, such as an optical fibre. However, the triangular elements are more than adequate for most applications, and were used throughout this work.

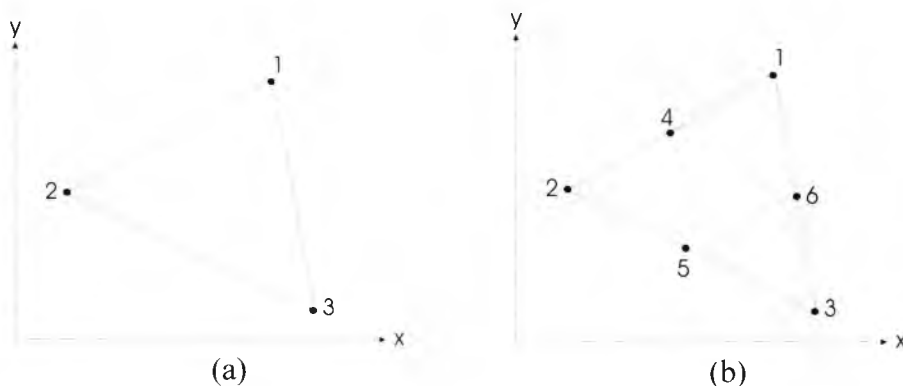


**Fig. 2.3** (a) Linear and (b) second order triangular elements (with labelled nodes).

Triangular elements, like line elements, can have both linear and higher order, typically quadratic, elements, as shown in Fig. 2.3. Higher order elements not only have nodes at the vertices of the triangle but also along each side of the triangle, as for the quadratic element in Fig. 2.3(b), as well as at the centre of the triangle, as for a cubic triangular element. However, as for the line elements, linear or first order triangular elements are

mostly used since there is much programming effort involved for higher order elements, and, therefore, linear triangular elements are employed throughout this work.

The whole concept of the finite element method is to replace the unknown variable,  $\phi$ , by a suitable expansion. Polynomials are generally used for these expansions. The field at any point in the domain,  $\phi(x,y)$  can be approximated as a set of discrete values at each node. The most simple triangular element, i.e. the linear triangular element, assumes a linear interpolation between the field values at the vertices of the triangle and the field at any point in the element,  $\phi_e(x,y)$  can be approximated as

$$\phi_e(x,y) = a_e + b_e x + c_e y \tag{2.15}$$

where  $\phi_e(x,y)$  is the electric or magnetic field, and  $a_e, b_e,$  and  $c_e$  are the coefficients of the polynomial expansion which are different for each element. This function is continuous across adjacent triangles such that if the field is interpreted as a third dimension it can be viewed as a surface with many triangular facets. Equation (2.15) is regarded as a complete polynomial for a first order triangular element. Complete polynomials for other (higher order) elements are obtained from the Pascal's triangle in  $x$  and  $y$  (Davies, 1989), as shown in Fig. 2.4.

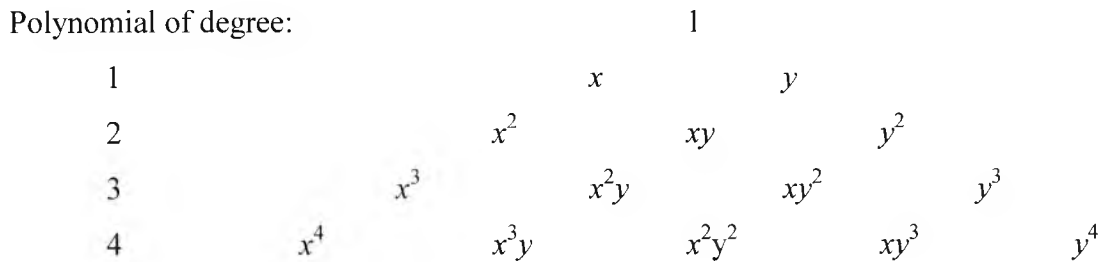


**Fig. 2.4** Pascal's triangle for complete polynomials.

The approximation of the field in the element can also be expressed another way as,

$$\phi_e(x,y) = \sum_{k=1}^3 N_k \phi_k^e = \begin{bmatrix} N_1 & N_2 & N_3 \end{bmatrix} \begin{Bmatrix} \phi_1 \\ \phi_2 \\ \phi_3 \end{Bmatrix}^e = \mathbf{N}\boldsymbol{\phi}^e \tag{2.16}$$

where  $\mathbf{N}$  is the shape function matrix and  $\boldsymbol{\phi}^e$  is the column vector corresponding to the elemental nodal field values.

Moreover, as mentioned above, it is essential that continuity is achieved across all adjacent elements and that  $\sum_k \mathbf{N}_k = 1$  at all points in the domain. This is to ensure convergence to the correct result (Zienkiewicz and Taylor, 2000).

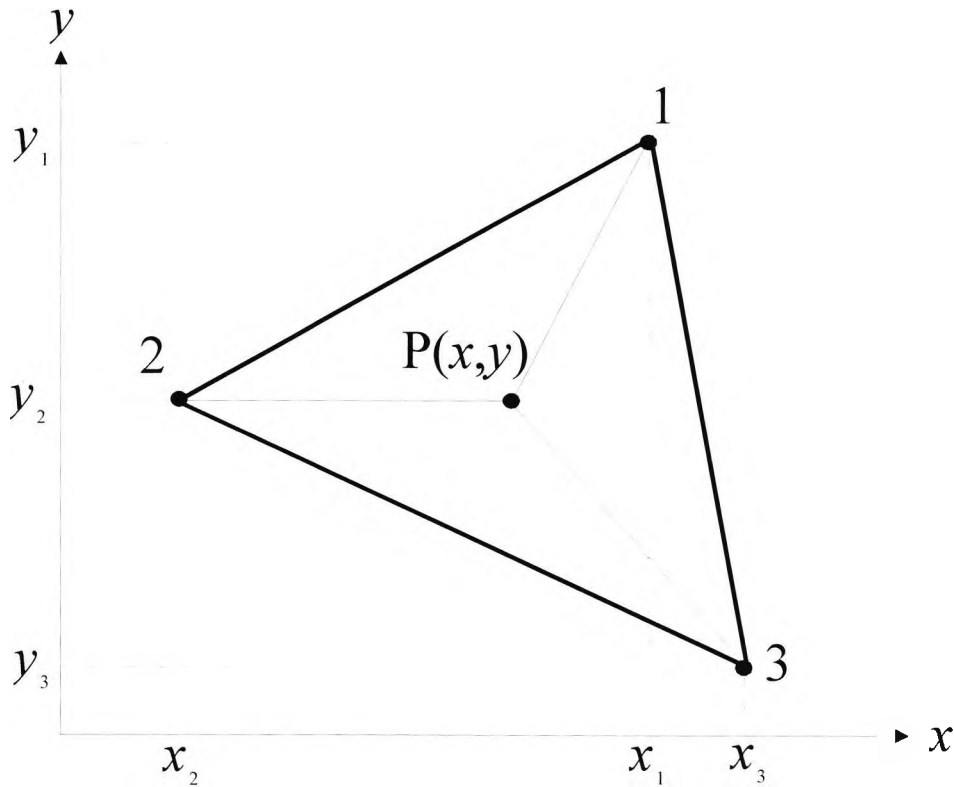


**Fig. 2.5** A linear triangular element with labelled nodes and co-ordinates for this element.

For the first order triangle in Fig. 2.5, where  $P(x,y)$  is any point on the surface of the triangle, the nodal values of the field  $\phi_1, \phi_2, \phi_3$  can be written as

$$\begin{bmatrix} \phi_1 \\ \phi_2 \\ \phi_3 \end{bmatrix} = \begin{bmatrix} 1 & x_1 & y_1 \\ 1 & x_2 & y_2 \\ 1 & x_3 & y_3 \end{bmatrix}^{-1} \begin{bmatrix} a_e \\ b_e \\ c_e \end{bmatrix} \quad (2.17)$$

Equation (2.17) can be rearranged as

$$\begin{bmatrix} a_e \\ b_e \\ c_e \end{bmatrix} = \begin{bmatrix} 1 & x_1 & y_1 \\ 1 & x_2 & y_2 \\ 1 & x_3 & y_3 \end{bmatrix} \begin{bmatrix} \phi_1 \\ \phi_2 \\ \phi_3 \end{bmatrix} \quad (2.18)$$

So from equations (2.15) and (2.18) it can be seen that

$$\phi_e(x, y) = [1 \quad x \quad y] \begin{bmatrix} 1 & x_1 & y_1 \\ 1 & x_2 & y_2 \\ 1 & x_3 & y_3 \end{bmatrix}^{-1} \begin{bmatrix} \phi_1 \\ \phi_2 \\ \phi_3 \end{bmatrix} \quad (2.19)$$

So comparing equation (2.16) and (2.19) gives

$$N_1(x, y) = \{(x_2 y_3 - x_3 y_2) + (y_2 - y_3)x + (x_3 - x_2)y\} / det \quad (2.20)$$

where *det* is the determinant of the 3x3 matrix in equation (2.19) and  $N_2$  and  $N_3$  are obtained by a cyclic exchange of 1→2→3 in equation (2.20).

Thus  $\{N\} \equiv [N]^T$  can be written as (Reddy, 1993),

$$[N]^T = \begin{bmatrix} N_1 \\ N_2 \\ N_3 \end{bmatrix} = \frac{1}{2A_e} \begin{bmatrix} x_2 y_3 - x_3 y_2 & y_2 - y_3 & x_3 - x_2 \\ x_3 y_1 - x_1 y_3 & y_3 - y_1 & x_1 - x_3 \\ x_1 y_2 - x_2 y_1 & y_1 - y_2 & x_2 - x_1 \end{bmatrix} \begin{bmatrix} 1 \\ x \\ y \end{bmatrix} \quad (2.21)$$

where  $T$  denotes the transpose of the shape function matrix and  $2A_e = det$ . Another name by which the shape functions  $N_1$ ,  $N_2$  and  $N_3$  are known is as interpolation functions.

The nodal values of the field  $\phi_1$ ,  $\phi_2$ ,  $\phi_3$  become the basis coefficients in the Rayleigh-Ritz approach (Davies, 1989). The shape functions are normalised with respect to their value such that they assume a value of 1 when at the vertex of the triangle associated with that shape function (i.e.  $N_1$  for node 1 of element, etc.) or 0 when at any other vertex. A more generalised form of normalisation can be done with respect to  $x$  and  $y$ , such that the same functions can then be applied to any kind of triangle. This can be achieved by using local (area) coordinates (Davies, 1989).

From Fig. 2.5,

$$L_1 = \frac{\text{area of } \Delta P23}{\text{area of } \Delta 123} \quad (2.22)$$

This can be written in matrix form as

$$L_1 = \frac{\begin{vmatrix} 1 & x & y \\ 1 & x_2 & y_2 \\ 1 & x_3 & y_3 \end{vmatrix}}{\begin{vmatrix} 1 & x_1 & y_1 \\ 1 & x_2 & y_2 \\ 1 & x_3 & y_3 \end{vmatrix}} = \frac{\begin{vmatrix} x_2 & y_2 \\ x_3 & y_3 \end{vmatrix} + (y_2 - y_3)x + (x_3 - x_2)y}{2A_e} \quad (2.23)$$

$$= \{(x_2 y_3 - x_3 y_2) + (y_2 - y_3)x + (x_3 - x_2)y\} / 2A_e$$

Similarly,

$$L_2 = \frac{\text{area of } \Delta P13}{\text{area of } \Delta 123}$$

$$= \frac{\begin{vmatrix} 1 & x_1 & y_1 \\ 1 & x & y \\ 1 & x_3 & y_3 \end{vmatrix}}{\begin{vmatrix} 1 & x_1 & y_1 \\ 1 & x_2 & y_2 \\ 1 & x_3 & y_3 \end{vmatrix}} = \frac{\begin{vmatrix} x_1 & y_1 \\ x_3 & y_3 \end{vmatrix} + (y_3 - y_1)x + (x_1 - x_3)y}{2A_e} \quad (2.24)$$

and

$$L_3 = \frac{\text{area of } \Delta P12}{\text{area of } \Delta 123}$$

$$= \frac{\begin{vmatrix} 1 & x_1 & y_1 \\ 1 & x_2 & y_2 \\ 1 & x & y \end{vmatrix}}{\begin{vmatrix} 1 & x_1 & y_1 \\ 1 & x_2 & y_2 \\ 1 & x_3 & y_3 \end{vmatrix}} = \frac{\begin{vmatrix} x_1 & y_1 \\ x_2 & y_2 \end{vmatrix} + (y_1 - y_2)x + (x_2 - x_1)y}{2A_e} \quad (2.25)$$

From these definitions it can be seen that

$$L_1 + L_2 + L_3 = 1 \quad (2.26)$$

And from the definitions if  $N_1, N_2, N_3$  and  $L_1, L_2$  and  $L_3$ , it can be seen that

$$L_1 = N_1 \quad L_2 = N_2 \quad L_3 = N_3 \quad (2.27)$$

This is true only for first order triangular elements.

For higher order elements, the shape functions have a relationship with the local area coordinates that is dependent on the Lagrange interpolation polynomial (Davies, 1989).

Now that the shape functions for the element have been discussed and it has been shown how the approximation of the unknown field in an element is found, the assembly of matrices [A] and [B], specified in equation (2.7), for each element can be next examined. This is given in Appendix A3.

## 2.5 Spurious Modes

There are two major issues to consider when modelling a waveguide structure using the finite element method. The first is that of spurious modes and the second is that of modelling the open space, an issue which will be discussed in Section 2.7.

These spurious or non-physical modes appear alongside the correct physical solutions only in the vector finite element analysis because, with the vector finite element method, the operator is no longer positive definite as for the scalar formulation (Rahman and Davies, 1984b). Moreover, the divergence equation (see equation (A1.4) in Appendix A1) which is implicit in the scalar wave approach (Koshiba *et al.*, 1984), is no longer so for the vector formulation. The Euler equations of the vector finite element method formulations satisfy the Helmholtz equations (or curl of the vector field) but not the divergence of the vector field ( $\nabla \cdot \mathbf{H}$ ), as in an analytical approach to Maxwell's equations. This is thought to be the cause of the spurious modes.

Once the eigenmodes have been computed, the identification of these spurious modes can be achieved through several means (Rahman and Davies, 1984b) including calculation of  $\nabla \cdot \mathbf{H}$  for all the modes, the value of which is quite high for the spurious non-physical solutions. These methods are all cumbersome and difficult to use, and it is therefore through the penalty method, which is used throughout this work, that this condition is forced before the eigenmode is obtained. This is achieved by adding a term to the variational formulation equation (2.10) as shown below

$$\omega^2 = \frac{\int (\nabla \times \mathbf{H})^* \cdot \hat{\epsilon}^{-1} \cdot (\nabla \times \mathbf{H}) d\Omega + \frac{\alpha_l}{\epsilon_0} \int (\nabla \cdot \mathbf{H})^* (\nabla \cdot \mathbf{H}) d\Omega}{\int \mathbf{H}^* \cdot \hat{\mu} \cdot \mathbf{H} d\Omega} \quad (2.28)$$

where  $\alpha_l$  is the penalty coefficient.

The divergence-free condition is applied in a least squares sense in that the higher the value of  $\alpha_l$ , the more heavily is the constraint applied to the corresponding Euler equation (Rahman and Davies, 1984c). Nevertheless, the value of  $\alpha_l$  is taken to be approximately  $1/\epsilon_g$ , where  $\epsilon_g$  is the dielectric constant of the core of the optical waveguide. However, if  $\alpha_l$  is taken to be higher, though there is a greater reduction of

the spurious modes, there is also a deterioration in the effective index of the optical guide for the correct eigenmodes, and this will be more significant near cut-off.

Just as the divergence-free term has been added to the variational formulation, the divergence-free term is added to the element matrices after they have been assembled purely on the basis of the first term of equation (2.28). The penalty term is computed in a separate subroutine, which is included in the main part of the program. There are added advantages to the use of this method, including a significant smoothness of the resulting field and the fact that there is no added increase in the matrix order and therefore the computational time.

As mentioned in Chapter 1, there are a number of methods by which the spurious modes are either reduced or eliminated (Chiang, 1994). However, the most striking of these other methods (and noted for the complete avoidance of the spurious modes) is through the use of the  $\mathbf{H}_t$  formulation (Fernández and Lu, 1996). Here only the  $H_x$  and  $H_y$  components of the  $\mathbf{H}$ -field are used: however, these are considered more than adequate for the representation of  $\mathbf{H}$  (Davies, 1993). Moreover, the removal of  $H_z$  is brought about by the incorporation of the zero-divergence condition (Fernández and Lu, 1996).

## 2.6 Assembly of the Global Matrices

As is seen in Appendix A3, the global matrices  $[\mathbf{A}]$  and  $[\mathbf{B}]$  of the eigenvalue equation (A3.24) may be obtained by using

$$[\mathbf{A}] = \sum_e [\mathbf{A}]_e$$

$$[\mathbf{B}] = \sum_e [\mathbf{B}]_e$$

To show the process of forming the global matrix the simple structure shown in Fig. 2.6 is taken as an example. Each element, of which there are 8, is numbered from 1 to 3 at the local nodes in an anticlockwise fashion. These nodes of the element are known as local nodes and the nodes numbered from 1 to 9 are the nodes over the whole structure. Thus the total number of nodes,  $n_p$ , is 9 and the total number of elements,  $n_{ele}$ , is 8.

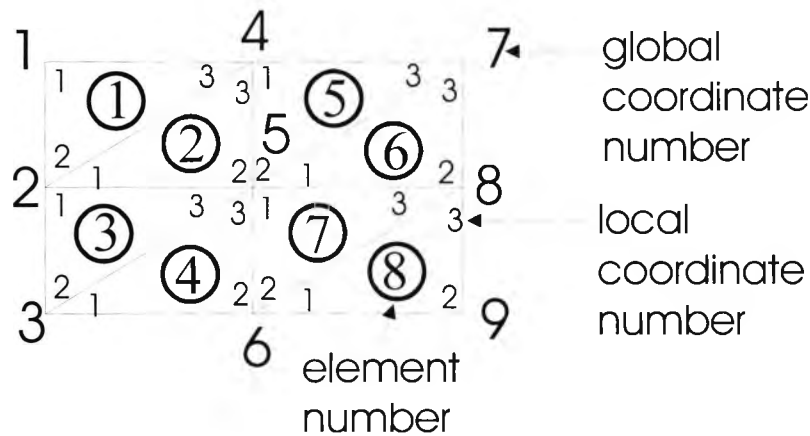


**Fig. 2.6** A simple structure discretised into eight elements. The circled numbers denote the element numbers.

For element 1:

$$\begin{aligned} 1_l &= 1_g \\ 2_l &= 2_g \\ 3_l &= 4_g \end{aligned}$$

For element 2:

$$\begin{aligned} 1_l &= 2_g \\ 2_l &= 5_g \\ 3_l &= 4_g \end{aligned}$$

For element 3:

$$\begin{aligned} 1_l &= 2_g \\ 2_l &= 3_g \\ 3_l &= 5_g \end{aligned} \quad \text{and so on.}$$

The subscripts  $l$  and  $g$  denote local node and global node, respectively.

The assembly of the global matrix is achieved with respect to these global nodes over the whole structure. Where a node or boundary of the element is shared between elements, the contribution from each element is added to the global matrix.

In Appendix A3 it was seen that both  $[A]_e$  and  $[B]_e$  are the  $9 \times 9$  element matrices for the vector  $\mathbf{H}$ -field, where each of the three nodes of the element is considered for each of the three components of the  $\mathbf{H}$ -field,  $H_x$ ,  $H_y$  and  $H_z$ . The assembly of the global matrix may therefore be better and more simply explained for a scalar  $H$ -field where only a single component of the  $\mathbf{H}$ -field is considered, e.g.  $H_y$ . The element matrices  $[A]_e$  and  $[B]_e$  are now  $3 \times 3$  for each element.

For element 1:

$$[A]_e = \begin{bmatrix} a_{11}^e & a_{12}^e & a_{13}^e \\ a_{21}^e & a_{22}^e & a_{23}^e \\ a_{31}^e & a_{32}^e & a_{33}^e \end{bmatrix} \quad (2.29)$$

where the row and column subscripts refer to the local nodes.

For example,  $a_{11}^e$  is the contribution from node 1 with respect to itself,

$a_{12}^e$  is the contribution from node 1 with respect to node 2, etc.

So when forming the global matrix  $[A]$  for all 9 nodes, it can be seen that the order of the matrix is  $n_p$ , the total number of nodes of the structure, which in this case is 9.

$$[A] = \begin{bmatrix} a_{11} & \cdots & a_{19} \\ \vdots & \vdots & \vdots \\ a_{91} & \cdots & a_{99} \end{bmatrix} \quad (2.30)$$

Each element,  $a_{rc}$ , is made up of the contributions of node  $r$  with respect to node  $c$ .

Global node 1 (i.e.  $a_{11}$ ) is only due to a single contribution of local node 1 of element 1 (i.e.  $(a_{11}^e)_1$ ).

Global node 1 with respect to global node 2 (i.e.  $a_{12}$ ) is only due to a single contribution of local node 1 with respect to local node 2, both of element 1.

Therefore the elements of  $[A]$  are

$$a_{11} = (a_{11}^e)_1 \quad (2.31)$$

where  $(a_{11}^e)_1$  denotes  $a_{11}^e$  for element 1

$$a_{12} = (a_{12}^e)_1 \quad (2.32)$$

$$a_{13} = 0 \quad (2.33)$$

since global nodes  $1_g$  and  $3_g$  are not directly connected.

$$a_{14} = (a_{13}^e)_1 \quad (2.34)$$

$$a_{15} = a_{16} = a_{17} = a_{18} = a_{19} = 0 \quad (2.35)$$

since, as for  $a_{13}$  (see equation 2.33), the global nodes  $5_g, 6_g, 7_g, 8_g, 9_g$  are not directly connected to  $1_g$ .

$$a_{12} = a_{21} \quad (2.36)$$

$$a_{22} = (a_{22}^e)_1 + (a_{11}^e)_2 + (a_{11}^e)_3 \quad (2.37)$$

$$a_{23} = (a_{12}^e)_3 \quad (2.38)$$

$$a_{24} = (a_{23}^e)_1 + (a_{13}^e)_2 \quad (2.39)$$

and so on.

So it can be seen that each term of the global matrix  $a_{rc}$  (where  $r \neq c$ , but the nodes  $r$  and  $c$  are connected) consists only of a single element contribution unless the boundary of the element is shared in which case there is a maximum of contributions from two elements. For  $a_{rc}$  (where  $r = c$ ) the contribution is nearly always made up of two or more contributions unless the node is not shared by other elements. Therefore, for  $a_{rr}$  there can be any number of element contributions depending on how many elements share the node.

### 2.6.1 Sparsity

The fact that the contribution to the global matrix for unconnected nodes is zero leads to very many of the matrix components being zero. Such a matrix is known as a sparse matrix.

The global matrices  $[\mathbf{A}]$  and  $[\mathbf{B}]$  from the eigenvalue equation (2.7) are highly sparse and their sparsity increases with the order of the matrices and decreases with the use of higher order shape functions (Silvester and Ferrari, 1990). Moreover, the type of matrix determines the nature of the matrix solver (Rahman, 1995). However, the algorithms employed for the solution of the sparse matrices leads to a reduction in the computational time and matrix size. This, together with the use of special storage schemes, allows for larger matrices to be used (Davies, 1989). The intention of this method is to generate the global matrices  $[\mathbf{A}]$  and  $[\mathbf{B}]$  as a one-dimensional array of non-zero elements,  $\mathbf{A}(k)$  and  $\mathbf{B}(k)$ , respectively, together with two additional one dimensional arrays,  $\mathbf{R}(k)$  and  $\mathbf{C}(k)$  which hold the information on the row and column number, respectively, of the non-zero element of the  $[\mathbf{A}]$  or  $[\mathbf{B}]$  matrix.  $k$  is the index of the four arrays.

In this study a sparse matrix algorithm, using a matrix routine that considers only the non-zero elements in the upper or lower triangle of the symmetric real matrices, solves the eigenvalue problem by an iteration process applied simultaneously to a subspace of

eigenvectors. This is called the method of subspace iteration (Bathe and Wilson, 1976). The largest number of nodes, and therefore the order of the  $[A]$  and  $[B]$  matrices, used in a structure with this method was  $201 \times 201$  ( $=40401$ ).

The advantage of this method is that no initial guess for the field vector is made, since a random generator is used to avoid any initial bias to the solution.

## 2.7 Infinite Elements

The dielectric waveguide is electromagnetically an unbound structure (Chiang, 1994) and so the field can, in principle, extend to infinity over all space, as the field decays in an exponential way outside the guide region. Near cutoff, the field decays slowly and extends a large distance away from the guide core into the substrate area, and it is therefore in this region of operation that the modelling of the open space is most important.

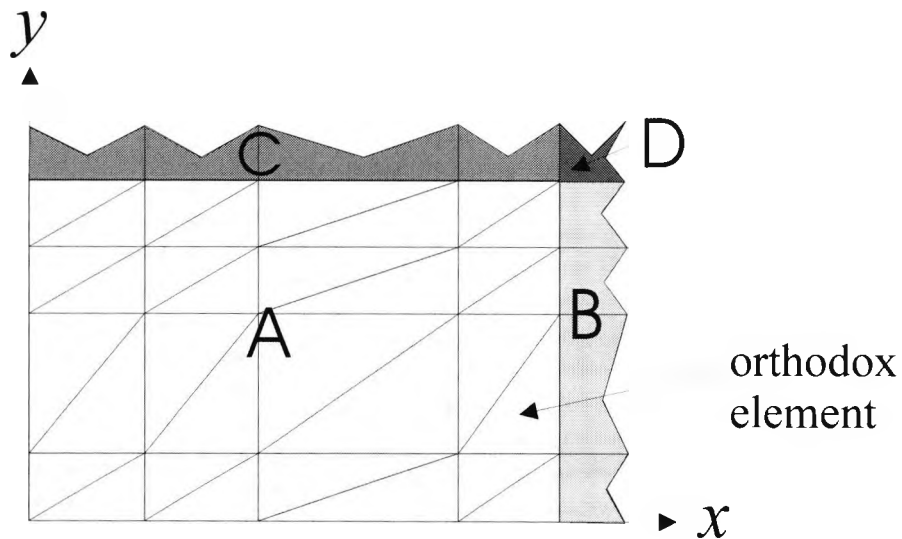


*Fig. 2.7 Part of a rectangular dielectric waveguide (with two-fold symmetry) discretised into finite and infinite elements.*

The analysis of the open space is not possible with orthodox finite elements and so a different approach has to be considered (Chiang, 1994; Vassallo, 1997). The method developed by Rahman and Davies (1984a), and the method used throughout this work,

is to apply infinite elements along the outer the boundaries together with the orthodox elements (triangular elements in shaded region A), as shown in Fig. 2.7 for a rectangular dielectric waveguide.

Although several other techniques have been applied for the treatment of unbounded structures, this is considered to be a much better, accurate and simpler method than a number of others (Rahman and Davies, 1984c). The use of the infinite elements allows the domain of interest to be extended to infinity by manipulating the shape function in any one of the four transverse directions (i.e. positive  $x$ , negative  $x$  or either of the  $y$  directions) without any increase in the order of the matrix. Since the field outside the core area is of an exponential nature, it is natural that the shape function should also be changed to allow for this. So if, in Cartesian coordinates for example, an element is extending to infinity in the positive  $x$  direction (as for infinite elements in shaded region B), then the shape function becomes (Rahman and Davies, 1984c)

$$N(x, y) = N_y(y), N_x(x) = N_y(y) \cdot \exp(-x/L) \quad (2.40)$$

where  $L$  is the decay length for positive  $x$  direction. The decay length should be the same for all elements that extend to infinity in the positive  $x$  direction so that each field component can be regarded as continuous over this unbounded domain. For elements extending to infinity in the positive  $y$  direction (as for infinite elements in shaded region C), then the shape function becomes (Rahman and Davies, 1984c)

$$N(x, y) = N_y(y), N_x(x) = N_x(x) \cdot \exp(-y/K) \quad (2.41)$$

where  $K$  is the decay length for positive  $y$  direction. Hence, for elements extending to infinity in any of the other transverse directions, similar shape functions can be obtained and the decay length is the same for any element extending to infinity in any one direction. For corner infinite elements (shaded infinite element D) the shape function becomes exponential in both  $x$  and  $y$  and so for the corner element which is in the positive  $x, y$  direction (Rahman and Davies, 1984c)

$$N(x, y) = N_0 \cdot \exp(-x/L) \cdot \exp(-y/K) \quad (2.42)$$

Any integration of the shape functions, or their derivatives, over the infinite elements is finite and easy to obtain (Rahman and Davies, 1984a).

The value of each decay parameter depends on the structure as well as the operating frequency. When choosing the value of the decay parameters, at first a 'guess' value is

taken. When the first optical field solution is obtained for the structure under examination, the decay parameters are also calculated for each transverse direction. The updated decay parameters are then substituted for the next iteration. With a few such iterations, the stationary or best value for the decay parameter can then be obtained (Rahman and Davies, 1984a).

## 2.8 Boundary Values

Although a number of boundary conditions can be applied if the waveguide cross-section is symmetrical (as shown in Appendix A2), boundary conditions and therefore the subsequent mesh dimensions are also imposed when field or potential values are known, e.g. on a metal electrode the potential of the structure is known.

So if the value of the field or potential is known at a certain node, the row of that node is consequently removed in all global matrices and column vectors that form the eigenvalue equation or any other matrix equation, and the column of the matrices corresponding to the node for which the field (or potential) is known is also removed but the right hand side column vector is updated accordingly. Although sparse matrix solvers are used throughout this project to solve the eigenvalue equations or other matrix equations, this idea can be more clearly explained using dense matrices, as in the example below.

Take the three equations

$$x + y + z = 3$$

$$3x + 4y + 5z = 12$$

$$4x + 5y + 6z = 15$$

These can be written in matrix form as

$$\begin{bmatrix} 1 & 1 & 1 \\ 3 & 4 & 5 \\ 4 & 5 & 6 \end{bmatrix} \begin{bmatrix} x \\ y \\ z \end{bmatrix} = \begin{bmatrix} 3 \\ 12 \\ 15 \end{bmatrix}$$

now if it is known that  $y=1$ , following the instruction given above for the matrix equation  $\mathbf{Ax}=\mathbf{b}$ ,

$$\left[ \begin{array}{c|cc} 1 & 1 & x \\ 3 & 5 & y \\ 4 & 6 & z \end{array} \right] = \left[ \begin{array}{c} 3 \\ 12 \\ 15 \end{array} \right]$$

$y$  is in the 2<sup>nd</sup> row of this column matrix and because it is known it is no longer needed as a variable in the matrix equation. So row 2 is removed from all matrices and column vectors. Those coefficients multiplied by  $y$  ( $=1$ ) have to be subtracted from  $\mathbf{b}$  in the matrix

equation as shown below. 
$$\left[ \begin{array}{c|c} 1 & x \\ 4 & z \end{array} \right] = \left[ \begin{array}{c} 3 - (1*1) \\ 15 - (5*1) \end{array} \right] = \left[ \begin{array}{c} 2 \\ 10 \end{array} \right]$$

Hence, column 2 has been effectively removed from matrix  $\mathbf{A}$  as these were the coefficients of  $\mathbf{A}$  being multiplied by  $y$ , and  $\mathbf{b}$  has been updated accordingly.

So now

$$x + z = 2$$

$$4x + 6z = 10$$

This yields

$$z = 1, x = 1.$$

This process shown above for a small dense matrix becomes much more complicated for sparse matrices.

## 2.9 Summary

This chapter has given a brief history of the finite element method together with the various formulations available for the solution of the electromagnetic field in an optical waveguide (obtained from the wave equation). It has been established that a vector  $\mathbf{H}$ -field formulation is superior to the corresponding  $\mathbf{E}$ -field formulation for the reason that the former can more easily deal with boundaries between dielectric materials. It has also been mentioned that the use of a vector formulation leads to the formation of non-physical spurious modes, and the nature of the methods, more particularly the penalty method, for eliminating such modes. Moreover, the optical waveguide is electromagnetically an open boundary problem and this can cause a number of problems near cutoff for the waveguide. The method of infinite elements has been found to be a much better, accurate and simpler method than a number of others.

The simple mechanics of constructing the element matrices is detailed in this chapter. This is dependent on the linear approximation of the field vector, from which the shape function of the linear triangular element is then obtained. The assembly global matrices have also been shown.

The finite element method is to be adapted and used in conjunction with a number of other methods throughout the whole of this work and therefore is the basis for all the numerical modelling in this thesis. It is expected that the use of the finite element in conjunction with these other methods will improve accuracy of the results for the electro-optic modulator structures to be examined. These new methods are detailed in Section 3.3 of the next chapter.



# 3

## *An Introduction to Electro-Optic Waveguide Modulators*

---

---

### **3.1 Introduction**

In chapter 1, an optical modulator was referred to as being a device that changes the irradiance (or direction originally with time but with both time and space for later devices) of the light passing through it. The modulator is an essential part of any communications network, as it is where the information-containing signal to be transmitted is incorporated with the carrier (from the light source), which in the case of an optical communications system is the laser beam. Hence, the light is then varied in time by the signal –through a controlling mechanism (i.e. the mechanism responsible for the main change in refractive index in the device) that arises from whether the device is, for example, electro-optic, magneto-optic, acousto-optic, etc. – and this signal is typically in the form of an electric field, a magnetic field or an acoustic wave, respectively.

In this chapter the main interest will be in the operation of the electro-optic modulator, which is primarily based on the linear electro-optic effect, and comparisons are made

with the semiconductor electroabsorption modulator, the only other significant electronically-controlled optical modulator. The change in refractive index for this latter type of device is dependent on a number of different effects (mainly carrier and, predominantly, field related effects) of which the linear electro-optic effect is one of the field-related effects.

The optical modulator became a necessity for laser control because the earlier lasers were in the form of solid state crystal or glass lasers. Hence, there was no way to directly modulate their output and external modulation was therefore required. Nevertheless, with the development of continuous wave (cw) semiconductor lasers in the late 1970s, direct modulation became an option. This is however fraught with problems of low bandwidth and high chirp (Brinkman *et al.*, 2000; Heismann *et al.*, 1997).

For early optical communications systems, electro-optic modulation was clearly the better option. The first electro-optic modulators were bulk crystal modulators (Kaminow and Turner, 1966), which were large and with high drive voltages. It was soon found that both  $\text{LiNbO}_3$  and  $\text{LiTaO}_3$  were superior in performance when compared to the other bulk crystals available. However, when these materials were later used in integrated optics (with Ti indiffused crystal to form waveguides), it was found that  $\text{LiNbO}_3$  was the superior of the two (Kaminow and Carruthers, 1973). Moreover,  $\text{LiNbO}_3$  is thermally, chemically and mechanically stable (Wooten *et al.*, 2000). Waveguide modulators were achievable, prior to the concept of integrated optics, with the p-n semiconductor modulator (Reinhart, 1968). The early semiconductor waveguide devices were fabricated from the indirect gap semiconductor GaP, the dimensions of which were similar to those of the bulk crystal modulators, and were operated in reverse bias.

Integrated optics promised smaller, more efficient and more cost effective devices. However, a true two-dimensional waveguide device had to be achieved to realise the concepts brought forward by the introductory paper on this subject (Miller, 1969). Ti-indiffusion in the  $\text{LiNbO}_3$  crystal resulted in two-dimensional channel waveguides. Modulators using this technology yielded more power efficient devices (Alferness, 1982). Double heterostructure p-v-n<sup>+</sup> GaAs/ $\text{Al}_x\text{Ga}_{1-x}\text{As}$  modulators also yielded much

improved drive voltages and therefore more power efficient devices (Reinhart and Miller, 1972) (where  $v$  indicates a lightly doped layer of n-type doping). The double heterostructure formed by the GaAs layer (where the GaAs layer is of higher refractive index than the  $\text{Al}_x\text{Ga}_{1-x}\text{As}$  layers;  $0 < x < 1$ ) sandwiched by the outer  $\text{Al}_x\text{Ga}_{1-x}\text{As}$  layers, produced the confinement of the light in one dimension while the strip electrode on the upper surface of the device produced the confinement in the second dimension. Further improvements were achieved if the GaAs layer was made to have strictly intrinsic doping (in reality there is still some slight unintentional doping) and the device was designed such that the depletion width only extended to roughly the width of the intrinsic GaAs layer (over the operation of the device). This was to seek to obtain a maximum but constant electric field over this region, such that any change in the refractive index as a consequence of the applied electric field also followed a similar trait (as the electric field).

Further advances in the field of electroabsorption modulators included the development of multiple quantum well (MQW) modulators (Miller *et al.*, 1985) and subsequently the development of the electroabsorption modulator – distributed Bragg reflector (DBR)/distributed feedback (DFB) laser modules (Brinkman *et al.*, 2000). A greater choice of materials and the availability of superior growth techniques led to a number of bulk semiconductor and MQW semiconductor waveguide modulators being developed for operation at different (typically longer) wavelengths (Ido *et al.*, 1996; Rolland *et al.*, 1992; Kawano *et al.*, 1997). The multifunction devices, such as the modulator-laser modules mentioned earlier, have been brought about through the successful use of selective area epitaxy (Brinkman *et al.*, 2000).

More recent improvements in the electro-optic modulators include the use of ridge  $\text{Ti:LiNbO}_3$  waveguides (Noguchi *et al.*, 1995) for  $\text{LiNbO}_3$  devices and also the significant developments seen recently in polymer waveguide modulators (Dalton, 2003; Bechtel *et al.*, 2003).

Important to device performance are the design of the electrodes (e.g. lumped or travelling wave (TW) with TW offering much higher bandwidths and lumped being much easier to design), the crystal cut, the buffer layer material and design (if one is used), the amount of dopant (if any) that is used and also the fabrication parameters.

Most electroabsorption waveguide modulators use a simple single waveguide phase modulator design, while among the electro-optic modulators a Mach-Zehnder interferometer or directional coupler type design is typically used, with the former being preferable for higher modulating bandwidths (Wooten *et al.*, 2000).

It is evident that fabrication and device design have a large effect on device characteristics. However, it will be shown in this and the subsequent chapters that some of these characteristics are at odds with each other such that one will worsen when the other improves. It is therefore easy to see that there is a need for device optimisation. This is indeed one of the primary reasons for modelling the device prior to fabrication, as today's optoelectronic devices are both complex and initially costly to fabricate. In order to model the device it is crucial to know the effect of each step of the device fabrication and how it may affect device performance. Likewise, in the model, it may also be helpful to split the device into sections (see Fig. 3.1 for a Ti:LiNbO<sub>3</sub> Y-branch modulator) such that each section can then be modelled separately and much more easily. As shown in the figure, Stage I consists of the input and output waveguides. These not only give the propagation loss of the waveguide but also the fibre-to-waveguide match, both of which are the main components of insertion loss. Moreover, the diffusion process or any etching process in the formation of the waveguides can also be modelled for the single guide. For this uniaxially birefringent material (i.e. LiNbO<sub>3</sub>), the crystal cut is also of importance to the propagation constant of the optical wave. Stage III is the active section of the device and for the purpose of waveguide modelling is the one of main interest. Here the electrode design is examined with respect to the metal used, the thickness of the electrodes (to which the signal is applied), the width of the electrodes and the separation between the electrodes, the buffer layer thickness and material. The drive voltage, bandwidth, optical loss from the electrode and many other characteristics can be determined in this section. Stage II is the remaining section where the split in the waveguide occurs. The branching waveguides in this section can be curved or with a constant angle between them. In either case the optical propagation loss in this section is higher than that for a straight guide, and any dissimilarity between the two branches is a contributing cause for a decrease in the extinction ratio (Heismann *et al.*, 1997) of the device.

As mentioned in Chapter 1, there are several numerical methods used to model optical devices. However, it was determined in Section 1.4.5 that the full vector  $\mathbf{H}$ -field formulation of the wave equation using the finite element method (FEM) was superior

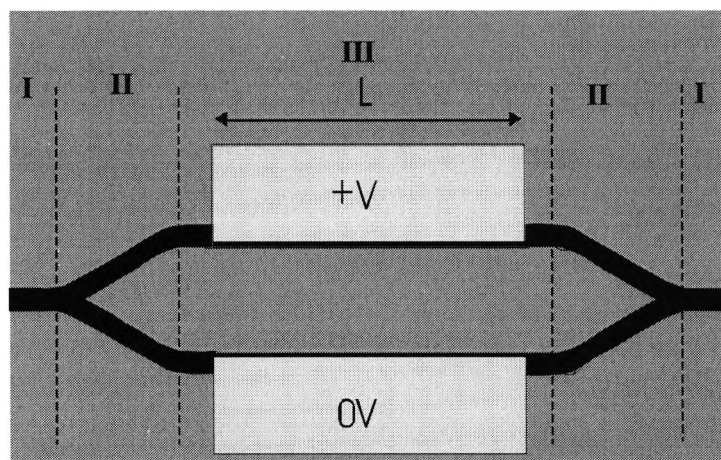


Fig. 3.1. A Y-Branch Modulator

to all other numerical and analytical techniques, especially for diffused Ti:LiNbO<sub>3</sub> waveguides. Moreover, the beam propagation method is considered to be one of the most powerful techniques for modelling waveguide bends (or Y-junctions) (Rajarajan *et al.*, 2000). It has also been shown (Wongcharoen *et al.*, 1997) that for power transfer calculations as for the directional coupler device, the least squares boundary residual method in conjunction with the FEM was superior to others (i.e. the overlap method, coupled mode theory or mode matching techniques), in particular for nonidentical and/or strongly coupled waveguides. Hence, it is these methods that are used to model the electro-optic modulator devices throughout the work reported in this thesis.

### 3.2 The Fabrication of Electro-Optic Devices

The key electro-optic modulator parameters and the manner in which they vary with the different device types has been given in the literature review in the previous section. However, not only is the design of these devices important to their characteristics, the method of fabrication also affects the device performance (Wooten *et al.*, 2000; Dagli,

1999). Hence, steps can be taken during fabrication to improve the device and eliminate any shortcomings.

### **3.2.1 Ti:LiNbO<sub>3</sub> Waveguide Modulator**

It has been established that LiNbO<sub>3</sub> has a very high intrinsic modulation bandwidth (Wooten *et al.*, 2000) with optical transparency between 420 and 5200nm (U-Oplaz Technologies, 1999). However, device switching speeds are limited by physical constraints (Wooten *et al.*, 2000) which are influenced by the design and the fabrication of the device. Nevertheless, the above property is indicative of the fact that there is very little wavelength dependence (compared with other materials e.g. Al<sub>0.38</sub>Ga<sub>0.62</sub>As) in an optical device fabricated from this material, and so it would be valuable to use for time division multiplexing (TDM) and wavelength division multiplexing (WDM) purposes.

Moreover, LiNbO<sub>3</sub> has large electro-optic, piezo-electric and elasto-optic coefficients (Strake *et al.*, 1988). These are beneficial when employing this material for electro-optic (Wooten *et al.*, 2000) and acousto-optic modulators (Tsai and Le, 1992), respectively.

However in this section fabrication issues are the main concern, in particular crystal cut, diffusion, etching and electrode fabrication. For etched ridge Ti:LiNbO<sub>3</sub> waveguides, not only is the control of diffusion parameters along the length of the guide essential for high-quality guides, but smooth sidewalls, good control etch depth and sidewall direction are also key to achieving low-loss waveguides with good optical confinement (Wooten *et al.*, 2000).

#### 3.2.1.1 Waveguide Fabrication

LiNbO<sub>3</sub> is compatible with conventional integrated-circuit processing technology (Wooten *et al.*, 2000). Wafers are now available in X-, Y-, Z-cuts with typical diameter sizes of 3". More recently 5" diameters have been reported (personal communication at ITCOM2001 – Sriram of SriCo).

The LiNbO<sub>3</sub> crystal is grown by the Czochralski technique (Ballman, 1965), as are semiconductor crystals. This process is controlled by the composition of the crucible, the thermal environment surrounding the melt (which should of the requisite low temperature gradient), the heat source to provide this, with the pulling and rotating mechanism and diameter control achieved by optical and weighing techniques (Fraser, 1989a). Single crystal boules are vertically drawn from the melt in the platinum crucible and then poled (Fraser, 1989b). Susceptibility of the crystal to photorefractive damage (mentioned in Section 1.3.4.1.2) can be lowered if Fe ion contaminants are kept to a minimum during the growth process (Wooten *et al.*, 2000).

Wafers are obtained by horizontally slicing the long crystal boule with low-speed annular saws (Fraser, 1989c). This is followed by lapping and polishing the wafer (Fraser, 1989c) in order to achieve optimum wafer surface flatness, which is important in minimising any variations in waveguide width across the wafer when defining the mask during the photolithography part of the waveguide fabrication.

The most common method of fabricating superior quality waveguides in LiNbO<sub>3</sub> that are suitable for modulator devices is Ti-indiffusion, and it is only this method of waveguide fabrication which will be described here. The wafer is first cleaned and then a layer of photoresist is deposited on the surface. Contact photolithography is then used to etch a window in the photoresist (McGillis, 1983). A layer of titanium of thickness,  $\tau$ , is then deposited onto the wafer surface using a number of methods among which rf sputtering is regularly used (Alferness, 1988). It can be seen that it is the mask written in the photoresist that then defines the width and direction of the titanium stripe. Photoresist solvent removes the unwanted titanium (Ti) and leaves the Ti stripe behind. The wafer is then placed in a diffusion furnace and then the time for and the temperature of the process are chosen, by design, to attain high quality guides. These are typically for 10 hours at 1000°C in an atmosphere of argon bubbled through a water column (Korotky and Alferness, 1987). This was found to be advantageous for minimising both the photorefractive effect in LiNbO<sub>3</sub> and the outdiffusion of Li<sub>2</sub>O – a process that causes planar waveguiding in the crystal. Uniformity of the Ti film as well as uniformly flat thermal zones in the furnace are also desirable for the preservation of the waveguide cross-section along its length (Wooten *et al.*, 2000). Then, the wafer is cooled in flowing oxygen in order to reoxidise the crystal (Korotky and Alferness, 1987).

If a tighter confinement of the optical field is desirable in any application, this can be provided by a ridge Ti:LiNbO<sub>3</sub> waveguide. Such a structure also has other advantages, although these are related to the design of the electrodes (this will be covered in Section 3.3.3. Ridge waveguides can be achieved by wet etching an area of the LiNbO<sub>3</sub> crystal that has already undergone a process of proton exchange (Laurell *et al.*, 1992) or by wet etching the  $-Z$  faces (only these can be etched for Z-cut LiNbO<sub>3</sub>) after selective domain inversion (Barry *et al.*, 1999). Although the method used by Barry *et al.* (1999) has one of the highest reported etch rates (of 40nm/min), both wet etching methods may suffer from inversion of the domain polarisation which occurs on the  $+Z$  faces during the diffusion process (Xu *et al.*, 1994) and hence are not suitable for conventional Ti indiffused guides on a Z-cut substrate. A similar effect has also been reported for a plate of pure LiNbO<sub>3</sub> (Nakamura *et al.*, 1987). Ridge waveguides can also be achieved by dry etching methods of ion milling (Burns *et al.*, 1999), reactive ion etching (Winnall and Winderbaum, 2000) or electron cyclotron resonance (ECR) plasma etching (Mitsugi *et al.*, 1998; Noguchi *et al.*, 1993). These processes are believed to be independent of substrate orientation: however, the rate of etching of these processes was found to be dependent on substrate orientation (Winnall and Winderbaum, 2000).

### 3.2.1.2 Electrode Fabrication

For high-speed devices, gold is generally used for the electrode material but for low speed devices (with modulation frequencies less than 100MHz) aluminium electrodes are satisfactory (Alferness, 1988). However, an optically transparent buffer layer may be deposited prior to the metal deposition for the electrodes. This is more important for devices designed for and supporting TM rather than TE polarised light, as the optical loss due to the metal electrodes is higher for TM polarised light. However, a buffer layer is also used for most high-speed devices as a means of matching the velocity of the electrical signal and the optical signal, since without it the former travels significantly slower than the optical wave. SiO<sub>2</sub> is a frequently used buffer layer and was deposited using the sputtering technique for earlier devices, but this method was replaced by chemical vapour deposition in order to achieve stable device characteristics and eliminate short-term drift (Korotky and Alferness, 1987). The instability from which Ti:LiNbO<sub>3</sub> modulators suffer is in the form of bias drift. Another technique of

etching away the buffer layer in the gap region between the electrodes would reduce the bias drift (Yamada and Minakata, 1981).

The bias drift is due to charge accumulation and/or migration and are both related to any mechanical stress to the applied to the crystal. The mechanical stress may be caused by the piezoelectric effect or the thermal change experienced by the crystal. This effect is known as the pyroelectric effect and it has been known to affect the long term stability of Ti:LiNbO<sub>3</sub> modulators (Korotky and Veselka, 1996). Bias drift has been more significant for Ti:LiNbO<sub>3</sub> modulators using Z-cut wafers. This is because of the electrical charge accumulation on the Z-faces during processing and is due to the crystal's piezoelectric and pyroelectric properties (Wooten *et al.*, 2000): hence the need for special handling procedures for the Z-cut wafers. Moreover, the bias drift, due to charge migration and build-up of pyroelectric charges, which occurs in modulators fabricated on Z-cut wafers, can be minimised by special design (Nayyer and Nagata, 1994; Higuma *et al.*, 2000) and packaging (Wooten *et al.*, 2000). Hence, there has been a move towards X-cut Ti:LiNbO<sub>3</sub> modulators.

A metal adhesion layer (typically titanium (Wooten *et al.*, 2000) or chrome (Alferness, 1988)) is next vacuum deposited across the entire buffer covered wafer, followed by a layer of gold. The electrode pattern is photolithographically defined using special lithographic processes which are needed to define the thick mask in order to maintain the cross-section of the RF electrodes (the thickness of which can range from a few  $\mu\text{m}$ s to more than  $15\mu\text{m}$ ) along the length of the device. The mask is then removed and the metal in the gaps etched away (Wooten *et al.*, 2000). However, even with these precautions a slight angle (of approximately  $85^\circ$  to the horizontal) is still obtained.

In order to be used for 'everyday' applications, both the optical and electrical signal need to be efficiently and effectively delivered to and from the device. However, first the wafer has to be diced into the appropriate devices, with the substrate end faces cut at an angle to the waveguides to eliminate reflections and then polished. The packaging of the device can be divided into the integrated-optic (i-o) chip, the optical fibre assemblies and the interconnects and housing (Wooten *et al.*, 2000). For most telecoms applications, the i-o chip is non-hermetically packaged. Moreover a polarisation-maintaining fibre is placed at the input pigtail to ensure the light polarisation to the

device is that for which it was designed. The electrical interconnects are then attached and soldered to the housing. The pigtailed chip is then mounted onto the housing and the electrical connection between the chip and interconnects are achieved through wire/ribbon bonds of appropriate dimension for optimal performance for high-frequency operation.

### 3.2.2 GaAs/Al<sub>x</sub>Ga<sub>1-x</sub>As Waveguide Modulator

Unintentionally-doped GaAs yields low loss waveguides of 0.5dB/cm (Sakamoto *et al.*, 1999). The main advantage over LiNbO<sub>3</sub> is that it can easily be integrated with other semiconductor devices on the same substrate (particularly regarding the laser, as it is now even possible to have multifunction devices on LiNbO<sub>3</sub> substrates today).

As mentioned in the previous section, LiNbO<sub>3</sub> is compatible with conventional integrated-circuit processing technology and therefore most of the processing technology has been discussed in the previous section. However, there are slight variations in the growth of the boule of GaAs (liquid encapsulated Czochralski instead of the basic Czochralski technique is used because the latter method cannot be used for GaAs - a dissociable compound (Grant, 1995)), the process of wafer production and the etching of ribs for the device design (wet etching can be used with citric acid for GaAs or Al<sub>x</sub>Ga<sub>1-x</sub>As materials (Sakamoto *et al.*, 1999), and the angle of the sidewalls was taken to be 52° to the horizontal (private communication with Marconi (now Bookham Technology))), and these variations from the standard can be found in a wide variety of published literature (Williams, 1990; Chang and Kai, 1994). Nevertheless one of the key areas of semiconductor device processing, not used for LiNbO<sub>3</sub> device processing but important for semiconductors, is epitaxial growth of the various layers of the modulator device and any doping which may be required for these layers. The methods used (typically molecular beam epitaxy (MBE) and metal organic chemical vapour deposition (MOCVD) (Dagli, 1999)) can easily be studied in the vast literature available on this subject (Williams, 1990; Chang and Kai, 1994). However, since this study concerns only electro-optic modulators, the GaAs/Al<sub>x</sub>Ga<sub>1-x</sub>As material modelled here is that which is intrinsic or rather unintentionally doped.

### 3.3 The Device Design Issues

Waveguides are typically designed using the optical wave equation, the formulation for which can be applied to diffused and non-diffused waveguides alike since each triangular element is able to have individual values for the properties involved in the formulation, i.e. the permittivity of the material. The diffusion process and the equations used to model it are given in the next part of this section. The shapes of the optical modes are important to the fibre-to-waveguide coupling loss and to the scattering loss of the guide such that if the mode is tightly confined, less light will escape due to inhomogeneities in the waveguide (which will be greater for the case of the etched ridge waveguides which can suffer both from nonuniformities in the channel waveguide definition and again during the etching of the ridge): however, this will subsequently increase fibre-to-waveguide coupling losses. The electrode design plays a part in the electrode loading loss, as well as the drive voltage of the device. Moreover, by assuming a quasi-TEM propagation of the electrical signal, this reduces the electric field calculation to that which can be found by the Laplace equation. Subsequently, the RF characteristics and electrical 3dB bandwidth can be obtained from this approach. However, this supposedly gives overestimated values compared with a full-wave analysis (Koshiha *et al.*, 1999). The drive voltage, bandwidth and insertion loss are the most important characteristics for a general waveguide modulator (Alferness, 1982). However, the power coupling from one waveguide to the other (for directional couplers) and the extinction (on-off) ratio are also both significant characteristics in the case of real non-ideal devices.

#### 3.3.1 Diffusion Process in the Formation of Ti:LiNbO<sub>3</sub> Waveguides

The diffusion of the titanium (Ti) from the surface into the LiNbO<sub>3</sub> crystal can be described by Fick's equation (Fouchet *et al.*, 1987)

$$\frac{\partial C}{\partial t} = D_x \frac{\partial^2 C}{\partial x^2} + D_y \frac{\partial^2 C}{\partial y^2} \quad (3.1)$$

where  $C$  is the Ti concentration/distribution in the  $(x,y)$  plane,  $t$  is the diffusion time,  $D_x$  and  $D_y$  are diffusion coefficients along  $x$  and  $y$ , respectively, and these follow the Arrhenius law

$$D_{x,y} = D_o^{x,y} e^{-E_o^{x,y}/kT} \quad (3.2)$$

where

$D_o^{x,y}$  are the diffusion constants along the  $x,y$  axes, and depend on the crystal cut (Fukuma and Noda, 1980)

$E_o^{x,y}$  are the activation energies in the  $x, y$  directions

$k$  is the Boltzmann constant and

$T$  is the diffusion temperature in Kelvin.

Equation (3.1) can also describe the diffusion of the  $H^+$  ions into the  $LiNbO_3$  substrate for the process of proton exchange (Januar *et al.*, 1992). However, the solution to this diffusion equation is dependent on the nature of the source, the nature of the medium and the nature of the diffusion (Fouchet *et al.*, 1987; Januar *et al.*, 1992; Crank, 1975). In the case of indiffusion into the  $LiNbO_3$  from the thin film of Ti deposited on the surface of the  $LiNbO_3$ , the source (i.e. the Ti) is considered to be an instantaneous source with the diffusion time being longer than that for the complete diffusion of the Ti into the  $LiNbO_3$  substrate. The diffusion is assumed to be deep into the substrate and the  $LiNbO_3$  medium is considered semi-infinite. The reason for the medium being treated as semi-infinite is that the boundary at  $y=0$  is impermeable — thus the diffusion only moves in the direction of positive  $y$  with the negative solution being considered to be reflected in the  $y=0$  plane since there is a symmetry in the  $x=0$  plane (the thin film was of width  $w$ , placed between  $x=-w/2$  and  $x=w/2$ ), and so the two positive and negative solutions can be added together (this is mathematically feasible since equation (3.1) is linear), and also that the Ti (through diffusion) does not reach the underside of the wafer even though the diffusion is assumed to be deep. Taking these assumptions into account, the resulting solution to Fick's second law of diffusion – equation (3.1) - is given below

$$C(x, y) = \frac{\tau}{d_y} \frac{1}{\sqrt{\pi}} * \exp\left[-\left(\frac{y}{d_y}\right)^2\right] * \left[ \operatorname{erf}\left(\frac{\frac{w}{2} + x}{d_x}\right) + \operatorname{erf}\left(\frac{\frac{w}{2} - x}{d_x}\right) \right] \quad (3.3)$$

where

$\tau$  = the thickness of the titanium layer

$w$  = width of the titanium layer or the effective width of the guide

$$d_{x,y} = \text{the diffusion length along the } x,y \text{ axes} = 2\sqrt{D_{x,y}t} \quad (3.4)$$

and  $t$  is the length of time of the diffusion process.

Hence, it can be seen that the diffusion rates depend on the stoichiometry of the crystal through  $D_o^{x,y}$  and  $E_o^{x,y}$ , and through  $T$  and  $t$  are dependent the diffusion environment (Korotky and Alferness, 1987). The close relationship between the Ti concentration in the LiNbO<sub>3</sub> crystal and the subsequent change in the refractive index is given in Chapters 4 and 5.

### 3.3.2 Insertion Loss

The main contribution to the insertion loss is the fibre-to-waveguide coupling loss, the propagation loss in the waveguide, the electrode loading loss and the waveguide bending loss.

The fibre-to-waveguide loss is made up of reflection or Fresnel losses (though these can be greatly minimised with index-matching fluids or anti-reflection coatings on the LiNbO<sub>3</sub> waveguide end faces) and the mismatch between the fibre and waveguide modes (which is a much stronger aspect than the reflection or Fresnel losses). However, a spot size converter can be designed and used to reduce the mismatch between the fibre and waveguide modes, and the analysis and success of such structures has been shown (Wongcharoen *et al.*, 2001) using the FEM in conjunction with the Least Squares Boundary Residual (LSBR) method. For more detail description of this method see Section 4.8.1. of this thesis.

The propagation loss is dependent on the scattering of the optical beam due to any nonuniformities in the waveguide definition (channel or ridge) or any absorption of the lightwave into the waveguide material (this is more of a problem for semiconductor MQW devices which suffer from high absorption, especially at wavelengths close to the bandedge of the device (Dagli, 1999) whereas for LiNbO<sub>3</sub> the propagation loss of these guides is given to be 0.2dB/cm at 1.55 $\mu$ m wavelength (Mitomi *et al.*, 1998) and generally becomes smaller for increasing wavelengths). For the purpose of this thesis, both sidewalls and waveguide definition along the length of the waveguide were considered to be smooth and constant, respectively. However, it would possible to

model any inhomogeneities in the waveguide with a vector-based beam propagation method (VBPM). Moreover, the absorption is not too high for both LiNbO<sub>3</sub> and unintentionally doped GaAs (Dagli, 1999) devices at 1.55μm (the operating wavelength for the devices modelled throughout the majority of this work) and so this is of no interest for the work of this thesis.

### 3.3.2.1 The Beam Propagation Method

The powerful **H**-field FEM (HFEM)-based modal solution approach can be used to obtain the modal field distributions of a bent waveguide after considering the conformal transformation. However, this formulation alone cannot be used to estimate the radiation loss. The beam propagation method (BPM) is one of the most commonly used methods to characterize optical bends because it is used to assimilate both discrete and radiation modes simultaneously. This procedure can be implemented either by the use of fast Fourier transforms (only suitable for weakly guided waveguides), the finite difference method (which takes up large computational resources) or the FEM. Scalar formulations cannot adequately treat 3D bends and so a vectorial (or as in this case a semi-vectorial finite element beam propagation method (SVFEBPM)) BPM has to be used (Obayya *et al.*, 2000a). It had also been shown earlier (Obayya *et al.*, 2000a) that a perfectly matched layer boundary in conjunction with the BPM is extremely useful to accurately calculate the radiation loss, and hence this method can be used to determine precisely the radiation loss of the bent waveguides, for both ridge and unetched waveguides.

Feit and Fleck introduced the BPM in 1978 (Feit and Fleck, 1978) to calculate the mode properties of optical fibres. In the SVFEBPM, a small longitudinal step along the direction of the light propagation is taken and calculations relating the fields at the input and output planes are performed using the FEM. Such calculations are repeated at each step of the propagating field.

The power associated with an optical beam propagating in the +z direction is given by (Obayya, 1999)

$$\mathbf{P} = \frac{n_0 Z_0}{2} \{\mathbf{h}_i\}^T [\mathbf{M}] \{\mathbf{h}_i\} \quad (3.5)$$

where

$n_0$  is the reference index of refraction (usually taken to be the average of the guide and substrate refractive indices)

$Z_0$  is the free space wave impedance =  $\sqrt{\frac{\mu_0}{\epsilon_0}} = 120\pi$  Ohms

$$[\mathbf{M}] = \sum_e \begin{bmatrix} [M_{xx}] & [0] \\ [0] & [M_{yy}] \end{bmatrix} \quad (3.6)$$

where

$$[M_{xx}] = [M_{yy}] = \left[ n^{-2} \int_i N_i N_j dA \right] \quad (3.7)$$

[0] is a 3x3 null matrix

and  $\{\mathbf{h}_t\} = \{\mathbf{h}_t\}_{m+1}$  is the column vector containing all the nodal values of the slowly varying transverse magnetic field components, which is found for each new propagation step from the iteration equation

$$[\mathbf{A}]_m \{\mathbf{h}_t\}_{m+1} = [\mathbf{B}]_m \{\mathbf{h}_t\}_m \quad (3.8)$$

where

$$[\mathbf{A}]_m = -2jn_0k[\mathbf{L}]_m + \theta \Delta z \{[\mathbf{K}]_m - n_0^2 k^2 [\mathbf{M}]_m\} \quad (3.9)$$

$$[\mathbf{B}]_m = -2jn_0k[\mathbf{L}]_m + (\theta - 1) \Delta z \{[\mathbf{K}]_m - n_0^2 k^2 [\mathbf{M}]_m\} \quad (3.10)$$

with

$\Delta z$  = propagation step size

$\theta$  = propagation step parameter (where  $\theta \geq 0.5$ )

$m, m+1$  denote the  $m^{\text{th}}$  and  $(m+1)^{\text{th}}$  propagation steps

$$[\mathbf{L}] = [\mathbf{M}] + \frac{1}{4n_0^2 k^2} ([\mathbf{K}] - n_0^2 k^2 [\mathbf{M}]) \quad (3.11)$$

Here  $[\mathbf{M}]$  and  $[\mathbf{K}]$  are global element matrices given by the summation of the contributions from all the elements.

$[\mathbf{M}]$  is as above

$[\mathbf{K}]$  is given by

$$[\mathbf{K}] = \sum_e \begin{bmatrix} [K_{xx}] & [K_{xy}] \\ [K_{yx}] & [K_{yy}] \end{bmatrix} \quad (3.12)$$

where

$$[K_{xx}] = \left[ \int_A (k^2 N_i N_j - n^{-2} \alpha_x^2 N_{ix} N_{jx} - n^{-2} \alpha_y^2 N_{iy} N_{jy}) dA + \int_l n^{-2} \alpha_x^2 N_i N_{jx} l_x dl \right] \quad (3.13)$$

$$[K_{yy}] = \left[ \int_A (k^2 N_i N_j - n^{-2} \alpha_x^2 N_{ix} N_{jx} - n^{-2} \alpha_y^2 N_{iy} N_{jy}) dA + \oint_l n^{-2} \alpha_y^2 N_i N_{jy} l_y dl \right] \quad (3.14)$$

$$[K_{xy}] = \int_A (n^{-2} \alpha_x \alpha_y N_{iy} N_{jx} - n^{-2} \alpha_x \alpha_y N_{ix} N_{jy}) dA + \oint_l n^{-2} \alpha_x \alpha_y N_i N_{jy} l_x dl \quad (3.15)$$

$$[K_{yx}] = \int_A (-n^{-2} \alpha_x \alpha_y N_{iy} N_{jx} + n^{-2} \alpha_x \alpha_y N_{ix} N_{jy}) dA + \oint_l n^{-2} \alpha_x \alpha_y N_i N_{jx} l_y dl \quad (3.16)$$

and where

$N_i$  is the one of the components of the shape function matrix, as defined by equation (2.36) with  $i, j=1, 2, 3$  representing one of the three nodes of the triangular element,

$N_{ix}, N_{iy}$  are the  $x$  and  $y$  derivatives of the shape function  $N_i$ , respectively,

$n$  is the refractive index of the element,

$k$  is the wave vector,

$l_x, l_y$  are the direction cosines between the outward vector  $n_i$  and the  $x$  and  $y$  directions, respectively,

and

$$\alpha_{x,y} = 1 - j \frac{3\lambda\rho^2}{4\pi md^3} \ln\left(\frac{1}{R}\right) \quad (3.17)$$

defines the necessary condition for perfectly matched layers (PML) (Obayya *et al.*, 2000a). This is such that the wave impedance of the PML placed around the computational domain of the waveguide is the same as that of the adjacent medium inside the computational domain and so this will allow unwanted radiation to leave the computational domain freely without reflection. Here,  $\lambda$  is the wavelength of operation,  $d$  is the width of the PML - which is constant in all directions,  $\rho$  is the distance inside the PML from the PML-computational domain interface and  $R$  is the allowable theoretical value of the reflection coefficient at the PML-computational domain interface.

The equations used above are for the Padè approximation of the solution to the non-paraxial BPM equation and is a better approach compared with the much simpler approximate paraxial equation (which is valid only for waves propagating very near to the axis of propagation,  $z$ ) (Hadley, 1992).

For a waveguide bend, the conformal transformation method (Heiblum and Harris, 1975) is used to convert the bent waveguide into a straight one with a modified index profile

$$n(u, v) = n(x, 0) \left(1 + x/R_c\right) \quad (3.18)$$

where  $n(x,0)$  and  $n(u,v)$  are the refractive index profiles in the original and transformed domain, respectively (where co-ordinates  $u$  &  $v$  in the transformed domain are related to co-ordinates  $x$  &  $z$  in the original domain),

and where  $R_c$  is the radius of curvature of the bend.

This relationship may then be used in conjunction with the SVFEBPM by substituting equation (3.18) into equations (3.7) and (3.13)-(3.16).

### 3.3.2.2 The Perturbation Technique

Good electrode design is an important consideration in maximizing the overlap between the optical and modulating fields, which leads to a reduction in  $V_\pi L$ . This overlap can be optimised by varying a number of fabrication parameters, including the buffer layer thickness. However, other device characteristics, e.g. the fibre-coupled insertion loss and the desired bandwidth (Korotky and Alferness, 1987), need also to be fully considered in the design. Nevertheless, the buffer layer is needed to reduce the optical loss due to the metal electrodes, particularly for TM-polarized light. The source of the optical loss is the complex refractive index of the metal. Hence, a buffer layer is needed to separate the optical field from the metal electrodes. Consequently, due to the decay of the modulating electric field in the buffer and the Ti:LiNbO<sub>3</sub> material (with greater decay in the buffer layer) there is, in fact, simply a decreasing overlap between the optical and (modulating) electric fields. The calculation of the optical loss due to the metal electrodes is determined using the perturbation method, in conjunction with the finite element method (Themistos *et al.*, 1995b).

Perturbation theory is part of those mathematical methods that are used to find an approximate solution to a problem, which cannot be solved exactly, by looking at a related problem for which there is a solution. It is applicable if the problem at hand can be formulated by adding a "small" term to the mathematical description of the exactly solvable problem. An example of this may be for an anisotropic leaky waveguide (Lu and Fejer, 1993) or a metal-clad optical waveguide (Themistos *et al.*, 1998). The resultant solution for the problem can be obtained either

- a) from a power series in terms of the small perturbation parameter, or
- b) directly from the variational expression.

The former consists of a series of terms of which the leading term is the solution of the solvable problem (e.g. a standard step optical fibre) while further terms describe the deviation in the solution. However, if a variational expression for the problem exists, then this is a quicker and more powerful approach. A solution to the perturbed problem will emerge if the known solution to the unperturbed problem is substituted as a trial function into a variational expression valid for the (perturbed) problem (Themistos, 1998), though this is subject to the boundary conditions of the perturbed problem.

Perturbation theory can be applied to find the gain or loss of the optical waveguide problem, but only when these amounts are small, by approximating the perturbed phase constant,  $\beta$ , and the field profiles  $\mathbf{H}$  and  $\mathbf{E}$  due to loss or gain, with the unperturbed values  $\bar{\beta}$ ,  $\bar{\mathbf{E}}$  and  $\bar{\mathbf{H}}$ , which are the solutions to the loss-free optical waveguide problem. The gain or loss is dependent upon the imaginary part,  $n'$  of the complex refractive index,  $\bar{n}$ . The limit of the perturbation technique is the value of  $n'$  at which the solution obtained by the perturbation approach diverges from the analytical approximation (Themistos, 1998).

In a dielectric medium, the attenuation constant,  $\alpha$ , due to dielectric losses, can be expressed as (Pantić and Mittra, 1986):

$$\alpha = \frac{P_d}{2P_\theta} \quad (3.19)$$

where  $P_d$  is the power dissipation in the dielectric material and  $P_\theta$  is the time-averaged power flow.

For a cross section,  $\Omega$ , of a discretised dielectric optical waveguide with any number of subregions,  $\Omega_k$ , with complex dielectric constant,  $\bar{\epsilon}_k$ , for each subregion the perturbation method can be applied by evaluating the attenuation constant for the whole guide, in terms of the electromagnetic field as (Pantić and Mittra, 1986; Mirshekar-Syahkal and Davies, 1982):

$$\alpha = \frac{\omega \sum_k \epsilon_k \tan \delta_k \int_{\Omega_k} |\mathbf{E}_0|^2 d\Omega}{2 \operatorname{Re} \int_{\Omega} (\mathbf{E}_0 \times \mathbf{H}_0^*) \cdot \hat{z} d\Omega} \quad (3.20)$$

where  $\omega$  is the angular frequency,  $\hat{z}$  is the unit vector along the z-axis,  $\mathbf{E}_0$  and  $\mathbf{H}_0$  are the unperturbed electric and magnetic field vectors for the lossless condition, respectively, and  $\tan \delta_k$  is the loss tangent of each subregion defined by:

$$\tan \delta_k = \frac{\varepsilon'_k}{\varepsilon_k} \quad (3.21)$$

where  $\varepsilon'_k$  and  $\varepsilon_k$  is the imaginary and real part, respectively, of the complex permittivity of each subregion, and the summation is carried out over all subregions. In using equation (3.20) it is assumed that both  $\mathbf{E}_0$  and  $\mathbf{H}_0$  remain unchanged in the presence of loss and that the value of the loss tangent is very small, i.e.  $\varepsilon'_k \ll \varepsilon_k$ . Moreover, a negative sign of  $\alpha$  indicates loss, while a positive would denote gain.

For a more accurate estimation of the gain/loss properties of the waveguide structures used in this thesis, a perturbation formula, used in conjunction with the full vector  $\mathbf{H}$ -field formulation (A3.1), can be employed for small losses. In such an approach, the contribution of all the three magnetic field components is considered in the calculation of the attenuation constant,  $\alpha$ . By using Maxwell's equations to express the electric field,  $\mathbf{E}$ , in terms of the magnetic field components,  $H_x$ ,  $H_y$  and  $H_z$ , the perturbation formula (3.20) can be written as:

$$\alpha = \frac{\sum_e \frac{\varepsilon'_e}{\varepsilon_e^2} \{\mathbf{H}\}_e^T [C] \{\mathbf{H}\}_e}{2 \sum_e \frac{1}{\varepsilon_e} \{\mathbf{H}\}_e^T [D] \{\mathbf{H}_t\}_e} \quad (3.22)$$

where the full  $\{\mathbf{H}\}_e$  and transverse  $\{\mathbf{H}_t\}_e$  element field vectors are

$$\{\mathbf{H}\}_e = \begin{Bmatrix} \{H_x\}_e \\ \{H_y\}_e \\ \{H_z\}_e \end{Bmatrix} \quad \{\mathbf{H}_t\}_e = \begin{Bmatrix} \{H_x\}_e \\ \{H_y\}_e \end{Bmatrix} \quad (3.23)$$

Here,  $\varepsilon_e$  and  $\varepsilon'_e$  are the real and imaginary parts of the dielectric permittivity in each element.

The element matrix  $[C]$  is given by

$$[C] = [Q][Q]^* \quad (3.24)$$

where

$$[Q] = \iint_{\Delta} \begin{vmatrix} \{0\} & -\beta\{N\} & j\{N_y\} \\ \beta\{N\} & \{0\} & -j\{N_x\} \\ -\{N_y\} & \{N_x\} & \{0\} \end{vmatrix} dx dy \quad (3.25)$$

Similarly, the element matrix  $[D]$  is given by:

$$[D] = \iint_{\Delta} \begin{vmatrix} \beta[G] & [0] \\ [0] & \beta[G] \\ -[X] & -[Y] \end{vmatrix} dx dy \quad (3.26)$$

where

$$[G] = \{N\} \{N\}^T \quad (3.27)$$

$$[X] = \{N_x\} \{N\}^T \quad (3.28)$$

$$[Y] = \{N_y\} \{N\}^T \quad (3.29)$$

where

$$\{N_x\} = \frac{\partial \{N\}}{\partial x} \quad (3.30)$$

$$\{N_y\} = \frac{\partial \{N\}}{\partial y} \quad (3.31)$$

and  $\{N\}$  is the shape function matrix, as defined by equation (A3.9).

### 3.3.3 Electrode Design

It is known for electro-optic modulator devices that the electrode length influences the drive voltage,  $V_{\pi}$ , as well as the bandwidth of the device (Noguchi *et al.*, 1998). A lower, and therefore a more definitive value for  $V_{\pi}$  is obtained by having the maximum overlap of optical and electric fields (Wooten *et al.*, 2000). This can be further improved by narrowing the ground electrode width (Dolfi and Ranganath, 1992), although this has yet to be confirmed for ridge waveguide modulator designs. However, the electrode design is particularly relevant for travelling wave modulators since the bandwidth, also an important characteristic for these devices, is limited by the conductor loss (of the electrodes) for the condition of both impedance and velocity matching as well as by the

requirement for maintaining the conversion efficiency along the entire interaction length of the device – and this can be achieved for electrodes with very-low-loss electrical waveguiding (Schmid, 2003). The analysis of the electrodes for calculating the potential bandwidth of a device can be achieved by a quasi-TEM approach (Koshiha *et al.*, 1999). The electrodes are treated as a transmission line and can be in the form of coplanar waveguide (CPW)-type electrodes or coplanar strip line electrode structures (Mitomi *et al.*, 1995). However, the CPW electrodes can provide a broader bandwidth with a thinner buffer layer and a thinner electrode, as well as being the easier of the two to fabricate. Hence, it is the CPW electrode that is used for the interferometric modulator (modelled in Chapter 5 of this thesis) as such a device would work well at high bandwidths (Wooten *et al.*, 2000).

The velocity matching condition is achieved when the microwave effective index,  $n_m$ , and the optical effective index,  $n_{eff}$ , are equal. An additional matching condition, impedance matching, is obtained by matching the characteristic impedance of the electrode,  $Z_c$ , to the internal impedance of the signal generator which is generally  $50\Omega$ .  $n_{eff}$ ,  $n_m$  and  $Z_c$  are given by (Koshiha *et al.*, 1999; Yi *et al.*, 1990),

$$n_{eff} = \frac{\beta}{k_0} \quad (3.32)$$

where  $k_0 = 2\pi/\lambda$  and  $\beta$  is the propagation constant for the optical mode

$$n_m = \sqrt{\frac{C}{C_0}} = \frac{1}{cv_m} \quad (3.33)$$

$$Z_c = \frac{1}{c\sqrt{CC_0}} \quad (3.34)$$

where  $v_m$  is the velocity of propagation of the modulating signal along the electrode

$c$  is velocity of light in free space

$C_0$  is the line capacitance of the electrodes in free space and the line capacitance of the electrodes in the presence of dielectric materials,  $C$ , is given by

$$C = \frac{Q}{V} = \frac{1}{V_0} \oint_S \epsilon_n \left( \frac{d\psi}{dn} \right) dl \quad (3.35)$$

where  $V_0$  is the applied voltage

$\psi$  is the scalar potential, found from the solution of the Laplace equation (Davies, 1989)

$\frac{d\psi}{dn}$  is the derivative of  $\psi$  with respect to the vector normal to the integrating

contour, S

and  $\epsilon_n$  is the relative dielectric constant along the direction normal to contour S.

It has been reported that for conventional channel waveguide modulators, thick electrodes are needed for matching the velocity of propagation of the electrical and optical signals but this reduces the characteristic impedance of the electrodes (Dagli, 1999), as well as developing a sloped sidewall in these thicker electrodes (by undercutting the metal) – which is thought to affect adversely the electrode characteristics (Koshiba *et al.*, 1999). In order to also match the characteristic impedance to  $50\Omega$  (since this is a standard terminating impedance for microwave circuits/ devices) there is a need to have narrow gap and width for the electrodes (Zhang and Miyoshi, 1995). This is very hard to fabricate and if the impedance matching is not achieved this leads to microwave reflections, which then cause excessive signal-bit-error for high-speed communications (Mitomi *et al.*, 1998). By etching the LiNbO<sub>3</sub> (which has a higher microwave dielectric constant than air) to form the ridge waveguide modulator the effective microwave index,  $n_m$ , decreases and so C, the capacitance per unit length of the electrode, reduces and the velocity of propagation of the electrical signal increases, as does the characteristic impedance (see equations 3.33 & 3.34). So it is then possible to achieve simultaneously both velocity and impedance matching without resorting to narrowing the gaps between the electrodes as well as the width of electrodes. Further, to obtain velocity matching the electrode thickness is thinner compared to that for the Ti:LiNbO<sub>3</sub> channel waveguide modulator.

In the case of both impedance and velocity matching, the 3dB bandwidth can be expressed as (Mitomi *et al.*, 1998)

$$\Delta f_L = A_L / (\alpha_0 L)^2 \quad (3.36)$$

where

the constant  $A_L$  was taken to be 41 for the electrical 3dB bandwidth

190 for the optical 3dB bandwidth

(for this case of both impedance and velocity matching)

$L$  is the length of the electrodes

$\alpha_0$  is the conductor loss at  $f=1\text{GHz}$  and is given by (Pantić and Mittra, 1986)

$$\alpha_c = \frac{P_c}{2P_0} \quad (3.37)$$

with

$$P_c = R_s \int_C |H_0|_{\text{tang}}^2 dl \quad (3.38)$$

$$P_0 = \text{Re} \int_S (E_0 \times H_0^*) \cdot \hat{z} dS \quad (3.39)$$

where

$|H_0|_{\text{tang}}$  is the magnitude of the tangential magnetic field at the conductor surfaces (along

line C) and S is the complete cross-section formed by the line C, and

$R_s$  is the surface resistance of the metal electrode given by (Ramo *et al.*, 1984)

$$R_s = \sqrt{\frac{\omega\mu_0}{2\sigma}} \quad (3.40)$$

where  $\mu_0$  is the free-space permittivity and  $\sigma$  is the conductivity of the metal electrode.

### 3.3.4 Other Features Involved

For directional couplers, the power transferred from one waveguide to the other can be modelled using the BPM approach (Obayya, 1999). However, this was found to be too time consuming for carrying out the calculation of power (Rajarajan *et al.*, 1996). As a result, for the strongly coupled directional coupler described in Chapter 4 of this thesis, the power transfer from one guide to another is found by approaching the least squares boundary residual (LSBR) method in conjunction with the method of Suematsu and Kishino (1977), which is based on the interference between the waveguide modes supported in a strongly coupled non-identical waveguide system. This is detailed in Section 4.8 of this thesis.

### **3.4 Summary**

It was seen from Chapter 1 that optical modulators are important to the optimal design of optical communications systems, and that the electrically controlled modulators were the most effective for high-speed communications than other options.

From this chapter it has been shown that the modulator device characteristics of drive voltage, the bandwidth and insertion loss are very important to achieve good device performance. With careful design and fabrication, these characteristics can be improved. However, careful design can only be achieved through powerful and accurate modelling. Improvements can be made by design optimisation based on the results obtained from such effective modelling. The formulations provided in this chapter have contributed to powerful and accurate modelling for electro-optic modulators and this will be shown in subsequent chapters.

# 4

## *Electro-Optic Directional Coupler Modulators*

---

---

### **4.1. Introduction**

There has been considerable interest in electro-optic waveguides over the past few decades, where the electro-optic material can be either semiconductor or dielectric crystal. Although dielectric crystals cannot be integrated with semiconductors, as there is no possibility of crystal growth on a semiconductor substrate, they can still be used as stand-alone devices and the dielectric crystal material in which most interest has been shown, because of its low transmission loss, large electro-optic, piezo-electric, acousto-optic and elasto-optic coefficients, high second order nonlinearity (Fouchet *et al.*, 1987; Strake *et al.*, 1988), as well as low chirp and high bandwidth, is lithium niobate ( $\text{LiNbO}_3$ ). Furthermore, metal indiffusion of  $\text{LiNbO}_3$  is one of the most important developments in the area of integrated optics (Chang, 2000), with titanium (Ti) being the most commonly used metal.

The concept of directional couplers (DCs) was introduced in the late 60s (Miller, 1969; Marcatili, 1969a) in the form of two parallel waveguides placed close together so that light in one guide can couple into the other via evanescent fields. Even at the time they were expected to become important circuit components for optics. Marcatili extended his numerical analysis method (see Chapter 1) for the single guide for analysing

coupling waveguides (Marcatili, 1969a). However, these were only passive components, with characteristics dependent only on their fabrication parameters. It was later conceived that these devices could be used as switches or intensity modulators by applying a field to both waveguides. This was proposed in the form of a three-electrode, two waveguide structure (Taylor, 1973), and this structure was later implemented in GaAs (Campbell *et al.*, 1975). A two-electrode structure was also fabricated at the same time in Ti:LiNbO<sub>3</sub> (Papuchon *et al.*, 1975), and of the two it was this two-electrode structure which was then mainly adopted. Both devices used channel waveguides, however, for GaAs and even LiNbO<sub>3</sub> based directional coupler devices of today, rib waveguides are also used (Mak and Yanagawa, 1994; Chang, 2000).

Directional couplers are now the basis for several guided-wave devices including multimode thermo-optic couplers (Moll and Dolfi, 1983) or even biosensors (Luff *et al.*, 1996), but are mainly used for optical switching systems (Kondo, 1993). However, they can be used as either an intensity modulator, a switch (Schmidt and Alferness, 1979), for filtering (Alferness and Schmidt, 1978) or mixing (Mickelson, 1993) or as a mode splitter (Mikami, 1980; Maruyama *et al.*, 1995). Directional-type switches are mostly employed for lower speed switching applications (compared with interferometric-type devices), where polarisation diversity may be required and small size with tighter electrode gaps more easily achieved (Wooten *et al.*, 2000). There are many devices that are collectively known as directional coupler (DC) devices, such as the DC device with uniform electrodes (Schmidt and Alferness, 1979) also called the switched DC, the reversed- $\Delta\beta$  DC switch (Korotky and Alferness, 1987) or one where the applied field produces changes in coupling coefficient,  $\kappa$ , (Alferness, 1988), which in some cases has been called a  $\Delta\kappa$  DC modulator (Schlaak, 1984; Chin, 1993). However, the uniform electrode DC required very rigid fabrication tolerances which was not the case for the reversed or alternating  $\Delta\beta$  DC. The most common examples of today's Ti:LiNbO<sub>3</sub> DC devices (Wooten *et al.*, 2000) are the reversed- $\Delta\beta$  coupler and the digital optical switch (Burns, 1992; Silberberg *et al.*, 1987). However, the first device with which to test the model would realistically be the uniform electrode DC. The reverse electrode  $\Delta\beta$  DC could be simulated by simply using the vectorial **H**-field FEM in conjunction with the least squares boundary residual (LSBR) method at the interface between each stage of this device (i.e the region of the parallel guides where the first electrode is located, region between electrodes, region of the parallel guides where the second electrode is

located). Moreover, this powerful and versatile method can be used to accurately model both channel and rib waveguides, the latter of which has been found difficult to accurately model using analytical or scalar methods (Koshiba, 1992).

Coupled mode equations can be used to describe the propagation through both the uncoupled and coupled parallel regions, as well as the unparallel regions (Januar *et al.*, 1992). However, there has been debate whether some formulations are only suitable for weakly coupled guides and are not suitable for the more strongly coupled guides simulated in this study. Therefore, a more suitable route that employed the LSBR method in conjunction with a model developed primarily for strongly coupled guides was used to calculate the power transfer between the parallel guides of the DC. This will be discussed in more detail in Section 4.8.2.

As seen in Chapter 3, the diffusion characteristics can be modelled by using the diffusion equation based on Fick's diffusion laws (see Section 3.3.1). It is universally believed that Ti indiffusion in the LiNbO<sub>3</sub> substrate follows the equations given in equation (3.3). The diffusion parameters are known to affect the value of index change in the LiNbO<sub>3</sub> substrate. How this affects the device characteristics, for a passive directional coupler, is examined in the first part of this chapter. The significance of other fabrication parameters to the device characteristics is also studied, and, wherever possible, the results obtained are confirmed by similar results in the literature.

Hence, the results given here will validate the model used here for not only Ti:LiNbO<sub>3</sub> DCs but also DC devices fabricated from other materials, since the refractive index model can easily be replaced by any other for this finite element method (FEM) based electro-optic device simulator.

## 4.2. Theory of the Uniform $\Delta\beta$ Directional Coupler Modulator

The layout for the  $\Delta\beta$  DC modulator (with uniform electrodes) considered is shown in Fig. 4.1. Briefly, the  $\Delta\beta$  DC modulator works on the principle that when no voltage is applied, the two guides are phase-matched, or are in synchronous phase, and light input

into guide 1 is completely coupled into guide 2 (cross-state) when the length of the device,  $L$ , is the same as the length over which the light couples,  $L_{c0}$ . This may be defined as,

$$L = L_{c0} = \frac{\pi}{\Delta\beta} \quad (4.1)$$

where  $\Delta\beta = \beta_e - \beta_o$

$L$  = the interaction length of the device

$L_{c0}$  = the coupling (or transfer) length, when no modulating voltage is applied

$\beta_e$  = the propagation constant for the symmetric or even supermode and

$\beta_o$  = the propagation constant for the anti-symmetric or odd supermode.

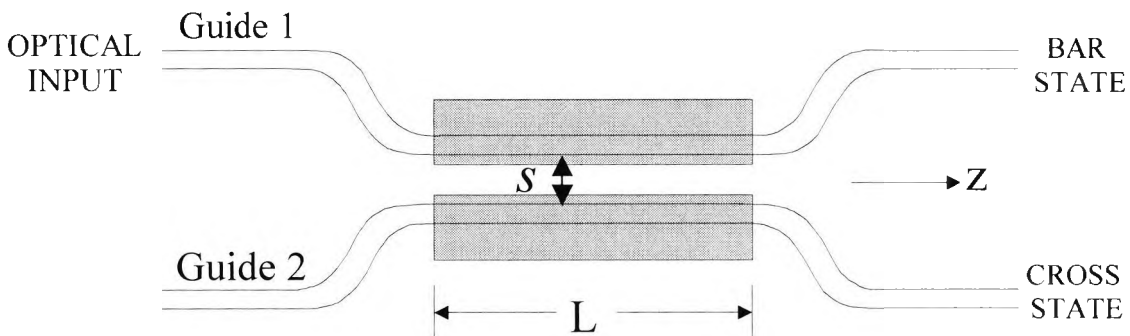


**Fig. 4.1** Layout of the uniform electrode directional coupler.

The term supermode is associated with the optical modes of the coupled waveguide system which, as for a single waveguide with an even mode (fundamental) and odd mode (first higher order mode), has an even and odd supermode. However, the odd supermode is not considered to be a higher order mode for these two coupled waveguides. Note that the term  $\Delta\beta$  in equation (4.1) is not to be confused with the term  $\Delta\beta$  used in the published literature on coupled mode theory (referenced in this chapter as  $\Delta\beta_{RS}$ ), in which  $\Delta\beta$  is equal to the difference between the propagation constants of the individual guides (see for example Schmidt and Alferness (1979)) rather than the difference between the odd and even supermodes as in equation (4.1). Also, the coupling length when no voltage is applied (as for equation (4.1)) is typically expressed in published literature on coupled mode theory as

$$L_{c0} = \frac{\pi}{2\kappa} \quad (4.2)$$

where  $\kappa$  is the coupling coefficient which describes the strength of the interguide coupling, and is dependent on the waveguide parameters, wavelength of operation and interwaveguide separation,  $s$  (Marcatili, 1969a; Alferness *et al.*, 1979).

When a voltage is applied, there is a change in the refractive index due to the applied electric field that can be made unequal in the two guides by implementing an appropriate electrode design. This leads to a mismatch in the phase velocities in both guides and also to a reduction in  $L_c$ . By adjusting the device parameters most of the power can be transferred back to guide 1 (the bar-state) – where the coupling length,  $L_c$ , is given by  $L_c = L_{c0} / 2$  – at the end of the DC. The voltage at which this occurs is termed  $V_\pi$ , the switching voltage. In this way power can be exchanged between the two waveguides continuously, as often as the length of the device permits.

Although coupled mode theory has been used to analyse (Marcuse, 1991) directional coupler devices, here it is only being used to explain the operation of these devices:

The interaction of the light in the two waveguides is described by the coupled wave equations (Schmidt and Alferness, 1979)

$$R' - j\delta R = -j\kappa S \quad (4.3)$$

$$S' + j\delta S = -j\kappa R \quad (4.4)$$

where  $R$  and  $S$  are the complex amplitudes of the light in guides 1 and 2, respectively, which vary slowly in the direction of propagation, the primes denote differentiation with respect to the propagation direction and  $\kappa$  is as described above.  $\delta = \Delta\beta_{RS}/2$ , where  $\Delta\beta_{RS} = \beta_R - \beta_S$  and  $\beta_R, \beta_S$  are the propagation constants of the light as for the individual guides 1 and 2, respectively.

If the light is input to one waveguide, then the crossover efficiency of light into the second waveguide is found from solving the above equations and given by (Alferness, 1982)

$$\eta = \frac{1}{1 + \left(\frac{\delta}{\kappa}\right)^2} \sin^2 \left\{ \kappa L \left( 1 + \left(\frac{\delta}{\kappa}\right)^2 \right)^{1/2} \right\} \quad (4.5)$$

However, this equation only comes about through the assumption of weak coupling (Hardy and Streifer, 1985).

For identical waveguides, when no voltage is applied  $\delta=0$  and so the crossover is described by

$$\eta = \sin^2 \kappa L \quad (4.6)$$

and so  $\eta=1$  when  $\kappa L=m\pi/2$  where  $m$  is an odd integer.

For non-identical waveguides (when an applied electric field makes the guides non-identical due to the electro-optic effect) there is always a phase-mismatch,  $\Delta\beta$ , between the waveguides is present. For the case when  $\eta$  equal zero (for the bar-state)

$$\frac{1}{1+(\delta/\kappa)^2} \sin^2 \left\{ \kappa L \left( 1 + \left( \frac{\delta}{\kappa} \right)^2 \right)^{1/2} \right\} = 0$$

which when rearranged gives

$$(\kappa L)^2 + (\delta L)^2 = (n\pi)^2 \quad (4.7)$$

If  $\kappa L=m\pi/2$  where  $m$  is an odd integer then

$$\Delta\beta L = m\pi \left[ \left( \frac{2n}{m} \right)^2 - 1 \right]^{1/2} \quad (4.8)$$

where  $n$  is the first integer greater than  $m/2$ .

So to achieve the first bar-state (or straight-through state),

$$\Delta\beta L = \pi\sqrt{3}.$$

This is known as the switching condition.

### 4.3 Diffused Anisotropic Ti:LiNbO<sub>3</sub> Guides For Directional Couplers

As mentioned in Chapter 1, there are two processes for waveguide formation in LiNbO<sub>3</sub>: that realized with annealed proton exchange (APE) in LiNbO<sub>3</sub> (Charczenko *et al.*, 1993) and with titanium (Ti) indiffusion into the LiNbO<sub>3</sub> crystal (Korotky and Alferness, 1987; Wooten and Chang, 1993). Although it is possible to model, using the finite element method, any arbitrary refractive index profile generated due to either fabrication process, in this work the latter fabrication method is only considered, mainly because this latter method was more extensively used and advantageous than the former. Typically, the diffusion of titanium in lithium niobate can be described by an

expression involving both the exponential function (*exp*) and the error function (*erf*) (Korotky and Alferness, 1987)

$$C(x, y) = \frac{\tau}{d_y} \frac{1}{\sqrt{\pi}} * \exp\left[-\left(\frac{y}{d_y}\right)^2\right] * \left[ \operatorname{erf}\left(\frac{\frac{w}{2} + x}{d_x}\right) + \operatorname{erf}\left(\frac{\frac{w}{2} - x}{d_x}\right) \right] \quad (4.9)$$

where

$\tau$  = the thickness of the titanium layer

$w$  = width of the titanium layer or the effective width of the guide

$$d_{x,y} = \text{the diffusion length along the } x,y \text{ axes} = 2\sqrt{D_{x,y}t} \quad (4.10)$$

$t$  is the diffusion time in hours

$C = C(x,y)$ , the Ti concentration profile in the transverse plane and

$D_{x,y}$  = the diffusivity along the  $x,y$  axes, respectively,

which follow the Arrhenius law (Fouchet *et al.*, 1987)

$$D_{x,y} = D_o^{x,y} e^{-E_o^{x,y}/kT} \quad (4.11)$$

where

$D_o^{x,y}$  are the diffusion constants along the  $x,y$  axes, and depend on the crystal cut (Fukuma and Noda, 1980)

$E_o^{x,y}$  are the activation energies in the  $x, y$  directions

$k$  is the Boltzmann constant

$T$  is the diffusion temperature in Kelvin.

However, equation (4.9) is just for a single waveguide: for a weakly coupled directional coupler device (Januar *et al.*, 1992) the equation for Ti concentration,  $\hat{C}$ , becomes

$$\hat{C}(x, y) = C\left[\left(x - \frac{w}{2} - \frac{s}{2}\right), y\right] + C\left[\left(x + \frac{w}{2} + \frac{s}{2}\right), y\right] \quad (4.12)$$

where  $s$  is the gap between the two guides of the directional coupler (see Fig. 4.2).

In terms of the midpoint to midpoint distance between the two guides,  $m$ , equation (4.12) can be rewritten as

$$\hat{C}(x, y) = C\left[\left(x - \frac{m}{2}\right), y\right] + C\left[\left(x + \frac{m}{2}\right), y\right] \quad (4.13)$$

Similarly, the refractive index profile can also be given by

$$n(x, y) = n_s + \Delta n * f(y) * h(x) \quad (4.14)$$

where

$$f(y) = \exp\left(-\frac{y^2}{d_y^2}\right) \quad (4.15)$$

$$h(x) = g\left(x - \frac{w}{2} - \frac{s}{2}\right) + g\left(x + \frac{w}{2} + \frac{s}{2}\right) \quad (4.16)$$

$$g(x) = \frac{1}{2} \left[ \operatorname{erf}\left(\frac{\frac{w}{2} + x}{d_x}\right) + \operatorname{erf}\left(\frac{\frac{w}{2} - x}{d_x}\right) \right] \quad (4.17)$$

and

$n_s$  = the refractive index of the LiNbO<sub>3</sub> substrate

Several authors (Fouchet *et al.*, 1987; Korotky and Alferness, 1987; Januar *et al.*, 1992) have attempted to derive an expression for  $\Delta n(x,y)$ , due to the concentration of the diffused titanium,  $C(x,y)$ . It is generally agreed that  $\Delta n_e$  is very nearly proportional to  $C$  (the Ti concentration) and that  $\Delta n_o$  has a nonlinear relationship with  $C$  (Fouchet *et al.*, 1987; Strake *et al.*, 1988; Korotky and Alferness, 1987; Januar *et al.*, 1992). In this work, the expressions for  $\Delta n_e$  and  $\Delta n_o$  used for device simulation, are those given by Korotky and Alferness (1987) and Fouchet *et al.* (1987), respectively, and have been chosen because both equations give a clearer representation of the diffusion mechanism since most, if not all, of the diffusion parameters have been incorporated into these equations. The expression for  $\Delta n_e$  reported by Korotky and Alferness (1987) is given below,

$$\Delta n_e = bC_o \quad (4.18)$$

where

$$b(\lambda) = 0.552 + 0.065/\lambda^2 \quad (4.19)$$

and

$$C_o = \frac{2}{\sqrt{\pi}} \frac{\tau}{d_y} \operatorname{erf}\left(\frac{w}{2d_x}\right) \quad (4.20)$$

Hence, the ordinary,  $n_o(x,y)$  and extraordinary  $n_e(x,y)$  refractive index profiles depend on the fabrication parameters, such as the width,  $w$ , and thickness,  $\tau$ , of the titanium layer, the diffusion temperature ( $T$ ) and time ( $t$ ) via the diffusion lengths,  $d_x$  and  $d_y$ , and these parameters are adjusted to enable an understanding of their effects on device

performance. However, it is thought that these parameters change the refractive index mainly through induced strain and also the photoelastic effect (Sugii *et al.*, 1978).

The reason for choosing to use the above set of equations over the others for the calculation of  $\Delta n_e$  was that this seemed more realistic in that it included  $w$  in the initial value of concentration of the Ti atoms in the LiNbO<sub>3</sub> substrate. The expression for  $\Delta n_o$  described by Fouchet *et al.* (1987) is given below,

$$\Delta n_o = [B_0(\lambda) + B_1(\lambda) \cdot \tau/d_y] (\tau/d_y)^{\alpha_o} \quad (4.21)$$

where

$$B_0(\lambda) = 0.0653 - 0.0315\lambda + 0.00709\lambda^2 \quad (4.22)$$

$$B_1(\lambda) = 0.478 + 0.464\lambda - 0.348\lambda^2 \quad (4.23)$$

and

$$\alpha_o \sim 0.5 \quad (4.24)$$

### 4.3.1. Structure of the Directional Coupler

A Ti indiffused Z-cut Y-propagating weakly coupled directional coupler modulator with guide width,  $w$ , of 9 $\mu\text{m}$ , separation between the guides,  $s$ , of 7.5 $\mu\text{m}$  and electrode separation,  $e$ , of 5 $\mu\text{m}$ , is first considered and used throughout this chapter unless otherwise stated. The cross-section of such a device is shown in Fig. 4.2. The metal electrodes are placed directly over the waveguides and a SiO<sub>2</sub> buffer layer of thickness,  $d$ , which is 0.2 $\mu\text{m}$  unless otherwise stated, is situated between the LiNbO<sub>3</sub> crystal and the electrodes. At the operating wavelength of 1.56 $\mu\text{m}$ , the extraordinary and ordinary refractive indices for LiNbO<sub>3</sub>, are taken to be  $n_e = 2.14$  and  $n_o = 2.21$  (Hobden and Warner, 1966), the change in the refractive index due to the Ti indiffusion is 0.01 for the extraordinary index and 0.005 for the ordinary index. Due to the nature of the uniaxial, birefringent LiNbO<sub>3</sub> material,  $D_o$  has different values in the direction of the bulk material and in the direction along the surface of the material and are termed  $D_{ob}$  and  $D_{os}$ , respectively.  $D_o$  is taken to be  $D_{ob}$  along  $y$  (where  $D_{ob}$  is  $D_o$  in the direction of the bulk material) and  $D_{os}$  along  $x$  (or the direction along the surface of the material).

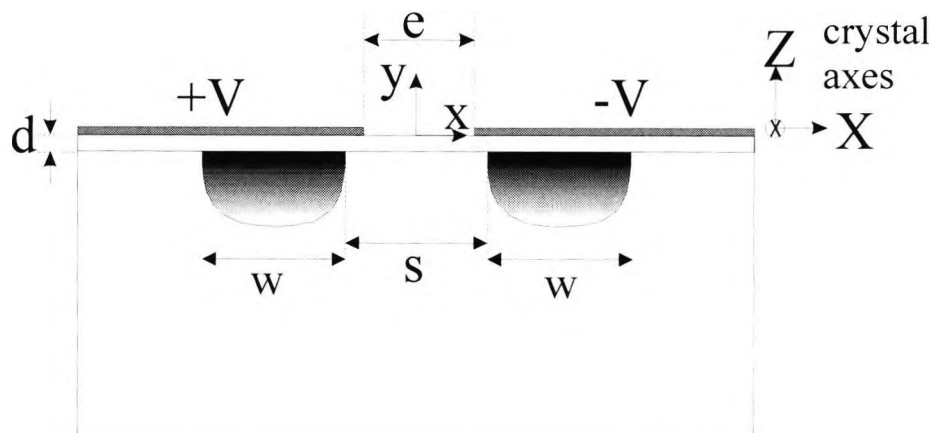


Fig. 4.2 Cross-section of uniform electrode  $\Delta\beta$  DC modulator.

Similarly,  $E_o$  is taken to be  $E_{ob}$  along  $y$  (or in the direction of the bulk material) and  $E_{os}$  along  $x$  (or the direction along the surface of the material). For conventional doping (where the concentrations of Ti in the  $\text{LiNbO}_3$  substrate are around  $0.5 \cdot 10^{21} \text{ cm}^{-3}$ ) the values of  $D_{ob}$  and  $E_{ob}$  are  $0.023 \text{ cm}^2/\text{s}$  and  $2.61 \text{ eV}$ , respectively (Veselka and Korotky, 1986) and  $D_{os}$  and  $E_{os}$  are  $7.37 \cdot 10^{-7} \text{ cm}^2/\text{s}$  and  $1.48 \text{ eV}$ , respectively (Fukuma and Noda, 1980). This gives diffusion lengths of  $4.75 \mu\text{m}$  for  $d_y$  and  $3.83 \mu\text{m}$  for  $d_x$ .

A rigorous numerical approach based on the vectorial  $\mathbf{H}$ -field finite element method has been developed and used in the simulation of the diffusion process of a  $\text{Ti}:\text{LiNbO}_3$   $\Delta\beta$  directional coupler modulator. The two-dimensional contour diagram of the diffusion profile for the above structure is shown in Fig. 4.3. The refractive index  $n_e(x,y)$  has been obtained from equation (4.14). The value of  $\epsilon_e(x,y)$ , the permittivity of the diffused structure, is obtained from the square of  $n_e(x,y)$ . However, this is only true for the range of optical frequencies – not for RF frequencies. The large diffusion lengths cause the spreading of the diffusion profile, but it can be seen from the tightly packed contour lines that the guides formed from the Ti indiffusion will still be well-defined. The diffusion lengths determine the shape of the profile while the peak refractive index caused by the Ti indiffusion determines the strength. The strength can be better seen with a lateral profile of refractive index of the  $\text{Ti}:\text{LiNbO}_3$  directional coupler as given in Fig. 4.4 (at a depth of  $0.676 \mu\text{m}$  from the surface of the  $\text{LiNbO}_3$  substrate). The distinct peaks in the refractive index profile indicate that the optical modes obtained for the guides of this device should be well confined with slight coupling between the guides. However, since the effective index was found to be around 2.142, which is very close to

the value of  $n_e$  for the unmodified LiNbO<sub>3</sub> crystal, this would indicate that the operation is near to the cutoff of the fundamental mode. This is confirmed by the optical modes

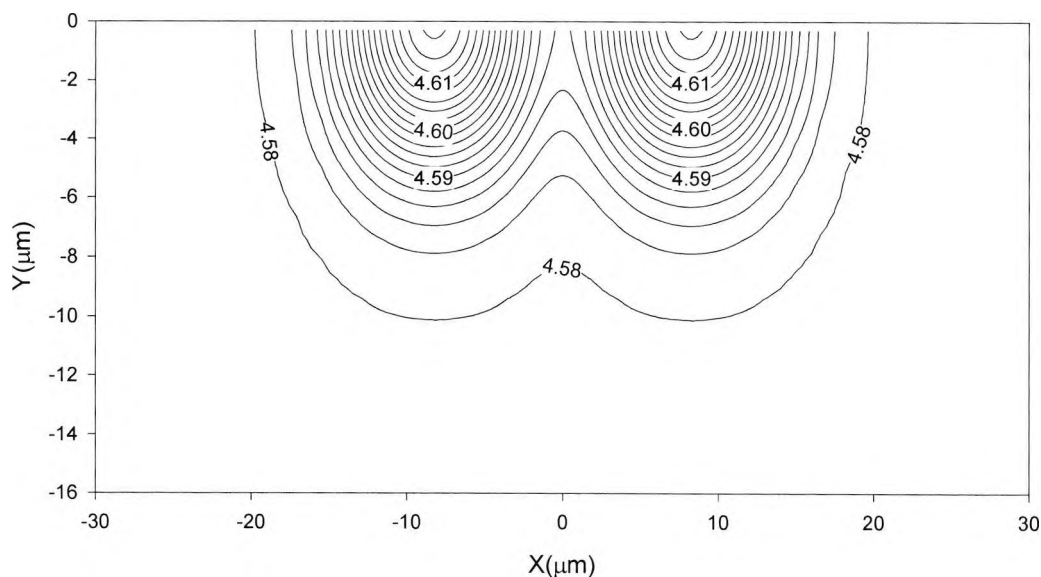


Fig. 4.3 2-d profile of the permittivity  $\epsilon_c(x,y)$  of the Ti-diffused structure shown in Fig. 4.5.

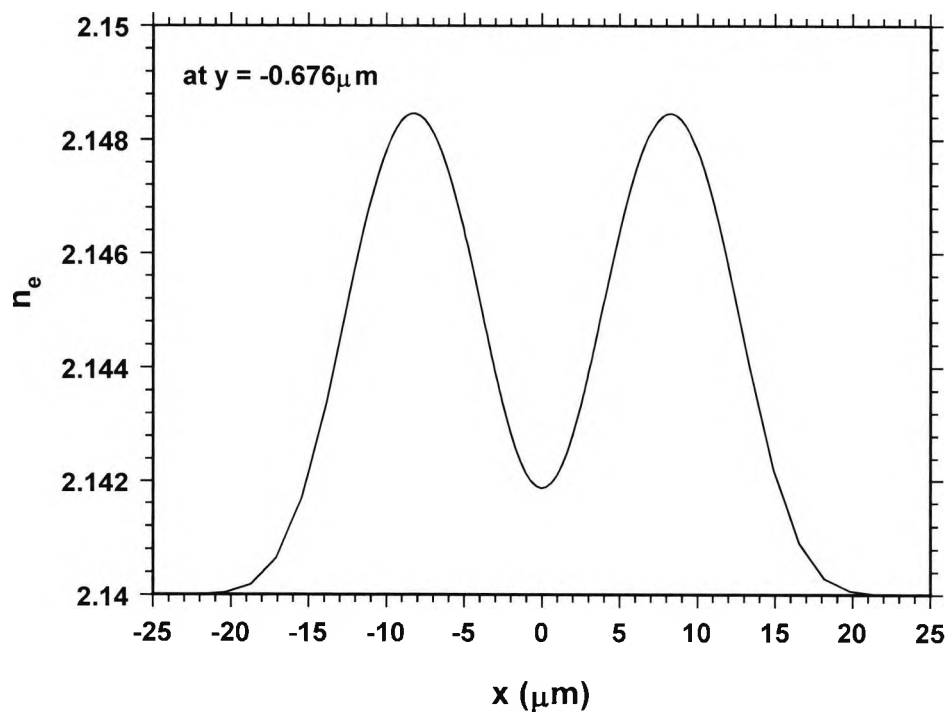
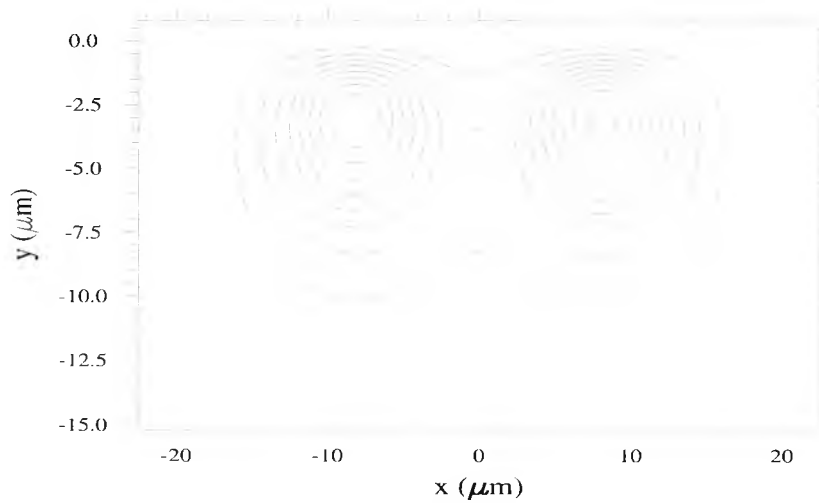
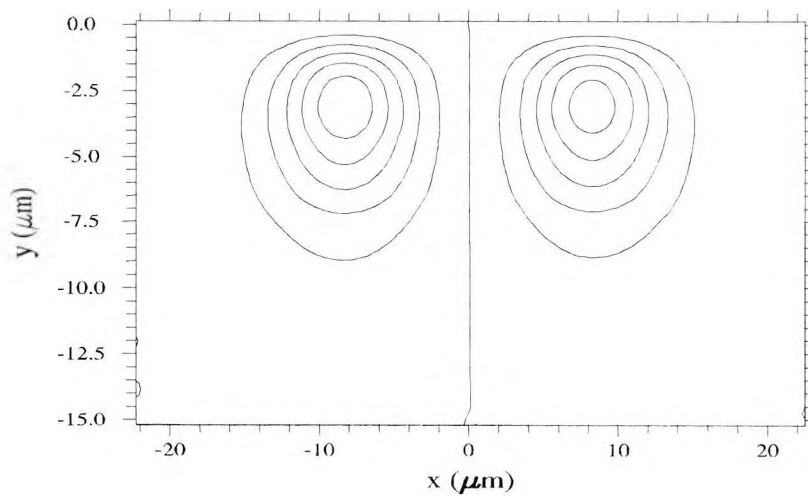


Fig. 4.4  $n_e(x,y)$  at a depth of  $0.676\mu\text{m}$  into the LiNbO<sub>3</sub> substrate.

obtained for this structure, as shown in Figs. 4.5 and 4.6 for the case when no voltage is applied, since they are quite large. However, the value of the geometric-mean diameter



**Fig. 4.5** The even supermode profile for a structure with  $t=6$  hours,  $\tau=1000\text{\AA}$  and  $T=1050^\circ\text{C}$ .



**Fig. 4.6** The odd supermode profile for a structure with  $t=6$  hours,  $\tau=1000\text{\AA}$  and  $T=1050^\circ\text{C}$ .

of the mode (Alferness, 1988) is found to be  $4.5\mu\text{m}$ , obtained from  $\sqrt{w_x w_y}$ , where the  $1/e$  intensity full depth,  $w_y$ , found to be  $3.6\mu\text{m}$ , which is much smaller than  $d_y$  ( $=4.75\mu\text{m}$ ) and the  $1/e$  intensity full width,  $w_x$ , is  $5.6\mu\text{m}$ , which is much smaller than  $2d_x$  ( $=7.66\mu\text{m}$ ); and the fact that  $4.5\mu\text{m}$  is smaller than these diffusion lengths (used in equation (4.20) to find the Ti concentration in the  $\text{LiNbO}_3$ ) demonstrates that the device is not really operating particularly close to cutoff. The simulated device emulates single-mode operation, as these two coupled modes were the only modes supported by the structure, and this leads to low insertion loss, low propagation and coupling loss (Veselka and Korotky, 1986).

The propagation constant for the even supermode,  $\beta_e$ , is always higher than that for the individual guides (when identical), and that of the odd supermode is always lower than that for the individual guides. However, as the inter-waveguide spacing is increased  $\beta_e$  decreases and  $\beta_o$  increases towards the value for the propagation constants for the (identical) individual guides (Wongcharoen, 1995).

In LiNbO<sub>3</sub> electro-optic coefficient  $r_{33}$  has the highest value, and hence this is also the case for the Ti:LiNbO<sub>3</sub> modulator. This yields the highest change for the extraordinary component of the refractive index,  $\Delta n_e(x,y)$  with an applied voltage, since conventionally,  $n_e$  is taken to be parallel to the optic axis, which is usually the Z-axis (in terms of the crystal axes). Taking the example of an X-cut or Y-cut LiNbO<sub>3</sub> crystal, the Z-axis will typically be parallel with the x-axis for the cartesian co-ordinates. The maximum electro-optic effect is only achieved when the electric field,  $\mathbf{E}$ , is parallel to the optic axis and the polarization of light is also in the same direction. This would indicate that the electric field,  $\mathbf{E}$ , component which would bring about this effect is  $E_x(x,y)$ . However, this field acts symmetrically on both guides of the directional coupler and hence yields a  $\Delta\kappa$  modulator (Lee *et al.*, 1993a), which is not of interest in this paper. For a Z-cut crystal, the Z-axis should be in the same direction as the y-axis for the cartesian co-ordinates. The  $E_y$  component of  $\mathbf{E}$  is asymmetric, which is required for the  $\Delta\beta$  modulator (where the refractive index change is also asymmetric due to the asymmetric field,  $E_y$ ). So as the LiNbO<sub>3</sub> has to be Z-cut, for the maximum electro-optic effect the polarisation of light needs to be quasi-TM. From this it can be easily observed that only the extraordinary refractive index,  $n_e$ , is necessary in order to find the modal solution both before and after application of the electric field; and also, that only  $n_e$  is changed by the application of the field. Therefore,  $n_o$  is not necessary for the simulation.

It should be mentioned at this stage that the size of the mesh is also important for the results obtained from numerical methods, as can be seen in Fig. 4.7. This shows  $L_{c0}$  vs the number of elements used in the mesh. It can be observed from this graph that for the Ti:LiNbO<sub>3</sub> directional coupler modulator structure being modelled in this chapter it is more important to have a larger number of elements along  $x$  than it is  $y$ , where for 136 divisions in  $x$  or above the value of  $L_{c0}$  stabilises even though the number of divisions in  $y$  is fixed at 33. However, when the number of divisions in  $x$  are fixed at 94, increasing the number of divisions in  $y$  does not result in a stable value of  $L_{c0}$ .

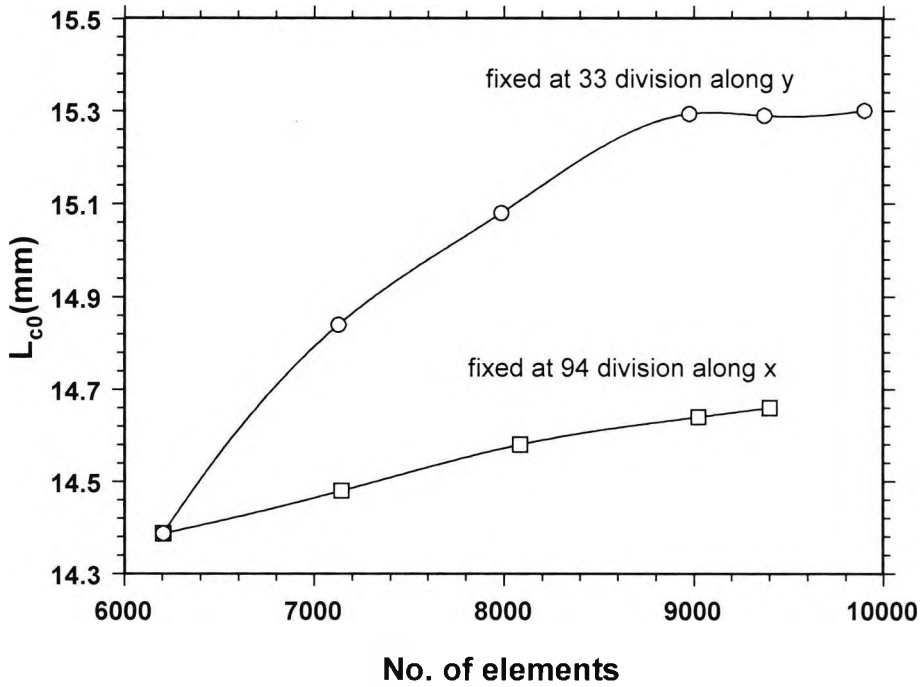


Fig. 4.7 Coupling length,  $L_{c0}$ , vs no. of elements for  $V=0$ .

#### 4.4. The Electro-Optic Effect on Ti:LiNbO<sub>3</sub> Directional Couplers

The vector  $\mathbf{H}$ -field formulation with the penalty functional can then be written as (Rahman and Davies, 1984c)

$$\omega^2 = \frac{\int (\nabla \times \mathbf{H})^* \cdot \hat{\epsilon}^{-1} (\nabla \times \mathbf{H}) d\Omega + \frac{\alpha_1}{\epsilon_0} \int (\nabla \cdot \mathbf{H})^* (\nabla \cdot \mathbf{H}) d\Omega}{\int \mathbf{H}^* \cdot \hat{\mu} \mathbf{H} d\Omega} \quad (4.25)$$

where  $\mathbf{H}$  is the vector magnetic field at the nodal points in the structure,

$\alpha_1$  is the penalty coefficient which leads to a reduction of spurious solutions,

$\hat{\epsilon}$  is the permittivity tensor which can be defined as

$$\hat{\epsilon} = \begin{bmatrix} \epsilon_{11} & \epsilon_{12} & \epsilon_{13} \\ \epsilon_{21} & \epsilon_{22} & \epsilon_{23} \\ \epsilon_{31} & \epsilon_{32} & \epsilon_{33} \end{bmatrix} \quad (4.26)$$

where for a uniaxial anisotropic material such as LiNbO<sub>3</sub> only  $\epsilon_{11}$  ( $= \epsilon_{22}$ ),  $\epsilon_{22}$  and  $\epsilon_{33}$  are the nonzero elements, and  $\epsilon_0$  is the permittivity in free space. Furthermore, integration is carried out over the entire cross-section of the directional coupler structure.

The finite element scalar formulation for the Laplace equation is (Davies, 1989)

$$\int (\nabla \psi)^* \hat{\epsilon} (\nabla \psi) d\Omega = 0 \quad (4.27)$$

where  $\psi$  is the scalar modulating potential. It should be noted that at low modulating frequency (or RF frequencies), the material permittivity  $\hat{\epsilon}$  for Ti:LiNbO<sub>3</sub> is significantly different from that at optical frequencies.

From the modulating potential, the modulating electric field can be obtained by the knowledge that

$$E_x = -\frac{d\psi}{dx} \text{ and } E_y = -\frac{d\psi}{dy} \quad (4.28)$$

Although  $\Delta n_{ij}$  is defined as (Alferness, 1988)

$$\Delta n_{ij} = r_{ij} E_j \quad (4.29)$$

it is well known that the  $r_{33}$  component is the largest and that the component of the modulating field  $\mathbf{E}$  in the direction of the optic axis,  $E_y$  (where  $y$  is in terms of the Cartesian co-ordinates), or  $E_Z$  (where  $Z$  is in terms of the crystal axes) causes the largest change due to the linear electro-optic effect. Therefore, the expression for the change in refractive index with applied electric field is

$$\Delta n(x, y, V) = -\frac{n^3}{2} r_{33} E_y(x, y) \quad (4.30)$$

given by the linear electro-optic or Pockels Effect.

The crystal cut is important in device fabrication. As mentioned above, the maximum electro-optic effect is only achieved when the electric field is parallel to the optical axis (which in terms of the crystal is the  $Z$ -axis - see Fig. 4.2) and the polarization of the light is also in the same direction. However, for the  $\Delta\beta$  modulator (where refractive index change is asymmetric due to the asymmetric field,  $E_y$ ), the LiNbO<sub>3</sub> has to be  $Z$ -cut and hence, the optical field polarization is quasi-TM.

Finally, the wave equation is again solved for the two waveguides of the directional coupler under an applied modulation voltage,  $V$ , with the new refractive index profile

$$n_{new}(x, y, V) = n_{old}(x, y) + \Delta n(x, y, V) \quad (4.31)$$

in order to obtain the coupling length for a given modulating voltage.

The voltage at which the coupling length is half that without the applied potential, due to an additional  $\pi$  radian phase shift, is known as  $V_\pi$  or the switching voltage, and in this case the majority of the output power will be output from guide 1 (see Fig. 4.1). This is known as the ‘bar-state’. The product of  $V_\pi L_{c0}$  is a valuable figure of merit for these electro-optic devices (Wooten *et al.*, 2000) and has been estimated for various fabrication parameters in subsequent sections of this chapter.

A new computer program has been developed to calculate the scalar modulating potential based on equation (4.27), using the finite element approach (Davies, 1989). From this scalar potential,  $\psi$ , the vector modulating field is calculated. Since the modulator has been chosen to be designed from Z-cut material, the component of the

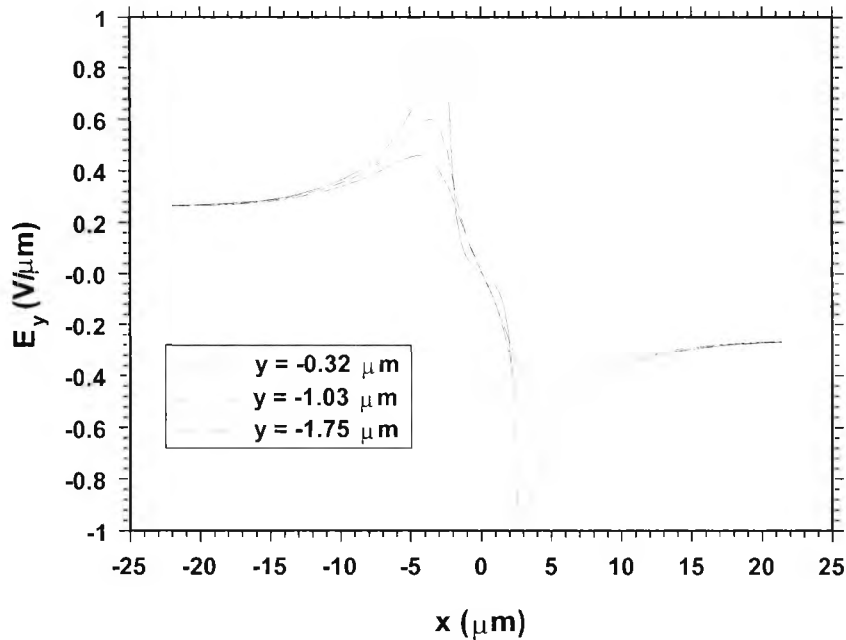


**Fig. 4.8** Plots of the  $E_y$  field for symmetric coplanar electrodes at (a)  $y = -0.32\mu\text{m}$ , (b)  $y = -1.03\mu\text{m}$ , (c)  $y = -1.75\mu\text{m}$ , for an applied voltage of  $7V$ .

electric field which will cause equal but opposite changes in  $\Delta n(x, y)$  for the two guides will be  $E_y(x, y)$ , as can be seen from the cross-section of the structure in Fig. 4.2. The

field  $E_y$  is plotted along the width of the structure at a number of depths ( $y = -0.32, -1.03, -1.75\mu\text{m}$  below the electrode) into the  $\text{LiNbO}_3$  structure and shown in Fig. 4.8. Most of the electric field drastically reduces at approximately  $1\mu\text{m}$  below the surface of the electrode. Similar results for the modulating electric field were given by Ramer (1982), which were obtained by employing conformal transformation for a simple structure. However, in this work a more rigorous finite element method is used to calculate the modulating electric field and, hence, the spatial changes in refractive index,  $\Delta n(x,y)$ , due to the electro-optic effect. The electric field is greatest at the internal edge of the electrodes, and decreases as  $|x|$  increases away from the centre of the structure. This means that there will be very little change in  $\Delta n(x,y)$  outside the guide area, as desired, and from this it can also be seen that there is not much overlap between the electric and optical fields. It can be observed that the maximum modulating field intensity will always be outside the optical waveguides, but, it is one of the main design objectives to increase the overlap between the modulating field and the optical field, as it can be best achieved by adjusting the electrode placement and buffer layer thickness. The  $E_x(x,y)$  profile, although not shown, is only effective for TE polarization, and causes the change in refractive index to increase equally in both guides. Therefore, it would not be useful for a  $\Delta\beta$  modulator.

Next, the changes in the extraordinary index  $\Delta n_e(x,y)$  are calculated using equation (4.30) and this is shown over the entire cross-section of the structure in Fig. 4.9, for  $e=5\mu\text{m}$ .  $\Delta n_e(x,y)$ , is antisymmetric, and this change in the extraordinary refractive index is negative in the left guide and is positive in the right guide. Although there is a small area outside the guide where  $\Delta n_e(x,y)$  is quite high, most of  $\Delta n_e(x,y)$  falls inside the guide area. The maximum change in the value of  $\Delta n_e(x,y)$  for the left guide (where the change in the extraordinary refractive index is negative) was found to be  $-7.7*10^{-4}$  at  $(x=-2.82, y=-0.44)$  and the average value of  $\Delta n_e(x,y)$  over the left guide was found to be  $-2.59*10^{-4}$ . However, the overlap between the electric and optical fields, causes the overlap integral and  $\Delta n_e(x,y)$  to change with, among a number of other fabrication parameters, the electrode separation,  $e$ .

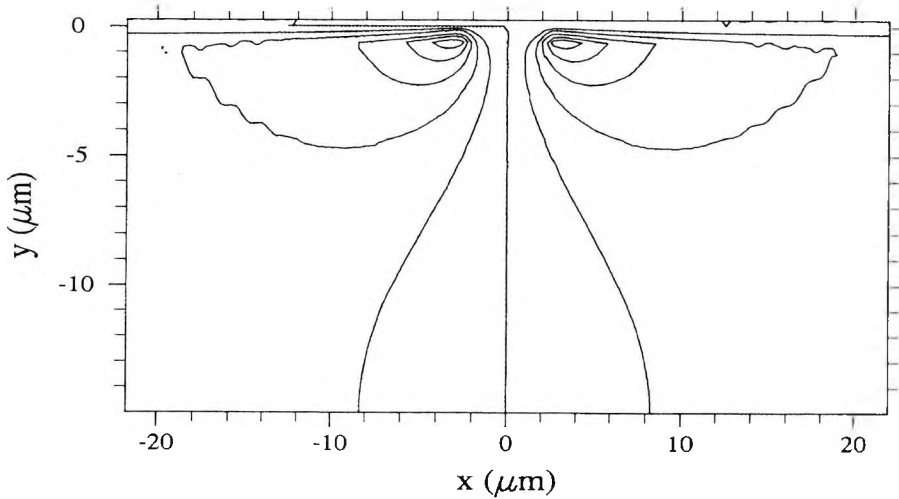


**Fig. 4.9** A contour plot of the change in the extraordinary refractive index,  $\Delta n_e$ , for an applied field,  $E_y$ .

Hence,  $\Delta n_e(x,y)$  was calculated for a number of values of applied voltage, and in each case the amended refractive index profile was input to the vector **H**-field FEM program in order to find the new modal solutions from which the coupling length,  $L_c$ , could be calculated by using equation (4.1). However, the coupling length is also affected by the non-parallel regions of the directional coupler, and the influence of the very weakly coupled transitional S-bends at the input and output section should reduce the length of the parallel section (Januar *et al.*, 1992). Nevertheless, in general this correction is quite small, and this small reduction in length has been accurately calculated by using a vector **H**-field FEM approach (Wongcharoen *et al.*, 1993).

Also, when voltage is applied to the device such that there is a change in the refractive index for each of the waveguides, for small inter-waveguide separations, the propagation constant of the first supermode,  $\beta_e$ , is always higher than  $\beta_2$ , the propagation constant for the individual guide 2 (which has the higher refractive index), and the propagation constant of the second supermode,  $\beta_o$ , is always lower than  $\beta_1$ , the propagation constant for the individual guide 1 (which has the lower refractive index) (Wongcharoen, 1995). However, for larger inter-waveguide separations  $\beta_e$  and  $\beta_2$  are found to be equal as are  $\beta_o$  and  $\beta_1$ . This is typically for inter-waveguide separations that are much larger than the waveguide widths.

Fig. 4.10 shows  $L_c$ , the coupling length, in mm vs applied voltage in volts, for guide separations of  $7.5\mu\text{m}$  and  $5\mu\text{m}$ . For each separation the coupling length reduces with increasing voltage. It can also be seen that as  $s$  decreases,  $L_{c0}$  (the coupling length when no field is applied) decreases. This can be clearly explained using the coupled mode

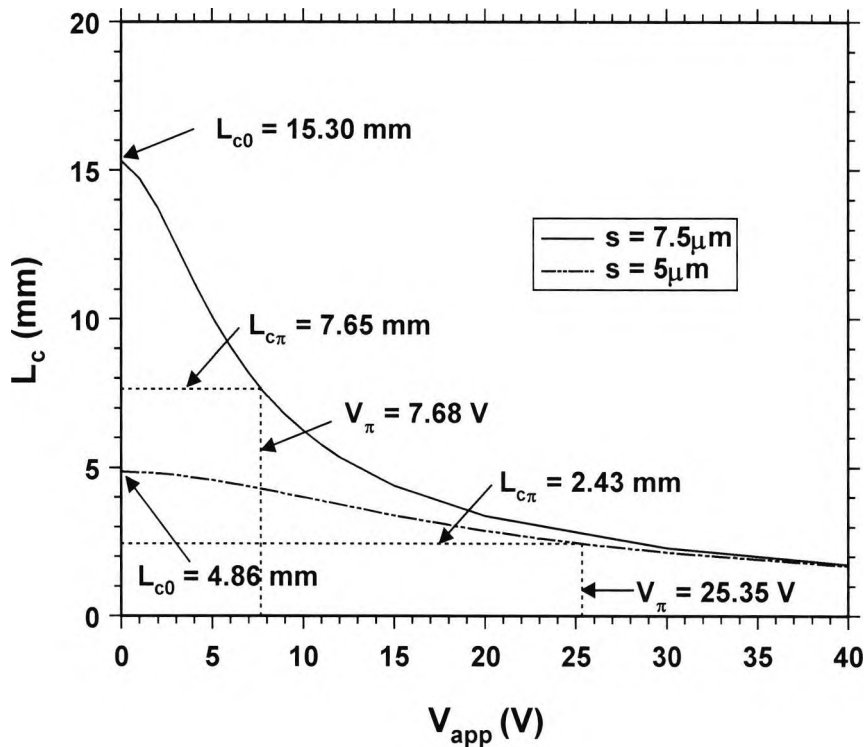
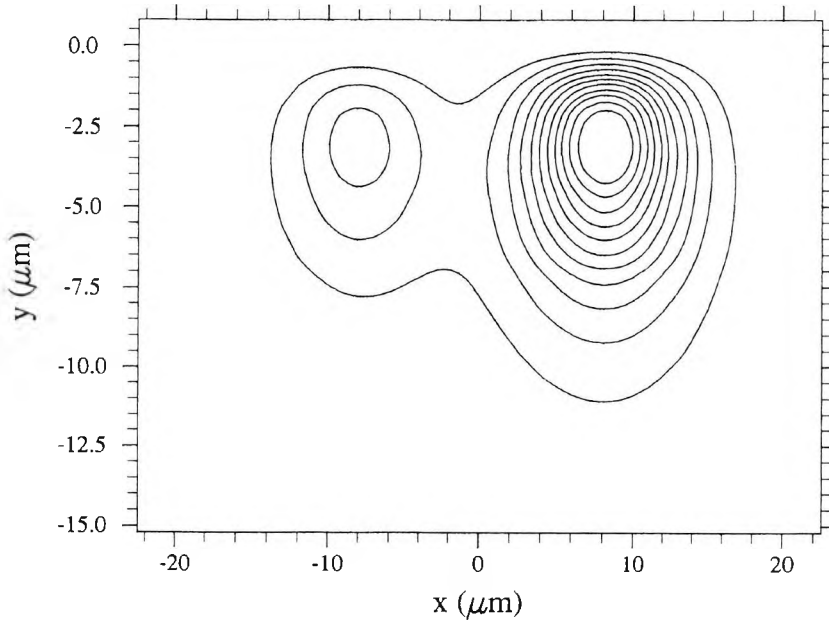


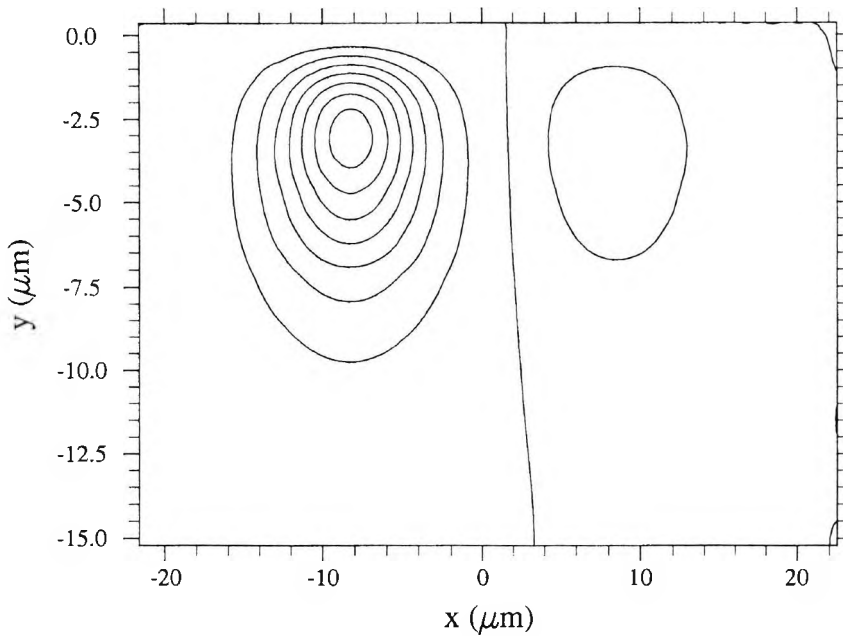
**Fig. 4.10** Coupling length,  $L_c$ , vs applied voltage for the two directional coupler waveguide separations,  $s$ , of  $7.5\mu\text{m}$  and  $5\mu\text{m}$ .

equations (Alferness, 1988): that as the guides move closer together it is easier for the light to couple from one guide into the other, such that light completely couples into the other waveguide over a shorter distance. In fact, this result is qualitatively in agreement with experimental results given by Alferness *et al.* (1979). Throughout this study  $L_{c0}$  is taken to be equal to the proposed device length. However, the voltage it takes to switch the device from the cross to the bar state is of much more interest to this study. For the smaller separation of  $5\mu\text{m}$  this voltage,  $V_\pi$ , is  $25.35\text{V}$  and for the larger separation of  $7.5\mu\text{m}$ ,  $V_\pi$  is  $7.68\text{V}$ . Although, the smaller voltage is more realistic for a practical device, the device length will also increase. The product  $V_\pi L_{c0}$  for the device with guide separation,  $s$ , of  $5\mu\text{m}$  is  $123.20\text{Vmm}$  and for the device with guide separation,  $s$ , of  $7.5\mu\text{m}$  is  $117.50\text{Vmm}$ . This slight variation ( $<5\%$ ) between  $V_\pi L_{c0}$  for the two different

values of  $s$  is due to numerical error in obtaining  $L_{c0}$  (since  $\beta_e$  and  $\beta_o$  are close together for the case when no voltage is applied – see equation (4.1)). It has recently been suggested that by introducing a region with a lower refractive index in the middle of the



(a)



(b)

**Fig. 4.11** The (a) even supermode and (b) odd supermode contour plots of the  $H_x$  field for 7V.

interaction region (i.e. between the two guides), the drive voltage of the  $\Delta\beta$  DC modulator can be further reduced (Okayama *et al.*, 2000). This can be reached by etching a groove between the waveguides as air has a much lower refractive index than that of Ti:LiNbO<sub>3</sub>. The coupling length can also be reduced by etching grooves on both sides of the two coupled waveguides (Liu *et al.*, 2001). However, care should be taken to control the wall tilt as this has found to affect the coupling length (Llobera *et al.*, 2002).

The even and odd modes for an applied voltage of 7V are shown in Figs. 4.11a and 4.11b, respectively. The even mode is mostly confined to the right guide, as there is an increase in the refractive index in the right guide and a corresponding decrease in the left guide, and the odd mode is mostly confined to the left guide. This naturally indicates that the difference in  $\beta$  for these two modes has increased leading to a lower coupling length than for the case when no modulation voltage was applied.

Throughout this work, the effective index,  $n_{eff}$ , remains at around 2.142, which is very close to the value of  $n_e$  for the unmodified LiNbO<sub>3</sub> crystal.

#### 4.5. Effects of Diffusion Parameters on Device Performance

It can be observed from equations (4.9) – (4.12) and (4.20) that  $\Delta n_e(x,y)$  is affected by  $t$ ,  $T$ ,  $\tau$  and  $w$  (as well as  $\lambda$ ). These first four parameters are in fact diffusion parameters, of which the first two affect the diffusion lengths and the second two affect the concentration of

**Table 4.1** A comparison of  $L_{c0}$ ,  $V_\pi$  and  $L_{c0}V_\pi$  for three different titanium layer thicknesses for a guide separation,  $s$ , of 7.5  $\mu\text{m}$ .

$\tau$ (Å)	$L_{c0}$ (mm)	$V_\pi$ (V)	$L_{c0}V_\pi$ (Vmm)
800	9.625	13.261	127.637
1000	15.302	7.682	117.520
1200	26.071	4.185	109.094

Ti in the LiNbO<sub>3</sub> substrate. Table 4.1 shows the coupling length (when no voltage is applied),  $L_{c0}$ , the switching voltage,  $V_{\pi}$ , and the product  $L_{c0} \cdot V_{\pi}$  for three different titanium layer thicknesses,  $\tau$ . The other properties important to diffusion, i.e.  $t$ ,  $T$  and  $w$ , were retained at the original values of 6 hours, 1050°C and 9 $\mu$ m, respectively. It can be observed that  $L_{c0}$  increases with increasing  $\tau$ . This is expected since  $\Delta n$  due to the Ti indiffusion increases with  $\tau$  (see equations (4.18)), which leads to more confined modes and, hence, a longer coupling length (Veselka and Korotky, 1986). However, even though  $L_{c0}$  increases with  $\tau$ , the overall product  $L_{c0} \cdot V_{\pi}$  follows  $V_{\pi}$  (though to a lesser degree) and decreases with increasing  $\tau$ . The diffusion parameter,  $d_{x,y}$  is not affected by  $\tau$ . However, the Ti concentration is affected by  $\tau$ , which in turn affects  $\Delta n$ .

**Table 4.2** A comparison of  $L_{c0}$ ,  $V_{\pi}$  and  $L_{c0}V_{\pi}$  for three different diffusion times for a guide separation,  $s$ , of 7.5 $\mu$ m.

$t$ (hours)	$L_{c0}$ (mm)	$V_{\pi}$ (V)	$L_{c0}V_{\pi}$ (Vmm)
4	39.717	2.550	101.28
6	15.302	7.682	117.52
8	9.517	13.827	131.59

Table 4.2 shows  $L_{c0}$ ,  $V_{\pi}$  and the product  $L_{c0} \cdot V_{\pi}$  for three different diffusion times. The diffusion time is varied by  $\pm 2$  hours from the original time of 6 hours. Again, the other properties  $\tau$ ,  $T$  and  $w$  were retained at the original values of 1000 $\text{Å}$ , 1050°C and 9 $\mu$ m, respectively. The coupling length decreases with (increasing)  $t$  since  $d_{x,y}$  increase with  $t$  and  $\Delta n$  decreases with  $t$ , hence the mode is less confined. Conversely, as the diffusion time increases,  $V_{\pi}$  increases and again the product of  $L_{c0}$  and  $V_{\pi}$  follows the same trend

**Table 4.3** A comparison of  $L_{c0}$ ,  $V_{\pi}$  and  $L_{c0}V_{\pi}$  for three different diffusion temperatures for a guide separation,  $s$ , of 7.5 $\mu$ m.

$T$ (°C)	$L_{c0}$ (mm)	$V_{\pi}$ (V)	$L_{c0}V_{\pi}$ (Vmm)
1025	35.781	2.850	101.98
1050	15.302	7.682	117.52
1075	8.885	15.318	136.10

as  $V_{\pi}$ . Table 4.3 shows  $L_{c0}$ ,  $V_{\pi}$  and the product  $L_{c0} \cdot V_{\pi}$  for the three different diffusion temperatures. Again, the other properties  $\tau$ ,  $t$  and  $w$  were kept at the original values of

1000Å, 6 hours and 9µm, respectively. The coupling length decreases with increasing temperature indicating a less confined mode as the temperature increases. As expected, the switching voltage increases and again the product with  $L_{c0}$ ,  $V_\pi$  follows the same trend as  $V_\pi$ .

As can be seen the coupling length has decreased with increasing temperature or time and conversely  $V_\pi$  has increased. From equation (4.10), it can be seen that as  $T$  or  $t$  increases,  $d_x$  and  $d_y$  also increase, which then causes a reduction in  $\Delta n$ . However, since the diffusion lengths  $d_{x,y}$  have increased, this indicates that the refractive index profile  $n(x,y)$  then decays more slowly, leading to larger effective guide dimensions and hence mode sizes. Thus  $L_{c0}$  decreases because the mode is less confined, and  $V_\pi$  increases because the two guided modes have become more strongly coupled. Again, the product of the switching voltage and coupling length follows the same trend as  $V_\pi$  since  $V_\pi L_{c0}$  also increases with increasing  $T$  or  $t$ . That  $V_\pi L_{c0}$  increases with increasing the diffusion time,  $t$ , and the diffusion temperature,  $T$ , has also been shown by Veselka and Korotky (1986) and Korotky and Alferness (1987), respectively.

A similar table for four different titanium layer widths,  $w$ , is shown in Table 4.4. Again,

**Table 4.4** A comparison of  $L_{c0}$ ,  $V_\pi$  and  $L_{c0}V_\pi$  for four different titanium layer widths for a guide separation,  $s$ , of 7.5µm.

$w$ (µm)	$L_{c0}$ (mm)	$V_\pi$ (V)	$L_{c0}V_\pi$ (Vmm)
7.5	6.828	19.218	131.22
8.5	11.576	10.386	120.23
9.0	15.302	7.682	117.52
9.5	20.203	5.743	116.03

the other properties  $\tau$ ,  $t$  and  $T$  were kept at the original values of 1000Å, 6 hours and 1050°C, respectively.  $L_{c0}$  increases with (increasing)  $w$ , which is expected as the change in the extraordinary index,  $\Delta n_e$ , increases with increasing  $w$ , and hence  $V_\pi$  and, therefore,  $L_{c0}V_\pi$  decreases with increasing  $w$ . Therefore, it was decided to take the values of  $\tau$ ,  $t$ ,  $T$  and  $w$  as 1000Å, 6 hours, 1050°C and 9µm, respectively.

In fact how well the mode is confined with these slight changes in the diffusion parameters can be observed from Figs. 4.12-4.15. Fig. 4.6 shows the odd supermode (when no voltage is applied) for the directional coupler modulator where the titanium layer thickness was  $1000\text{\AA}$ , the diffusion time was 6 hours and the diffusion

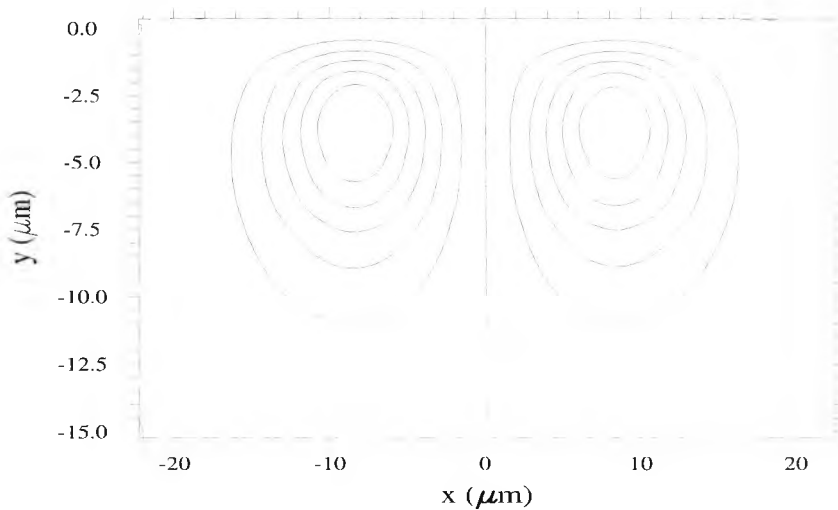


**Fig. 4.12** The odd supermode profile for an increase in diffusion temperature,  $T$ , to  $1075^{\circ}\text{C}$ .

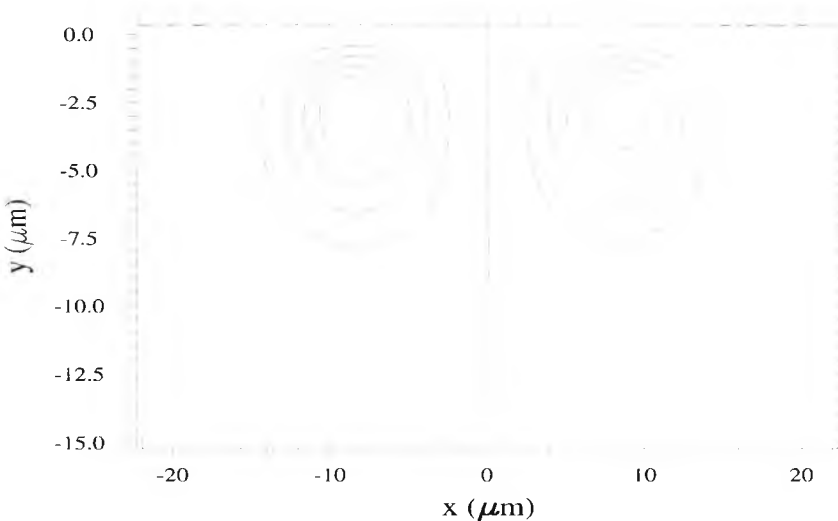


**Fig. 4.13** The odd supermode profile showing the change with an increase in  $\tau$  to  $1200\text{\AA}$ .

temperature was  $1050^{\circ}\text{C}$ . Also, the width of the titanium layer was taken as  $9\mu\text{m}$ . When the diffusion temperature is then increased to  $1075^{\circ}\text{C}$  the mode size as shown in Fig. 4.12 increases and is therefore less confined. This is synonymous with an earlier statement in this section in which it was explained that the coupling length decreases for

any increase in  $T$  because the mode is less confined. Similarly, the mode is tightly confined with an increase in  $\tau$  of  $1200\text{\AA}$ , as shown in Fig. 4.13, and the effect of this was shown by an increase in  $L_{c0}$ , as given in Table 4.1. The mode is again more tightly confined, for the case of lowering the diffusion time to 4 hours, as shown in Fig. 4.14 and follows the general trend of increased coupling length for a more tightly confined mode. This may be the case for the overall mode size, however the horizontal full width half maximum (FWHM) of the mode profiles shown in Figs. 4.6 and 4.14 is nearly equal, whereas the vertical FWHM of these two modes is much smaller for that in Fig. 4.14 compared with that shown in Fig. 4.6. This is also shown to be the case by Gu *et al.* (2002) for TM polarised light in X-cut Ti:LiNbO<sub>3</sub> DCs. However for TE polarised

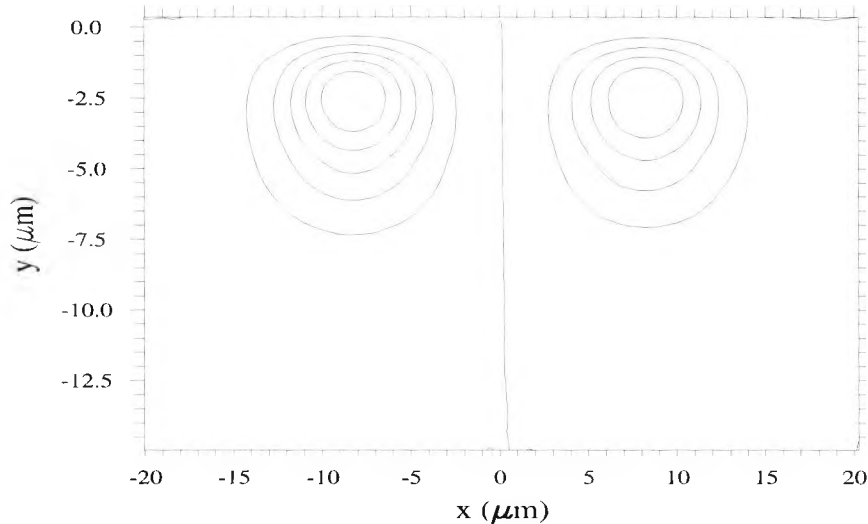


**Fig. 4.14** The odd supermode profile showing the change with a decrease in  $t$  to 4 hours.

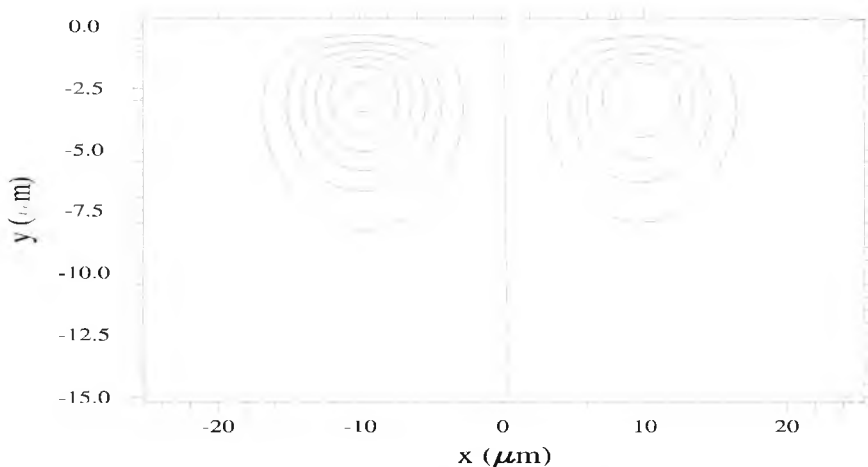


**Fig. 4.15** The odd supermode profile showing the change with an increase in  $w$  to  $9.5\mu\text{m}$ .

light, the horizontal FWHM decreases with decreasing diffusion time as does the vertical FWHM.

The odd supermode profile for an increased titanium layer width of  $9.5\mu\text{m}$  from  $9\mu\text{m}$  is shown in Fig. 4.15. As for the previous mode profiles, since there is an increase in  $w$ , which is accompanied by an increase in  $L_{c0}$  as observed in Table 4.4, there is a decrease in the mode size as expected for a tightly confined mode. In agreement, a graphical representation of the results in Table 4.4 can be seen in Fig. 4.16, which shows that  $L_{c0}$  decreases with decreasing width of the titanium layer,  $w$ . This would indicate that the

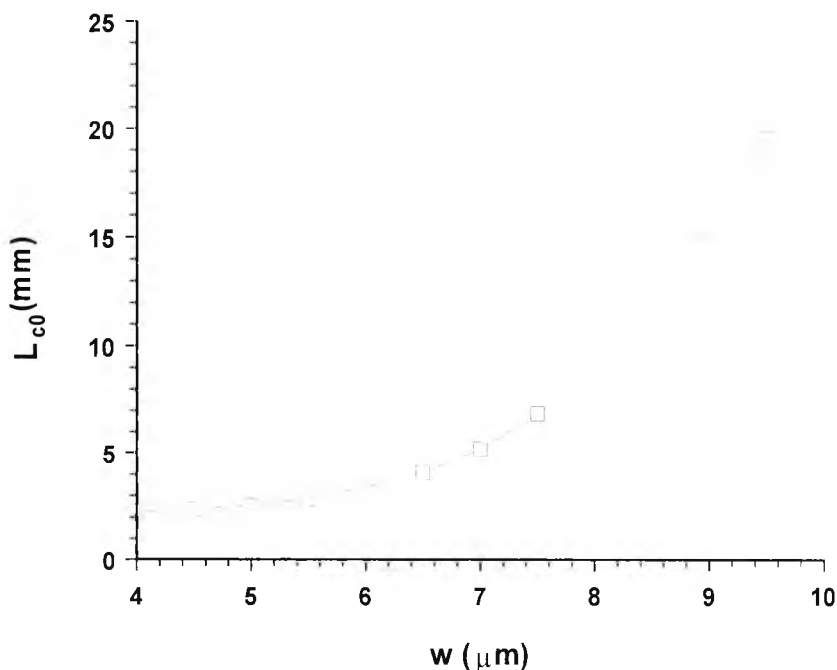


**Fig. 4.16** The variation of  $L_{c0}$  with  $w$ .

mode size increases with decreasing  $w$  since  $L_{c0}$  decreases only when the mode is less confined. Indeed, as shown in Fig. 4.17, the mean mode size  $\sqrt{w_x w_y}$  increases rapidly as  $w$  decreases from  $9\mu\text{m}$  down to  $4\mu\text{m}$  where it comes close to modal cutoff (where the device would operate as a spot size expander, though this is not of interest for the work in this thesis). However, even when  $w$  is increased from  $9\mu\text{m}$  up to  $15\mu\text{m}$  it can be seen that the mean mode size increases, although somewhat minimally. The mean mode size is minimum in the region between  $9$  and  $13\mu\text{m}$ . However, in this region of larger width it is likely that the directional coupler will be in a multimode regime of operation, which although can be modelled, is not of interest in this work as it is

preferred for optical devices to have single-mode operation, meaning  $w$  should be less than  $9\ \mu\text{m}$  for this directional coupler device. Taking the mean mode size of a single-mode fibre to be  $5\text{--}8\ \mu\text{m}$  at a wavelength of  $1.56\ \mu\text{m}$  (Korotky and Alferness, 1987), it would seem that a titanium layer width,  $w$ , of between  $7\ \mu\text{m}$  and  $9\ \mu\text{m}$  (where  $w_x$  is at a minimum) would give better coupling between the fibre and directional coupler as well as providing a reasonably well confined mode, and this shows that the structure for this study of the directional coupler, with a value for  $w$  of  $9.0\ \mu\text{m}$ , falls into this region of good coupling between fibre and directional coupler and good mode confinement.

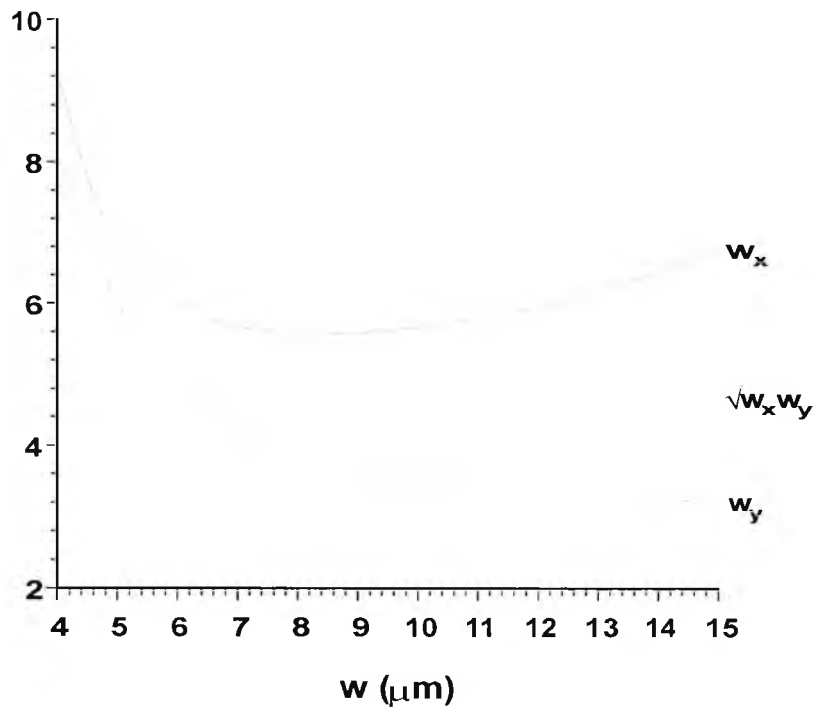


*Fig. 4.17* The variation in mean mode size with  $w$ .

It has been shown in this part of the work that diffusion parameters are important for device operation. However, other parameters such as wavelength,  $\lambda$ , electrode separation,  $e$ , guide separation,  $s$ , and the buffer layer thickness,  $d$ , as well as the electrode and buffer layer materials are also important to device operation. This will be further investigated in subsequent sections of this chapter.

#### 4.6. Fabrication Effects on Drive Voltage

From Fig. 4.18 it can be seen how the coupling length ( $L_{c0}$ ) and switching voltage ( $V_\pi$ ) vary with guide separation,  $s$ , and it can also be seen that the  $L_{c0}V_\pi$  product decreases slightly with the increasing separation. However, there is a trade-off between the switching voltage and  $L_{c0}$  since for separations greater than  $7.5\mu\text{m}$ , the coupling length rises quite sharply, and this will therefore mean an increased device length. This is because  $\beta_c$  decreases sharply with increasing waveguide separation whereas  $\beta_o$  has negligible change in its value (Charczenko *et al.*, 1993). However, as the switching voltage needs to be at a more practical value (i.e.  $\leq 10\text{V}$ ), a higher separation is desired, and, it would seem that a separation of  $7.5\mu\text{m}$  can be considered appropriate for further study.

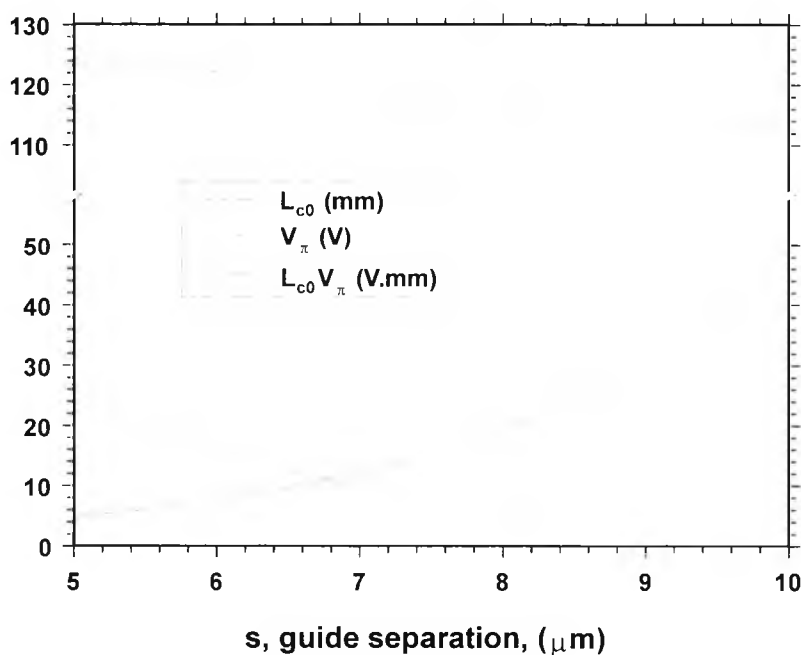


**Fig. 4.18** Coupling length,  $L_{c0}$ , switching voltage,  $V_\pi$ , and the product of coupling length and switching voltage,  $L_{c0}V_\pi$ , vs waveguide separation,  $s$ .

The buffer layer thickness,  $d$ , influences the overlap between the modulating and optical fields, and a similar approach to that detailed above shows changes in  $V_\pi$  and  $L_{c0}$  with varying  $d$  which can be observed in Fig. 4.19. The variation of  $L_{c0}$  (shown by  $\square$ ) is small with the buffer thickness,  $d$ , but the switching voltage  $V_\pi$  (shown by  $\circ$ ) shows a sizeable increase, which is understandable because as the buffer layer thickness

increases, the overlap between the modulating and optical fields decreases (Ramer, 1982), hence  $V_\pi$  has to increase. It has also been shown experimentally (Bulmer and Burns, 1984) that an addition of 200nm to the buffer layer gives an increase in  $V_\pi$  of 40%, which is close to our simulated value of  $\sim 35\%$  for the structure studied here. Furthermore, the optical mode size increases slightly with increase in  $d$  ( $L_{c0}$  slightly decreases) and, according to Veselka and Korotky (1986), the product of the switching voltage and the coupling length product,  $L_{c0}V_\pi$ , generally increases with increasing width and depth of the mode size.

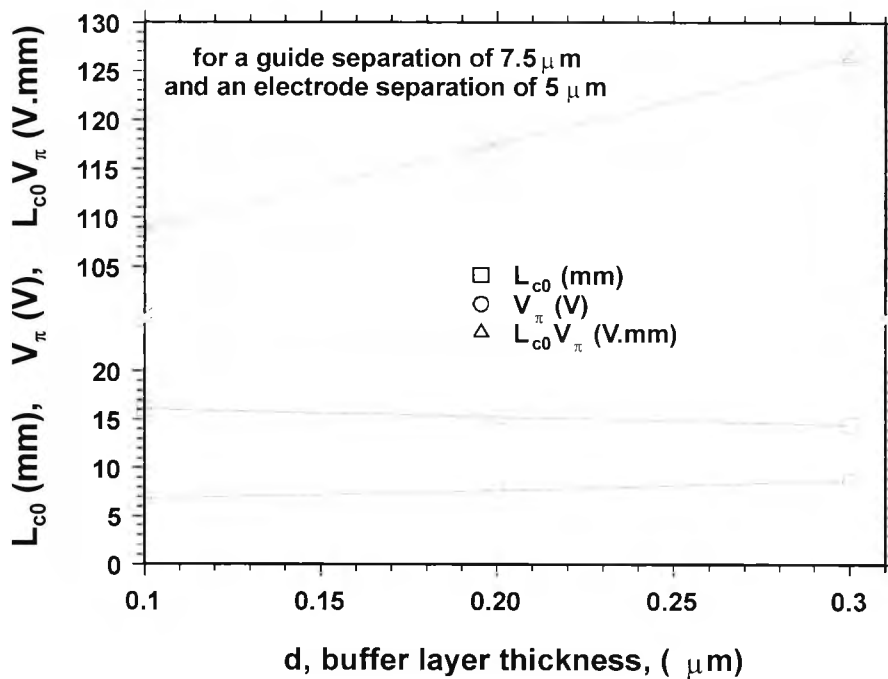
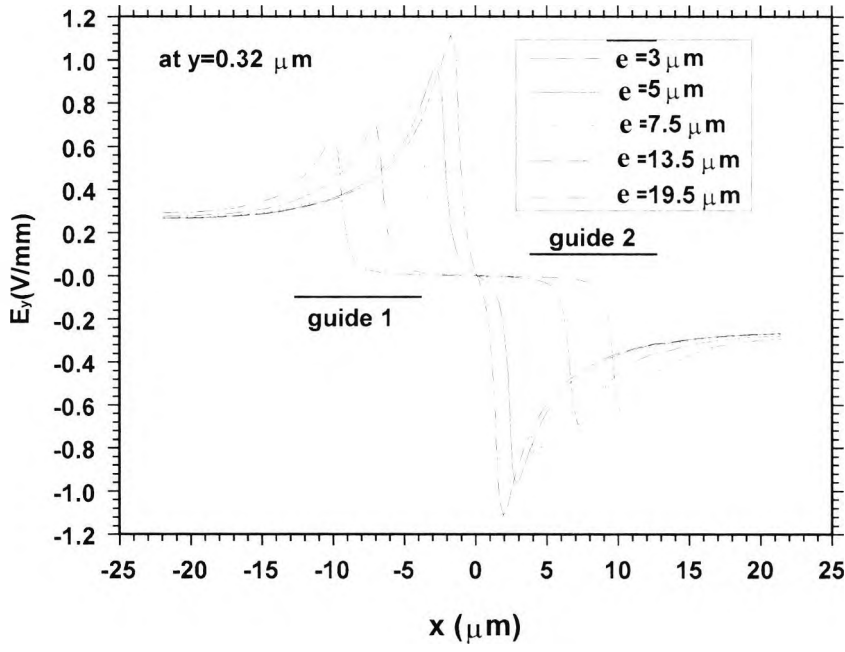


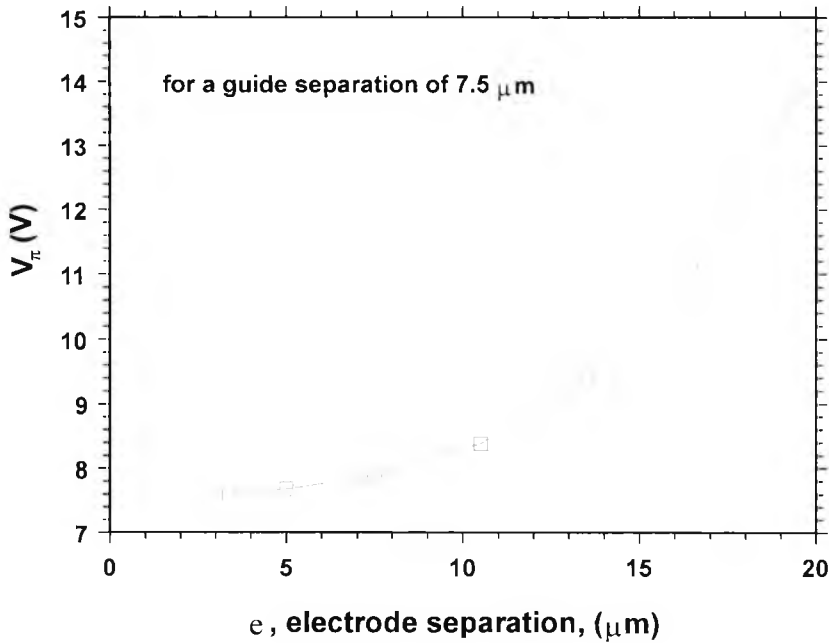
**Fig. 4.19** Coupling length,  $L_{c0}$ , switching voltage,  $V_\pi$ , and the product of coupling length and switching voltage,  $L_{c0}V_\pi$ , vs buffer layer thickness,  $d$ .

From Fig. 4.8, it is clear that the peak of the applied field,  $E_y$ , is at the edges of the electrodes. Hence, keeping the separation between the waveguides,  $s$ , fixed while varying the separation between the electrodes,  $e$ , will influence the device performance. In Fig. 4.20a it can be seen that for  $e=3\mu\text{m}$ , the peak of the  $E_y$  field is outside the two waveguides. It can also be observed by increasing the electrode separation,  $e$ , that although the peak of the  $E_y$  field can be brought inside the guide region, unfortunately, the peak values also reduce. This in fact is in agreement with simulated results reported by Marcuse (1982). The overall device performance for different values of  $e$  has been calculated and this, in terms of  $V_\pi$ , is shown in Fig. 4.20b. This figure shows that  $V_\pi$

increases with  $e$  and, since in this work  $L_{c0}$  is almost independent of the separation between the electrodes,  $e$ , this would also be true for  $V_{\pi} L_{c0}$ , as reported by Wooten and Chang (1993). The overlap integral is ultimately reflected by the  $V_{\pi}$  curve, and our numerical simulations show that  $V_{\pi}$  is lowest in value and the overlap integral is highest



(a)



(b)

**Fig. 4.20** (a) The applied field,  $E_y$ , with variation in electrode spacing,  $e$ , and (b) The variation of switching voltage,  $V_{\pi}$ , with electrode separation,  $e$ .

in value, respectively, for an electrode separation of  $3\mu\text{m}$ . However, since both the values of  $V_\pi$  and the overlap integral flatten out for electrode separations less than  $7.5\mu\text{m}$ , there is no need to decrease the separation to  $3\mu\text{m}$  since a smaller electrode separation causes RF propagation loss, due to increased capacitance in the electrodes, for high speed devices (Alferness, 1988).

**Table 4.5** A comparison of  $L_{c0}$ ,  $V_\pi$  and  $L_{c0} V_\pi$  for three different titanium thicknesses for four guide separations.

S ( $\mu\text{m}$ )	$\tau$ ( $\text{\AA}$ )	$L_{c0}$ (mm)	$V_\pi$ (V)	$L_{c0}V_\pi$ (Vmm)
5.0	800	3.845	35.248	135.471
	1000	4.862	25.350	123.240
	1200	6.659	17.228	114.720
6.0	800	5.599	23.422	131.140
	1000	7.747	15.770	122.170
	1200	11.512	9.748	112.219
7.5	800	9.625	13.261	127.637
	1000	15.302	7.682	117.520
	1200	26.071	4.185	109.094
10.0	800	20.229	6.378	125.023
	1000	45.138	2.500	112.850
	1200	92.4	1.067	98.498

In Table 4.5  $L_{c0}$ ,  $V_\pi$ ,  $L_{c0}V_\pi$  are given for three different Ti thicknesses (the original thickness being  $1000\text{\AA}$ ), at 4 different separations,  $s$ . As can be seen the general trend for each separation is that as the Ti thickness is increased  $L_{c0}$  increases. This is understandable since as  $\tau$  increases  $\Delta n_e$  also increases and hence  $L_{c0}$  increases since the mode is more confined and the length over which the light couples from one guide into the other increases. Results from Alferness *et al.* (1979) also show that  $L_{c0}$  increases with  $\tau$ . The fact that the mode size reduces with increasing  $\tau$  is in agreement with the work of Korotky and Alferness (1987). Table 4.5 also shows that  $V_\pi$  decreases with both (increasing)  $\tau$  and  $s$ . Similarly, since the increase in the titanium thickness,  $\tau$ , causes the two modes to become more well-confined, the switching voltage,  $V_\pi$ , decreases since the switching voltage is minimized for small optical modes (Alferness, 1988). From Table 4.5 it can also be observed that the overall product of  $L_{c0}$  and  $V_\pi$  reduces with the

titanium thickness,  $\tau$ , for all the waveguide separations,  $s$ . The trend that  $L_{c0}V_{\pi}$  decreases with a smaller mode size has been mentioned by Veselka and Korotky (1986).

#### 4.7. Optical Loss due to Metal Electrodes

Electrode design is an important issue in order to maximize the overlap between the optical and electric fields. The overlap can be optimized by varying a number of fabrication parameters, including buffer layer thickness. However, due to the decay of the electric field in the buffer and the Ti:LiNbO<sub>3</sub> material there is, in fact, only a small overlap between the optical and electric fields. Nevertheless, the buffer layer is needed in order to reduce the optical loss due to the lossy metal electrodes. The perturbation method is used in conjunction with the finite element method (Themistos *et al.*, 1995a) to calculate the optical loss due to the metal electrodes. This is given in more detail in Chapter 3.

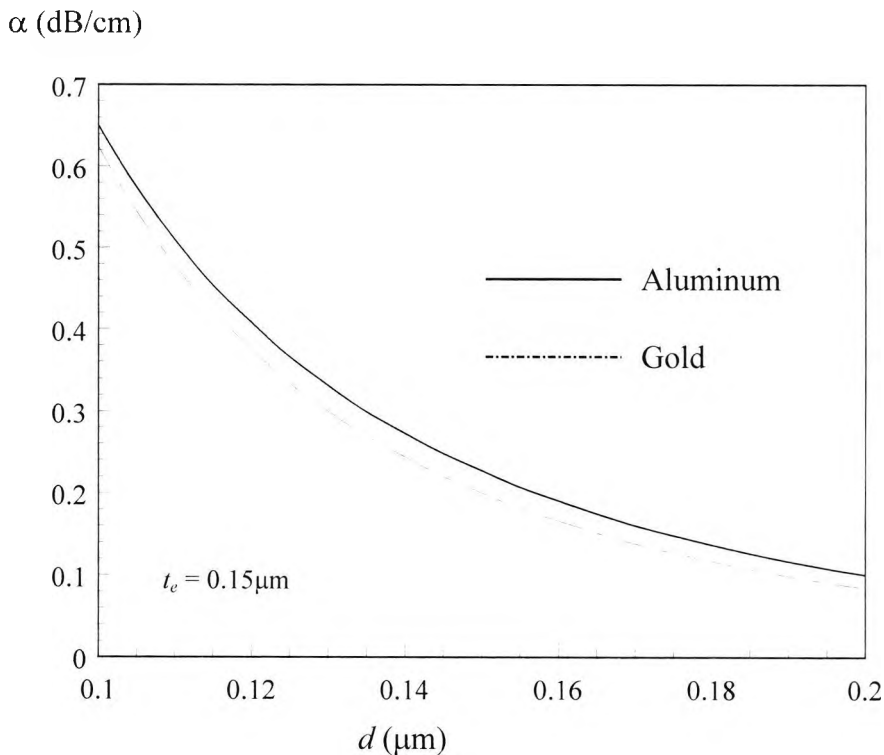


**Fig. 4.21** The optical loss (for a quasi-TM mode) due to the electrodes,  $\alpha$ , vs buffer thickness,  $d$ , for the gold and aluminium electrodes of thickness,  $t_e = 0.15 \mu\text{m}$ .

In Fig. 4.19 it has been shown that the  $L_{c0}V_{\pi}$  product increases with buffer thickness. However, it is well known that both TE and particularly TM-polarized modes will suffer modal loss due to the proximity of the lossy electrodes. A perturbation approach (Themistos *et al.*, 1995a) has been used to calculate the modal loss,  $\alpha$ , for the quasi-TM mode and this is shown in Fig. 4.21 for aluminium (Al) and gold (Au) electrodes for an electrode thickness of  $0.15\mu\text{m}$ . The complex refractive index for Al and Au were taken to be  $1.44-j16$  and  $1.55-j11.5$ , respectively, at a wavelength of  $1.56\mu\text{m}$ . As the buffer layer increases,  $\alpha$  decreases, though there is also less loss for gold electrodes, which is to be expected. So a thicker buffer layer is needed in order to reduce the absorption loss by shifting the modal field away from the metal electrodes (Marcuse, 1982), but, as shown earlier in Fig. 4.19, an increased buffer layer thickness also means a higher  $L_{c0}V_{\pi}$  product. However, Fig. 4.21 shows that  $\alpha$  decreases rapidly with  $d$ , at first, but then gradually steadies off at a thickness of approximately  $0.16\text{-}0.17\mu\text{m}$ . Hence, a buffer layer thickness of  $0.16\text{-}0.17\mu\text{m}$  appears to be ideal.

It is also known that the quasi-TM mode suffers from more loss than the quasi-TE mode. It was observed in this study (see Fig. 4.22) that this effect was very pronounced for small buffer layer thickness from  $0.1\text{-}0.2\mu\text{m}$ , but for buffer layer thicknesses of

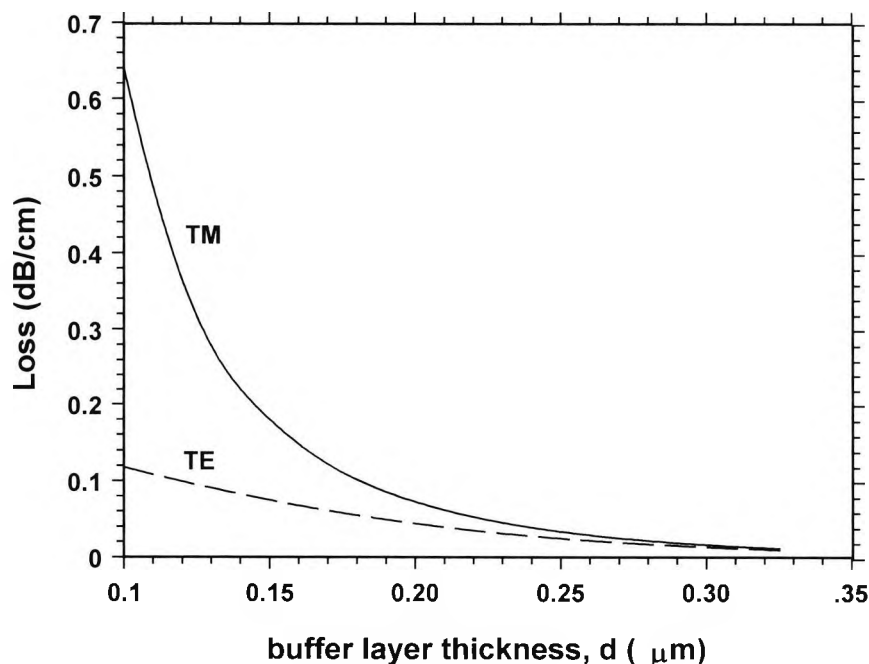


**Fig. 4.22** The optical loss due to gold electrodes vs buffer layer thickness,  $d$ , for both TE and TM polarised light for  $t_e=0.15\mu\text{m}$ .

0.25 $\mu\text{m}$  and above, there was little difference between the loss due to the metal electrodes for the two modes of either polarisation. The optical loss also appears to be steadily decreasing with increasing  $d$  for both light polarisations.

Moreover, it has also been observed by others that there is also a slight reduction and increase in the effective index for the TM and TE-polarization, respectively, due to the proximity of the metal electrodes (Duthie and Edge, 1991). In fact loss is also dependent on the material of the buffer layer as well, and with more accurate loss-tangent data for these materials, their effect can also be easily studied. However,  $\text{SiO}_2$  was taken to be the buffer layer material for this study, as it is commonly used for  $\text{Ti:LiNbO}_3$  electro-optic devices.

## 4.8. Power Transfer

The operation of the directional coupler was given in the introductory section of this chapter. It has been made clear that the device operates by light transfer from one guide into the other. The uniform  $\Delta\beta$  coupler considered for this study is designed for  $L$ , the device length, to be equal to  $L_{c0}$ , the coupling length when no voltage is applied, so that light is completely coupled from guide 1 to guide 2 by the end of the device length.  $V_\pi$  is the voltage applied to the device in order that the coupling length is half of the length of the device and there is a  $\pi$  phase shift between the light input to the device and that which is output from the device. Hence in this case, the light from guide 1 couples to guide 2 and back to guide 1 along the total length of the device.

So the nature of the power transfer along the device is a very important feature of the directional coupler modulator.

### 4.8.1. LSBR

Although the FEM can provide an accurate calculation of the coupling length, the LSBR approach has been used to estimate the variation of the power transfer efficiency

with the modulating potential. The coupled mode approach could also be used to estimate the power transfer efficiency as well as the mode-matching technique or using overlap integrals, but it has been shown earlier (Wongcharoen, 1995) that the LSBR method is a powerful approach for practical waveguides when they are nonidentical and/or strongly coupled. In this approach the coefficients of the two supermodes are calculated by enforcing the continuity of the tangential electric and magnetic fields, in a least squares (Rahman and Davies, 1988) sense, by which method the power in the two guides (1 & 2) of the directional coupler may be calculated for a number of applied voltages.

Using the LSBR method it is possible to find the power transfer between two butt-coupled guides using the individual modes of the guides or the power transfer between the two guides in the coupled system using the supermodes of the coupled guides, and both approaches are used in this study. However, the primary aim for this study is use this method to find the amplitudes of the even and odd supermodes for section II,  $b_1$  and  $b_2$ , respectively.

It is first assumed that a single isolated guide (section I) is butt-coupled to one of the two guides forming the directional coupler (section II), as shown in Fig. 4.23. The error integral for the LSBR method at the boundary between sections I and II is

$$J = \int (\mathbf{E}_{t_I} - \mathbf{E}_{t_{II}})^2 d\Omega + \alpha_{\text{wf}} Z_0^2 \int (\mathbf{H}_{t_I} - \mathbf{H}_{t_{II}})^2 d\Omega \quad (4.32)$$

where in section I,

$$\begin{aligned} \mathbf{E}_{t_I} &= \text{incident} + \text{reflected mode} \\ &= \mathbf{E}^i + \sum a_n \mathbf{E}_n^r \end{aligned} \quad (4.33)$$

and in section II,

$$\begin{aligned} \mathbf{E}_{t_{II}} &= \text{transmitted mode} \\ &= \sum_{n=1}^N b_n \mathbf{E}_n^t \end{aligned} \quad (4.34)$$

for the tangential electric field,  $\mathbf{E}$ .

Also  $a_n$  and  $b_n$ , are coefficients of the reflected and transmitted modes, respectively.

A similar set of expressions is available for the magnetic field,  $\mathbf{H}$ .

The only requirement here is the continuity of the tangential field components at the boundary between sections I and II

$$H_{t_i} = H_{t_{ii}} \quad (4.35)$$

$$E_{t_i} = E_{t_{ii}} \quad (4.36)$$

where  $E_t$  and  $H_t$  are the electric and magnetic fields transverse to the direction of propagation.

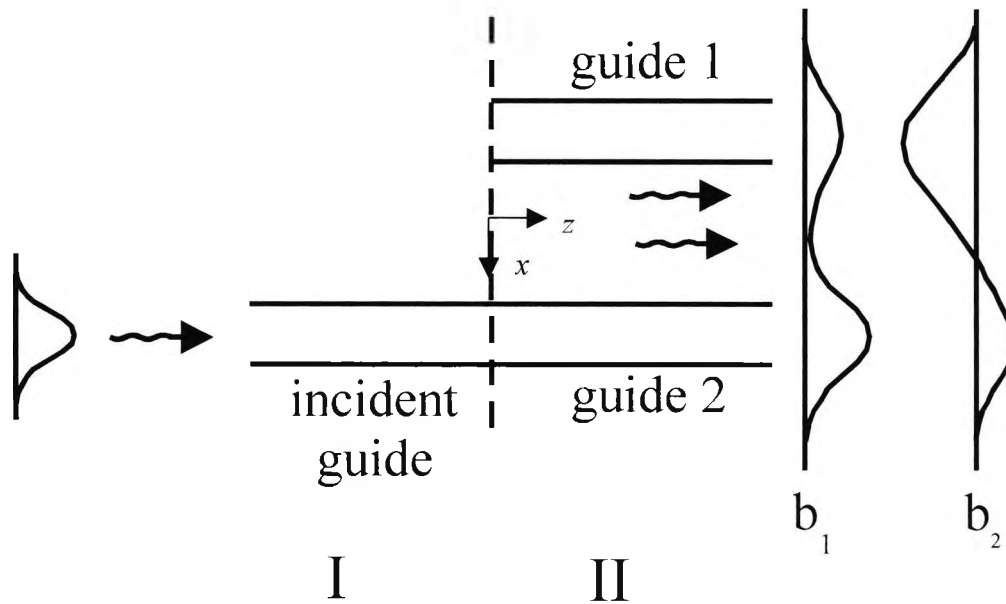


**Fig. 4.23** An isolated guide butt-coupled (section I) to the directional coupler (section II).

Also,  $\alpha_{wf}$  is a weighting factor to balance E and H field error functions and is proportional to  $1/(n_{\text{eff}})^2$  and  $Z_o$  is the characteristic impedance of the device/ waveguide.

$\sqrt{\alpha_{wf} Z_o}$  is the effective impedance of the material, however  $\alpha_{wf}$  and  $Z_o$  need to be considered separately because of the differing materials/structures in sections I and II.

The error integral is calculated over the whole discontinuity interface and not just at some specific points as for the mode matching method. In addition, even though there is single-mode operation for the particular directional coupler modulator studied in this chapter, the LSBR method is also superior for multimode devices over the traditional overlap integral methods since it is possible to involve all the supported modes in the error integral at the discontinuity interface.

Furthermore, as the two adjacent waveguides of the directional coupler are placed such that the tail of the field supported by one waveguide overlaps the other waveguide, it is clear that the overlap is responsible for the coupling between the two waveguides. The incident wave launched into guide 2 (see Fig. 4.23) is taken to have a total power of  $P_0$ .

Through the minimisation part of the formulation, equation (4.32) is reduced to the linear matrix eigenvalue equation

$$[C]\{x\} = \{v\} \quad (4.37)$$

where

$[C]$  is the square matrix generated from the modal eigenvectors for all the incident reflected and transmitted modes

$\{v\}$  is the array that considers just the incident mode, generated from the modal eigenvector for this mode

$\{x\}$  is the solution of equation (4.37): an array consisting of the coefficients of the reflected and transmitted modes,  $a_i$  and  $b_i$ , respectively, for the chosen incident mode.

In this case of single mode waveguides, there is only one chosen incident mode, and  $b_1$  and  $b_2$  are the coefficients of the transmitted even and odd supermodes, respectively.

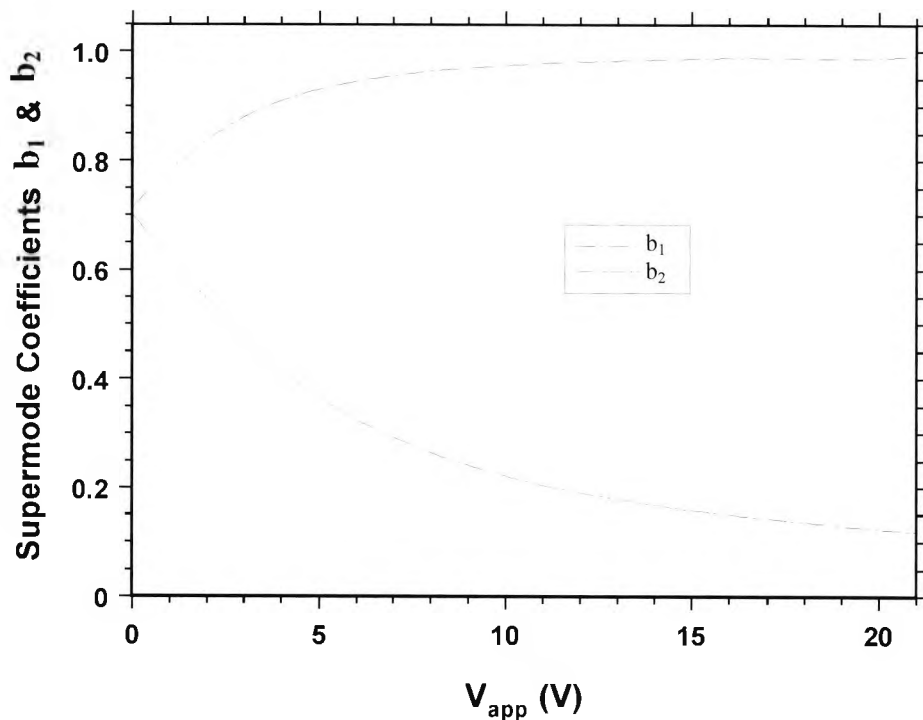


Fig. 4.24 Supermode coefficients indicating the amplitude of the even and odd supermodes,  $b_1$  and  $b_2$ , respectively, in guide 2.

For the case of identical waveguides, and no applied voltage (i.e. the waveguides are in synchronous phase),  $b_1$  and  $b_2$  are equal, as shown in Fig. 4.24.  $b_1=b_2\cong 0.707=\frac{1}{\sqrt{2}}$ ,

where 0.707 is the modal coefficient for both transmitted even and odd supermodes. Therefore, the power coefficient for both modes,  $b_1^2$  and  $b_2^2 \approx 0.5$ , showing that the two supermodes carry equal power for the case of no applied voltage. However, as voltage is applied, and the refractive index in guide 2 decreases as that in guide 1 increases by the same amount,  $b_1$  and  $b_2$  become vastly different.  $b_1$  increases with applied voltage until  $V_\pi$ , after which it no longer increases; while  $b_2$  gradually reduces with applied voltage, although less for the higher voltages.

#### 4.8.2. Power Transfer Theory

It has been made clear in the preceding sections that directional coupler modulators exhibit at first a strong coupling and when a voltage is applied to appropriately placed electrodes a high degree of asymmetry occurs for the coupler. The method used in this section is that of Suematsu and Kishino (1977) in conjunction with the LSBR method is for strongly coupled waveguides.

The method used by Suematsu and Kishino (1977) is based on the interference between waveguide modes supported by the coupled waveguide system. The structure used, by way of example, by the authors consists of five layers with two of the slabs being of higher refractive index such that waveguiding occurs in these layers. Hence, the refractive index only varies in the direction transverse to the plane of the slabs and not in the plane ( $x$  or  $z$ ). It is also assumed that the waveguides are lossless. For this method the coupling coefficient is described as the power transfer ratio between the two guides, and it is shown that the power transfer is not complete for this strongly coupled system.

For directional couplers that are in synchronous phase, only for small inter-waveguide separations is there less than complete power transfer and for larger waveguide widths the power transfer always remains close to unity. However when the two waveguides of the directional coupler are no longer identical and therefore no longer in synchronous phase, the maximum power transfer reduces with increasing difference in both the

refractive index between the two waveguides and the waveguide width. This is due to increasing phase mismatch with differing refractive index or waveguide width. Moreover, as the inter-waveguide separation increases for the case of nonidentical waveguides the maximum power transfer decreases to zero.

It has been recently shown that this method can be extended to encompass strongly coupled channel waveguides (Wongcharoen *et al.*, 1997), as for the phase matched directional coupler modulator used in this study. Since the isolated waveguides of the directional coupler modulator are single mode, only the even and odd modes shown in Figs. 4.5 and 4.6 are supported by this coupled waveguide system and are orthonormal with respect to the Poynting power (Suematsu and Kishino, 1977). These modes have a different propagation constant and the difference between them increases as the guides become more strongly coupled (Wongcharoen, 1995). The modes, each with different propagation constants, therefore travel at slightly different phase velocities and in doing so alternatively add and cancel with each other. This means that the resultant guided wave, being a combination of these modes, can be seen to exchange power periodically (Suematsu and Kishino, 1977).

Hence, the guided wave for the structure given in Figs. 4.1 and 4.2 can therefore be expressed in terms of  $E(x,y,z)$  and  $H(x,y,z)$

$$E(x, y, z) = b_1 E_e(x, y) e^{-j\beta_e z} + b_2 E_o(x, y) e^{-j\beta_o z} \quad (4.38)$$

$$H(x, y, z) = b_1 H_e(x, y) e^{-j\beta_e z} + b_2 H_o(x, y) e^{-j\beta_o z} \quad (4.39)$$

where  $b_1$  and  $b_2$  were found using the LSBR method as explained in the section above.

The wave is normalised by

$$\int_{-\infty}^{\infty} E^*(x, y, z) H(x, y, z) dy dx = |b_1|^2 + |b_2|^2 = 1 \quad (4.40)$$

where  $x=0$  is taken to be at the midpoint between the two waveguides of the directional coupler.

The power density is given by the Poynting vector

$$\begin{aligned} P(x, y, z) &= \text{Re} \left[ E^* \times H \right] = \text{Re} \left[ E^*(x, y, z) H(x, y, z) \right] \\ &= b_1^2 E_e^*(x, y) H_e(x, y) + b_2^2 E_o^*(x, y) H_o(x, y) \\ &\quad + b_1 b_2 \left[ E_e^*(x, y) H_o(x, y) + E_o^*(x, y) H_e(x, y) \right] \cos \left[ (\beta_e - \beta_o) z \right] \end{aligned} \quad (4.41)$$

By integrating over each side of  $x=0$  (see Fig. 4.2 for the position of  $x=0$ ), the power in each waveguide can be expressed as a function of the propagation distance  $z$ . Therefore, the power fraction in guide 1 is given by

$$P_1(z) = \int_{-\infty}^0 P(x, y, z) dx dy$$

$$= b_1^2(1 - \xi_{ee}) + b_2^2(1 - \xi_{oo}) - b_1 b_2(\xi_{eo} + \xi_{oe}) \cos[(\beta_e - \beta_o)z] \quad (4.42)$$

where

$$\xi_{ij} = \int_0^{\infty} E_j^*(x, y) H_i(x, y) dx dy, \quad (i, j = e, o) \quad (4.43)$$

At  $z=0$ , maximum power is observed in guide 2. The power is gradually transferred from guide 2 to guide 1 along  $z$ . However, a small fraction of the power should remain in guide 2 and this is termed the uncoupled factor. Likewise, there should be a small fraction of power that is never transferred from guide 1.

From equations (4.42) and (4.43), it is possible to express the power in both waveguides at  $z=0$  as

$$P_1(z=0) = b_1^2(1 - \xi_{ee}) + b_2^2(1 - \xi_{oo}) - b_1 b_2(\xi_{eo} + \xi_{oe}) \quad (4.44)$$

$$P_2(z=0) = b_1^2 \xi_{ee} + b_2^2 \xi_{oo} + b_1 b_2(\xi_{eo} + \xi_{oe}) \quad (4.45)$$

and more generally at any propagation distance  $z$

$$P_1(z) = b_1^2(1 - \xi_{ee}) + b_2^2(1 - \xi_{oo}) - b_1 b_2(\xi_{eo} + \xi_{oe}) \cos[(\beta_e - \beta_o)z] \quad (4.46)$$

$$P_2(z) = b_1^2 \xi_{ee} + b_2^2 \xi_{oo} + b_1 b_2(\xi_{eo} + \xi_{oe}) \cos[(\beta_e - \beta_o)z] \quad (4.47)$$

$P_1(z)$  and  $P_2(z)$ , for the case when no voltage is applied to the directional coupler modulator shown in Figs. 4.1 and 4.2, are shown by the dashed lines in Fig. 4.25. When the light is launched into guide 2 (at  $z=0$ ), as predicted by equation (4.44) for strongly coupled guides the majority of the power is in guide 2 (94.6% in this case) but a small amount of power is in guide 1 (5.4% in this case). As  $z$  increases, power is transferred from guide 2 to guide 1 until  $z=L_{c0}$ , where  $L_{c0}=15.3$  mm, from where power from guide 1 is transferred back to guide 2. This is shown in Fig. 4.26 where for the mode profile at  $z=0$  the power is mainly in guide 2, at  $z=L_{c0}$  it is primarily in guide 1 and at

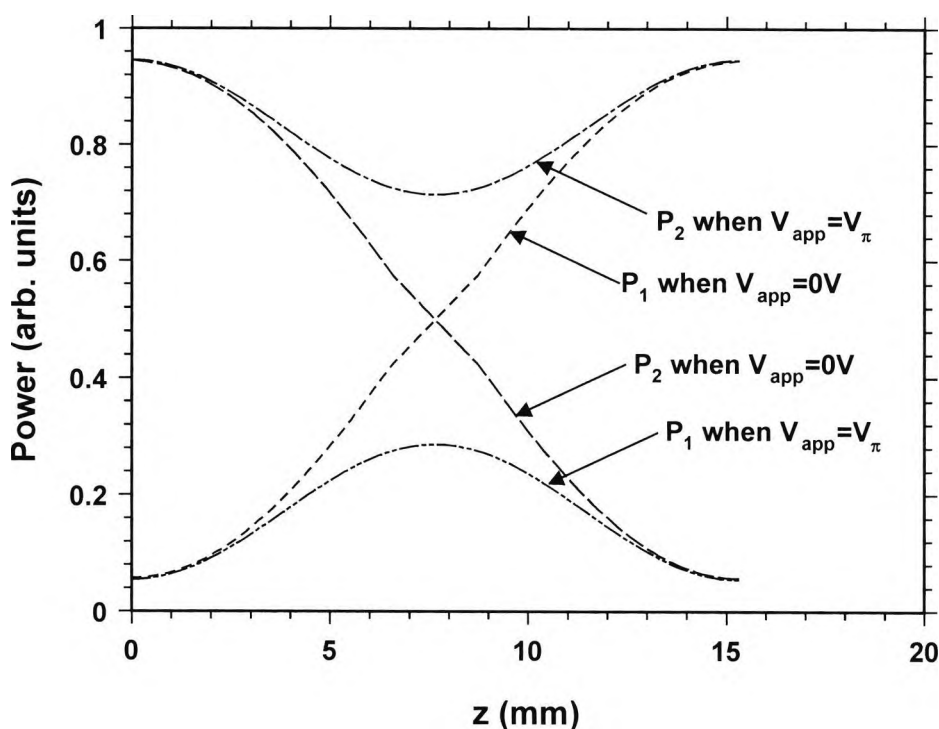


**Fig. 4.25** The variation in power in guide 1,  $P_1$ , and in guide 2,  $P_2$ , with  $z$ , for no applied voltage and an applied voltage of  $V_\pi$  ( $z$  is varied from 0 to  $L_{c0}$ ).

$z=2L_{c0}$  the power is mainly in guide 2 again. It is assumed that the waveguides are lossless, that there is no variation in the device along  $z$ .

$P_1(z)$  and  $P_2(z)$  for the case when a voltage of  $V_\pi$  is applied to the directional coupler modulator shown in Figs. 4.1 and 4.2, such that there is a phase shift of  $\pi$  between the light output from the device and that input to the device, are shown by the dash-dotted line in Fig. 4.25. As mentioned earlier, for the case of no applied voltage the power in both guides varied from zero to almost unity along  $z$ . For the case of an applied voltage of  $V_\pi$ , only approximately 25% of the light launched in guide 2 is transferred to guide 1. This is due to the phase mismatching that occurs in the uniform electrode  $\Delta\beta$  directional coupler modulator as a consequence of applied voltage. Also, maximum power transfer from guide 2 to guide 1 occurs for  $z=L_c=L_{c0}$  and the power completely returns to guide 2 by the distance  $z=2L_c=L_{c0}$ . The mode profiles in Fig. 4.27 show the majority of power to be in guide 2 at  $z=0$ . At  $z=L_c=L_{c0}/2$  there is a small transfer of power into guide 1 but the majority of power remains in guide 2, and at  $z=2L_c=L_{c0}$  the power is again almost completely in guide 2.

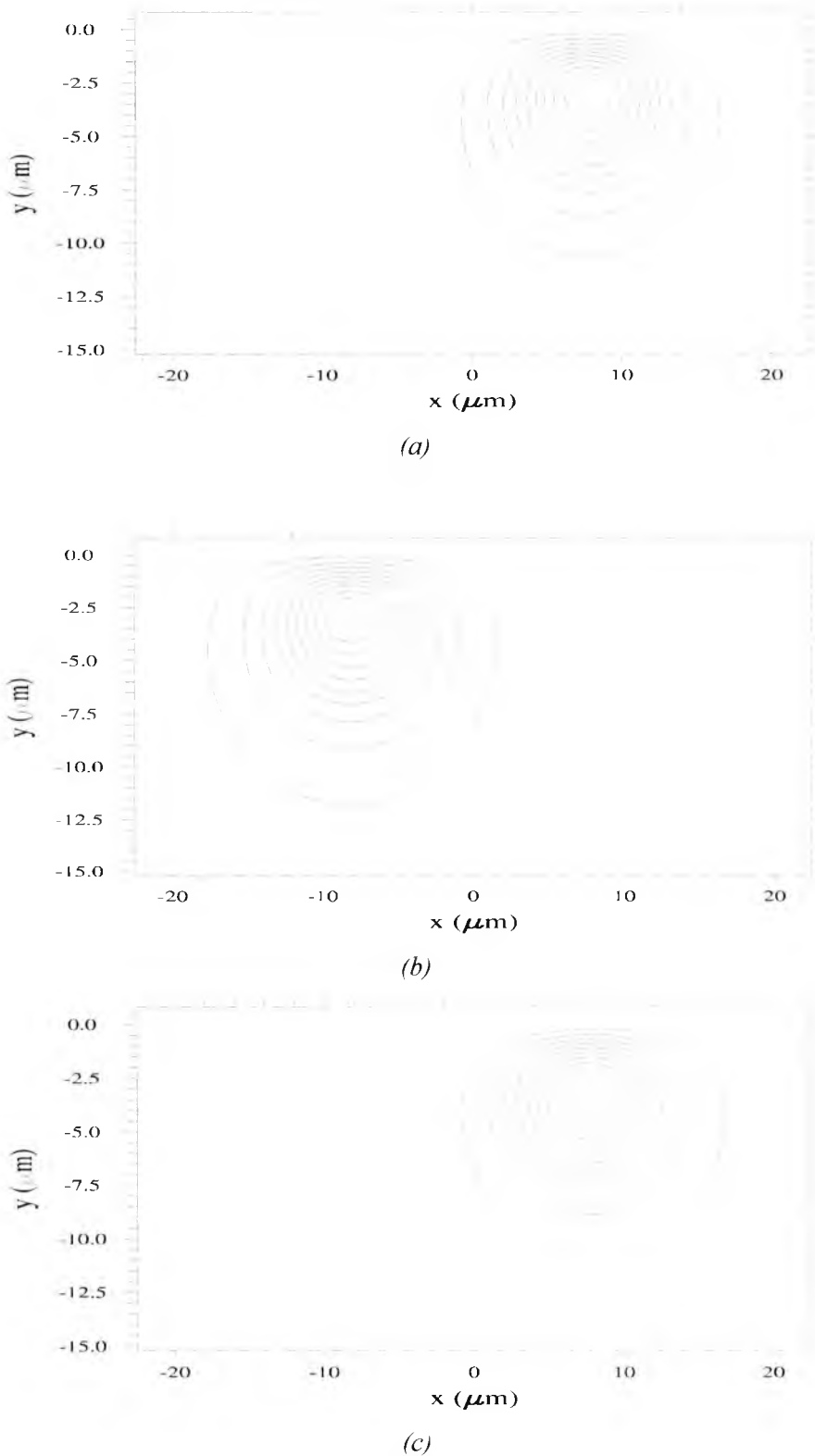


**Fig. 4.26** Mode profile for the  $\text{Ti}:\text{LiNbO}_3$  directional coupler modulator for no applied voltage at (a)  $z=0$ , (b)  $z=L_{c0}$ , (c)  $z=2L_{c0}$ .

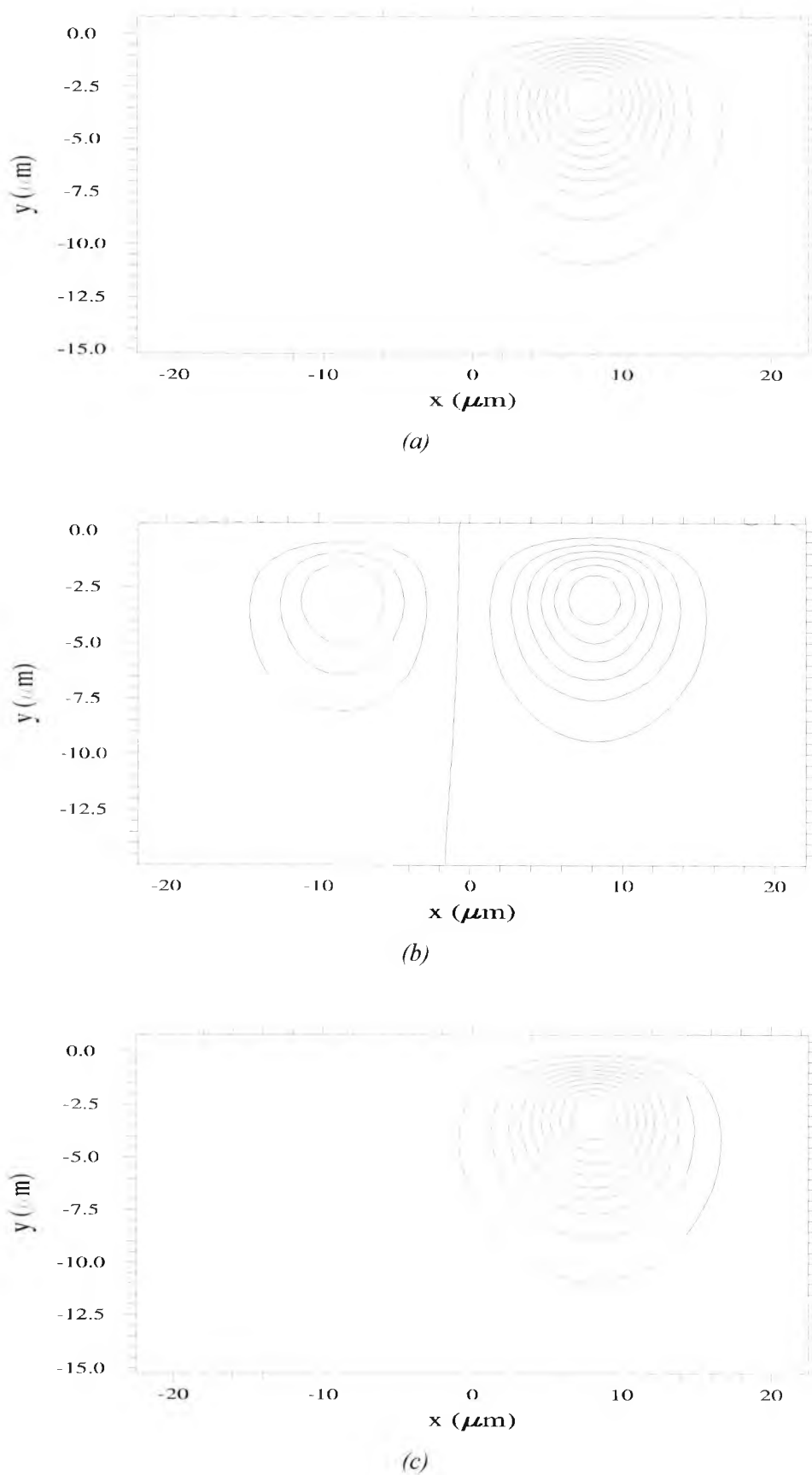


**Fig. 4.27** Mode profile for the  $\text{Ti}:\text{LiNbO}_3$  uniform electrode  $\Delta\beta$  directional coupler modulator for an applied voltage of  $V_\pi$  at (a)  $z=0$ , (b)  $z=L_c=L_{c0}/2$ , (c)  $z=2L_c=L_{c0}$ .

The crosstalk of the device is defined as the undesired coupling from one channel to the other and can be expressed as

$$\text{crosstalk(dB)}=10 \log_{10}(P_1/P_2) \quad (4.48)$$

The crosstalk for this device at  $V=0$  is rather low at  $-12.43\text{dB}$  because of the strongly coupled guides. Moreover, crosstalk becomes much smaller (worse) with increasing voltage (see Figs. 4.28 and 4.29) or decreasing coupling lengths (Rajarajan *et al.*, 1999) because of the vastly unequal supermode coefficients (see Fig. 4.24). However, there are ways in which crosstalk can be improved for these directional coupler devices (e.g. (Korotky and McCaughan, 1986)).

The solid line in Fig. 4.28 shows the relationship between the maximum power transferable ( $P_{max}$ ) from guide 2 to guide 1 and applied voltage. The monotonic reduction of the maximum possible power,  $P_{max}$ , is due to the increase of phase mismatching with modulating voltage. Furthermore, the applied voltage also causes the

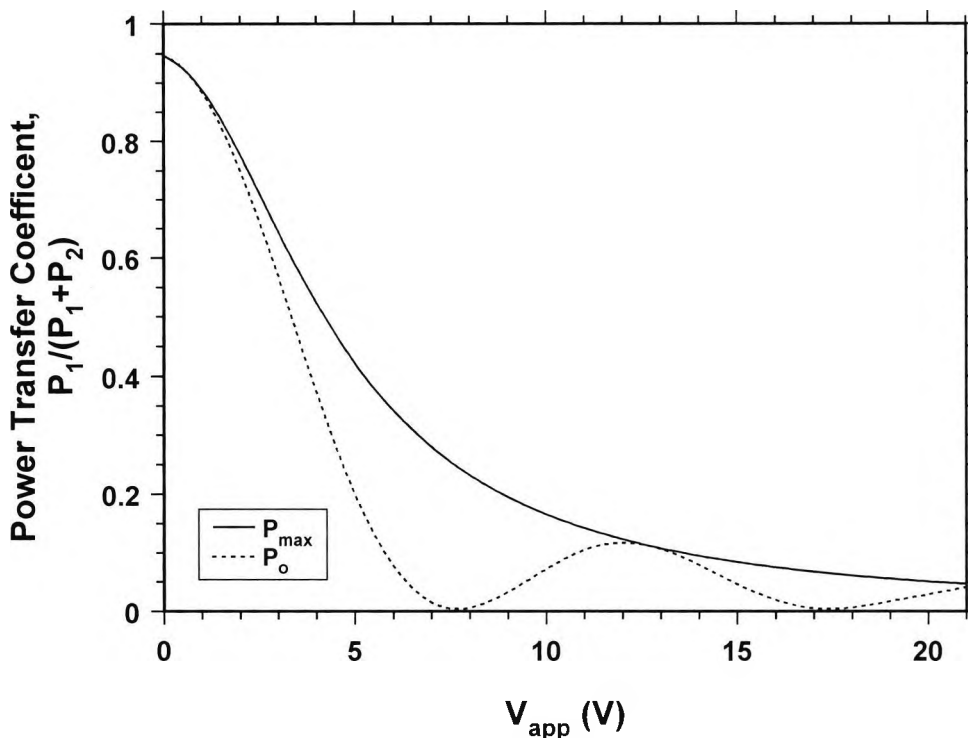
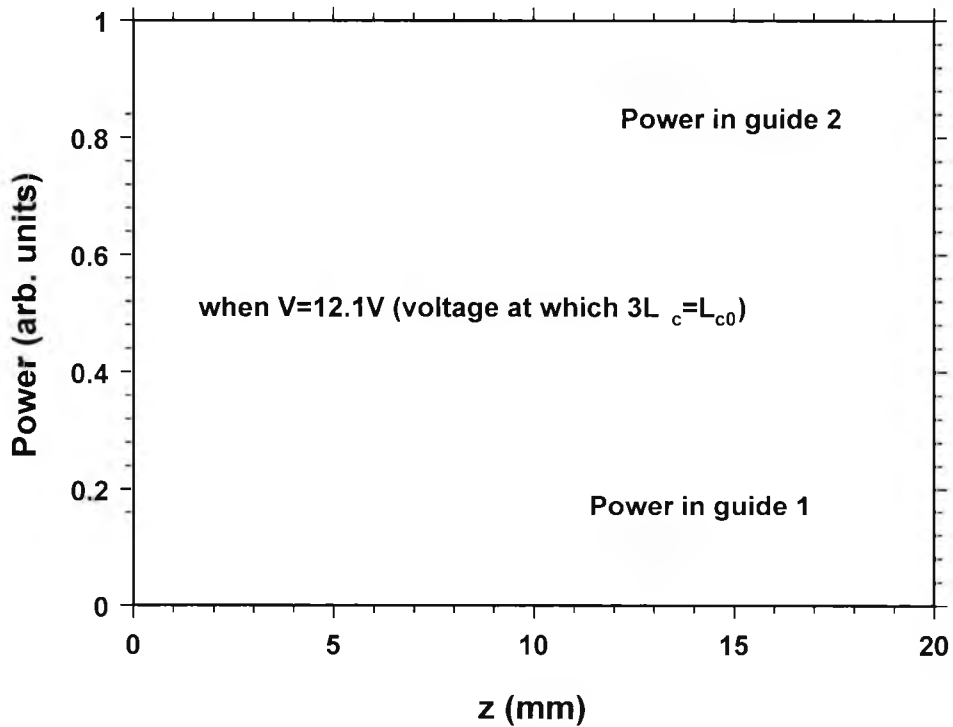


Fig. 4.28 Maximum power transfer from guide 2 to guide 1 of the  $\Delta\beta$  directional coupler, and the output power in guide 1 for a waveguide separation of  $7.5\mu\text{m}$ .

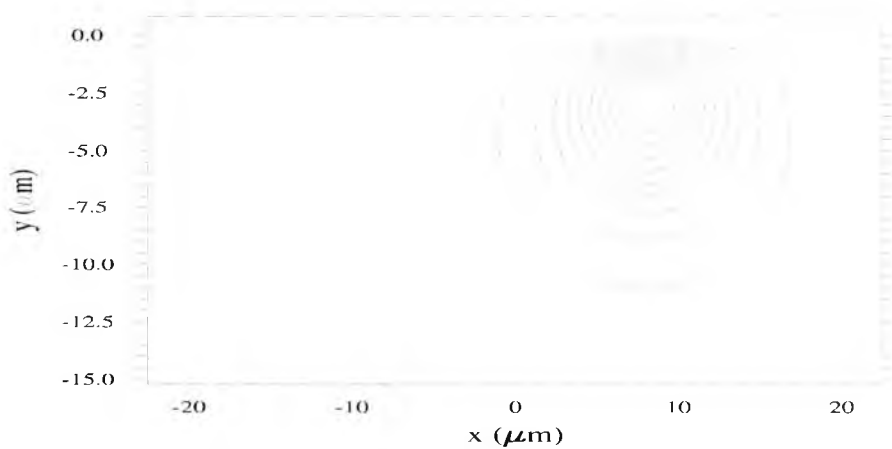
coupling length to change, and if the device length,  $L \neq L_{c0}$ , then the power output ( $P_o$ ) at the end of guide 1 will be even less than that at  $L = L_{c0}$  (i.e.  $P_{\max}$ ) due to the variation in power with the cosine of  $(\beta_e - \beta_o)z$  (see equation (4.46)) and this is shown by the dotted line in Fig. 4.28. Furthermore, it can be reinforced, from this graph, that when the voltage  $V = V_\pi$  and  $L_c = L_{c0}/2 = L/2$ , all the possible amount of the power which was transferred to guide 2 from guide 1 (at  $z = L_c$ ) is now transferred back to guide 2 from guide 1 (at  $z = L = 2L_c$ ), leaving zero power in guide 1.

As observed in Fig. 4.28, the power transfer coefficient for the directional coupler modulator modelled in this study is 0.946 at  $V=0$ . Gu *et al.* (2002) obtained similar values for power transfer coefficients for a number of Ti:LiNbO<sub>3</sub> directional coupler modulator structures supporting single mode TM polarised light. As mentioned earlier, the directional coupler modulator, modelled for this study in the present chapter, also supported single mode light of this polarisation and so a suitable comparison can be made.

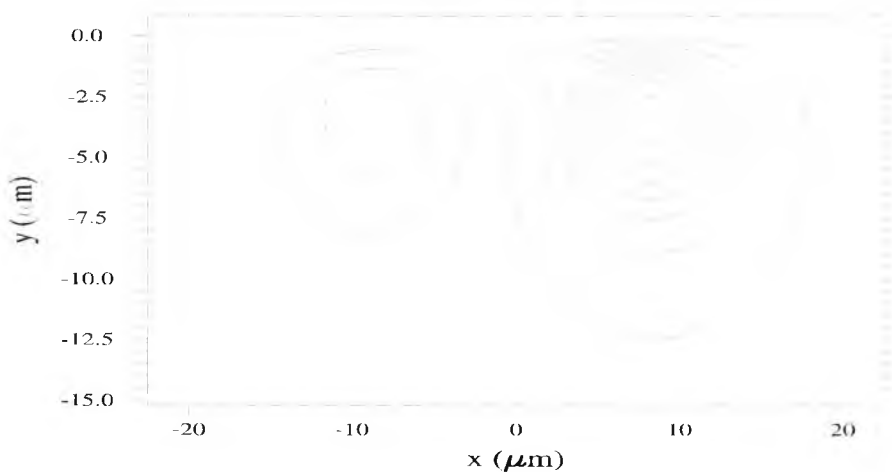


**Fig. 4.29** The variation in power in guide 1,  $P_1$ , and in guide 2,  $P_2$ , with  $z$  for an applied voltage of 12.1V ( $z$  is varied from 0 to  $L_{c0}$ ).

Similarly, at the second maxima in the curve for  $P_o$ , (i.e. at  $V=12.1V$ ), the maximum possible power is transferred back to guide 1 again at  $z=L=3L_c$ . However, this maximum value is much smaller than for  $z=L_c$  or  $z=2L_c$  due to the increased phase mismatching with increasing voltage. In fact this can be seen from both this figure (i.e. Fig. 4.28) and Fig. 4.29 that only approximately 10% of the light launched into guide 2 is transferred into guide, and this amount can be seen to vary with  $z$ . The power in guide 1 is minimum at  $z=0$ , maximum at  $z=L_c=L_{c0}/3$ , minimum again at  $z=2L_c=2L_{c0}/3$  and maximum again at  $z=3L_c=L_{c0}$ . This pattern is confirmed by the mode profiles given in Fig. 4.30. It is anticipated that a similar model for the reverse  $\Delta\beta$  electrode DC modulator may show a similar reduction in  $P_{max}$  with applied voltage. However, the amount cannot be known without a full study, as given here for the uniform electrode  $\Delta\beta$  directional coupler.



(a)



(b)

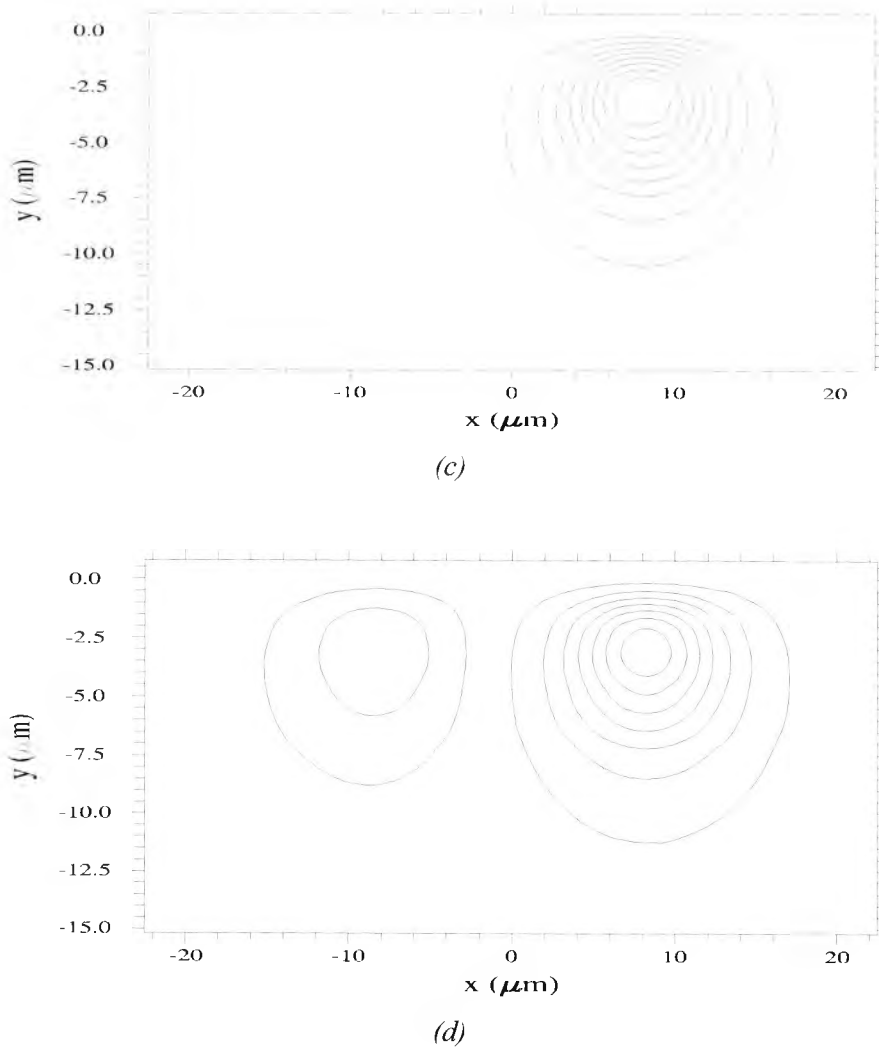


**Fig. 4.30** Mode profile for the Ti:LiNbO<sub>3</sub> uniform electrode  $\Delta\beta$  directional coupler modulator for an applied voltage of 12.1V at (a)  $z=0$ , (b)  $z=L_c=L_{c0}/3$ , (c)  $z=2L_c=2L_{c0}/3$ , (d)  $z=3L_c=L_{c0}$ .

## 4.9. Summary

A rigorous numerical approach based on the FEM has been developed and utilized in the simulation and optimisation of an electro-optic directional coupler based  $\Delta\beta$  modulator. In this case a particular type Z-cut titanium diffused example is considered in detail, but the approach is versatile enough for its application to a wider range of electro-optic modulators. A realistic diffusion profile has been considered and the effects of various fabrication parameters such as diffusion temperature, diffusion time, guide separation, electrode separation, electrode material, buffer layer material, buffer

layer thickness, crystal cut, guide width and device length have been studied. Moreover, the spatial distribution of the refractive index change due to the electro-optic effect has been considered.

In summary, the following observations have been made:

- the profile of the electric field is similar to those given by Ramer (1982)
- as the waveguides move closer together  $L_{c0}$  decreases (this is in agreement with experimental results given by Alferness *et al.* (1979))
- $V_{\pi}L_{c0}$  was 131.59Vmm for the structure modelled and was similar if not better than 150Vmm given by Veselka and Korotky (1986) for a similar structure with identical parameters.
- as  $\tau$  increases,  $L_{c0}$  increases (this is in agreement with Veselka and Korotky (1986)), but the optical mode size reduces (this is in agreement with Korotky and Alferness (1987)) – and so  $V_{\pi}$  is minimized for small optical modes (in agreement with Alferness (1988))
- $V_{\pi}L_{c0}$  increases with diffusion time and temperature (this is in agreement with Korotky and Alferness (1987))
- decreasing the electrode separation,  $e$ , would lead to increased overlap between the electric and optical fields, but this is known to cause an increase in the RF propagation loss of these devices (this is in agreement with Marcuse (1982) and Wooten and Chang (1993))
- an increase in buffer layer of 200nm was found to increase  $V_{\pi}$  by  $\sim 35\%$  and this is somewhat better than the 40% increase experimentally shown by Bulmer and Burns (1984)
- although the device performance improves with the reduction of the buffer layer thickness,  $d$ , the optical propagation loss increases.
- the effective index for TE and TM polarised light is slightly reduced due to the proximity of metal electrodes (this is in agreement with Duthie and Edge (1991))
- crosstalk becomes worse for increased applied voltage and therefore decreasing  $L_{c0}$  (this is in agreement with Rajarajan *et al.* (1999))
- power transfer coefficients of 0.946 for  $V=0$  have also been shown by Gu *et al.* (2002) for a number of DC modulators supporting single mode TM polarised light

The numerical approach developed here can now be used to design and optimise other practical electro-optic guided-wave modulator devices.

## *Ti:LiNbO<sub>3</sub> Interferometric Modulators*

---

---

### **5.1 Introduction**

The idea of the interferometric modulator originally came from bulk optics. The Mach-Zehnder interferometer, invented over one hundred years ago, was used monitor changes in refractive index and is still used for many optical measurements. However, the integrated optics version of this type of device offers many advantages over its bulk equivalent (Jaeger and Young, 1989; Kondo, 1993).

The first demonstration of an interferometric modulator using Ti-diffused LiNbO<sub>3</sub> strip waveguides was in the form of the balanced bridge modulator switch (Ramaswamy *et al.*, 1978). This is an analogue of the bulk Mach-Zehnder interferometer, and is now called a Mach-Zehnder modulator. The directional couplers, which act as 3dB couplers for the interferometric modulator, were replaced by Y-branches at both input and output (Auracher and Keil, 1980; Leonberger, 1980). However, such a device had first been proposed using ZnSe (Martin, 1975). Nevertheless, these two devices essentially operate on the same principles but with the Mach-Zehnder interferometric modulator having the advantage of routing signals from, (or to) either of the two input (or two output) ports. A more recent form of 3dB coupler can be achieved using a multimode

interference (MMI) device (Sakamoto *et al.*, 1999). However, these devices have been fabricated using semiconductor material.

The theory of interferometric modulators will be given in the next section. From this it should be clear that these devices are preferable to directional coupler-based modulators for high-speed devices (Wooten *et al.*, 2000). High bandwidths have been achieved using travelling wave electrodes, using the radio frequency (rf) techniques of velocity and impedance matching. However, early attempts yielded bandwidths of typically 12GHz (Kawano *et al.*, 1989). These were increased to ~20GHz using a shielding plane over the surface of the device and further increased to 44GHz by using narrow ground electrodes (Dolfi and Raganath, 1992). It was not really until the introduction of etched ridge Ti:LiNbO<sub>3</sub> waveguides that the very promising results for bandwidths (3dB electrical) of 75GHz (Noguchi *et al.*, 1998) were obtained. Even though there is a trade-off between bandwidth and drive voltage due to the length of the device, the drive voltage for the ridged waveguide interferometer is smaller than, and therefore an improvement on, its channel waveguide counterpart. This is due to tighter mode confinement (Ashley *et al.*, 1989) as a consequence of the ridge waveguide, which can also be realised by obtaining a higher peak refractive index change due to the Ti indiffusion into the LiNbO<sub>3</sub> substrate. However, this problem can be further alleviated if the overlap between the optical and electrical fields could somehow be maximised in order that the device length can then be shortened and hence bandwidth increased, which may be achieved with device design or electrode design: hence, the purpose of this study. The underlying principle of operation for these Ti:LiNbO<sub>3</sub> devices remains to be the linear electro-optic effect.

One of the greatest areas of loss particularly for the Y-branch modulators is the radiation through the bends in the waveguides. It is therefore beneficial to keep the Y-branch angles small (typically <1°) in order to minimise losses. The finite element method on its own is not enough to model the radiation losses due to these bends and so it can be used in conjunction with the beam propagation method. This is one of the most effective and accurate methods for such purposes (Rajarajan *et al.*, 2000). It will be seen that the bending losses can be optimised with etch depth of the ridged Ti:LiNbO<sub>3</sub> waveguides, as can be also attained for the drive voltage. In fact it is possible to further optimise the drive voltage by adjusting a number of fabrication parameters.

## 5.2 Theory of Interferometric Modulators

As mentioned earlier, interferometric modulators were superior to directional coupler devices in many ways. The better bandwidth-voltage performance of the interferometric modulator compared with the directional coupler based modulator is because of the lower electrical signal loss that can be attained with the interferometric modulator (particularly when used with RF electrodes) and also because the variation in the switching characteristics for directional couplers are not completely cyclic as for interferometric modulators. The lower electrical attenuation results from an electrode width and gap that is larger than is possible for the directional coupler (Heismann *et al.*, 1997).

Moreover, it possible to obtain a high extinction ratio for the interferometric modulator independent of the modulation drive frequency. This is not so for the directional coupler, which has an extinction ratio that is sensitive to local variations in the ratio of the phase-velocity difference to the coupling coefficient in addition to the global difference (McCaughan and Korotky, 1986).

The most basic and easiest to fabricate is the Y-branch structure, shown in Fig. 5.1. However, typically the voltage applied to the lower arm is  $-V$  instead of the  $0V$  shown in Fig. 5.1.

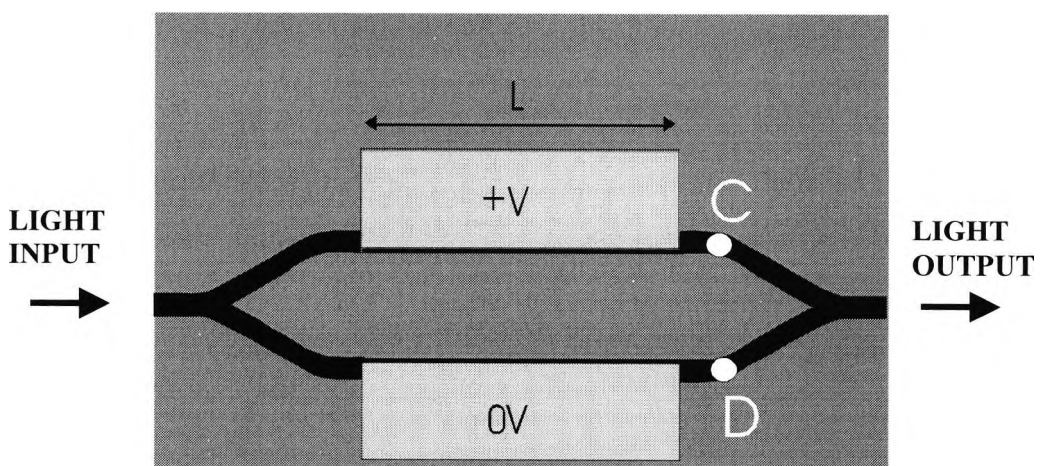


*Fig. 5.1 Structure for a Y Branch Modulator.*

As can be seen, it has only a single input port and a single output port. This configuration is named after the Y-shaped junctions that are used to split and recombine the optical power into and from both waveguide arms. Ideally, both the splitting and recombining is attained in equal amounts.

In this ideal situation the device works as described below. The incoming wave is then split equally via the power splitting Y branch, and each half of the optical power then propagates over each arm of the interferometer. The two waveguides that form the arms of the interferometer are separated such that no evanescent coupling can occur between the light in the two guides. The optical paths of the two arms are typically equal.

The operation of the Mach-Zehnder interferometer is primarily through the phase difference,  $\Delta\phi$ , obtained between the two arms of the device by application of a voltage, where

$$\Delta\phi = \Delta\beta.L \quad (5.1)$$

and  $\Delta\phi$  is the phase difference between the arms of the interferometer

$$\Delta\beta = \beta_1 - \beta_2$$

$\beta_{1,2}$  are the propagation constants in guides 1 and 2 respectively, and

$L$  is the electrode length

Without the application of a voltage to the device, no phase shift is induced between the interferometer arms since  $\Delta\beta=0$  and the two components of the input wave then combine in phase (constructively) via the output Y-branch, and then the output wave continues undiminished (compared to the input wave) in the output waveguide, i.e. the maximum amount (if not the 100% for the case of an ideal modulator) of light is transmitted for  $V=0$ . This is regarded as the ON state of the modulator (Heismann *et al.*, 1997).

When voltage is applied to the two arms via the electrodes shown in Fig. 5.1,  $\Delta\phi$  increases and decreases cyclically. However, when the voltage applied to the arms of the interferometer is such that there is a  $\pi$  phase shift between the light waves in the two waveguides, then as the two components of the input wave combine (destructively) at the Y-branch, most of the light is radiated into the substrate and a minimum amount of

light is transmitted at the output port. The extinction of the light at the output depends on the ideality of the modulator. This is regarded as the OFF state of the modulator (Heismann *et al.*, 1997).

The cyclic behaviour of the output intensity of the modulator can be seen by the equation

$$I = I_0 \cos^2\left(\frac{\Delta\phi}{2}\right) \quad (5.2)$$

where  $I_0$  is the maximum output power in the absence of modulation voltage.

From equation (5.1) this can be written as

$$I = I_0 \cos^2\left(\frac{\Delta\beta L}{2}\right) \quad (5.3)$$

but since

$$\beta = kn_{eff} = \frac{2\pi}{\lambda} n_{eff} \quad (5.4)$$

where  $k$  is the freespace wavenumber ( $=2\pi/\lambda$ )

and  $n_{eff}$  the effective refractive index of the guide,

equation (5.2) can now be written as (Heismann *et al.*, 1997)

$$I = I_0 \cos^2\left(\frac{\pi\Delta n_{eff} L}{\lambda}\right) = I_0 \cos^2\left(\frac{\pi}{2} \cdot \frac{V}{V_\pi}\right) \quad (5.5)$$

where  $V_\pi$  is the half wave voltage (i.e. the voltage at which the phase shift between the optical field in the is  $\pi$  radians) or drive voltage.

From equations (5.2)-(5.5) it can be seen that the Y-junction modulator is sensitive to the induced phase difference between the waveguide arms. Moreover, these equations show how the electrooptic phase modulation is converted into amplitude modulation, an important characteristic of these dual guide electrooptic waveguide modulators.

Furthermore, since the two Y-branches of this interferometer should provide balanced power splitting and recombining, the power is divided in half, which in terms of decibels (dB) is a lowering of power by 3dB. Hence the Y-branch located near the input of the device is termed a 3dB splitter and the Y-branch located near the output of the device is termed a 3dB combiner (Alferness, 1988).

In fact because of its single input and single output this modulator can sometimes be referred to as an on/off modulator. However, other on/off modulators also include modulators based upon other devices such as active Y-branches (Leigh, 1996), cutoff modulators (Neyer and Sohler, 1979) and polarisation TE↔TM modulators (Alferness, 1979a). The important modulator characteristics for these devices are the on/off extinction ratio, required drive voltage, the modulator speed or bandwidth and chirp.

In the nonideal case the power division by the Y branches may be unequal. If the power division of the first Y branch is given by a ratio of  $a^2:1-a^2$  (Heismann *et al.*, 1997), by ignoring any losses due to the change in direction of the guide and propagation losses in the guide, the field at points C and D (in Fig. 5.1) is given by

$$E_C = aE_m e^{j\Delta\phi_1} \quad (5.6)$$

and

$$E_D = \sqrt{1-a^2} E_m e^{j\Delta\phi_2} \quad (5.7)$$

where  $E_m$  is the electric field component of the input optical field,  $\Delta\phi_1$  is the electrooptically induced phase change in the first arm and  $\Delta\phi_2$  is the electrooptically induced phase change in the second arm.

Now, if the power division of the second Y branch is given by a ratio of  $b^2:1-b^2$  (Heismann *et al.*, 1997), the output field can be described by

$$E_{out} = bE_C + \sqrt{1-b^2} E_D \quad (5.8)$$

$$E_{out} = E_m \left\{ a b e^{j\Delta\phi_1} + \sqrt{1-a^2} \sqrt{1-b^2} e^{j\Delta\phi_2} \right\} \quad (5.9)$$

Now in the case of an ideal split

$$a^2 = 1 - a^2 = 1/2$$

$$b^2 = 1 - b^2 = 1/2$$

$E_{out}$  becomes

$$E_{out} = \frac{E_m}{\sqrt{2}} \left\{ e^{j\Delta\phi_1} + e^{j\Delta\phi_2} \right\} \quad (5.10)$$

this can be rewritten as

$$E_{out} = E_m \left[ e^{j(\Delta\phi_1 + \Delta\phi_2)/2} \right] \cos[(\Delta\phi_1 - \Delta\phi_2)/2] \quad (5.11)$$

now if  $\Delta\phi_2 = -\Delta\phi_1$ , giving total phase difference between the two arms of  $2 \Delta\phi_1$  then

$$E_{out} = E_m \cos(\Delta\phi_1) \quad (5.12)$$

From the Poynting vector

$$\mathbf{P} = \mathbf{E} \times \mathbf{H} \quad (5.13)$$

it can be seen that  $P \propto E^2$ , and so it is possible to see the similarity between equation (5.12) and (5.2).

In fact the splitting ratio of the Y-junctions plays an important role in determining the extinction ratio of the device. If the splitting ratio for the two Y-junctions is as mentioned above,  $a^2:1-a^2$ , for the first Y branch and an ideal splitting of  $1/2:1/2$  for the second Y branch, with  $a^2=1/2+\varepsilon$ , it has been shown that the extinction ratio (ER) of the device in dB is  $-10\log_{10}(\varepsilon^2/2)$  (Heismann *et al.*, 1997). This shows that a splitting ratio in the first arm cannot be worse than 0.545:0.455 in the first Y branch if the overall extinction ratio of the Y-branch modulator is to be greater than 30dB. The performance of these devices is inextricably linked by the electrode length and high bandwidths are obtained with shorter lengths whereas low drive voltages are obtained with longer electrodes. This is true for all electro-optic modulators and so the Y-branch modulator follows the same principles.

Similarly, there may be inequalities between the lengths of the two arms of the interferometer. This will lead to a built-in or intrinsic phase-difference. Analogue applications, require the device to be biased at the centre of the linear part of the transfer function of the Y-junction modulator. For the simple structure shown in Fig. 5.1, this can be achieved with the addition of an initial or intrinsic phase difference between the interferometer arms of  $\pi/2$ , which can be simply realised by increasing the length of one interferometer arm by  $\lambda_g/4$  with respect to the other arm (Bulmer and Burns, 1984). This idea will be used for part of this study, in Section 5.7 of this chapter.

The Y-branch modulator detailed above can also be described as a 1x1 Mach-Zehnder modulator, named after its bulk optic equivalent the Mach-Zehnder interferometer. The term 1x1 refers to the modulator having a single input and a single output. However, either or both the Y-branches can be replaced by 3dB directional couplers or MMI-based 3dB couplers, in which case there are then two inputs and/or outputs.

In the case of the output Y-branch being replaced by the 3dB directional coupler, the device is referred to as a 1x2 Mach-Zehnder switch-modulator (Heismann *et al.*, 1997). This device is more advanced in that the light can be switched between two output waveguides instead of switching between maximum light output or light being lost in the substrate. Otherwise the principle of operation of these devices is essentially the same as for the Y-branch modulator.

The device that is mostly referred to as a Mach-Zehnder interferometric modulator is the 2x2 Mach-Zehnder modulator, where both input and output Y-branches have been replaced by 3dB directional couplers. This again works on the same principle as the Y-branch modulator, only for this device the light can be input using either one of the two inputs of the directional coupler and can be output from either of the two outputs. Again this device is attractive for routing and multiplexing, as was the 1x2 Mach-Zehnder interferometer.

Another option is a multimode interference (MMI)-based 3 dB splitter (Soldano and Pennings, 1995). Generally this device consists of a centre region that is a multimode waveguide and limited in both lateral and transverse dimensions. The MMI coupler is much smaller than the other two options. However, the Y-branch is a much simpler device. Moreover, MMI couplers have been fabricated in only semiconductor materials (Sakamoto *et al.*, 1999), whereas the Y-branch and directional couplers have been successfully realised in a large range of materials.

### **5.3 The Comparison Between An Unetched Channel Waveguide And An Etched Ridge Waveguide**

In Chapter 3 the various etching techniques for the fabrication of ridge waveguides in lithium niobate were detailed. Of these methods Barry *et al.* (1999) noted that the titanium diffused lithium niobate waveguides yielded the best results for propagation losses in straight guides. However, the etching was achieved following spatially selective domain inversion and not the standard dry etching methods of ion milling (Burns *et al.*, 1999), reactive ion etching (Winnall and Winderbaum, 2000) or ECR

plasma etching (Mitsugi *et al.*, 1998). Using ion milling gave an additional waveguide loss of only 0.1-0.2dB/cm when compared with channel waveguides without etched ridges. However, Noguchi *et al.* (1995) attribute a 0.3-1dB excess propagation loss due to the roughness of the sidewalls of the ridges.

Although dry etching is used mainly to attain straight sidewalls, in the case of the three methods mentioned above, sidewalls of between 55° (Winnall and Winderbaum, 2000) and 85° (Burns *et al.*, 1999) were actually obtained. This last result is reasonably close to 90°. Noguchi *et al.* (1995) used a straight sidewall for their quasi-TEM analysis and found that the results were closely matched with experimental results. This supports the case for use of vertical cavity walls within the model. However, a widening ridge would be obtained with slanted sidewalls and this would couple the incoming light from the single mode fibre more efficiently.

### 5.3.1 Structure for a Single Guide

The first structure to be investigated in this study is that of a single waveguide, shown in Fig. 5.2. The refractive indices of the structure are as shown where  $n_a$  is the refractive index of air, with a value of 1, the refractive index of the silicon dioxide (also known as silica) buffer layer,  $n_b$ , was found to have a value of 1.46 for a wavelength of operation

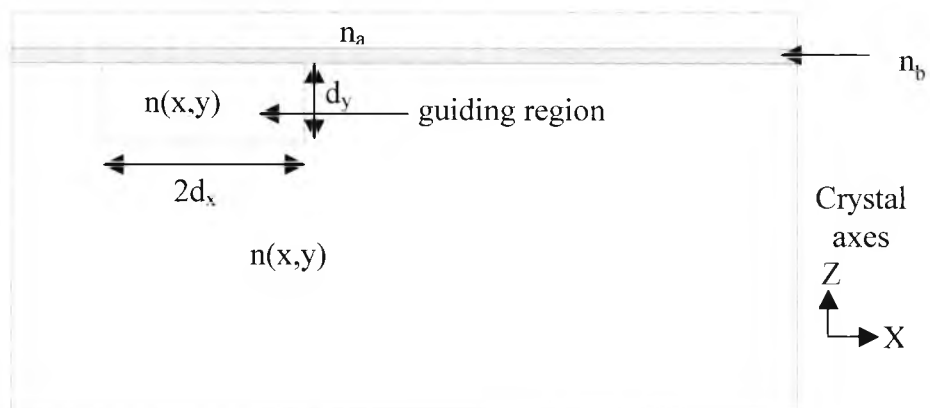


**Fig. 5.2** The structure of the unetched Ti:LiNbO<sub>3</sub> channel waveguide.

of 1.55 $\mu$ m and the region where the Ti has been diffused into the LiNbO<sub>3</sub> crystal is represented by the refractive index profile,  $n(x,y)$ , which is generally described in terms of the exponential function ( $exp$ ) and the error function ( $erf$ ) (Wooten and Chang, 1993). This is given by

$$n(x,y) = n_s + \Delta n * f(y) * h(x) \quad (5.14)$$

where

$$f(y) = \exp\left(-\frac{y^2}{d_y^2}\right) \quad (5.15)$$

$$h(x) = g\left(x - \frac{w}{2} - \frac{p}{2}\right) + g\left(x + \frac{w}{2} + \frac{p}{2}\right) \quad (5.16)$$

$$g(x) = \frac{1}{2} \left[ \operatorname{erf}\left(\frac{w/2 + x}{d_x}\right) + \operatorname{erf}\left(\frac{w/2 - x}{d_x}\right) \right] \quad (5.17)$$

$n_s$  = the refractive index of the LiNbO<sub>3</sub> substrate

$\Delta n$  is the maximum change in refractive index of the LiNbO<sub>3</sub> due to titanium diffusion

and

the diffusion lengths given by

$$d_{x,y} = 2\sqrt{D_{x,y}t} \quad (5.18)$$

$$D_{x,y} = D_o^{x,y} \exp\left(-\frac{E_o^{x,y}}{kT}\right) \quad (5.19)$$

where

$D_o^{x,y}$  are the diffusion constants along the  $x,y$  axes, and depend on the crystal cut (Fukuma and Noda, 1980)

$E_o^{x,y}$  are the activation energies in the  $x, y$  directions

$p$  = gap between the two guides of the modulator (edge to edge – see Figs. 5.18 & 5.19)

and

$w$  = width of the titanium layer prior to diffusion.

For this single waveguide structure  $h(x) = g(x)$ .

Since LiNbO<sub>3</sub> is a uniaxially anisotropic crystal, the refractive index is viewed as  $n_e$  (the extraordinary refractive index) along the optic axis of the crystal (usually taken along the  $Z$  axis of the crystal) and  $n_o$  (the ordinary refractive index) along the other two axes. The  $Z$  and  $X$  axes of the  $Z$ -cut  $Y$ -propagating LiNbO<sub>3</sub> crystal are clearly labelled in Fig. 5.2.

The refractive index of the LiNbO<sub>3</sub> crystal are calculated using the Sellemeier equations (Hobden and Warner, 1966):

$$n_e^2 = 4.5820 + 0.099169/(\lambda^2 - 0.04443) - 0.02195\lambda^2 \quad (5.20)$$

$$n_o^2 = 4.9048 + 0.11768/(\lambda^2 - 0.04750) - 0.027169\lambda^2 \quad (5.21)$$

where  $n_{e,o}$  is  $n_s$  in equation (5.14).

For  $\lambda=1.55\mu\text{m}$ ,  $n_e=2.138$ ,  $n_o=2.211$ .

The expressions for the change in refractive index due to Ti indiffusion,  $\Delta n_e$  and  $\Delta n_o$ , can be obtained from those given by Korotky and Alferness (1987), Fouchet *et al.* (1987) or Strake *et al.* (1988) as shown in Chapter 3. All sets of equations give a clear representation of the diffusion mechanism since most, if not all, of the diffusion parameters have been incorporated into these equations. However, researchers in this field have not conclusively identified the microscopic mechanism of the index change associated with the incorporation of Ti into the crystal (Korotky and Alferness, 1987), hence the need to choose with care the set of diffusion equations used to model the diffused refractive index profile of the Ti:LiNbO<sub>3</sub> structure/device under examination. The following section is an example of this.

### 5.3.1.1 Calculation of the Refractive Index Profile

The diffusion parameters taken for this particular structure are a diffusion temperature of 1000°C, a diffusion time of 10 hours, and the thickness,  $\tau$ , and width,  $w$ , of the titanium (Ti) layer prior to diffusion of 0.09 $\mu\text{m}$  and 6 $\mu\text{m}$ , respectively (Noguchi *et al.*, 1995). The operating wavelength is 1.55 $\mu\text{m}$ . As before, for a Z-cut LiNbO<sub>3</sub> crystal,  $D_o^x=7.37\times 10^{-7}\text{cm}^2/\text{s}$ ,  $E_o^x=1.48\text{eV}$  (Fukuma and Noda, 1980),  $D_o^y=0.023\text{cm}^2/\text{s}$ ,  $E_o^y=2.61\text{eV}$  (Veselka and Korotky, 1986). From equation (5.18),  $d_x=3.831\mu\text{m}$ ,  $d_y=3.923\mu\text{m}$ . These two diffusion lengths are very similar in value – a fact which is in agreement with Wooten and Chang (1993).

The peak extraordinary index change can be described by (Korotky and Alferness, 1987)

$$\Delta n_e = b(\lambda)C_0 \quad (5.22)$$

where

$$b(\lambda)=0.552+0.065/\lambda^2 \quad (5.23)$$

$$C_0 = \frac{2}{\sqrt{\pi}} \frac{\tau}{d_y} \operatorname{erf}\left(\frac{w}{2d_x}\right) \quad (5.24)$$

Using the diffusion lengths obtained from above, this gives  $\Delta n_e=0.01097$ .

This is considerably low for  $\Delta n_e$ , for this structure, as the values obtained by Koshiha *et al.* (1999) are of a much higher value of 0.0146. In fact the diffusion equations used to obtain  $\Delta n_e$  in that paper were based on those given by Strake *et al.* (1988). The value for the effective refractive index of the guide,  $n_{eff}$ , obtained by Noguchi *et al.* (1995) of 2.15 points to a still higher value of  $\Delta n_e$  (through the titanium layer thickness) (Korotky and Alferness, 1987) than obtained by obtained by Koshiha *et al.* (1999), as the value of  $n_{eff}$  obtained by Koshiha *et al.* (1999) is given by 2.142. If the refractive index of the guiding region is high, the size of the mode is smaller than the size of the waveguide and the mode size does not reduce any further because the overlap between the optical mode and waveguide is good. Nevertheless, this argument is not conclusive as there are other factors, mainly involved with the numerical modelling method, which could also lead to an increase in  $n_{eff}$ , such as a smaller mesh (see Table 5.1). It should be noted here that the effective index values quoted from Noguchi *et al.* (1995) and Koshiha *et al.* (1999) are for etched waveguide MZIs and should be lower than for the channel waveguides. This is because the etched ridge waveguides are surrounded by a lower index material (i.e. SiO<sub>2</sub> and air) than LiNbO<sub>3</sub> and so reduce the overall effective index. However, the same principle of higher value for the effective refractive index of the guide,  $n_{eff}$ , pointing to a much higher value of  $\Delta n_e$  applies to both channel waveguides and ridged waveguides.

The peak extraordinary index change described by Strake *et al.* (1988) are given below:

$$\Delta n_e = d_e(\lambda)EC_0 \quad (5.25)$$

$$\Delta n_o = d_o(\lambda)(FC_0)^{0.55} \quad (5.26)$$

where

$$d_e(\lambda) = \frac{0.839\lambda^2}{\lambda^2 - 0.0645} \quad (5.27)$$

$$d_o(\lambda) = \frac{0.67\lambda^2}{\lambda^2 - 0.13} \quad (5.28)$$

$$C_o = \frac{1}{a} \frac{\tau}{d_y} \quad (5.29)$$

$$E = 1.2 \cdot 10^{-23} \text{ cm}^3$$

$$F = 1.3 \cdot 10^{-25} \text{ cm}^3$$

$$a = 1.56 \cdot 10^{-23} \text{ cm}^3 \text{ (Bulthuis, 1998)}$$

This gives the result of  $\Delta n_e = 0.0152$  and  $\Delta n_o = 0.00636$ .

However, for a recent software application produced by Alcatel for modelling interferometric-based modulators, where the diffusion model is based on the above equations first proposed by Strake *et al.* (1988), the values for  $E$  and  $F$  are given as  $E = 1.56 \cdot 10^{-23} \text{ cm}^3$  and  $F = 1.3 \cdot 10^{-25} \text{ cm}^3$  (Bulthuis, 1998), which gives  $\Delta n_e = 0.0198$  and  $\Delta n_o = 0.00609$ .

This last set of values of peak index change (associated with the Ti indiffusion) appears to be rather high, while the previous set of values appears to be lower than expected from the modulator fabricated by Noguchi *et al.* (1995). It was therefore considered that perhaps the average of the two values for both extraordinary and ordinary refractive index change (in this case  $\Delta n_e = 0.0175$  and  $\Delta n_o = 0.00623$ ) may give a value closer to that for the real structure.

Lastly, another method to calculate the peak index change due to the Ti indiffusion into the LiNbO<sub>3</sub> crystal has also been described by Fouchet *et al.* (1987) and are given below:

$$\Delta n_{e,o} = [B_0(\lambda) + B_1(\lambda) \cdot \tau/d_y] \left( \tau/d_y \right)^{\alpha_{e,o}} \quad (5.30)$$

where

for  $n_e$ :

$$B_0(\lambda) = 0.385 - 0.43\lambda + 0.171\lambda^2 \quad (5.31)$$

$$B_1(\lambda) = 9.13 + 3.85\lambda - 2.49\lambda^2 \quad (5.32)$$

for  $n_o$ :

$$B_0(\lambda) = 0.0653 - 0.0315\lambda + 0.00709\lambda^2 \quad (5.33)$$

$$B_1(\lambda) = 0.478 + 0.464\lambda - 0.348\lambda^2 \quad (5.34)$$

and

$$\alpha_e \sim 0.78, \alpha_o \sim 0.5$$

This gives  $\Delta n_e = 0.0178$  and  $\Delta n_o = 0.00633$ .

This value of  $\Delta n_o$  is very close to that obtained from the set of equations and fitting parameters given by Strake *et al.* (1988), whereas this value of  $\Delta n_e$ , which is slightly higher than the value given by Strake *et al.* (1988), is close to the value obtained from an average of the fitting parameters given by both Strake *et al.* (1988) and Bulthuis (1998).

The fact that these last two sets of equations, given by Strake *et al.* (1988) and Fouchet *et al.* (1987), did not consider the width of the titanium layer prior to diffusion,  $w$ , in the calculation for  $\Delta n_{e,o}$  is not a truly accurate picture for the diffusion process, however, the first set of equations given by Korotky and Alferness (1987) – which consider  $w$  – give too low a value to be acceptable as being close to reality. Hence the necessity of taking one of the last two sets of equations (Strake *et al.*, 1988; Fouchet *et al.*, 1987) as a model for the change in refractive index of LiNbO<sub>3</sub> due to Ti indiffusion. However, both these sets of equations come with limitations: those given by Strake *et al.* (1988) are well approximated in the region where the concentrations of the waveguides ( $C_0$ ) given by equation (5.30) are below  $0.5 \cdot 10^{21} \text{cm}^{-3}$  (which is not the case for this particular study/problem –  $C_0 = 1.47 \cdot 10^{21} \text{cm}^{-3}$ ) and those given by Fouchet *et al.* (1987) are true only for the range of wavelengths between  $0.6 \mu\text{m}$  and  $1.6 \mu\text{m}$  (which is the case for this particular study/problem).

So for this study, while it was possible to model the diffusion based on the equations given by Strake *et al.* (1988) or Fouchet *et al.* (1987), it was the latter of the two sets of equations (the model used by Fouchet *et al.* (1987)) that were chosen for the model used in this study, where  $\Delta n_e = 0.0178$  and  $\Delta n_o = 0.00633$  (for  $\alpha_e = 0.78$ ,  $\alpha_o = 0.5$ ).

### 5.3.2 The Optical Characteristics of the Waveguides

In Chapter 3 it was explained that since LiNbO<sub>3</sub> is a uniaxially anisotropic crystal, the refractive index is viewed as  $n_e$  (the extraordinary refractive index) along the optic axis of the crystal (usually taken along the  $Z$  axis of the crystal) and  $n_o$  (the ordinary

refractive index) along the other two axes. The example of structure to be used in this section is for Z-cut LiNbO<sub>3</sub>. This is because the etch rate of Z-cut LiNbO<sub>3</sub> is nearly double that for X-cut LiNbO<sub>3</sub> (Winnall and Winderbaum, 2000) and, therefore, deeper ridge heights can be obtained from Z-cut samples. For this crystal cut, as explained in Chapter 4, the maximum electro-optic change in refractive index occurs when the polarization of the light is quasi-TM. Hence, any dominant mode supported by the channel waveguide will be of the form  $H_x^{rq}$ . Moreover, it was found that for the structure detailed in Section 5.3.1.1 only the fundamental mode quasi-TM fundamental mode  $H_x^{11}$  is supported.

However, it was also necessary to determine a satisfactory mesh size for the vector H-field finite element solver. Variation of the propagation constant,  $\beta$ , with mesh size is

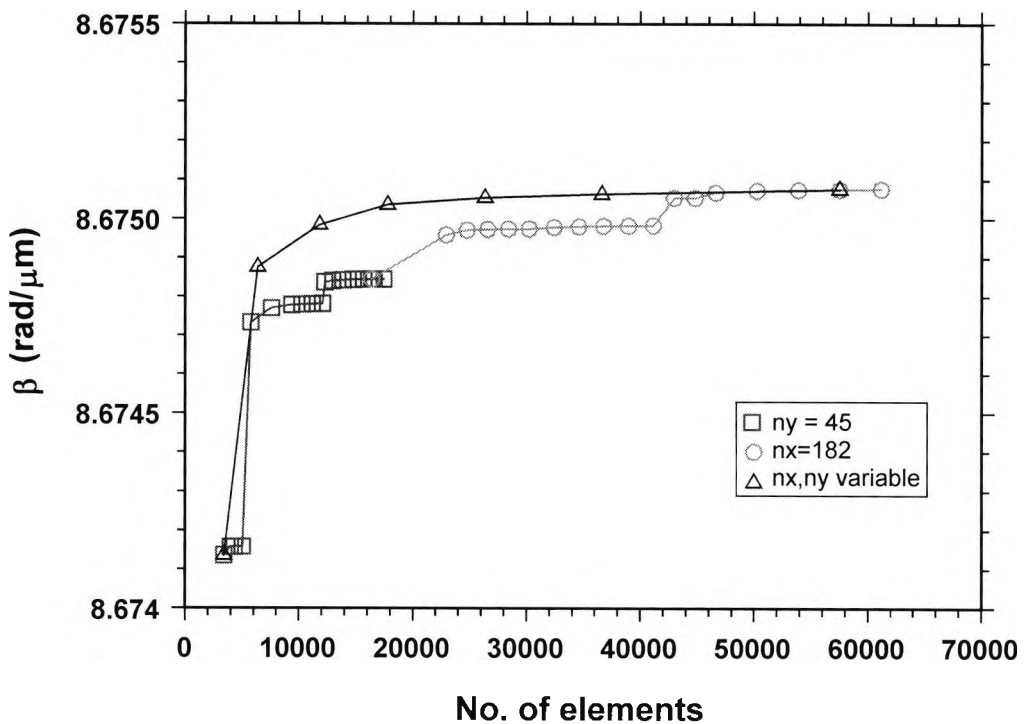


**Fig. 5.3**  $\beta$  vs no. of elements, for the cases when only  $n_x$  is changed (with  $n_y$  held constant), when only  $n_y$  is changed (with  $n_x$  held constant) and when both  $n_x$  and  $n_y$  are varied.

shown in Fig. 5.3. The three curves are self explanatory in that the one with the open square symbols is where the mesh size is varied but the number of divisions in the  $y$ -direction,  $n_y$ , are fixed at 45, the curve with the open circles represents the variation in  $\beta$  with mesh size for the case when the number of divisions in the  $x$ -direction,  $n_x$ , are

fixed at 182, and the curve with the open triangular symbols is for the case when neither the number of divisions in  $x$ ,  $n_x$ , nor the number of divisions in  $y$ ,  $n_y$ , are fixed at any value. Atkinson's interpolation formula could not be used because mesh size was not increased with a fixed geometric ratio (Rahman and Davies, 1985).

The increase in the number of elements leads to insignificant change in  $\beta$  with any further increase in number of elements greater than  $(2*101*88=)17776$  for which the corresponding value of  $\beta$  was 8.6750354. The highest number of elements used was  $(2*182*168=)61152$  for which the corresponding value of  $\beta$  was 8.6750765. This means that there is only a 0.004% increase between the two values. However, there was a 600% increase in CPU time when using the larger mesh. Hence,  $2*101*88$  elements were used throughout this part of the study.

The size of the guiding region is typically  $2d_x$  by  $d_y$ , since the diffusion in  $x$  can occur in either direction in  $x$ . For the mesh size chosen, the diffusion profile is given in Fig. 5.4. It can be seen from this diffusion profile that, as expected, any changes in the refractive index of the LiNbO<sub>3</sub> substrate occurs mainly in the guiding region shown in Fig. 5.2 of width  $2d_x$  in  $x$  and  $d_y$  in  $y$ . The thickness of the buffer layer is typically taken to be  $0.6\mu\text{m}$ , unless otherwise stated.

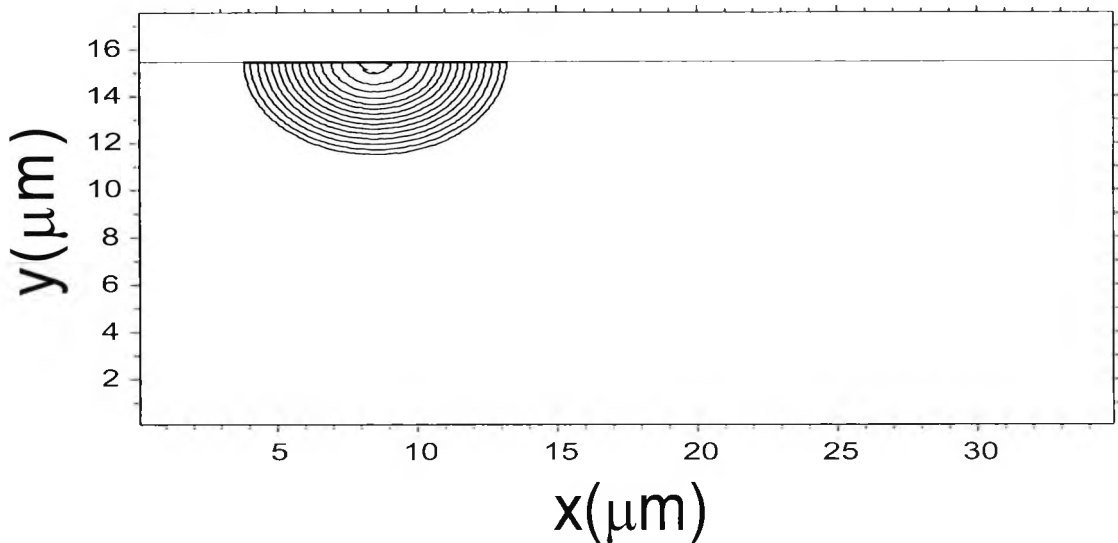


*Fig. 5.4 The diffusion profile of the single Ti:LiNbO<sub>3</sub> diffused channel waveguide.*

For TM-polarized light, the  $H_x^{11}$  is the (quasi-TM) fundamental mode, and this is shown in Fig. 5.5 for the unetched single guide structure. The (extraordinary) effective index of

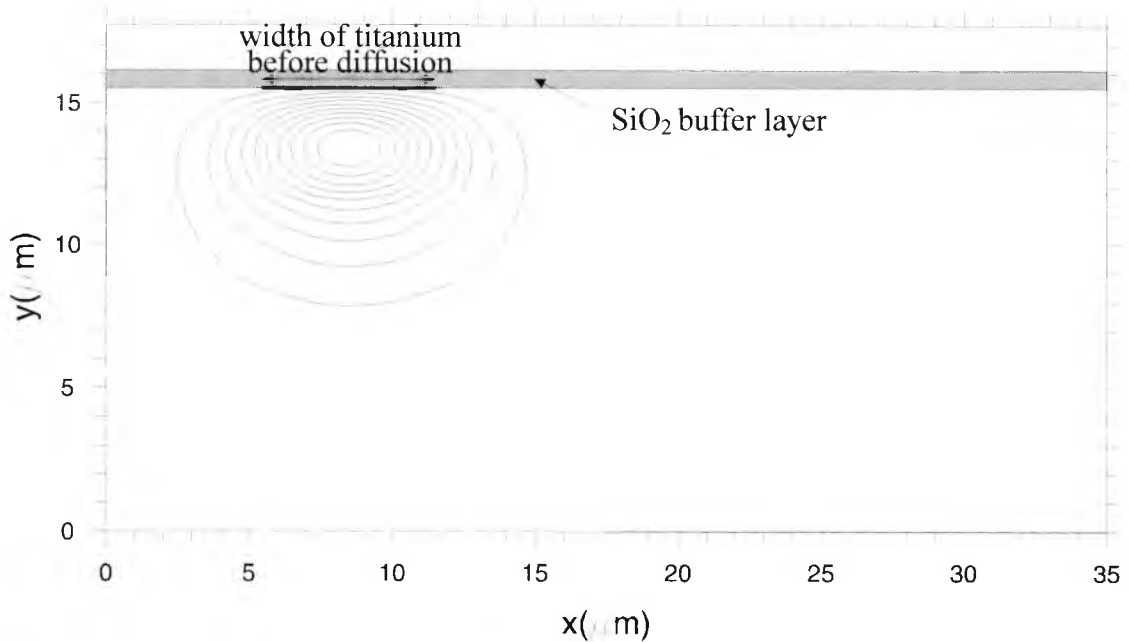
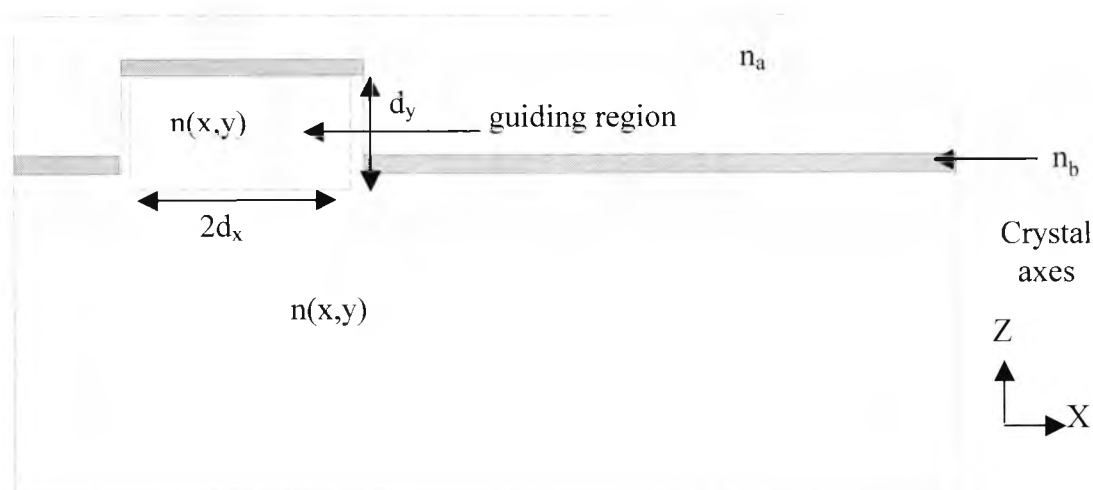


Fig. 5.5 Optical mode for the channel Ti:LiNbO<sub>3</sub> waveguide.

the guide,  $n_{eff}(=\beta/k_0)$ , where  $k_0$  is the freespace wavenumber, is 2.1400. Comparing this with the extraordinary LiNbO<sub>3</sub> substrate index,  $n_e=2.138$ , would indicate that the optical mode is operating near cutoff. Due to the fact that the waveguide index profile,  $n_{e,o}(x,y)$ , is diffused, the optical mode is not so well confined in the lateral dimension, but this is expected. However, the mode profile in Fig. 5.5 is larger than the guiding region. This again indicates that the device is operating very near to but slightly above the cutoff, as is indicated by the 1/e intensity full depth,  $w_y$ , of 4.36 $\mu\text{m}$ , which is larger than  $d_y$  ( $=3.923\mu\text{m}$ ) and the 1/e intensity full width,  $w_x$ , of 7.463 $\mu\text{m}$ , which is within a width of  $2d_x$  ( $=7.662\mu\text{m}$ ). This gives a mean mode size (defined by  $\sqrt{w_x w_y}$  (Alferness, 1988)) of 5.704 $\mu\text{m}$ . The value of the mode eccentricity, given by  $w_x/w_y$ , for this structure is 1.72, which is believed to indicate a well-confined, symmetric mode (Korotky and Alferness, 1987). It was found that the guide supports only the fundamental mode for each polarization. Therefore, the simulated device emulates single-mode operation near cutoff, which should essentially lead to low insertion loss (Veselka and Korotky, 1986). Furthermore, the width of the titanium strip prior to diffusion,  $w$ , influences the mode size (Korotky and Alferness, 1987), as seen in the previous chapter, where the mode size is at first reduced with increasing titanium strip width until a minimum is reached

and thereafter increases. This is however more true for  $w_x$  than  $w_y$ . The diffusion depth also controls the mode size (Korotky and Alferness, 1987). The thickness of the titanium layer, similar to the width of the titanium layer, prior to diffusion is at first responsible for decreasing the mode size with increasing thickness until a certain thickness, after which the mode size hardly changes and effective index of the mode supported by the resultant waveguide formed in the LiNbO<sub>3</sub> substrate increases (Korotky and Alferness, 1987). An increased change in refractive index with increasing titanium layer thickness, and the increased effective index of the mode, leads to smaller bending losses (for the bends which are present at the input and output of a multi-input device).

The only other way of improving bending losses is to use a ridged waveguide structure, shown in Fig. 5.6. For most electro-optic devices the use of a ridge waveguide structure generally confines the optical mode to the waveguide area and consequently improves device performance in a number of ways, as will be seen in subsequent sections. The etching procedure has been described in Section 3.2.1.1 of this thesis. The ridge height was taken to be 3.5 $\mu\text{m}$  (Noguchi *et al.*, 1995), and the ridge width was taken as 9 $\mu\text{m}$ . The thickness of the buffer layer for this structure was also taken to be 0.6 $\mu\text{m}$ .



**Fig. 5.6** The structure of the etched Ti:LiNbO<sub>3</sub> ridge waveguide.

The calculation of the refractive indices for the LiNbO<sub>3</sub> substrate and the Ti-indiffused region should be as for the channel waveguide. The mesh size used for modelling the etched ridge waveguide was the same as for the channel waveguide (i.e. number of elements of  $2*101*88=17776$ ).

Diffusion profile for the etched ridge waveguide structure is given in Fig. 5.7. Again the diffusion profile is confined to the expected guide region shown in Fig. 5.6. This is only

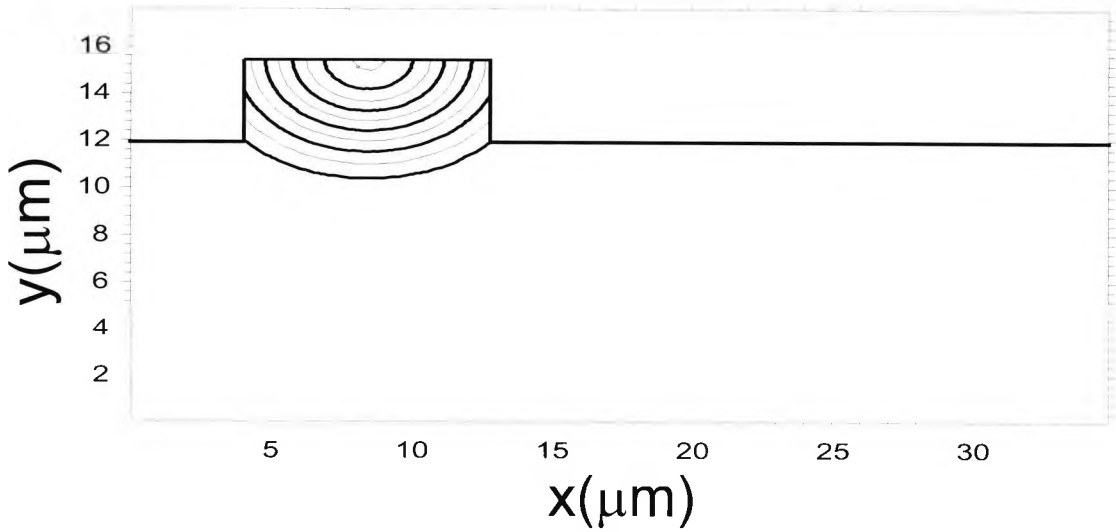


Fig. 5.7 The diffusion profile of the etched ridge waveguide.

because the width of the ridge is larger than  $2d_x$ . If the width of the ridge were smaller than  $2d_x$ , then the width of the ridge would confine the guiding region laterally. If this were the case and if  $d_y$  were smaller than the height of the ridge, the guiding region would be confined to the ridge, otherwise the guiding region would be laterally confined by the width of the ridge for the distance of the height of the ridge, after which the guiding region would again be laterally confined by  $2d_x$ .

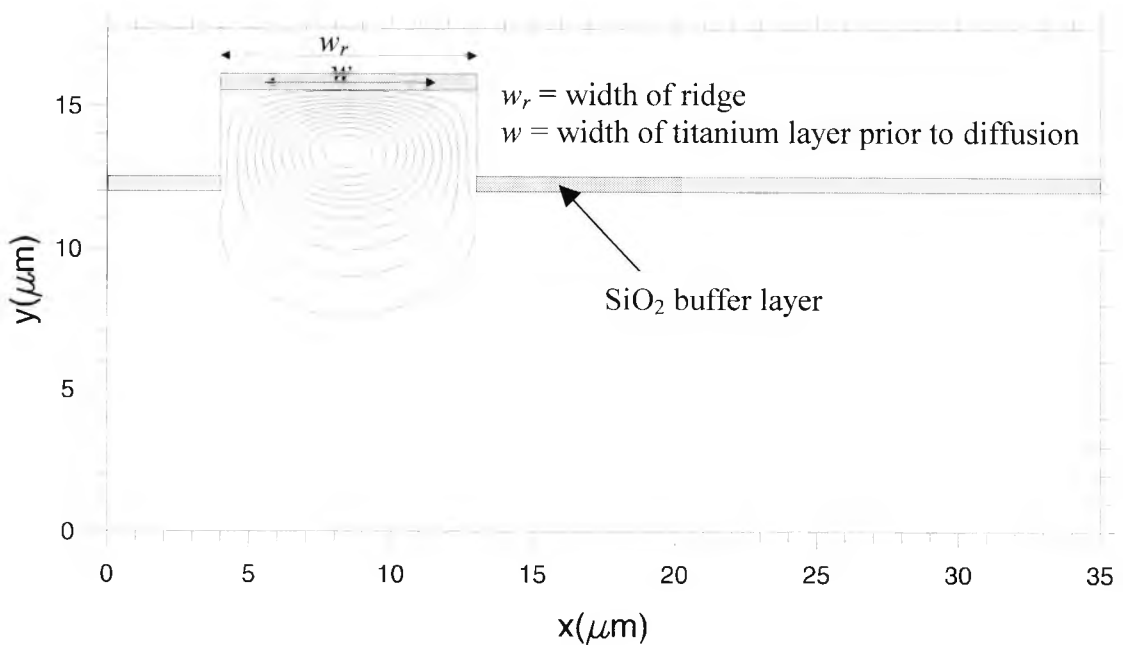


Fig. 5.8 Optical mode for the etched ridge Ti:LiNbO<sub>3</sub> waveguide.

As can be seen in Fig. 5.8, the optical mode is much more confined for this structure due to the nature of the ridge waveguides. Moreover, it can be seen from this figure that the mode was for a ridge height of 3.5 $\mu$ m. It is of interest to note that this guide supports only the fundamental mode. As mentioned in the previous section the effective index for the etched ridge waveguide is expected to be lower than for the channel waveguide. This is due to the etched ridge waveguide being mainly surrounded by a lower refractive index material (SiO<sub>2</sub> buffer layer, which in turn is surrounded by air) rather than LiNbO<sub>3</sub> as for the channel waveguide. The value for  $\beta$  for this structure (for a 2\*101\*88 mesh size) was 8.6734608, which gives an effective index of 2.1397. This is a 0.014% difference in effective index between the channel and etched ridge waveguide. This difference is lower than expected. However, due to the presence of air on both sides of the waveguides the modes are more tightly confined than for the channel waveguide (seen in Fig. 5.5). This is the advantage of the etched ridge waveguides since the tightly confined mode leads to smaller device geometry (Ashley *et al.*, 1989).

It is expected that propagation loss should improve for etched ridge waveguides because of the reduced coupling between the parallel waveguides in the interaction region (Haga *et al.*, 1986) caused by the resultant groove formed between the etched waveguides. This is because a more tightly confined mode than for the channel waveguide, should produce a marked reduction in any stray coupling due to imperfections in this region. It is clear from previous observations (see Section 4.5) concerning mode size that the diffusion parameters must also play a part in the propagation loss of the waveguide, since mode size changes with a number of diffusion parameters. However, in reality the greater part of the propagation loss in these waveguides is due to the roughness of the sidewalls, since propagation losses of 0.3-1 dB/cm have been reported for etched ridge waveguides (Noguchi *et al.*, 1995) yet for unetched channel waveguides propagation losses of only 0.1dB/cm have been reported (Suche *et al.*, 1985).

As mentioned in the previous chapter, the size of the mode is also important to the coupling of light from an optical fibre to the Ti:LiNbO<sub>3</sub> waveguide. Also mentioned was the fact that the size of the mode could be controlled by the parameters involved in the diffusion process. As the size of the mode increases to approximately that of the mode from the fibre, coupling loss from waveguide to fibre and vice versa decreases.

However, as also observed in Chapter 4, the switching voltage increases with increasing mode size. Hence, there is a trade-off between coupling loss and switching loss. Nevertheless, by using waveguide tapers (Komatsu *et al.*, 1986) or spot-size converters (Rahman *et al.*, 1996) optimum waveguide coupling can be achieved without the need to worsen the switching voltage characteristics. However, insertion loss includes coupling loss, propagation loss, bending loss and electrode loading loss (Alferness, 1988). Therefore, there is a trade-off between insertion loss and switching voltage. From the mode profile shown in Fig. 5.8, the 1/e intensity full depth,  $w_y$ , is calculated to be 4.35 $\mu\text{m}$ , which is larger than  $d_y$  ( $=3.923\mu\text{m}$ ) and the 1/e intensity full width,  $w_x$ , is 6.348 $\mu\text{m}$ , which is well within a width of  $2d_x$  ( $=7.662\mu\text{m}$ ). In this case, the lateral dimension of the spotsize of the optical mode,  $w_x$ , is reduced due to the formation of the ridge. This gives a mean mode size of 5.255 $\mu\text{m}$ , given by  $\sqrt{w_x w_y}$  (Alferness, 1988). The value of the mode eccentricity, given by  $w_x/w_y$ , for this structure is 1.46. The mean mode size for the etched ridge waveguide compared with the unetched channel waveguide has reduced by 7.87%. The change is not so large, because there is very little change in  $w_y$  when compared to the unetched channel waveguide. In fact there is very little variation in mode size with  $h$ , the height of the rib, for values of  $h$  between 0 $\mu\text{m}$  and 6 $\mu\text{m}$ . Nevertheless, it is to be seen in the following sections as to how significant the etched ridge waveguide is for bending loss and switching characteristics of a Mach-Zehnder based interferometric modulator compared to a similar device using unetched channel waveguides.

### 5.3.3 Comparison of Optical Bends using Channel and Etched Ridge Waveguides

Optical bends are an essential part of optical modulators. The abrupt bends such as the Y-branch used in the modulator of the same name, and the S-bends more typically used with Mach-Zehnder modulators and directional couplers are real structures. This part of the study is to examine how the etched ridge waveguide compares with a channel waveguide when calculating bending losses. A more generic 90° bend (Ganguly *et al.*, 1998) is feasible to use for making this comparison.

A semi-vectorial finite element-based beam propagation method (FEBPM) is used to calculate the bending losses. The method used is described in Chapter 3. It is clear from the description that the variables for this method are  $\theta$ ,  $R$ ,  $\Delta z$  and the width of the PML layer. When  $\theta = 0.5$ , the Crank-Nicolson scheme is attained, with  $\theta$  greater than 0.5 a non-Crank-Nicolson scheme is achieved. It is known that  $\theta = 0.5$  can generate instability in the solution in the form of high frequency oscillations (Obayya, 1999) – see Fig. 5.9. This can, however, be removed by increasing  $\theta$ , but this leads to increased

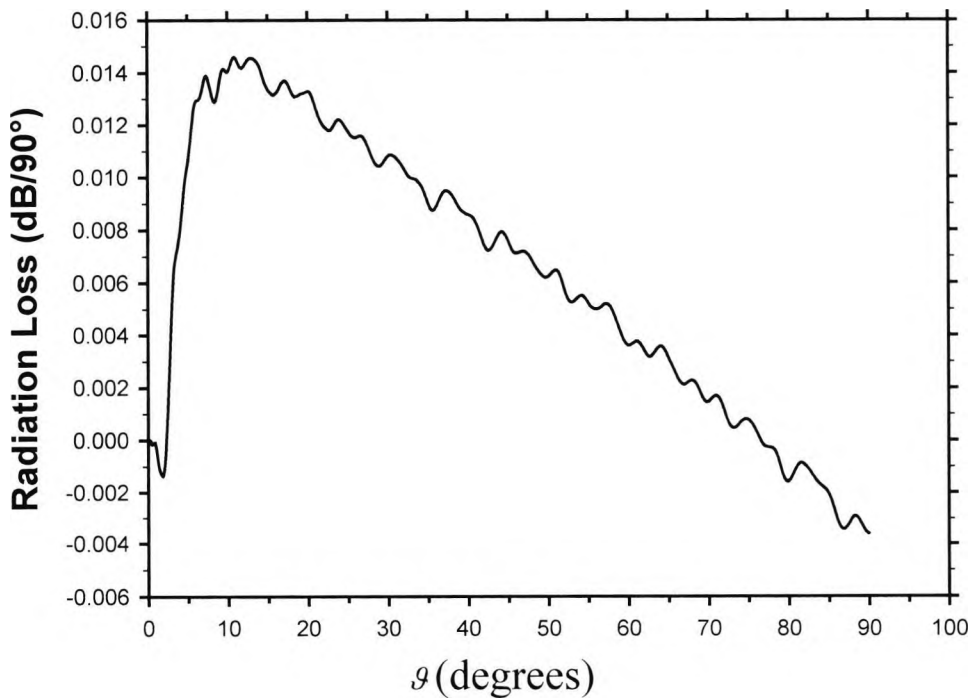


**Fig. 5.9** The resulting instability in radiation loss along the 90° circular bend when BPM parameter  $\theta$  is taken to have a value of 0.5.

propagation losses which are of a purely non-physical, numerical nature. Therefore, it is considered necessary to have  $\theta$  as near as possible to 0.5. In Fig. 5.9  $g$ , representing the distance in degrees around the circular optical bend and which varies between 0° and 90° (for this study), is not to be confused with  $\theta$ , the BPM parameter which varies between 0.5 and 1.0. Fig. 5.10 shows the change in radiation loss with increasing  $\theta$  relative to that radiation loss at  $\theta = 0.51$  for a 90° circular bend for an unetched channel waveguide. The variation of radiation loss with  $\theta$  is linear for the 90° circular bends with radii of 5mm, 7mm and 10mm. This is in agreement with other results (Obayya, 1999). The value of  $\theta$  for this study was therefore chosen to be closest to that for the

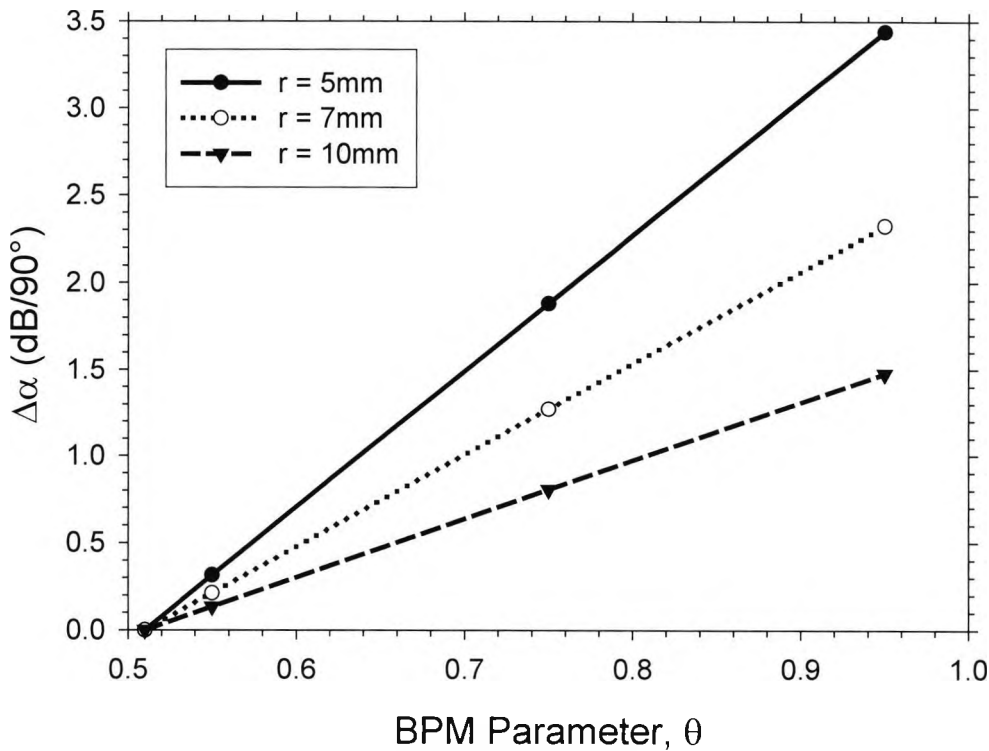
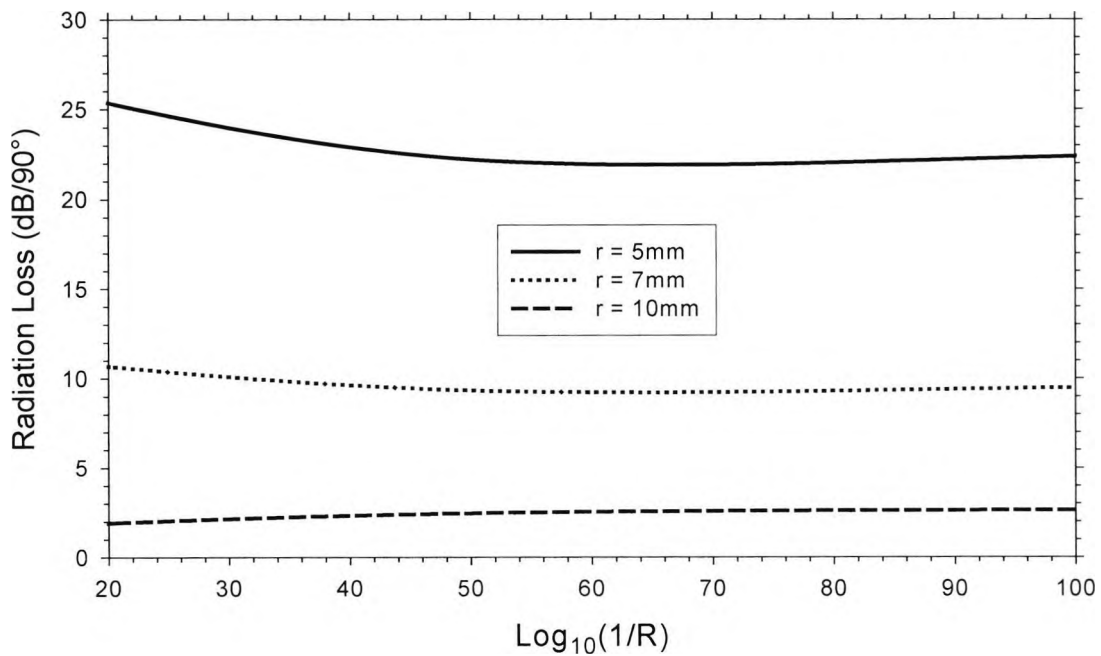


Fig. 5.10 The change in radiation loss,  $\Delta\alpha$ , with increasing BPM parameter  $\theta$ .

Crank-Nicolson scheme, at 0.51, since it gives the lowest radiation loss without becoming unstable.

The other variable that was investigated in this study was the theoretical reflection coefficient,  $R$ , at the interface between the computational domain and the PML. The variation obtained for this study is shown in Fig. 5.11. For all three radii studied, the variation in radiation loss became small for those values of  $R$  smaller than  $1 \times 10^{-60}$ . Moreover, there was very little in radiation loss for the larger radii of 7 and 10mm. The smaller radius circular bend of 5mm, showed a much larger change in radiation loss for the values of  $R$  larger than  $1 \times 10^{-50}$ , therefore, a value of  $1 \times 10^{-50}$  was chosen for  $R$  for this study.  $\theta$  was kept at 0.55 for this small section of the study to give exaggerated difference in radiation loss in order to determine the optimum value for  $R$ .

The step in the axial direction  $z$ ,  $\Delta z$ , was fixed at  $2\mu\text{m}$ . No study was undertaken for this parameter, as it was considered a reasonable value for this parameter (Obayya, 1999). The thickness of the PML was also fixed at  $1\mu\text{m}$  (Obayya, 1999).



**Fig. 5.11** The variation in radiation loss with a decreasing reflection coefficient,  $R$ , at the interface between the computational domain and the PML for three bends of differing radii,  $r$ .

Fig. 5.3 showed the variation in beta with the number of elements used in the mesh generation for the finite element method, the numerical method used throughout this project. Fig. 5.12 shows both the variations in  $\beta$  and the variation in radiation loss with the number of elements of the mesh for a 90° circular bend with a 10mm radius. In fact, the variation in radiation loss with the number of elements in the mesh mirrors the variation in beta with the number of elements in the mesh, with the exception that beta increases and stabilises with increasing mesh size whereas the radiation loss decreases and stabilises with increasing mesh size. The mesh for Figs. 5.10 and 5.11 was 3420 elements: hence, the reason that the radiation loss was large in Fig. 5.11. Again, the smaller mesh size was used to exaggerate differences in values in order to take the best value for  $R$ .

The conclusion from this figure, as from Fig. 5.3, is that a reasonable size mesh to choose would be that with  $2 \times 101 \times 88 = 17776$  elements. Although, the best value of  $\theta$  was determined to be 0.51, for Fig. 5.12,  $\theta$  was kept at 0.55. This is because this part of the study was to show the variation in radiation loss with one parameter (mesh size),

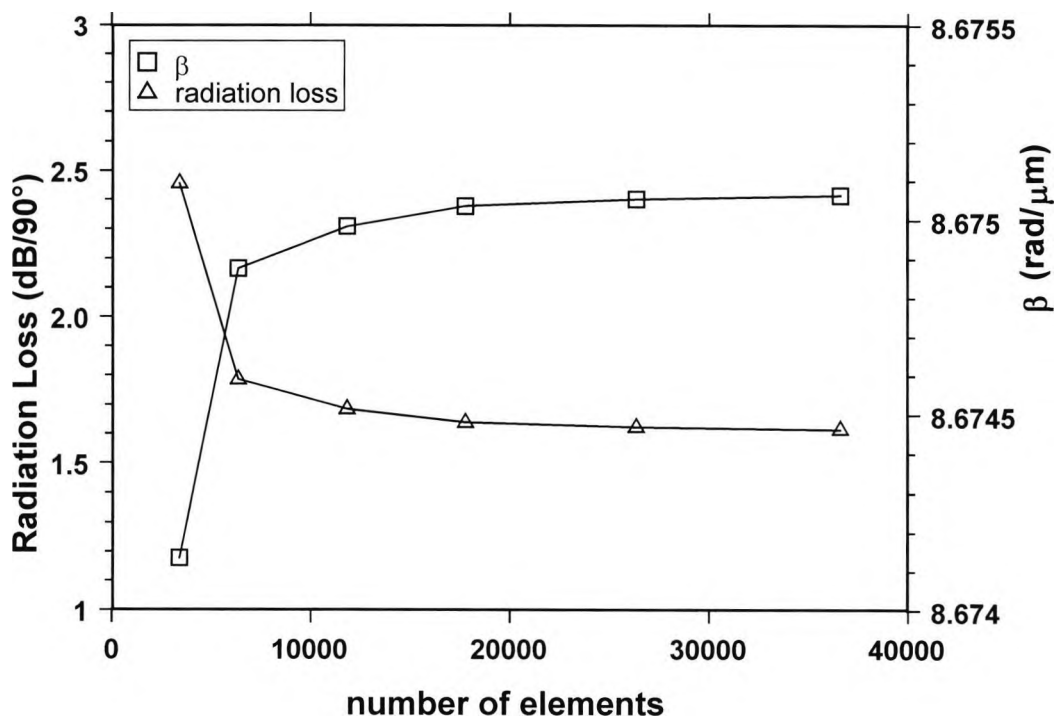
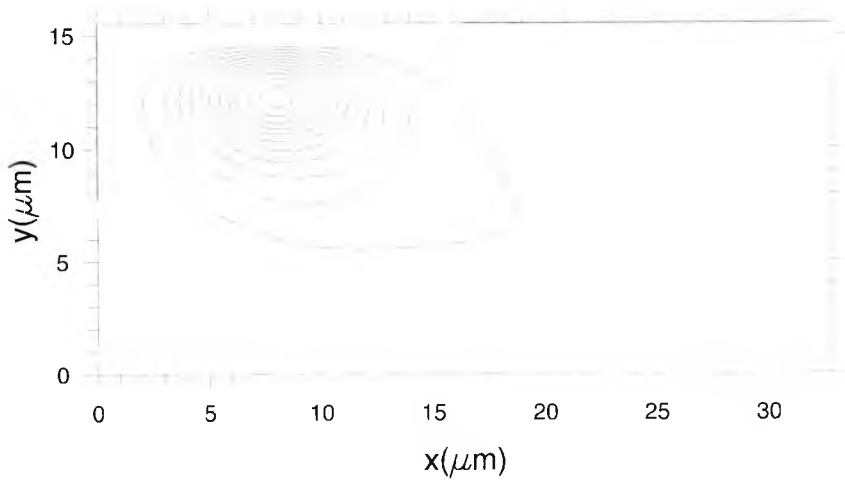


*Fig. 5.12 The variations in  $\beta$  and the variation in radiation loss with the number of elements of the mesh for a 90° circular bend with a 10mm radius.*

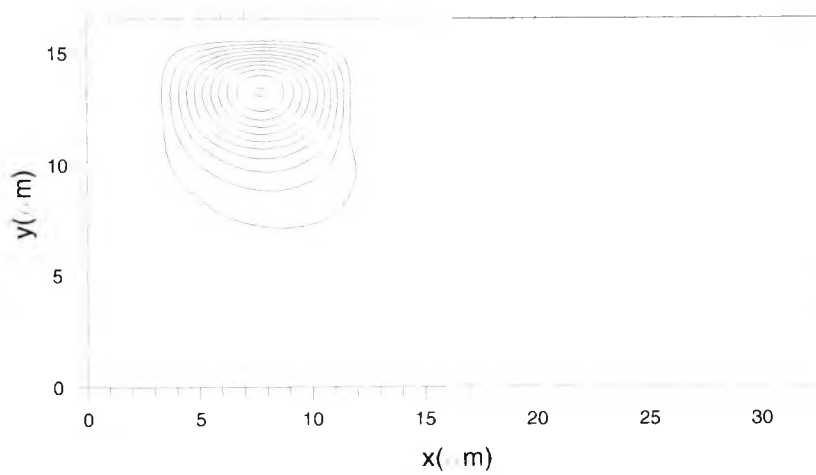
and so the manner of the variation and not the actual values of radiation loss are important. The value of  $\theta$  for any subsequent figures is 0.51.

Fig. 5.5 shows the optical mode for an unetched channel waveguide at  $z=0$ , i.e at the start of the 90° circular bend. Fig. 5.13 shows the optical mode at the output of a 90° circular bend for an unetched channel waveguide with a radius of 7mm. Comparing these two figures, it is clear that a significant amount of power from the waveguide is leaking into the LiNbO<sub>3</sub> substrate at the output of the 90° circular bend. The power leaking from the waveguide along the bend linearly increases with distance culminating in a significant propagation loss of 6dB at the output 90° circular bend, as will be seen from Fig. 5.15.

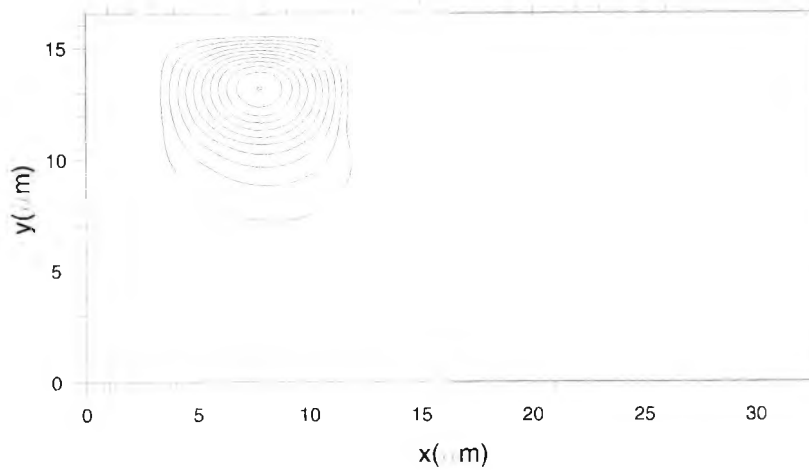
Fig. 5.14. shows the progress of the optical mode through a 90° circular bend for an etched ridge waveguide with a radius of 7mm and ridge height of 4.5 $\mu\text{m}$ . Fig. 5.8 shows the optical mode for an etched ridge waveguide at  $z=0$ , i.e at the start of the 90° circular



**Fig. 5.13** The optical field at the output of a 90° circular bend for a 7mm radius for the unetched waveguide MZI modulator.



(a)



(b)

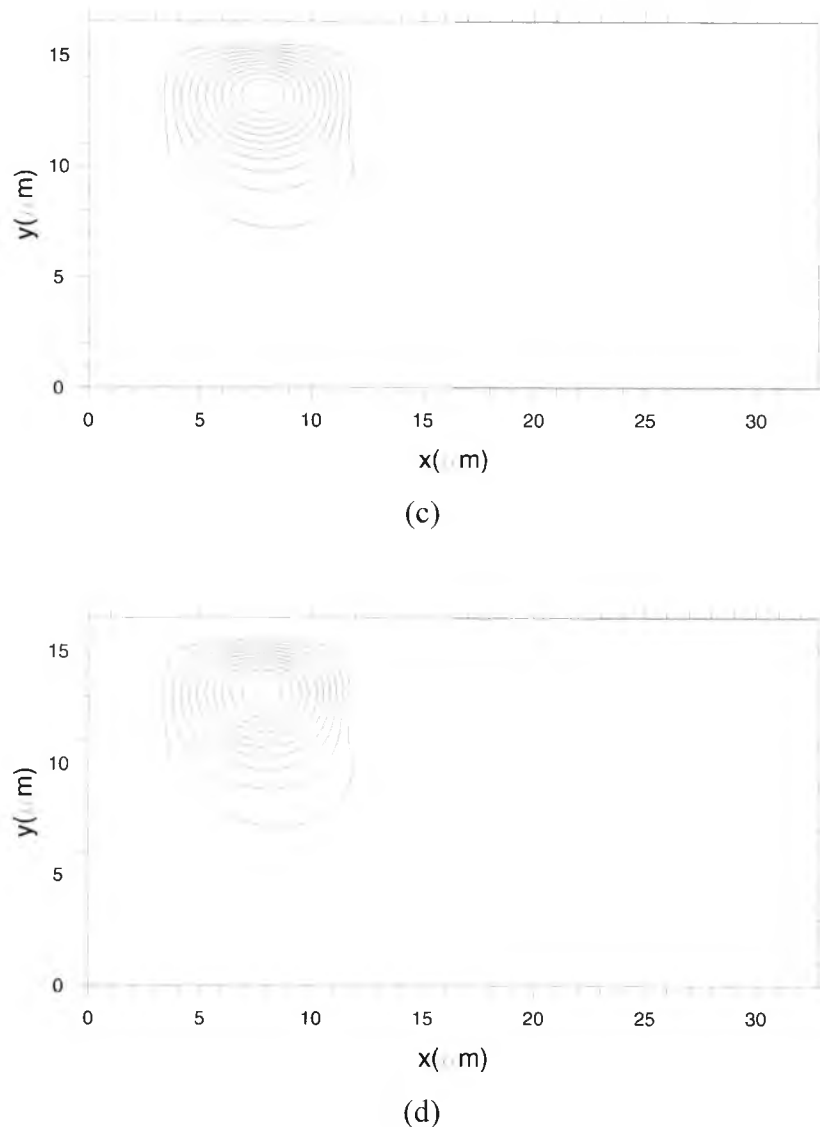


**Fig. 5.14** The optical field (a)  $\frac{1}{4}$ , (b) halfway, (c)  $\frac{3}{4}$  along and (d) at the output of a  $90^\circ$  circular bend for a 7mm radius for the etched ridge waveguide MZI modulator of etch depth  $4.5 \mu\text{m}$ .

bend. As can be observed, there is very little variation in the optical mode as it progresses along the circular bend. This is due to the fact that the mode is well confined to the guiding region of the waveguide, and hence there is very little leakage from the waveguide. The difference in radiation loss between unetched channel waveguide  $90^\circ$  circular bends and etched ridge waveguide  $90^\circ$  circular bends of a fixed radius of 7mm can be seen in Fig. 5.15. Moreover, it can also be observed that radiation loss decreases with the increasing ridge height of the etched ridge waveguide circular bend. The slight nonlinearity at the start of the three curves in Fig. 5.15 may be due to the change in direction that the mode experiences on entering into the circular bend, since the mode moves towards the outer edge of waveguide. This is normally termed as transition loss (Ganguly *et al.*, 1998).

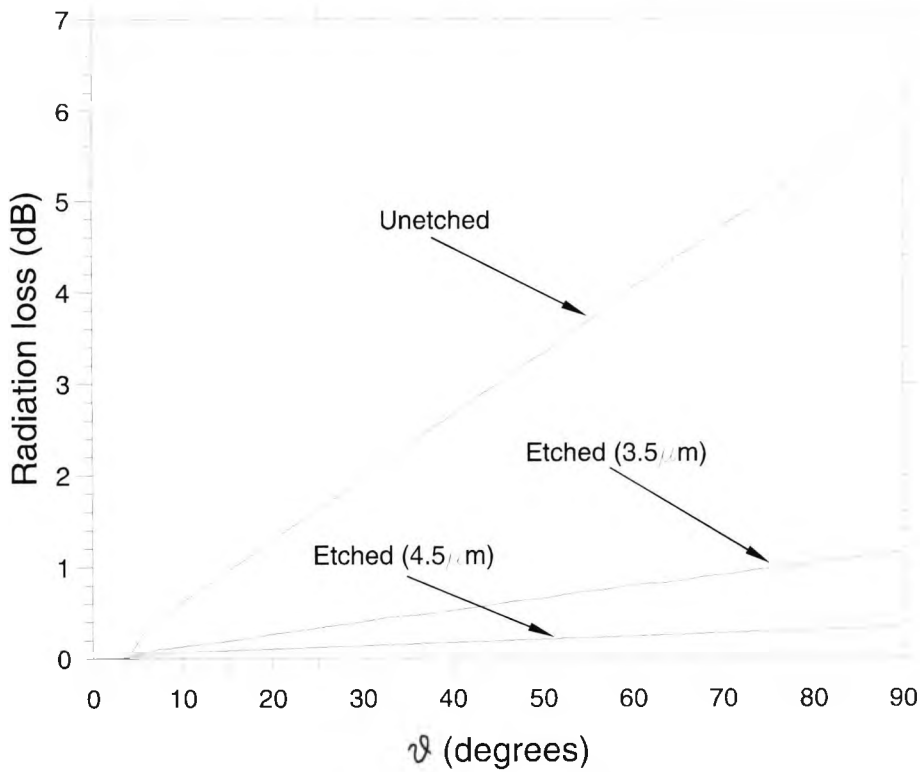


**Fig. 5.15** Radiation loss vs  $\vartheta$  for the unetched MZI modulator, and the etched ridge waveguide MZI modulator for ridge heights of 3.5  $\mu\text{m}$  and 4.5  $\mu\text{m}$ , all of which have a bending radius of 7mm.

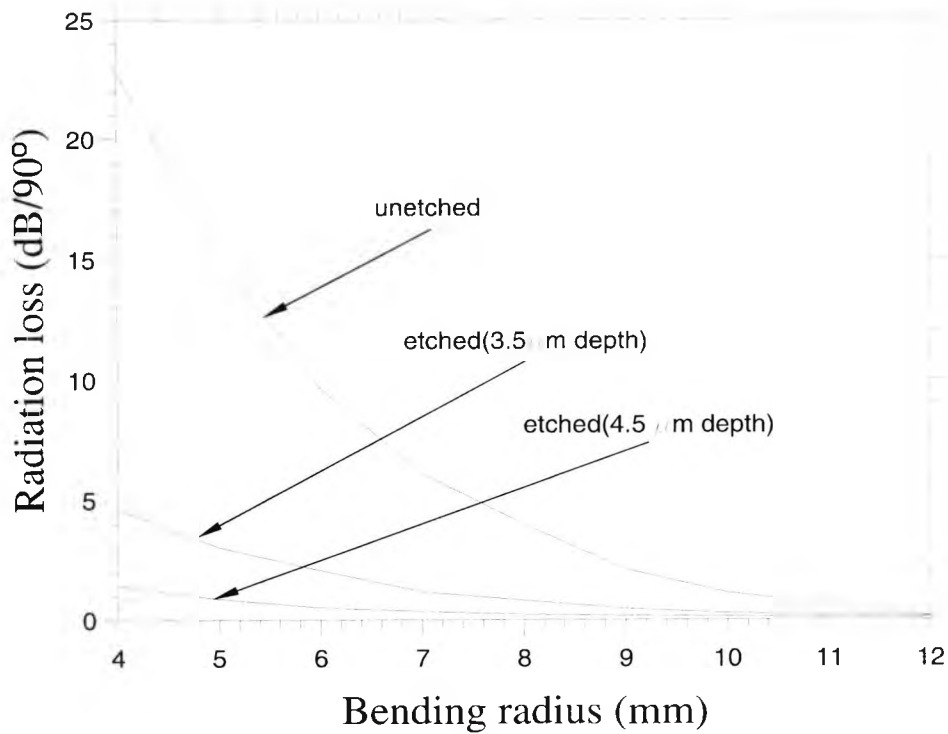


**Fig. 5.16** Radiation loss for a 90° circular bend vs the radius of the bend for an unetched MZI modulator and etched MZI modulators with etch depths of 3.5  $\mu\text{m}$  and 4.5  $\mu\text{m}$ .

Finally, the relationship between bending loss and the radius of the circular bend is shown in Fig. 5.16. This was realised for an unetched channel waveguide, and etched ridge waveguides with ridge heights of 3.5 $\mu\text{m}$  and 4.5 $\mu\text{m}$ , as for Fig. 5.15. As expected, for all three cases, the bending loss decreases with increasing radius. However, the bending loss was significantly lower for the etched ridge waveguides than for the unetched Ti:LiNbO<sub>3</sub> waveguides. A lower loss occurs for the etched ridge waveguides due to the optical mode being strongly confined in the lateral directions for the etched waveguides. It was also found that the bending loss for the ridge of 4.5  $\mu\text{m}$  was smaller than that for 3.5  $\mu\text{m}$ , as in Fig. 5.15. However, to etch a ridge deeper than 5  $\mu\text{m}$  takes a very long time (Mitsugi *et al.*, 1998), as mentioned in Chapter 3, and neither is there any further reduction in switching voltage for etch depths greater than 4.5  $\mu\text{m}$ , as will be seen later in this chapter.

So, for an etched waveguide, the bending radius of the input and output waveguides are reduced compared to an unetched waveguide while retaining a reasonable output of light since the losses will remain low. For example, if  $\alpha_r$ , the radiation loss per 90° circular bend, is 0.3dB for a waveguide with an etch depth of 4.5  $\mu\text{m}$  and a bending radius of 7.3mm, then to achieve the same loss for an etch depth of 3.5  $\mu\text{m}$  the bending radius has to be 9.85mm (giving a 35% increase in device length compared with an etch depth of 4.5 $\mu\text{m}$ ) and, similarly, to achieve the same loss for an unetched waveguide the bending radius has to be 11.7mm (giving a 60% increase in device length compared to that with an etch depth of 4.5 $\mu\text{m}$ ). This implies that not only will an etched ridge waveguide, with an etch depth of 4.5 $\mu\text{m}$ , lead to a shorter interaction length, but also that the bending input/output (I/O) waveguide lengths will be shorter too, causing a significant overall reduction of the device size.

Also, taking the example of a bend radius of 7 mm, it can be seen from Fig. 5.16 that the optical loss due to the waveguide bends,  $\alpha_r$ , for the unetched guide is 6.096 dB and for the guide with an etch depth of 4.5  $\mu\text{m}$  it is 0.338 dB for 90° bends. This implies that  $\alpha_r$ (dB) for a guide with a 4.5  $\mu\text{m}$  etch depth is only 5.54% of that for an unetched guide. Since the modal field in unetched bend waveguides deviates considerably from that in straight waveguides, a lateral shift between the guides of the order of 1 $\mu\text{m}$  may be necessary to reduce butt-coupling loss. Such an offset would not be necessary for an etched bend waveguide because there the mode is mostly confined to the higher

refractive index ridge section of the waveguide and hardly any lateral shift occurs for the etched ridge waveguide. Hence, it is clear that etched ridge waveguides would be of great benefit when fabricating optical bends in Ti:LiNbO<sub>3</sub> devices.

## 5.4. The Comparison between an Unetched Channel Waveguide and an Etched Ridge Waveguide Interferometer

The work achieved for the single guide was used for the study on optical radiation loss for 90° circular bends, and was a preparation for the work on the Y branch interferometer detailed in the remaining part of the chapter.

### 5.4.1 Structure of the Interferometric-based Modulator

The interferometer as shown in Fig. 5.1 is for single arm operation, i.e. the electric field, due to the voltage applied to the electrode, only acts on one arm and therefore the subsequent change in refractive index, due to the linear electrooptic effect, only occurs for that arm of the Y-branch interferometer. A more advantageous approach would be to

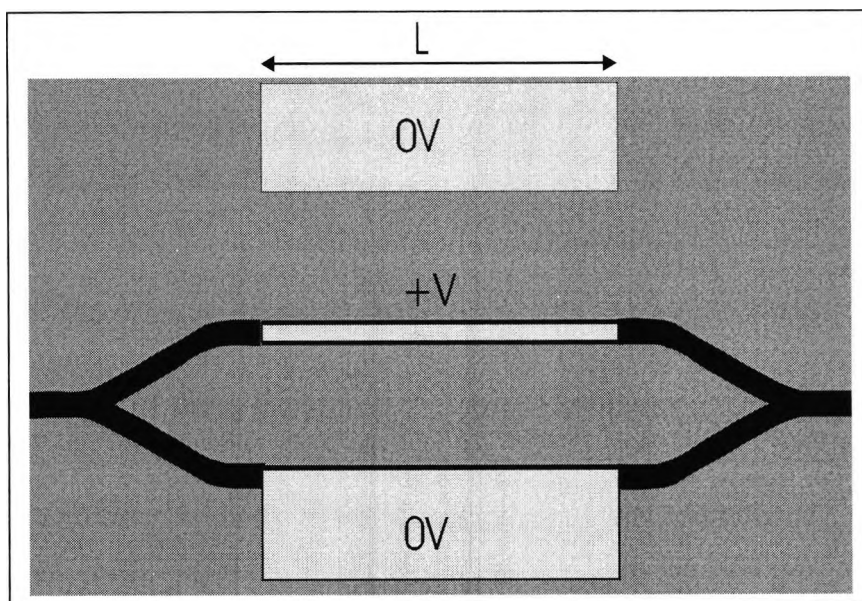


**Fig. 5.17** The layout of both the unetched and etched Mach-Zehnder interferometric (MZI) modulators.

use a push-pull operation. For the Y-branch interferometer this involves a three-electrode configuration as shown in Fig. 5.17, where the central electrode is used for both applying bias to the device as well as the RF signal. Hence, it is sometimes termed the hot electrode. The other two outer electrodes are therefore typically ground electrodes. The cross-section of the structure using unetched channel waveguides is given in Fig. 5.18. For most electro-optic devices the use of a ridge waveguide structure

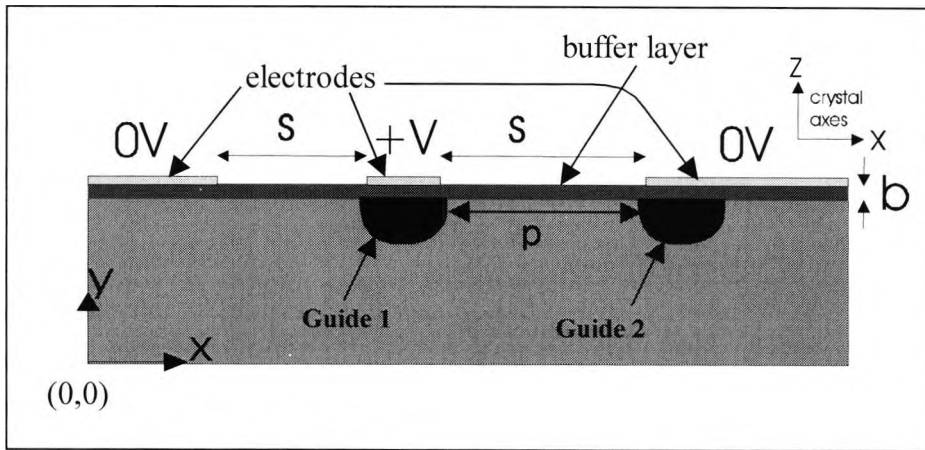


Fig. 5.18 The cross-section of the unetched MZI modulator.

generally confines the optical mode to the waveguide area and consequently improves device properties. The cross-section of the structure using etched ridge waveguides is given in Fig. 5.19. As for the single guide structure, the ridge waveguides for this interferometric structure were also taken to have straight vertical walls.

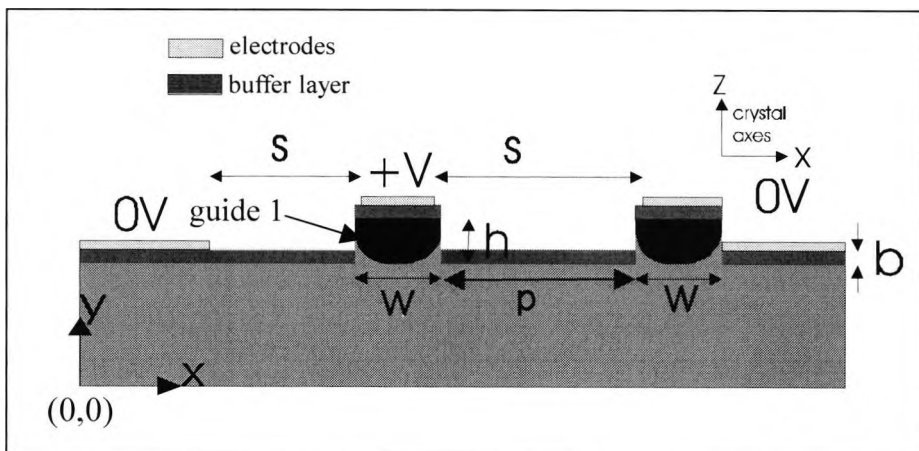


Fig. 5.19 The cross-section of the etched MZI modulator with etch depth,  $h$ .

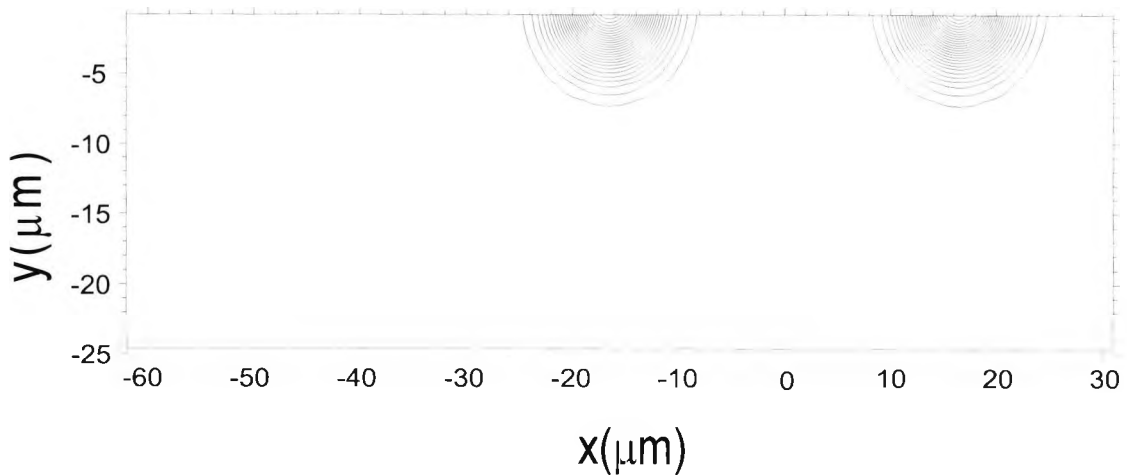
The refractive indices used are as for the single guide in the previous section. The calculation of the diffusion profile is also achieved as for the single guide with the exception that equation (5.16) is used instead of equation (5.17) since there are two guides. As for the single guide structure, the thickness of the SiO<sub>2</sub> buffer layer was initially taken to be 0.6  $\mu\text{m}$ . Also, the interaction length of the device,  $L$ , is taken to be 2cm.

At this stage as for the single guide, a satisfactory mesh size was determined. For both structures, even when no voltage is applied the central electrode, two optical quasi-TM fundamental modes are obtained for these two-waveguide structures. The first mode appears in one waveguide and the second in the other waveguide. Ideally for the case when no voltage is applied the optical modes should be degenerate, i.e. have the same  $\beta$  value. However, due to the nature of all numerical methods being an approximation, it is very near degenerate (the difference in  $\beta$  for these two modes is  $6 \times 10^{-7}$  for the unetched channel waveguide interferometer and  $7.8 \times 10^{-6}$  for the etched ridge waveguide interferometer). The effective index for these two structures is approximately 2.1389 for the etched and 2.1396 for the unetched. In this case there is a 0.0003% difference in effective index between the channel and etched ridge waveguide. The effective index for the etched guide is slightly lower as part of the LiNbO<sub>3</sub> has been etched away and replaced by mainly air and perhaps a little SiO<sub>2</sub> (if the sidewalls are slightly sloped and not fully 90° to the horizontal (Winnall and Winderbaum, 2000; Burns *et al.*, 1999)). However, due to the presence of air on both sides of the waveguides the modes are more confined. A similar procedure was followed as for the single waveguide structure in finding the appropriate mesh size, which due to the effective doubling of the structure

**Table 5.1**  $\beta$  values for optical modes in guide 1 and 2 of the etched ridge waveguide interferometric modulator and the resulting effective index vs mesh size.

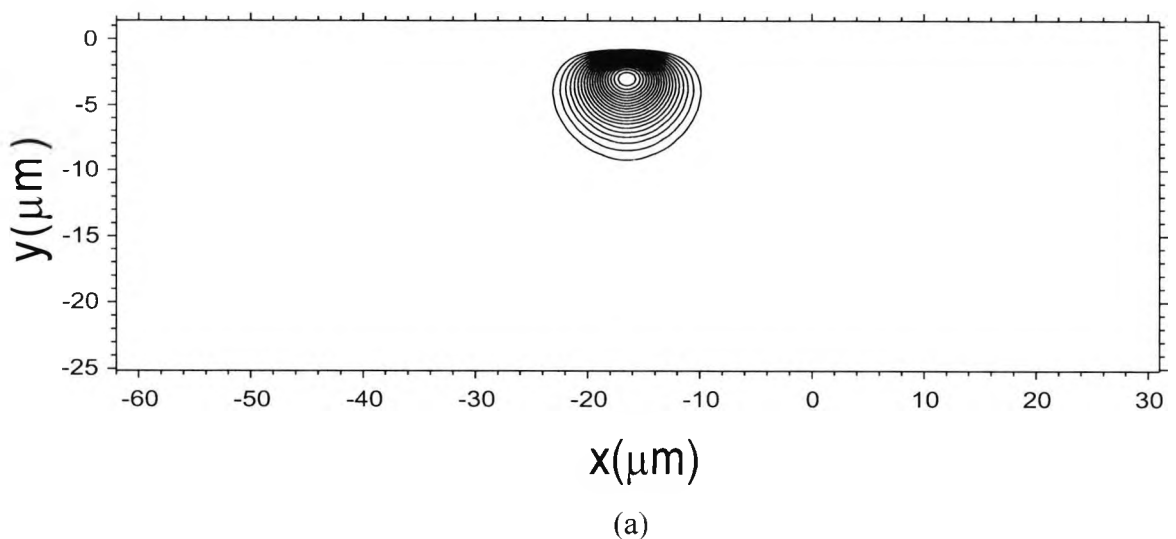
Properties	Mesh Size		
	2*161*42=13524	2*250x45=22500	2*313x85=53210
$\beta_e$	8.6719517	8.6703459	8.6699590
$\beta_o$	8.6719463	8.6703381	8.6699556
$n_{eff}$	2.1393	2.1389	2.1388

compared with the single guide structure, was also constrained by the time taken to run the mode solver programs and the Laplace solver in the sequence detailed in Chapter 4. The meshes used in this study were typically 250x41 for the unetched waveguide modulator and 250x45 for the etched waveguide modulator. The values of  $\beta$  and  $n_{eff}$  for the etched waveguide modulator are shown for three mesh sizes in Table 5.1. There is very little difference in effective index for the optical modes between the larger of the two meshes, indicating that a mesh size of 22500 elements is more than adequate.



**Fig. 5.20** The diffusion profile of the Ti:LiNbO<sub>3</sub> channel waveguide interferometric modulator.

The diffusion profile for the unetched waveguide modulator, of cross-section shown in Fig. 5.18, is shown in Fig. 5.20. As expected, due to the distance between the two guides of 24 $\mu\text{m}$ , the diffusion profiles of the two guides are set apart and distinct. The width and depth of the profile for each of the two guides are as for the single guide.



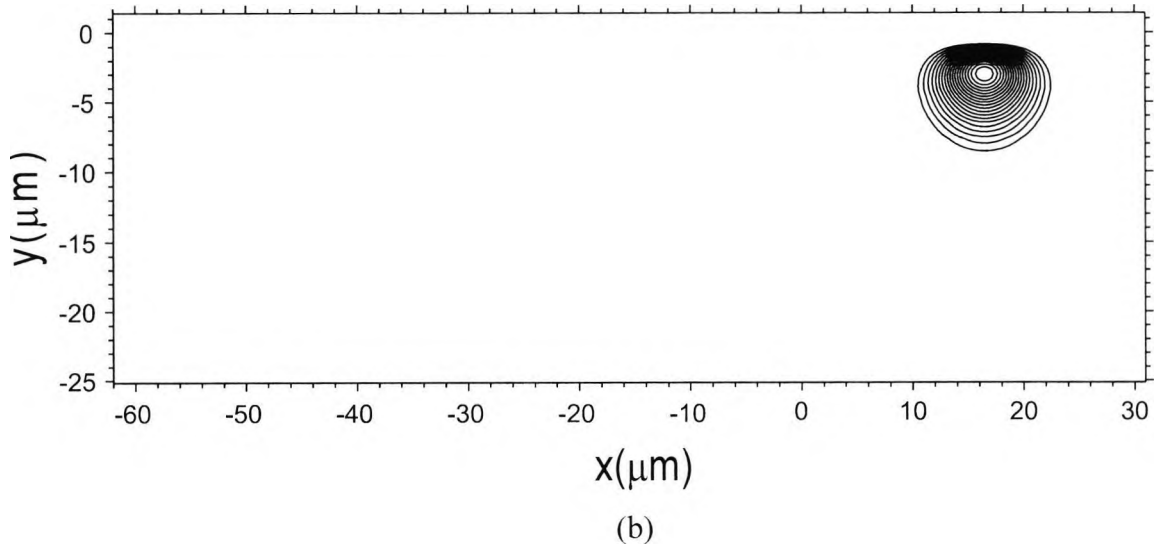


**Fig. 5.21** Quasi-TM fundamental near-degenerate optical modes for the two guides of the Ti:LiNbO<sub>3</sub> channel waveguide interferometric-based modulator.

Therefore, as expected the two near-degenerate  $H_x^{II}$  modes obtained for each guide both have the same profile as for the single guide, with the same width and depth, as shown in Fig. 5.21. The same applies for the etched ridge waveguide interferometric modulator, although as for the single etched ridge waveguide both the diffusion profile shown in Fig. 5.22, and optical modes, as shown in Fig. 5.23, are laterally confined by the ridge width, therefore forcing the both profiles to be distinct and apart by the separation of the two ridge waveguides of 24 μm.

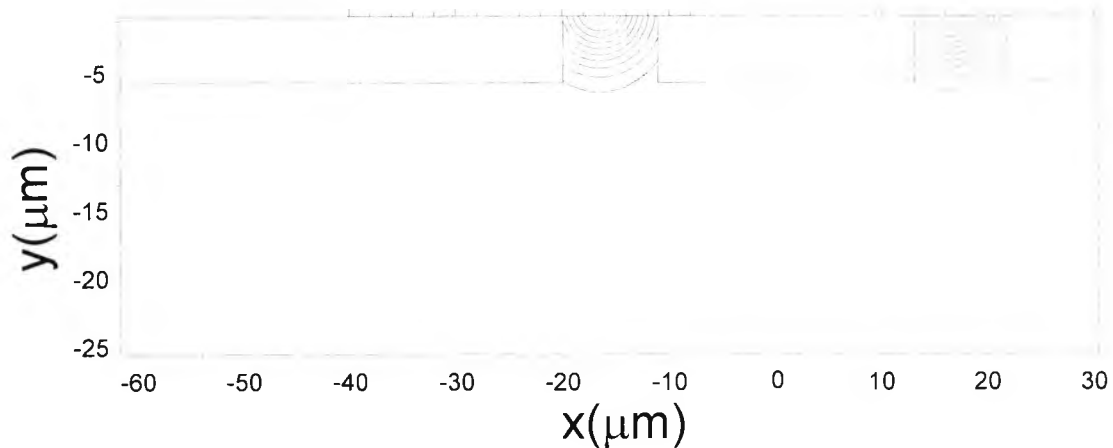
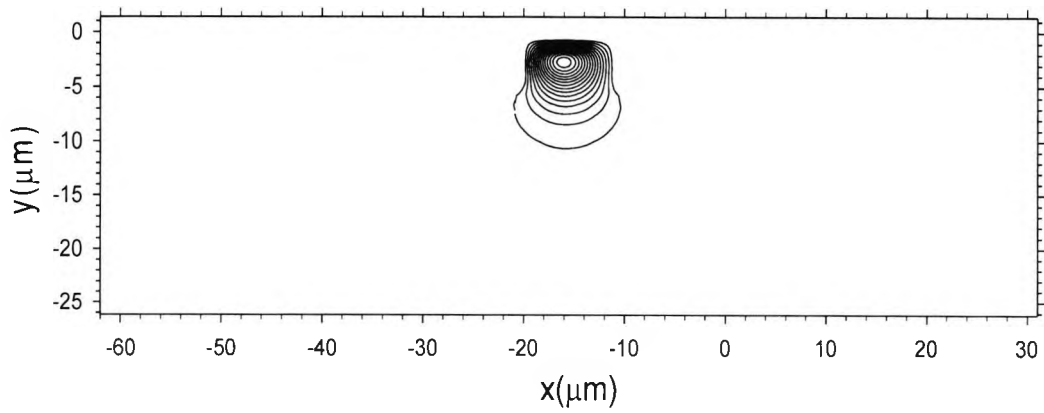
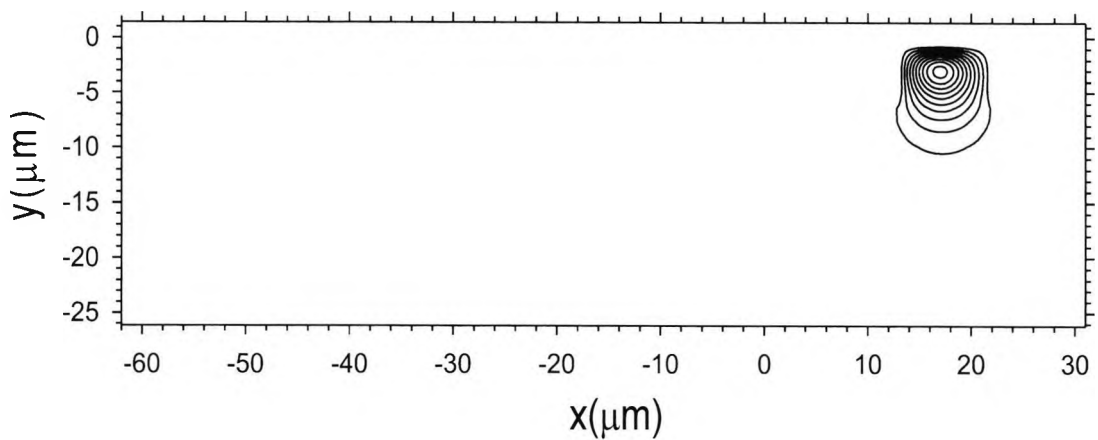


**Fig. 5.22** Diffusion profile of the Ti:LiNbO<sub>3</sub> etched ridge waveguide interferometric-based modulator.



(a)



(b)

*Fig. 5.23 Quasi-TM fundamental near-degenerate optical modes for the two guides of the Ti:LiNbO<sub>3</sub> etched ridge waveguide interferometric-based modulator.*

#### 5.4.2 Electrooptic Characteristics

Up to now these results have been for a device with no applied voltage, the principle of operation of a modulator is to obtain change in the amount of light output by the device as a consequence of material changes made to the device mainly by application of an electric field.

5.4.2.1 The Nature of the Electric Field

As mentioned in Chapter 3, LiNbO<sub>3</sub> is a dielectric crystal. With this comes the implication that there are no free carriers and hence the crystal is an insulator. Since there is no free charge, the more general Poisson equation

$$\nabla \cdot (\epsilon \nabla V) = \rho \quad (5.35)$$

where  $\epsilon$  is the permittivity tensor,  $V$  is the applied voltage and  $\rho$  is the resultant charge becomes

$$\nabla \cdot (\epsilon \nabla V) = 0 \quad (5.36)$$

since  $\rho=0$  for LiNbO<sub>3</sub>.

Equation (5.36) is called the Laplace equation.

As explained in Chapter 3,  $\epsilon$  is taken as the dielectric tensor of LiNbO<sub>3</sub> at lower microwave (modulating) frequencies. Equation (5.36) can then be rewritten for uniform cross-section (i.e.  $\partial/\partial z = 0$ ) as

$$\epsilon_{xx} \frac{\partial^2 V}{\partial x^2} + \epsilon_{yy} \frac{\partial^2 V}{\partial y^2} = 0 \quad (5.37)$$

since the non-zero components of the permittivity tensor,  $\epsilon_{xx}$ ,  $\epsilon_{yy}$  (and  $\epsilon_{zz}$ ) are constants. For Z cut LiNbO<sub>3</sub> these are taken as 43 for  $\epsilon_{xx}$ , and 28 for  $\epsilon_{yy}$  and  $\epsilon_{zz}$ , respectively, for the calculation of the electro-optic effect. The dielectric constant used for SiO<sub>2</sub> in this same computation is 3.9. The central electrode width was taken to be 8  $\mu\text{m}$  and the electrode separation was taken to be 25  $\mu\text{m}$ . Also, the interaction length of the device,  $L$ , is taken to be 2cm.

The  $y$ -component of the vector modulating electric field,  $E_y(x,y)$ , was calculated from the scalar potential,  $\psi$ , using the FEM (Davies, 1989) and this, as well as the position of the electrodes, is shown in Fig. 5.24. As expected, the field is heavily concentrated under the central electrode but evidence of a lower concentration under the two ground electrodes is also visible. In fact, it can be seen that due to the symmetrical placement of the electrodes, the modulating electric field is also symmetrical and so the field acting in the 2<sup>nd</sup> waveguide, which is placed under one of the ground electrodes, is small compared with that of the 1<sup>st</sup> guide, which is placed directly under the central electrode. However, due to the presence of the buffer layer, which is essential to minimize optical

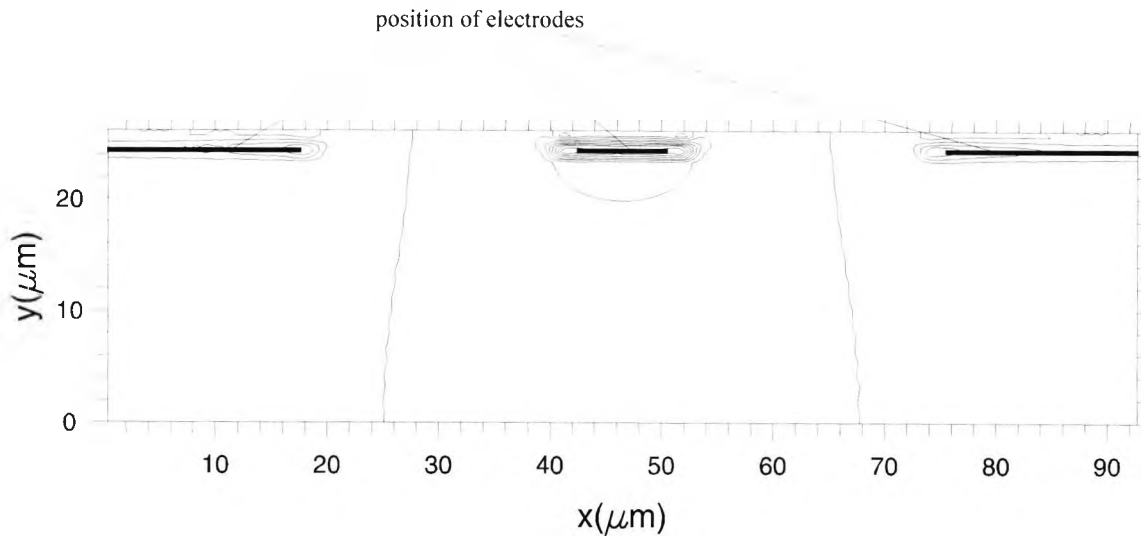


**Fig. 5.24** The  $E_y$  component of the modulating electric field  $\mathbf{E}$  for the unetched MZI modulator for an applied voltage of 5V.

losses due to the metal electrodes for TM-polarized light, it appears that a reasonable proportion of the modulating electric field is acting in the buffer layer because of the flatter profile of the modulating electric field and so the overlap between the optical and modulating electric fields is not so high as would be the case if no buffer layer were present.

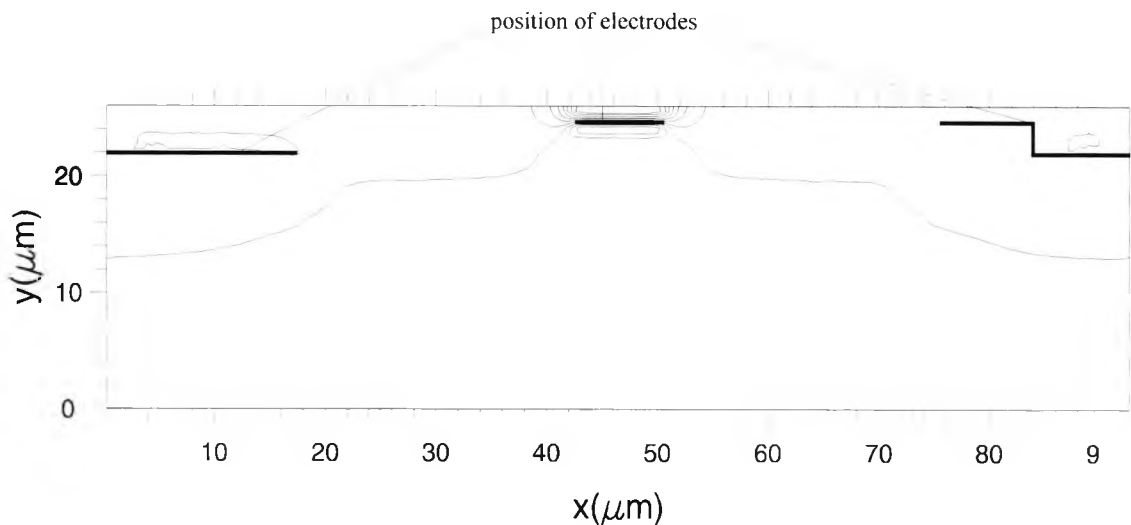


**Fig. 5.25** The  $E_y$  component of the modulating electric field  $\mathbf{E}$  for the etched MZI modulator with ridge height of 3.5  $\mu\text{m}$  for an applied voltage of 5V.

The modulating electric field  $E_y(x,y)$ , obtained from the scalar modulating potential,  $\psi$ , (Davies, 1989) as well as the position of the electrodes for the etched ridge waveguide

modulator is shown in Fig. 5.25. The field is more concentrated around the central electrode, and therefore in the waveguide directly under this electrode, for this etched structure compared with the unetched structure. Hence most of the modulating electric field is acting in guide 1 with virtually no field present in the 2<sup>nd</sup> waveguide, and this has a much less “push-pull” effect than for the unetched waveguide MZI. This feature has also been shown for  $\psi$  by Koshiha and Tsuji (1998) for a similar structure.

So operation for the etched ridge waveguide modulator is essentially that of the single arm interferometer in Fig. 5.1, when considering the switching voltage characteristics of the device. This is not the case for bandwidth characteristics, as the coplanar waveguide (CPW) electrodes have been found to be superior to the asymmetric coplanar strip line (A-CPS) electrode structures (Mitomi *et al.*, 1995).

#### 5.4.2.2 The Linear Electrooptic Effect

As a consequence of the applied electric field the LiNbO<sub>3</sub> crystal experiences a change in refractive index,  $\Delta n_{ij}$ , that is linear to this modulating electric field  $\mathbf{E}(E_x, E_y, E_z)$ . This is known as the linear electro-optic or Pockels effect. The refractive index change  $\Delta n_{ij}$  is first defined as

$$\Delta\left(\frac{1}{n^2}\right)_i = \sum_{j=1}^3 r_{ij} E_j \quad (5.38)$$

where

$$i=1, \dots, 6$$

$r_{ij}$  for LiNbO<sub>3</sub> is given by

$$r_{ij} = \begin{bmatrix} r_{11} & r_{12} & r_{13} \\ r_{21} & r_{22} & r_{23} \\ r_{31} & r_{32} & r_{33} \\ r_{41} & r_{42} & r_{43} \\ r_{51} & r_{52} & r_{53} \\ r_{61} & r_{62} & r_{63} \end{bmatrix} = \begin{bmatrix} 0 & -r_{22} & r_{13} \\ 0 & r_{22} & r_{13} \\ 0 & 0 & r_{33} \\ 0 & r_{51} & 0 \\ r_{51} & 0 & 0 \\ -r_{22} & 0 & 0 \end{bmatrix} \quad (5.39)$$

where

$$r_{13}=8.6$$

$$r_{22}=3.4$$

$$r_{33}=30.8$$

$r_{51}=28$

at a wavelength of 633nm, although these values were also used at 1.55 $\mu$ m (Koshiha, 1999).

It is important to note here that upper case letters are used when referring to the crystal axes, and lower case letters when referring to Cartesian co-ordinates.

The equation of the index ellipsoid in the presence of an electric field is written in full as for equation (B.1) of Appendix B

$$\begin{aligned} \left(\frac{1}{n_x^2} - r_{22}E_Y + r_{13}E_Z\right)X^2 + \left(\frac{1}{n_y^2} + r_{22}E_Y + r_{13}E_Z\right)Y^2 + \left(\frac{1}{n_z^2} + r_{33}E_Z\right)Z^2 \\ + 2r_{51}E_YYZ + 2r_{51}E_XXZ - 2r_{22}E_XXY = 1 \end{aligned} \quad (5.40)$$

When this is then expressed in the quadratic form as for equation (B.4) of Appendix B and using the relationship

$$\Delta n = -\left(\frac{n^3}{2}\right)\Delta\left(\frac{1}{n^2}\right) \quad (5.41)$$

it is possible to rewrite  $\Delta n$  in the form of a much smaller 3x3 matrix (Alferness, 1988)

$$\Delta n_{ij} = -\frac{n^3}{2} \begin{pmatrix} -r_{22}E_Y + r_{13}E_Z & -r_{22}E_X & r_{51}E_X \\ -r_{22}E_X & r_{22}E_Y + r_{13}E_Z & r_{51}E_Y \\ r_{51}E_X & r_{51}E_Y & r_{33}E_Z \end{pmatrix} \quad (5.42)$$

where  $n$  is either  $n_e$  or  $n_o$ .

Therefore, for a  $Z$ -cut  $Y$ -propagating LiNbO<sub>3</sub> substrate for which the incident optical field is polarised along any of the crystallographic axes,  $X$ ,  $Y$  or  $Z$  (as for the quasi TE or TM modes), the index perturbation then only occurs for the diagonal elements 11, 22 and 33

$$\Delta n_x = \Delta n_{11} = -\frac{n_x^3}{2}(-r_{22}E_Y + r_{13}E_Z) \quad (5.43)$$

$$\Delta n_y = \Delta n_{22} = -\frac{n_y^3}{2}(r_{22}E_Y + r_{13}E_Z) \quad (5.44)$$

$$\Delta n_z = \Delta n_{33} = -\frac{n_z^3}{2}(r_{33}E_Z) \quad (5.45)$$

This is a crucial aspect for switches and modulators (Alferness, 1988).

Equations (5.43)-(5.45) can then be written as

$$\Delta n_x = \Delta n_{11} = -\frac{n_o^3}{2}(r_{13}E_Y) \quad (5.46)$$

$$\Delta n_z = \Delta n_{22} = -\frac{n_o^3}{2}(r_{13}E_y) \quad (5.47)$$

$$\Delta n_y = \Delta n_{33} = -\frac{n_e^3}{2}(r_{33}E_y) \quad (5.48)$$

in terms of Cartesian co-ordinates, as  $E_y=E_z=0$  (where  $Y$  is in terms of crystal axes and  $z$  is in terms of Cartesian co-ordinates). This is because the cross-section of the device is unchanged along  $z$  and so  $E_z = \frac{dV}{dz} = 0$

It is well known that the  $r_{33}$  component is the largest of the electro-optic coefficients,  $r_{ij}$ , and that the component of the modulating field  $\mathbf{E}$  in the direction of the optic axis (which was taken as being along  $Z$  in terms of crystal axes), or  $E_Z$  (where  $Z$  is in terms of the crystal axes), causes the largest change due to the linear electro-optic effect. However, if the LiNbO<sub>3</sub> is  $Z$  cut, as for the structures in Figs. 5.18 and 5.19, then in terms of Cartesian co-ordinates, this component of the electric field can be written as  $E_y$ . In which case, the expression for the change in refractive index with applied electric field can be written as

$$\Delta n_e(x, y, V) = -\frac{n_e^3}{2}r_{33}E_y(x, y) \quad (5.49)$$

From the modulating electric field,  $E_y(x, y)$ , the change in the diffused extraordinary refractive index profile,  $\Delta n_e(x, y)$ , for the unetched channel waveguide modulator is found using equation (5.49), and this, together with the position of the electrodes, is

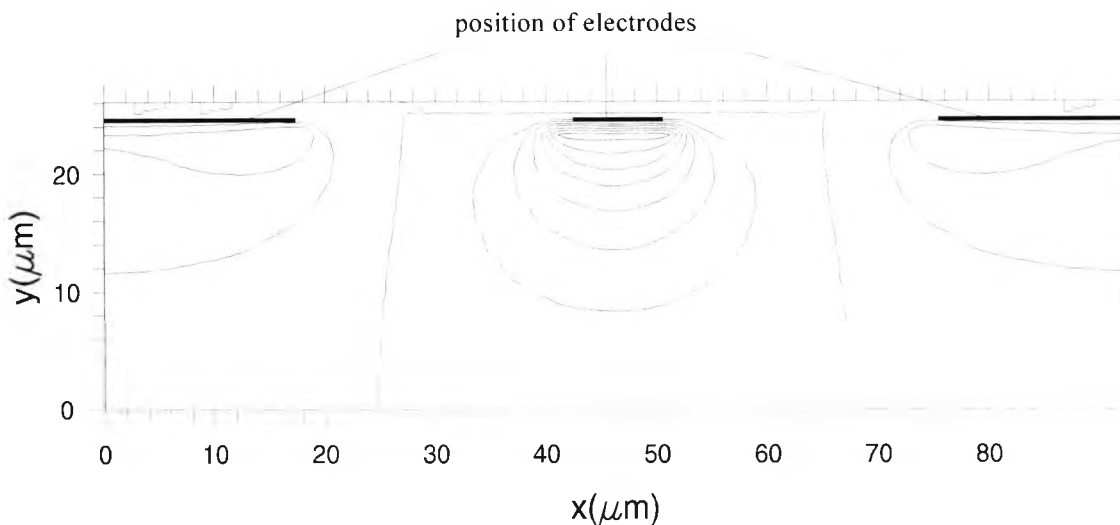


**Fig. 5.26** The change in refractive index due to an applied electric field,  $\Delta n_e(x, y)$ , for an applied voltage of 5V for the unetched MZI modulator.

shown in Fig. 5.26 to be opposite yet unequal in magnitude for the two guides, due to the small and negative modulating electric field in the 2<sup>nd</sup> waveguide. In this case,  $\Delta n_{e_{max}}(1^{\text{st}} \text{ guide})=0.45 \cdot 10^{-4}$ ,  $\Delta n_{e_{min}}(2^{\text{nd}} \text{ guide})=-0.22 \cdot 10^{-4}$ , and this implies that the fraction of the modulating electric field in the 2<sup>nd</sup> guide is about half that in the 1<sup>st</sup> guide.

As for the unetched waveguide MZI, the modulating electric field and consequently the change in refractive index, due to the applied (modulating) electric field, for the etched ridge waveguide modulator, is unequal and opposite in magnitude for the two guides. The diffused extraordinary refractive index change profile,  $\Delta n_e(x,y)$ , for the etched ridge

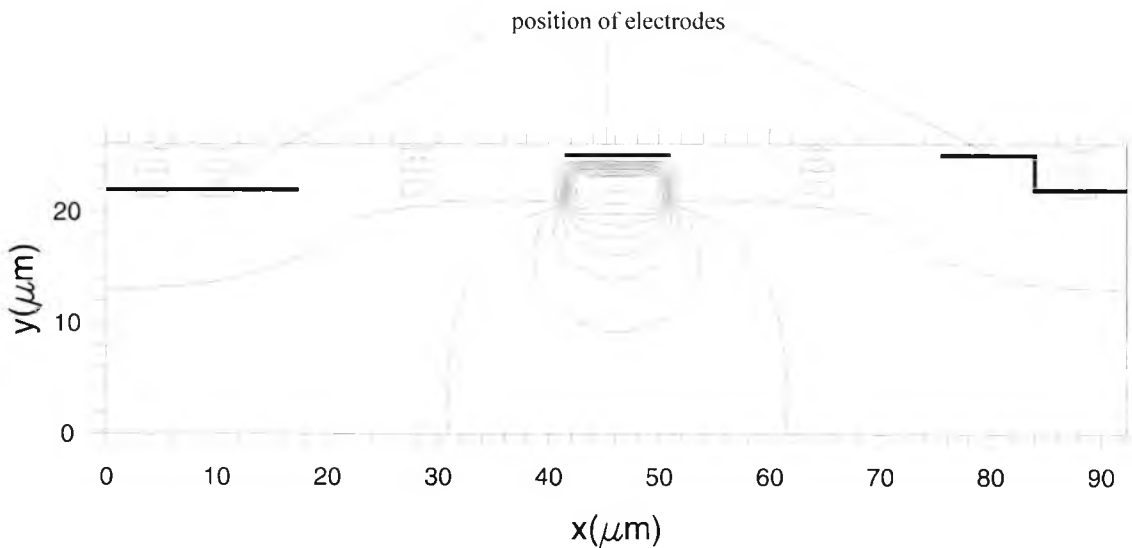


**Fig. 5.27** The change in refractive index due to an applied electric field,  $\Delta n_c(x,y)$ , for an applied voltage of 5V for the etched MZI modulator with ridge height of 3.5  $\mu\text{m}$ .

waveguide modulator is again found using equation (5.49), and this, together with the position of the electrodes, is shown in Fig. 5.27. Thus,  $\Delta n_{e_{max}}(1^{\text{st}} \text{ guide})=0.11 \cdot 10^{-3}$ ,  $\Delta n_{e_{min}}(2^{\text{nd}} \text{ guide})= -0.11 \cdot 10^{-4}$ , and this implies that the fraction of the modulating electric field in the 2<sup>nd</sup> guide is one-tenth of that in the 1<sup>st</sup> guide. This lower value in guide 2 is much smaller than the result obtained for the unetched structure. However, the index change in the 1<sup>st</sup> waveguide is much higher in this case (more than double) than for the unetched MZI modulator, which implies better performance.

Finally, the wave equation is again solved for the two waveguides of the directional coupler under an applied modulation voltage,  $V$ , with the new refractive index profile

$$n_{new}(x, y, V) = n_{old}(x, y) + \Delta n(x, y, V) \quad (5.50)$$

in order to obtain the phase change between the two modulator arms with applied voltage for both the etched ridge and unetched channel waveguide interferometric modulator. As mentioned in Section 5.2.1, it is the voltage with which a  $\pi$  phase shift is obtained that is of interest for the interferometric modulator. At this voltage, there is either no output for a Y-branch interferometric modulator or the output is from the other of the two outputs, than that used to output light at  $V=0$ , for a 1x2 or 2x2 interferometric modulator. This voltage can be obtained, numerically, by taking the phase between the light in the two arms of the interferometric modulator at any two voltages and then either using interpolation or extrapolation, since it is well-known that any change in phase between the light in the two arms is linear with change in voltage.

$V_{\pi}L$ , the product of the voltage at which the phase difference,  $\Delta\phi$ , between the two arms of the MZI is  $\pi$  radians and the length of the electrodes, is one of the most important device characteristics for a guided wave electro-optic device.  $V_{\pi}L$  for the unetched waveguide device was found to be 10.98 Vcm, for a buffer layer thickness of 0.6  $\mu\text{m}$ . For slightly different optical parameters, Noguchi *et al.* (1998) obtained  $V_{\pi}L$  of 13 Vcm for their unetched MZI modulator, and this is in good agreement with our numerically simulated result of  $V_{\pi}L$  of 14.09 Vcm when using the same parameters as Noguchi *et al.* (1998).

Due to the small changes in  $\beta$  with voltage, there is no significant change in these two effective indices for the above structures, and so for both structures the effective index,  $n_{eff}$ , is approximately 2.14.

## 5.5 The Effect of Fabrication Parameters on the Operation of the Etched Ridge Waveguide Modulator

It is well known that fabrication parameters are important to the optimisation of the device performance. Hence, these fabrication parameters were next varied in order to obtain an optimised the device performance.

It has been previously reported that the use of etched ridge waveguides in the interferometric modulator improves the interaction between the optical fields and modulating electric field by concentrating these fields in the ridged regions (Noguchi *et*

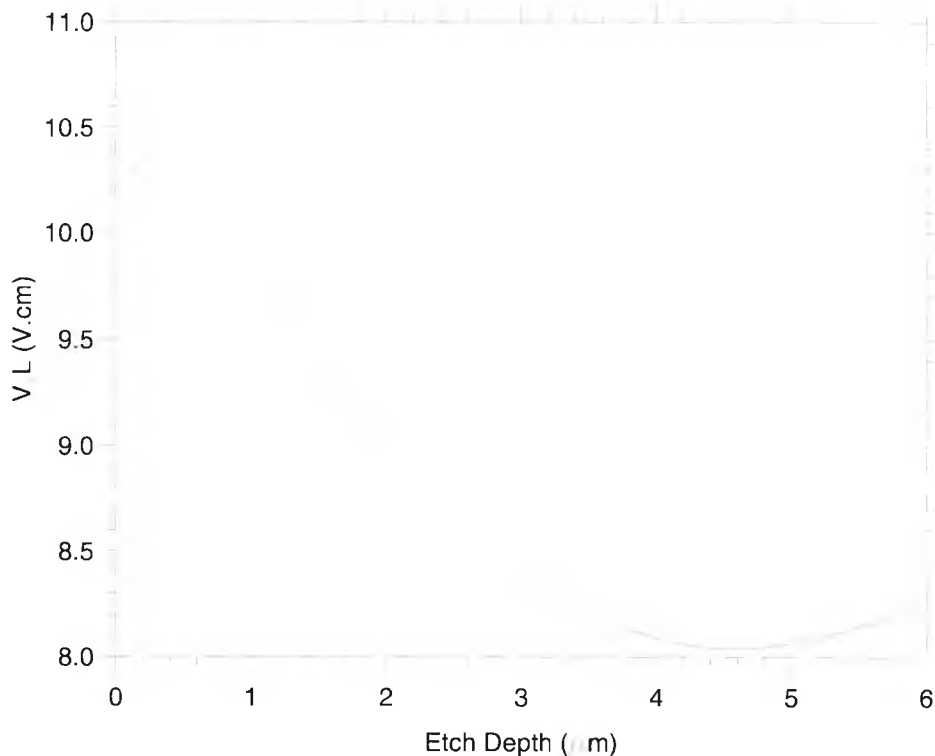


**Fig. 5.28**  $V_{\pi}L$  vs ridge height,  $h$ , for the etched MZI modulator, showing the optimum  $h$  for such a structure.

*al.*, 1993), and so the driving voltage decreases. In Fig. 5.28 it can be observed how  $V_{\pi}L$  varies with ridge height,  $h$ . This shows that  $V_{\pi}L$  reduces with an increasing value of  $h$  and reaches a minimum after which there is only a negligible increase. For a similar structure, such as that given by Noguchi *et al.* (1998), their result for  $V_{\pi}L$  of approximately 8.0 Vcm is very close to our value of 8.22 Vcm. At a value of  $h$  of 4.5 μm,  $V_{\pi}L$  is minimum at 8.03 Vcm. Moreover, the etch depth is limited by the etch rate of the LiNbO<sub>3</sub> (Mitsugi *et al.*, 1998). Hence, the optimum value for the ridge height in this case is taken to be 4.5 μm and this is used for all subsequent work in this study.

It was, however, found by Noguchi *et al.* (1993, 1995) that the optimum ridge height was approximately 3.5 μm. This may be because the 1/e intensity (full depth) of the optical mode,  $w_y$ , for the structures used by these authors was found to be 3.5 μm

whereas for the ridged waveguide modulator designed for this study it was 4.5 $\mu\text{m}$ , making it optimum when  $w_y$  becomes of the same dimension as the ridge height.

The manner in which  $V_{\pi}L$  changes, for the etched ridge interferometric modulator, with a number of other fabrication parameters, as listed in Table 5.2, is discussed below. The

**Table 5.2** A table showing variation in  $V_{\pi}L$  with a number of fabrication parameters.

Original $\tau=90\text{nm}$ , $w=6\mu\text{m}$ , ridge width= $9\mu\text{m}$ , buffer layer thickness= $0.6\mu\text{m}$ , ridge height = $4.5\mu\text{m}$ , electrode separation= $25\mu\text{m}$ & central electrode width= $8\mu\text{m}$ giving $V_{\pi}L=8.03\text{Vcm}$		
Properties modified	$V_{\pi}L$	% change
$\tau=80\text{nm}$	8.576	+6.80%
$\tau=100\text{nm}$	7.772	-3.21%
$w=7\mu\text{m}$	7.723	-3.82%
$w=8\mu\text{m}$	7.605	-5.29%
ridge width= $8\mu\text{m}$	7.495	-6.67%
ridge width= $10\mu\text{m}$	8.552	+6.50%
electrode separation= $23\mu\text{m}$	7.996	-0.42%
electrode separation= $27\mu\text{m}$	8.097	+0.83%
central electrode width= $7\mu\text{m}$	8.490	+5.73%
central electrode width= $9\mu\text{m}$	7.910	-1.49%
buffer layer thickness= $0.45\mu\text{m}$	7.342	-8.57%
buffer layer thickness= $0.75\mu\text{m}$	8.775	+9.28%

device under consideration is a ridge guide MZI device with an etch depth of 4.5  $\mu\text{m}$ . If  $\tau$ , the thickness of the Ti strip before diffusion, is increased from the original 90nm to 100nm, then  $V_{\pi}L$  decreases. This arises because for an increase in  $\tau$ , the optical mode becomes better confined and consequently  $V_{\pi}$  decreases for small optical modes (Veselka and Korotky, 1986). If the Ti strip width prior to diffusion,  $w$ , increases,  $V_{\pi}L$  again decreases. This is because the overlap of the optical and electric field increases. However, the propagation losses may be greater (Noguchi *et al.*, 1998) because of the

proximity of the optical mode to the edge of the ridges. Furthermore, if the ridge width increases from 9 μm to 10 μm, with the electrode separation kept at 25 μm, then the term  $V_{\pi}L$  increases by 6.50%. Similarly, when the ridge width is kept at 9 μm but the electrode separation increases to 27 μm,  $V_{\pi}L$  increases only slightly by 0.83%. This is to be expected since the modulating electric field strength acting in the guides will fall, so the overlap strength will decrease and hence  $\Delta n_e(x,y,V)$  will decrease. This result is in agreement with that of Noguchi *et al.* (1995). If the central electrode width increases from 8 to 9 μm,  $V_{\pi}L$  decreases. This occurs because the region over which there is a stronger electric field (modulating) increases, and so the overlap strength between the electric and optical fields increases. Similarly, if any of the six listed quantities, i.e.  $\tau$ ,  $w$ , the ridge width, the electrode separation, the central electrode width and the buffer layer thickness, decrease by the same amount by which they were increased, then the converse of that which was observed for a positive change in value now occurs for  $V_{\pi}L$ . However, it can be seen that the amounts by which  $V_{\pi}L$  changes for equal positive and negative changes in the six listed parameters are not necessarily equal. Interestingly, it can be observed that a small change in electrode separation does not significantly affect  $V_{\pi}L$ . This is because the electrode separation was originally quite large compared with the other dimensions of the modulator. However, narrowing the ground electrode to similar dimensions as the hot electrode has been found to further reduce  $V_{\pi}L$  (Dolfi and Raganath, 1992). It has also been suggested that increasing waveguide refractive index can also achieve this (Wooten *et al.*, 2000), although a method to achieve this has not been recommended. As was seen in Chapter 4, this can be obtained by increasing  $\tau$  and a number of other diffusion parameters. However, a realistic understanding of the diffusion mechanism needs to be obtained before the diffusion parameters are drastically adjusted.

So it can be seen that  $V_{\pi}L$  detailed above may be reduced by making further variations in the fabrication parameters. This would be particularly necessary in the case of an increased buffer layer, which, as will be seen in subsequent sections of this chapter, leads to an increased  $V_{\pi}L$ , but is required for velocity and impedance matching in the device.

## 5.6 Electrode Design

It was seen in the previous section that the electrode spacing and central electrode width and buffer layer are important to electrode design. However, optical loss (due to the metal electrodes) as well as conductor loss are both important aspects of electrode design.

### 5.6.1 Optical Loss due to the Metal Electrodes

After etch depth, the next most significant parameter is the buffer layer thickness, for which there was found to be a linear (and significant) change in  $V_{\pi}L$ , as shown in Fig. 5.29. In this figure it can be seen that  $V_{\pi}L$  varies from 8.03 Vcm for a 0.6  $\mu\text{m}$  thick buffer layer to about 10.2 Vcm for a 1  $\mu\text{m}$  layer. As the buffer layer increases, so the electrode moves further away from the waveguide area. Hence  $V_{\pi}L$  increases with the increase of buffer layer thickness since the overlap of the modulating electric and optical fields reduces.

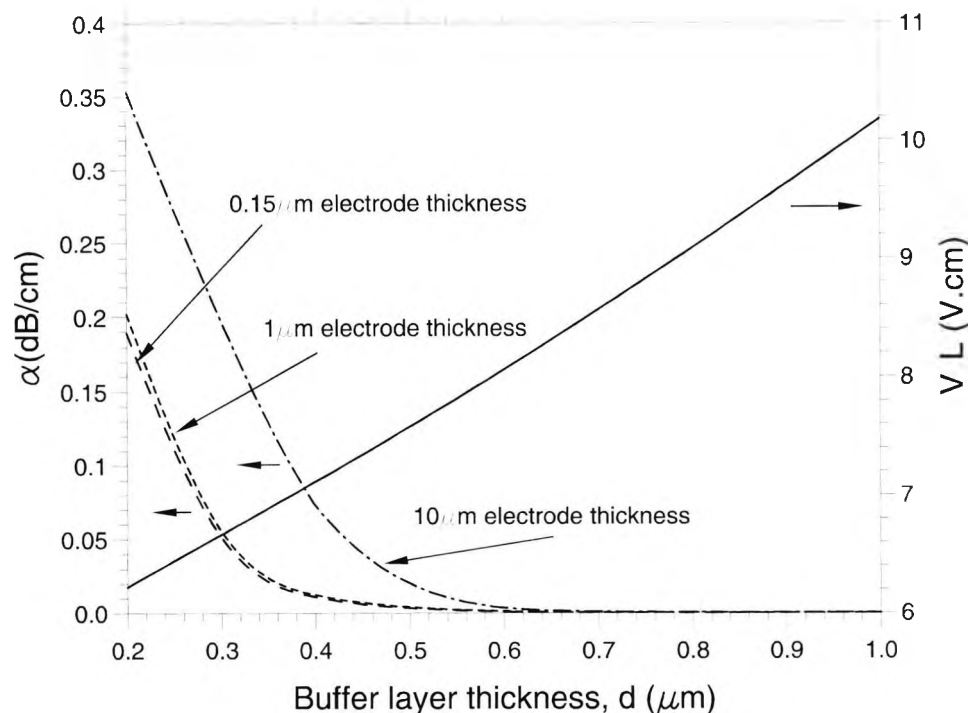


**Fig. 5.29** Optical loss due to metal electrodes vs buffer layer thickness for 3 electrode thicknesses of 0.15  $\mu\text{m}$ , 1.0  $\mu\text{m}$  and 10  $\mu\text{m}$  and  $V_{\pi}L$  vs buffer layer thickness, for the etched MZI modulator with a 4.5  $\mu\text{m}$  ridge height.

Nevertheless, the buffer layer is needed, to reduce the optical loss due to the lossy metal electrodes, particularly for TM-polarized light. As seen in Chapter 3, the source of the optical loss is the complex refractive index of the metal. Consequently, due to the decay of the modulating electric field in the buffer and the Ti:LiNbO<sub>3</sub> material there is, in fact, only a decreasing overlap between the optical and (modulating) electric fields. The calculation of the optical loss due to the metal electrodes is determined using the perturbation method, in conjunction with the finite element method (Themistos *et al.*, 1995a). Fig. 5.29 also shows the optical loss due to the metal electrodes for three electrode thicknesses of 0.15 $\mu\text{m}$ , 1.0 $\mu\text{m}$  and 10.0 $\mu\text{m}$ , and this is shown to decrease with increasing buffer layer thickness. This arises due to a decreasing penetration of the optical field into the metal electrode, the source of the optical loss, due to the increase in the buffer layer thickness. Hence, there is a trade-off between loss due to the electrodes and  $V_{\pi}L$  as the buffer layer thickness increases. However, there is only a slight increase in the optical loss due to the metal electrodes with the electrode thickness, for the three thicknesses used in this part of the study, as is shown in Fig. 5.29. Moreover,  $V_{\pi}L$  does not significantly change with electrode thickness, as also shown by Noguchi *et al.* (1995).

### 5.6.2 The Electrode Design for Impedance and Velocity Matching

Although electrode thickness does not significantly influence  $V_{\pi}L$ , it is a key parameter to optimise the velocity and impedance matching. Fig. 5.30 shows the relationship between the effective microwave index,  $n_m$ , and the characteristic impedance,  $Z_c$ , with the buffer layer thickness,  $d$ , for two values of metal electrode thicknesses,  $t_e$ , of 5 $\mu\text{m}$  and 10 $\mu\text{m}$ , and etched ridge heights,  $h$ , of 0 $\mu\text{m}$  (unetched), 3.5 $\mu\text{m}$  and 4.5 $\mu\text{m}$ , with  $d$  varying from 0.3 $\mu\text{m}$  to 1.6 $\mu\text{m}$ .  $n_m$  and  $Z_c$  are defined in equations (3.33) and (3.34) and  $n_{\text{eff}}$  is defined as  $\beta/k_0$  (where  $k_0$  is the freespace wavenumber).  $Z_c$  varies linearly with  $d$  for all four combinations of  $h$  and  $t_e$  given in figure. Since it was found that  $n_{\text{eff}}$  is close to 2.14 for all three values of  $h$  (i.e. 0, 3.5 and 4.5 $\mu\text{m}$ ),  $n_m$  should be close to this value.  $Z_c$  is usually taken as 50 $\Omega$  since this is a standard terminating impedance for microwave circuits/ devices.

For a ridge height of  $4.5\mu\text{m}$  and electrode thickness of  $10\mu\text{m}$ ,  $Z_c$  is equal to  $50\Omega$  for a value of  $d$  of about  $1.1\mu\text{m}$ . However,  $n_m \cong 2.14$  for  $d \cong 1.44\mu\text{m}$ . So a compromise could be made by choosing  $d$  equal to  $1.3\mu\text{m}$  at which  $Z_c \cong 51.5\Omega$  and  $n_m \cong 2.175$ . For a lower value of  $t_e$  of  $5\mu\text{m}$ , but with the same value for  $h$ , both  $Z_c$  and  $n_m$  are much higher than their corresponding values for  $t_e$  of  $10\mu\text{m}$ , with  $Z_c \cong 50\Omega$  now for  $d \cong 0.55\mu\text{m}$  and  $n_m \cong 2.14$

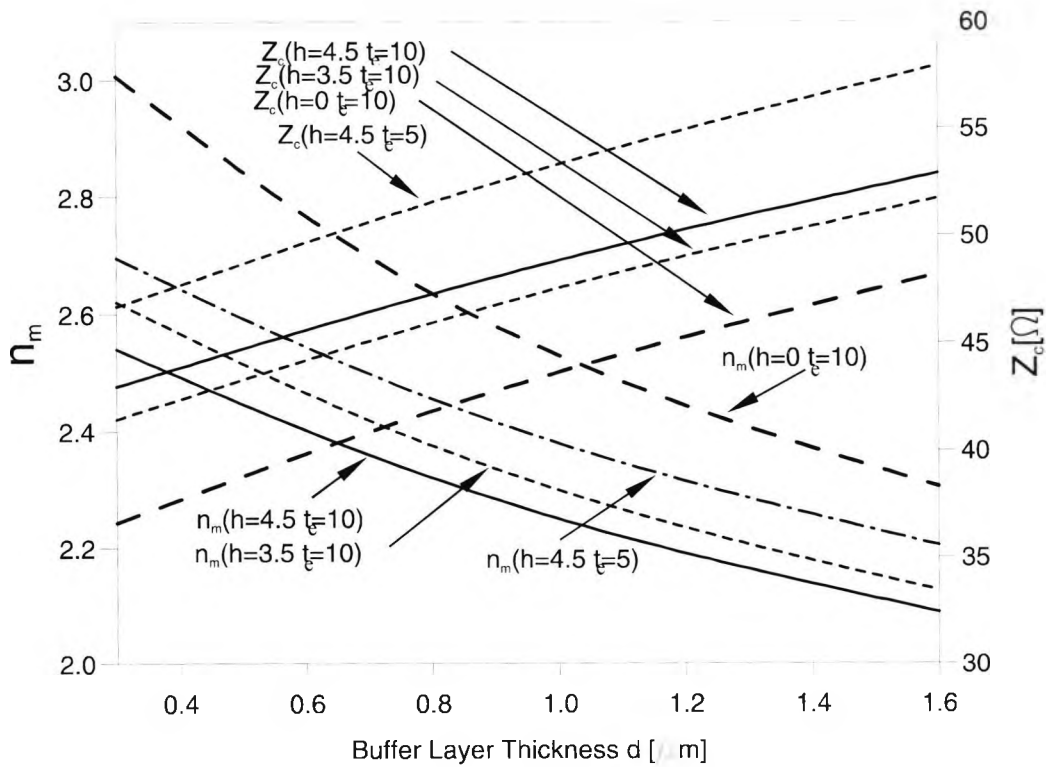


**Fig. 5.30** The microwave effective index,  $n_m$ , and characteristic impedance of the electrodes,  $Z_c$ , vs buffer layer thickness,  $d$ .

for a high  $d$  of greater than  $1.6\mu\text{m}$ . Although not shown in Fig. 5.30, for an even higher  $t_e$  of  $15\mu\text{m}$ , but with the same value for  $h$ , both  $Z_c$  and  $n_m$  are now much lower than their corresponding values for  $t_e$  of  $10\mu\text{m}$ , with  $Z_c \cong 50\Omega$  for a value of  $d$  much greater than  $1.6\mu\text{m}$  and  $n_m \cong 2.14$  for  $d \cong 1.03\mu\text{m}$ .

Keeping the same electrode thickness, with  $t_e$  of  $10\mu\text{m}$ , and lowering the ridge height to  $3.5\mu\text{m}$  and then to  $0\mu\text{m}$ , results in  $Z_c$  decrease and  $n_m$  increase with decreasing ridge height. Moreover, as can be seen in the above description, both  $Z_c$  and  $n_m$  can be increased or decreased by decreasing or increasing  $t_e$ , respectively, even for these lower ridge heights. However, it can be clearly observed that none of the combinations of

ridge heights,  $h$ , and metal electrode thicknesses,  $t_e$ , gives a value of buffer layer thickness,  $d$ , where  $Z_c \cong 50\Omega$  and  $n_m = n_{eff} \cong 2.14$ , as required for velocity and impedance matching. It was then found that for  $h=4.5\mu\text{m}$  and  $t_e=11.15\mu\text{m}$  at  $d=1.296\mu\text{m}$ , both  $Z_c=50.03\Omega$  and  $n_m=2.14$  match simultaneously. It is expected that a similar procedure can be used to find the values of  $t_e$  and  $d$  at which  $Z_c \cong 50\Omega$  and  $n_m \cong n_{eff}$  for any ridge height that may be specified. However, with a much thicker buffer layer,  $V_\pi L$  also increases beyond 11 Vcm, leading to either an increased drive voltage or an increased device length, with the associated disadvantages of increased losses. From this figure it can be noted that for the ridge structure, the electrode thickness needed to match  $n_m$  and  $n_{eff}$  is much thinner than for the unetched waveguide modulator, as reported by Burns *et al.* (1999).

Variations of conductor loss,  $\alpha_c$ , normalized at 1GHz, with the buffer layer,  $d$ , are shown in Fig. 5.31. The conductor loss due to the lossy metal electrodes can be calculated by using a perturbational approach (Pantić and Mittra, 1986), as seen in

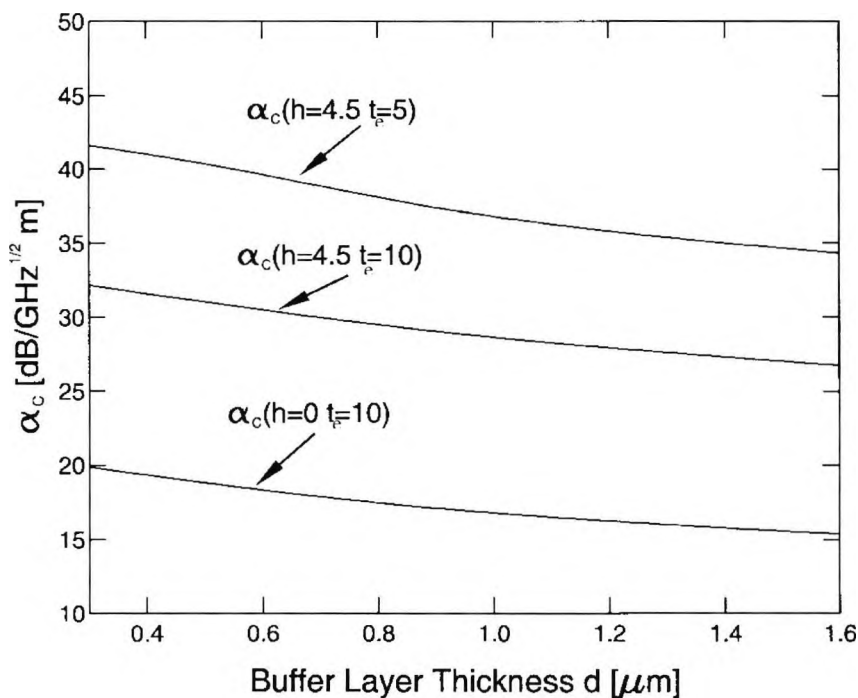


**Fig. 5.31** The conductor loss,  $\alpha_c$  vs buffer layer thickness,  $d$ , for a number of electrode thicknesses,  $t_e$ , and ridge heights,  $h$ .

Chapter 3. It can be seen that  $\alpha_c$  decreases with both an increasing buffer layer and with an increasing electrode thickness,  $t_e$ , and there is a smaller increase with the etched

ridge height,  $h$ . Also,  $\alpha_c$  plays an important role in determining the electrical/modulation bandwidth of a modulator when it is phase matched. For a buffer layer thickness,  $d$ , of 0.5 $\mu\text{m}$ , the electrode gap,  $s$ , of 25 $\mu\text{m}$ , and the etch depth,  $h$ , of 4.5 $\mu\text{m}$ , our simulated results show the electrode thickness,  $t_e$ , should be 28 $\mu\text{m}$  for phase matching, and the corresponding conductor loss,  $\alpha_c$ , is 0.263dB/cm at 1GHz. These results agree well with those of Noguchi *et al.* (1998). However, using equation (3.36), the electrical bandwidth is calculated to be 184 GHz. Although this value seems unrealistic, Minkata (2001) obtained even higher calculated results (of 292 GHz) for perfect velocity and impedance matching conditions. However, the same author has also stated that ‘...the actual bandwidth is less than a limited bandwidth based on the structural dispersion and the material dispersion...’; and equation (3.36) gives the limited bandwidth to which Minakata (2001) has referred.

## 5.7 Uses of Mach-Zehnder Interferometers for Sensing Devices

The majority of integrated-optic sensors employ a Mach-Zehnder interferometer type arrangement, as in the case of the high-voltage sensor design discussed below. A number of other sensor devices which include a passive Ti:LiNbO<sub>3</sub> Mach-Zehnder interferometer in their design are a temperature sensor (Johnson *et al.*, 1982), a gas sensing device (Fushen, 1997) and a silicon micromachined Mach-Zehnder interferometer for pressure sensing (Pavelescu *et al.*, 1997).

Even though bulk electro-optic crystals can also be used as high-voltage sensors, there are clear advantages of using integrated waveguide devices over bulk components (Jaeger and Young, 1989). Fabrication methods can include a capacitive divider to reduce the high voltage (from the high voltage line) to a voltage suitable for use with the Y-branch interferometer (Jaeger and Young, 1989), a Y-branch interferometer able to withstand high-voltage by using electrode spacing of 1mm (Kingsley and Sriram, 1995) where the electrodes are on the top and bottom of the crystal, and one where several buried hot electrodes are placed at a certain range of distances from the buried common ground electrode, which is placed between the branches of the interferometer,

thereby increasing the sensing range on the same substrate (Yim and Shin, 1998). These three designs are mentioned as examples rather than expressing the opinion that these are the only way to fabricate high-voltage sensors.

The majority of integrated optic voltage sensors have used an *X*-cut LiNbO<sub>3</sub> substrate (Yim and Shin, 1998). The main advantage for modulators formed with an *X*- or *Y*-axis crystal cut is that they are essentially thermally stable, require no buffer layer, and hence will not suffer from pyroelectric effects or buffer-related drift effects (Greenblatt *et al.*, 1995) as for a modulator formed using a *Z*-cut LiNbO<sub>3</sub> substrate which requires a buffer layer in order to minimize optical loss. The disadvantage with the *X* or *Y* crystal cut is that it requires a three-electrode arrangement to be used in a push-pull manner and so leads to higher capacitance of the device (Alferness, 1988), which indicates that operation at as high a speed as is possible with *Z*-cut LiNbO<sub>3</sub> modulators may not be achieved since the bandwidth will be lower. However, for the high voltage sensor high-speed operation is not required since the operation will be typically at 50/60 Hz (mains voltage) signals. Moreover, this higher device capacitance may actually be an advantage to the sensor that uses a capacitive divider to convert high voltage to one suitable for use with the *Y*-branch interferometric modulator, as the maximum sensing voltage is dependent on the ratio of the small capacitance from sensor to high voltage line,  $C_t$ , to the larger capacitance from the sensor to ground,  $C_g$  (Jaeger and Young, 1989).

Two of the three high voltage sensor structures (Kingsley and Sriram, 1995; Yim and Shin, 1998) given as examples (in an earlier paragraph) used annealed proton exchange to form the guides, one of these structures used ferroelectric domain inversion techniques to obtain reverse poling in one arm. A more popular method of waveguide formation in LiNbO<sub>3</sub> is through Ti indiffusion of the dielectric crystal, as it supports more than one light polarisation and is generally thought to incur less propagation loss, even for etched ridge waveguides (Barry *et al.*, 1999).

The simplest of these three structures, mentioned in the previous paragraph, takes the form of a capacitive divider fabricated from *Z*-cut LiNbO<sub>3</sub> and mounted onto the same platform as the *X*-cut *Y*-branch interferometer to create the high voltage sensor (Jaeger and Young, 1989). It is the thickness of the dielectric capacitive divider that is responsible for the range of high voltages which may be accessed (through the divider)

by the interferometer. However, it is only the design of the interferometer that is of interest in this study and to which the following pages will be allotted.

Firstly, it was proposed that a Y-branch interferometer based on the design employed by Jaeger and Young (1989) was modelled in this section of the chapter and the results then compared with those obtained experimentally by these authors. In order to achieve this goal the model used to simulate the devices in the earlier sections of this chapter would have to be extended to include X-cut Ti:LiNbO<sub>3</sub> modulators. The structure is given in Fig. 5.32, where the centre-to-centre gap between the waveguides,  $s+w$ , was fixed at 60 $\mu\text{m}$ . The width of the waveguides,  $w$ , was varied between 6 $\mu\text{m}$  and 16 $\mu\text{m}$ , and  $e$ , the gap between the electrodes was varied between 10 $\mu\text{m}$  and 20 $\mu\text{m}$ .

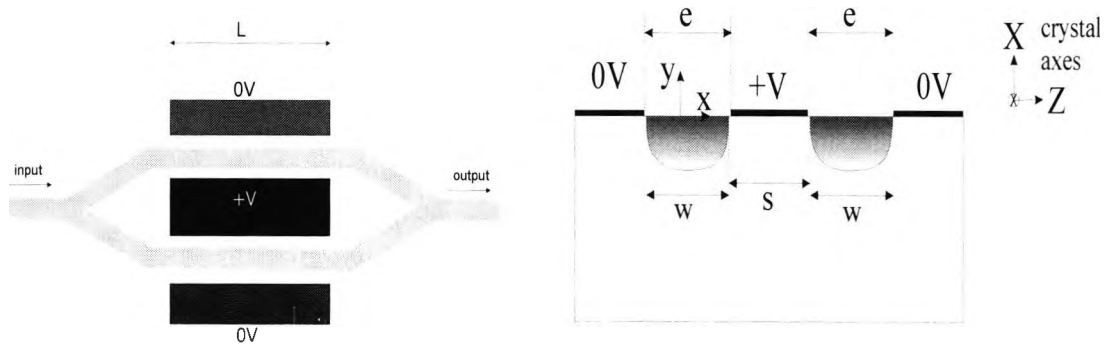


**Fig. 5.32** Schematic of the Mach-Zehnder interferometer considered: (a) layout and (b) cross-section.

The Mach-Zehnder arrangement shown in Fig. 5.32, is not only the basis for the majority of integrated-optic sensors (Jaeger and Young, 1989; Yim and Shin, 1998), but for components in other communications systems (Bulmer and Burns, 1984; Alferness, 1988), as mentioned in Sections 5.1 and 5.2. A number of variations in the type of structure shown in this figure exist, as shown in Section 5.2, but which all follow a very similar principle of operation.

For the diffusion parameters,  $T=980^\circ\text{C}$ ,  $t=6$  h, using equation (5.18) with diffusion constants,  $D_0^{x,y}$  and activation energies,  $E_0^{x,y}$ , given by Fukuma and Noda (1980) for  $y$ -plate LiNbO<sub>3</sub> (i.e.  $D_0^x = 2.5 \times 10^{-5} \text{cm}^2/\text{s}$ ,  $D_0^y = 3.47 \times 10^{-2} \text{cm}^2/\text{s}$ ,  $E_0^x = 1.54 \text{eV}$ ,  $E_0^y = 3.47 \times 10^{-2} \text{eV}$ ), it was found that  $d_x=11.75 \mu\text{m}$ ,  $d_y=6.18 \mu\text{m}$ . Hence, the diffusion length

along  $x$ ,  $d_x$ , is nearly twice that along  $y$ ,  $d_y$ , which is usually the case for a  $X$ - or  $Y$ -cut LiNbO<sub>3</sub> crystal (Wooten and Chang, 1993), and because of this the lateral diffusion for the waveguides extends over a width of 37.5 $\mu\text{m}$ , yet the diffusion depth is around 10 $\mu\text{m}$ . However, as seen in the previous sections of this chapter for  $Z$ -cut LiNbO<sub>3</sub> the diffusion lengths  $d_x$  and  $d_y$  are comparable, as are consequently the diffusion depths and widths of the waveguides for that structure. The operating wavelength was taken to be 633nm: the same as for Jaeger and Young (1989). It is well known that photorefractive effects occur at wavelengths lower than 1 $\mu\text{m}$  and these can cause propagation loss. At 0.633 $\mu\text{m}$ ,  $n_e$  and  $n_o$  for LiNbO<sub>3</sub> are 2.2020 and 2.2865 (Hobden and Warner, 1966). Furthermore, at this wavelength a titanium layer thickness prior to diffusion,  $\tau$ , of 40nm will lead to  $\Delta n_e$  and  $\Delta n_o$  of 0.00147 and 0.00188, respectively (Korotky and Alferness, 1987). At longer wavelengths even lower values of  $\Delta n_e$  and  $\Delta n_o$  will be attained (see equation (5.23)), so leading to even larger optical modes.

The width of the titanium strip prior to diffusion,  $w$ , directly affects  $\Delta n_{e,o}$ , the increase in extraordinary and ordinary refractive indices, respectively, of the LiNbO<sub>3</sub> due to the Ti concentration and the variation of  $V_\pi$  with  $w$  was observed for this study. The large lateral diffusion length,  $d_x$ , leads to the waveguides of the interferometer, including those formed with  $w$  as small as 6  $\mu\text{m}$ , being very multimoded, which may be adequate or even good for sensors, but not for other communications applications where a single-moded device is required. It is for this reason that the extinction ratio was found to be low (Jaeger and Young, 1989), as the output power will be a result of the interaction between all the guided modes. However, for this application it was understood that extinction ratio is less important than the intrinsic phase. Intrinsic or initial phase (phase difference for zero applied voltage) can be attained by adding  $\lambda_g/4$  to the length of one of the arms of the interferometer; or by tight control of the initial quantity of impurity in, and the stoichiometry of, the LiNbO<sub>3</sub> substrate (Wooten *et al.*, 2000). It is common to choose this initial phase to be  $\pi/2$ , in order to achieve linear operation of the device (Bulmer and Burns, 1984). Linearity is a requirement for all analogue applications, including sensor applications. Since almost all modulators have nonlinear transfer functions, they have to operate at certain bias points such that they have good linearity and an intermodulation-free (from harmonics) dynamic range (Dagli, 1999). However, the suggested asymmetric device then suffers from 3 dB greater loss than a similar

symmetric interferometer, because it is operating about its half-maximum transmission point (Bulmer and Burns, 1984).

As mentioned previously, the electrode configuration is dependent on the crystal cut. Taking the example of an *X*-cut or *Y*-cut LiNbO<sub>3</sub> crystal, the *Z* direction of the crystal will then typically be parallel with the *x*-axis (in terms of Cartesian co-ordinates). The maximum electro-optic effect is only achieved when the electric field,  $\mathbf{E}$ , is parallel to the optic axis (which is commonly accepted to be in the *Z* direction of the crystal) and the polarisation of light is also in the same direction. This would indicate that the component of the electric field,  $\mathbf{E}$ , which would bring about this effect is  $E_x(x,y)$ . In order to achieve a phase difference between the two guides of the interferometer, a three-electrode arrangement can be used to operate the device in a push-pull fashion. In this case, in order to achieve the maximum electro-optic effect the polarization of the light needs to be quasi-TE.

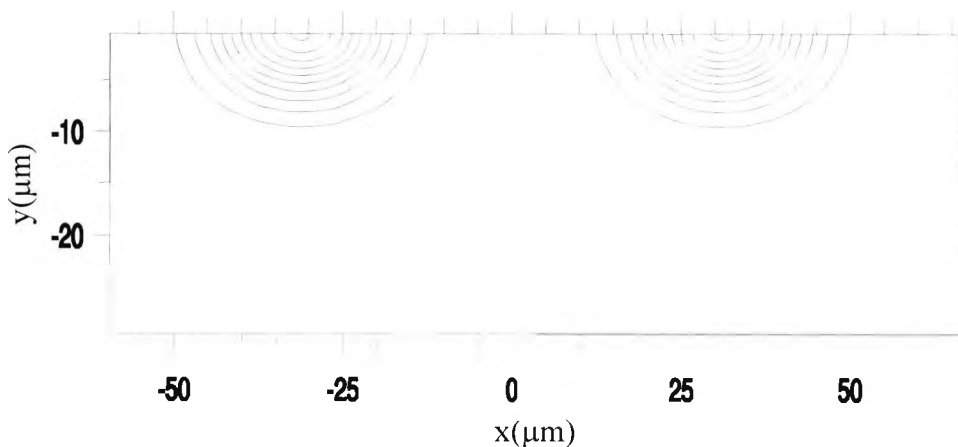


**Fig. 5.33** Diffusion profile for the Mach-Zehnder interferometer shown in Fig. 5.32.

Hence, it can be easily observed that only the extraordinary refractive index,  $n_e$ , affects the modal solution both before and after application of the electric field and also, that only  $n_e$  is changed by the application of the field. Therefore,  $n_o$  is not significant to this simulation.

The calculation of the refractive index of the device (with centre-to-centre waveguide separation of 60 $\mu\text{m}$ ) and, hence, the diffusion profile is determined as in Section 5.3.1.

The refractive index profile,  $n_e(x,y)$ , for the Ti indiffused X-cut Y-propagating LiNbO<sub>3</sub> substrate is shown in Fig. 5.33.

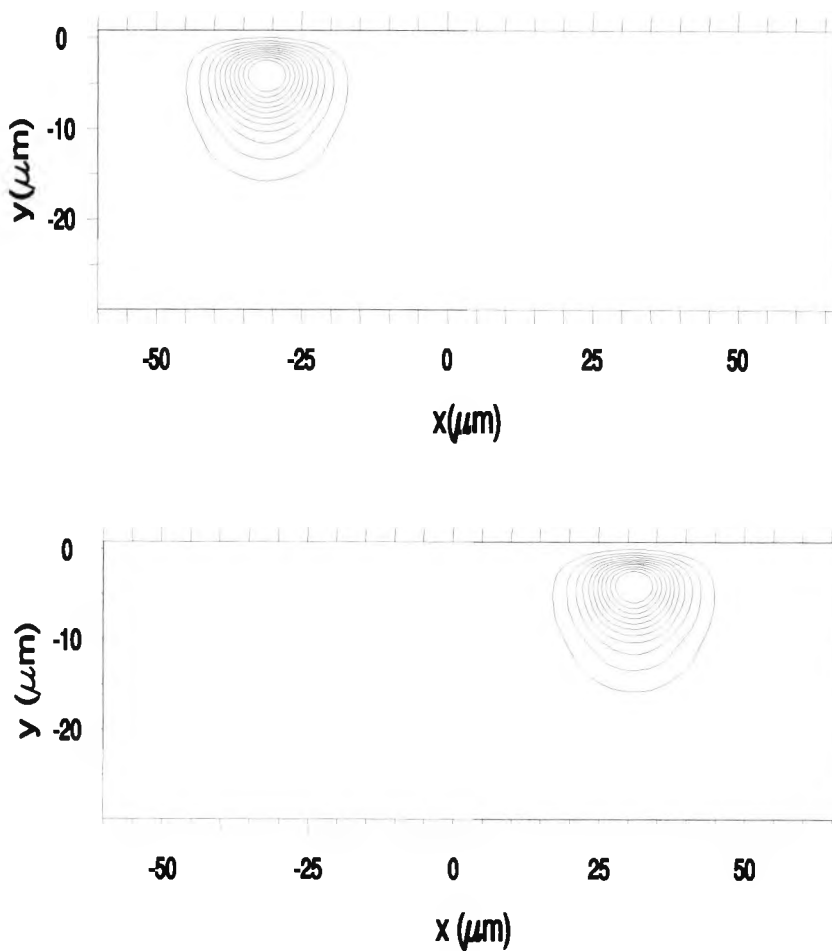
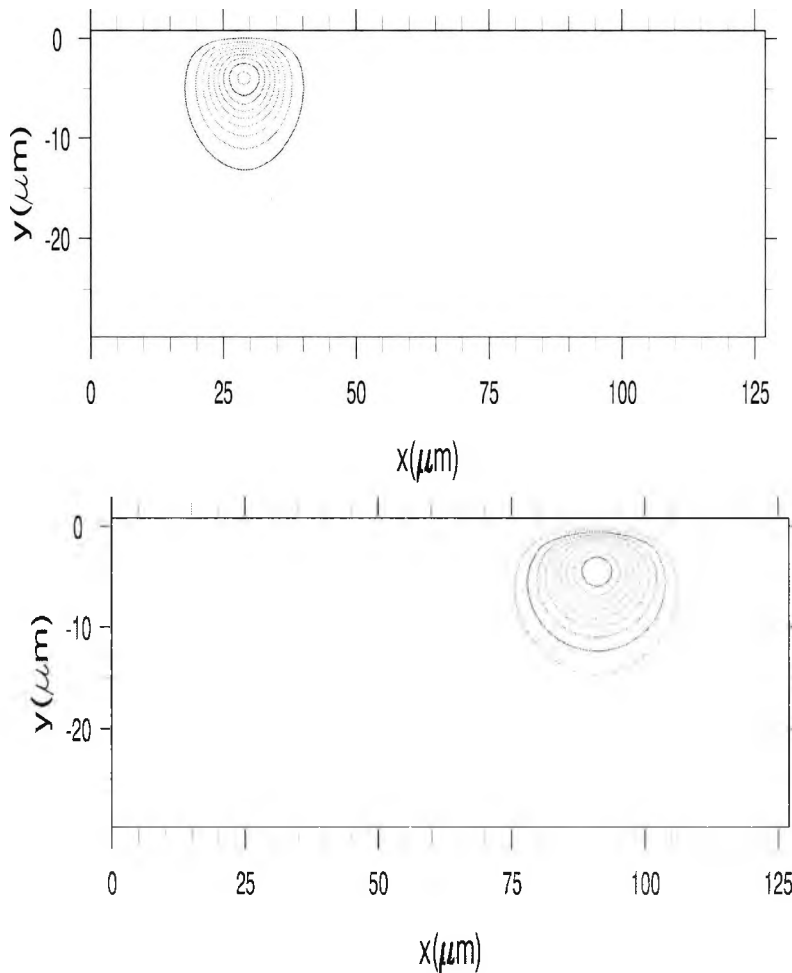


Fig. 5.34 Degenerate quasi-TE fundamental optical modes at  $V=0$ .

The degenerate fundamental optical modes when no voltage is applied to the electrodes are given in Fig. 5.34. The optical propagation constant,  $\beta$ , for these two modes is  $21.8602055 (n_{eff}=2.2023)$  and  $21.8602022 (n_{eff}=2.2023)$ . The  $1/e$  intensity full width,  $w_y$ , for these modes is  $18.36 \mu\text{m}$  and the  $1/e$  intensity full depth,  $w_x$ , is  $8.87 \mu\text{m}$ . The effective indices for both the modes are close to that of the LiNbO<sub>3</sub> substrate index and that the mode depth is larger than  $d_y$ , indicates operation may be close to cutoff.

When a voltage is applied to the electrodes of an interferometric modulator in a push-pull fashion as shown in Fig. 5.32, the refractive index increases in the left arm and decreases in the right arm. Hence, the mode becomes more tightly confined in the left arm and larger in the right arm compared with the optical modes for  $V=0$  (in Fig. 5.34). These modes are no longer degenerate. Fig. 5.35 shows the optical modes for  $V_{\pi}$ , which



**Fig. 5.35** Degenerate quasi-TE fundamental optical modes at  $V=V_\pi$

for  $w$  of  $6\mu\text{m}$  and electrode separation,  $e$ , of  $10\mu\text{m}$  was found to be approximately  $17.4\text{V}$ . For this study the electrode length,  $L$ , is assumed to be  $1\text{mm}$ , unless otherwise indicated. There is a clear difference between the modes at  $V=0$  and those at  $V=V_\pi$ .

Fig. 5.36 shows  $\Delta\phi$  and  $L_\pi$  vs voltage,  $V$  for the waveguide width,  $w=6, 8$  and  $16\mu\text{m}$ .  $L_\pi$  is the proposed electrode length at any particular voltage such that the product of  $\Delta\beta L_\pi$  gives a  $\pi$  phase difference between the two arms of the interferometer, i.e. guides 1 and 2. The corresponding electrode gaps,  $e$ , are  $10, 12$  and  $20\mu\text{m}$  for  $w=6, 8,$  and  $16\mu\text{m}$ , respectively. Hence, it is clear that the distance from the waveguide edge (where the waveguide width,  $w$ , is defined as the titanium (Ti) strip width prior to diffusion) to the electrode edge is kept at a constant distance of  $2\mu\text{m}$ , for both the inner and outer electrodes. It can be seen in Fig. 5.36 that  $L_\pi$  is large for smaller values of  $V$  and decreases with increasing values of  $V$ , as expected since  $\Delta\beta$  and  $L$  are inversely

proportional to each other, as seen in equation (5.1). As expected,  $V_\pi$  decreases with decreasing  $w$ . This is because in reducing  $w$ , the electrodes are brought closer together and hence the magnitude of the electric field increases in the region of the waveguide.

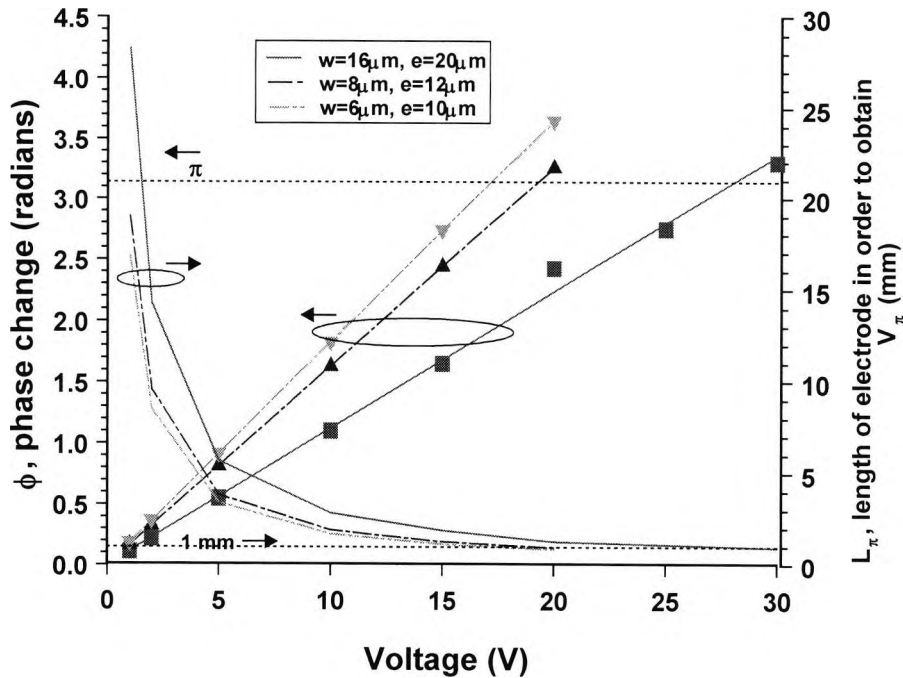


Fig. 5.36 Variation of  $\Delta\phi$  and  $L_\pi$  with sensing voltage,  $V$ .

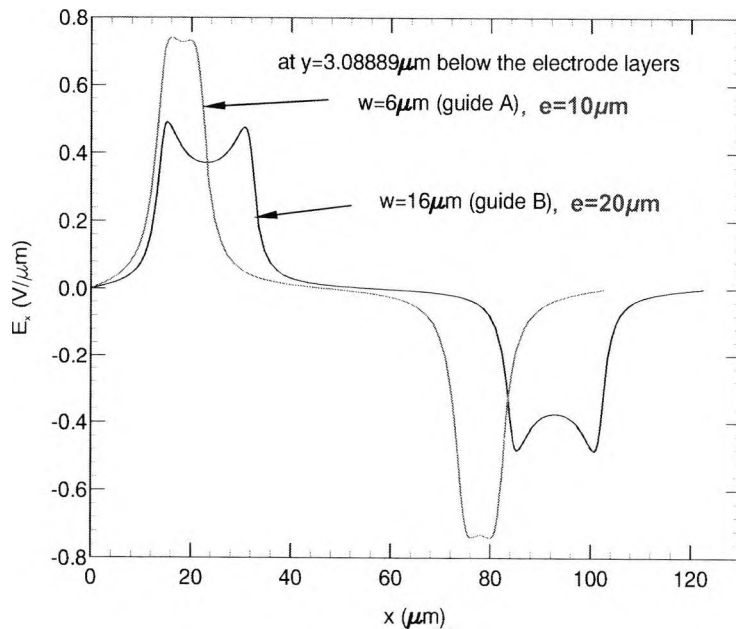
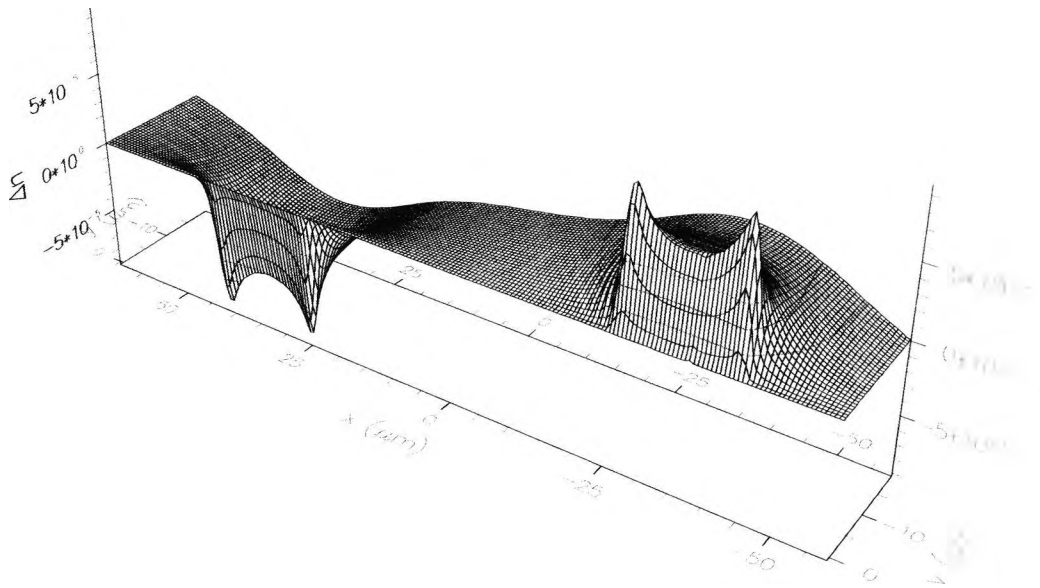
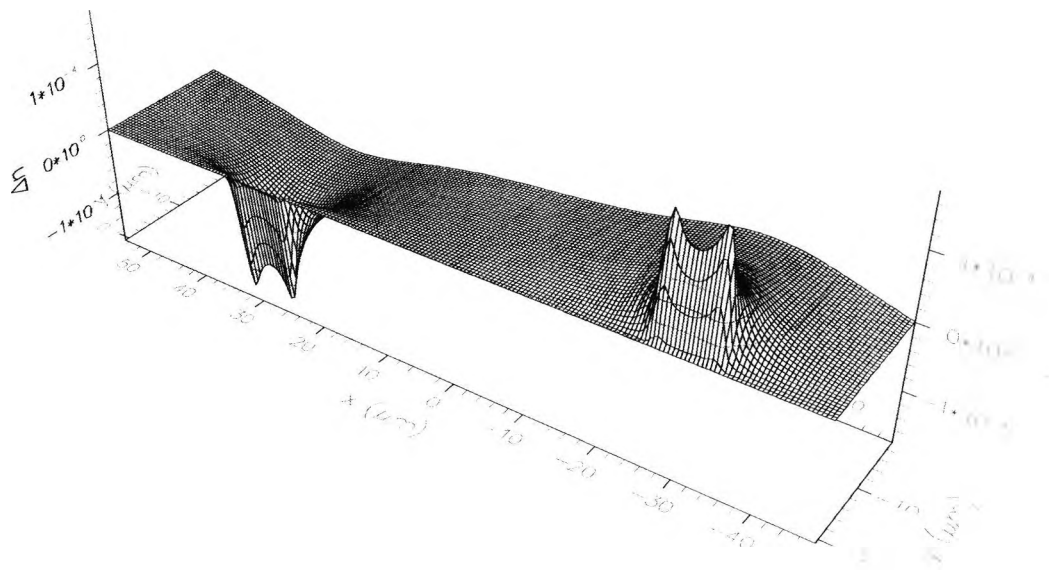


Fig. 5.37 Variation of the sensing field,  $E_x$ , along the waveguide centre for an applied voltage of 10V.

This can be seen in Fig. 5.37, where  $E_x$  (in terms of Cartesian co-ordinates) or  $E_z$  (in terms of the crystal axes) is given for both  $w=16\ \mu\text{m}$  with  $e=20\ \mu\text{m}$  and also for  $w=6\ \mu\text{m}$  with  $e=10\ \mu\text{m}$ . Moreover, since the magnitude of the electric field increases in the waveguide region, the overlap between the optical and electric fields also increases.



(a)



(b)

**Fig. 5.38** The spatial profile of the refractive index change,  $\Delta n$ , for a given applied voltage,  $V=10\text{V}$  when: (a)  $w=16\ \mu\text{m}$  and (b)  $w=6\ \mu\text{m}$ .

Another notable feature in Fig. 5.37 is that the electric field is definitely not flat in the region of the waveguide, as is assumed in a large number of studies (Jaeger and Young, 1989). These studies only used a simple analysis of electrode design rather than the rigorous numerical approach undertaken for this study. As expected, since  $\Delta n$  is directly proportional to  $E_z$ , a similar effect can be seen in Fig. 5.38 where the 3-d plots for  $\Delta n(x,y)$  for  $w=16\ \mu\text{m}$  and  $w=6\ \mu\text{m}$  are shown.

Fig. 5.39 shows the phase difference for a same waveguide width,  $w$ , but for different electrode gaps. This shows that as the electrode gap decreases, the phase change increases for a given sensing voltage. This is because the electric field intensity increases in the region of the waveguide, as the electrode gap decreases for any size waveguide (see Fig. 5.37), and so the overlap between the optical and electric fields

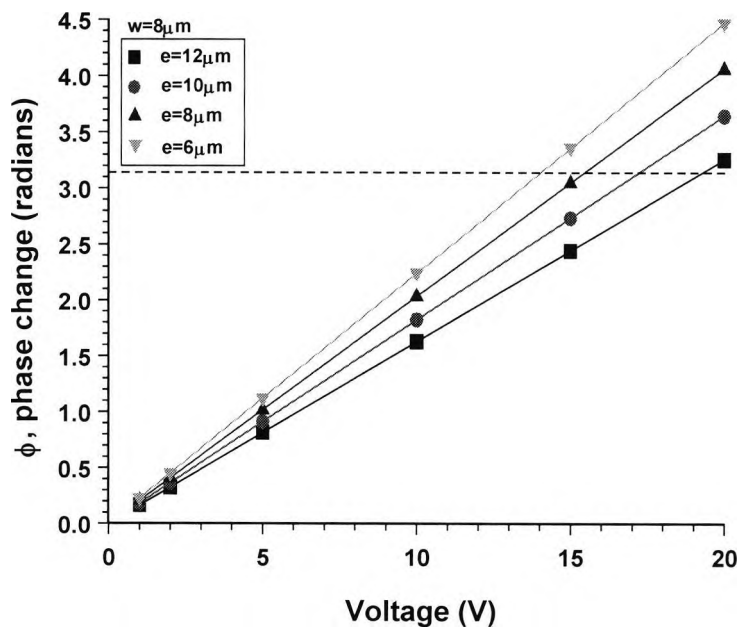


Fig. 5.39 Variation of  $\Delta\phi$  with different electrode gaps,  $e$ .

increases. Hence  $V_\pi$ , the sensing voltage for which a phase difference of  $\pi$  (represented by the dotted line in Fig. 5.39) is obtained, decreases with the reduction of the electrode gap,  $e$ . There is, however, likely to be an increase in optical loss due to the proximity of the metal electrodes to the waveguides. This problem can be alleviated by the application of a buffer layer between the LiNbO<sub>3</sub> surface and the electrodes. However, this again would lead to a decrease in the overlap between the optical and electric fields and would therefore lead to an increase in  $V_\pi$ . Nevertheless, use of a buffer layer would

lead to the device suffering from pyroelectric or bias drift effects, and so would definitely not be used for sensor applications. Moreover, depending on the design of the electrodes, a decrease in the electrode gap could lead to an increase in the total surface area of the metal and this will lead to increased capacitance of the device, which would adversely affect the capacitive divider.

Hence, for the purposes of this section of the study and to conform the validity of this model it is essential to perform a simulation of the device proposed by Jaeger and Young (1989) using identical fabrication parameters. It was found that for a centre-to-centre waveguide separation of 70 $\mu\text{m}$ , with electrode separation,  $e$ , of 20 $\mu\text{m}$  and length of electrodes of 1 $\mu\text{m}$ ,  $V_\pi$  was found to be 41.73V. This is very close to the value found experimentally by Jaeger and Young (1989) of 45V.

## 5.8 Summary

It is therefore clear that the use of a ridge waveguide in the MZI device improves a number of device characteristics, particularly  $V_\pi L$ .

In summary the following observations can be made:

- variation of radiation loss with  $\theta$  is linear for circular bends of any radii (in agreement with Obbaya (1999))
- radiation loss decreases with ridge height
- there is a significant reduction in the overall length of the MZI device due to the use of the etched ridge waveguide (since tighter optical modes leads to smaller device geometry (Ashley *et al.*, 1989))
- for the etched ridge modulator, modulating field is mainly around the central electrode with very little around the ground electrode (in agreement with Tsuji and Koshiha (1998))
- for the simulated unetched channel waveguide modulator, with parameters identical to those given by Noguchi *et al.* (1998), a  $V_\pi L$  of 14 Vcm was obtained. This compared well with their value of 13 Vcm from experimental results. However, the structure which was proposed in this work gave a  $V_\pi L$  of 10.98 Vcm

- for the simulated etched ridge waveguide modulator, with parameters identical to those given by Noguchi et al. (1998), a  $V_{\pi}L$  of 8.22 Vcm was obtained. This compared well with their value of 8.0 Vcm from experimental results. However, the structure which was proposed in this work gave a  $V_{\pi}L$  of 8.03 Vcm
- for a reasonable and fixed value of  $V_{\pi}$  a reduction in the interaction length,  $L$ , occurs for the etched ridge waveguide device compared to the unetched device
- $V_{\pi}L$  did not significantly reduce with electrode thickness (in agreement with Noguchi et al. (1995))
- a reduced electrode thickness,  $t_e$ , is obtained for the etched ridge waveguide interferometric modulator compared with the unetched device when both velocity and impedance matching are required (in agreement with Burns *et al.* (1999))
- device size can also be reduced laterally, when using an etched ridge waveguide, by placing the two arms of the MZI closer together without the fear of evanescent coupling since when the separation between the waveguides (and therefore electrode separation) was varied there was negligible change in  $V_{\pi}$  (this is in agreement with Noguchi *et al.* (1995)) This is because air (which has a much lower refractive index than LiNbO<sub>3</sub>) is separating the two ridge waveguide

Although, a smaller radius can be achieved with the etching of the Ti:LiNbO<sub>3</sub> waveguides for the circular bends leading to the Y-junction, these are still larger than those achievable with semiconductor rib waveguide devices (Zucker *et al.*, 1990). This is because the refractive index difference between the guiding region and the substrate for these p-i-n doped semiconductor waveguides is typically much larger than that achievable with Ti indiffusion into the LiNbO<sub>3</sub> substrate.

It would have been interesting to observe whether the device characteristics would be affected by incorporating sloping sidewalls into the model, even though it was reported otherwise. This issue can be examined in the next chapter.

The small study on the sensor has given additional information on how electrode design and crystal cut (affects the half wave voltage.

- for X- or Y-cut LiNbO<sub>3</sub> for Ti indiffusion  $d_x \sim 2d_y$
- it was shown that the results from the model corresponded (from suite of programs used in this work,  $V_{\pi}$  was 41.73V and from experiment results in published work

(Jaeger and Young, 1989) for same device 45V) with those obtained from the literature for a comparable device.

This model can now have other features added to it or be used as a core set of programs for other electro-optic modulators or LiNbO<sub>3</sub> devices.

# 6

## *GaAs/Al<sub>x</sub>Ga<sub>1-x</sub>As Electrooptic Waveguide Modulator*

---

---

### **6.1 Introduction**

Although Ti:LiNbO<sub>3</sub> electro-optic modulators have many positive features, the main drawback with using this material is the fact that it cannot be monolithically integrated with other semiconductor devices, more specifically with semiconductor lasers which are used as a source of light in the optical circuit. This is because there is no possibility of growing a semiconductor on the LiNbO<sub>3</sub> crystal substrate or vice versa. Even though LiNbO<sub>3</sub> has been experimented with as a light source (Baumann *et al.*, 1996) it has never been found to be anywhere near as efficient as any standard laser source. Semiconductor modulators therefore have the major advantage of integrating with other semiconductor devices (particularly semiconductor lasers), as well as having other advantages and disadvantages (Dagli, 1999), over their dielectric counterparts and these will be covered in the following sections. The tendency towards integration on the same chip is due to smaller size and greater efficiency of such a multi-function unit/device, which should ultimately lead to a cheaper fabrication process.

For semiconductor materials, horizontal (transverse) waveguiding is achieved from

sandwiching a higher refractive index material (e.g. GaAs) between the lower refractive index materials (e.g. AlGaAs). In Section 1.4.1 of Chapter 1 of this thesis it was shown in some detail as to how the light is guided in these simple planar waveguide structures. Lateral waveguiding is typically achieved through etching a rib into the structure, and hence a waveguide with two-dimensional optical confinement in the transverse direction is formed. Typically 90° vertical ribs are achieved through dry-etching (Heaton *et al.*, 1995) whereas slanted ribs are more commonly obtained by wet-etching (Sakamoto *et al.*, 1998) and both of these are considered in this work.

Of the semiconductors available, undoped GaAs-based materials are more commonly used, especially among travelling wave (TW) modulators (Dagli, 1999), as both devices and drive circuits are more easily designed than for GaAs TW modulators that use a  $n^+$  buried epitaxial layer (which acts a ground plane). Also, it is typical that the epitaxial layers are lattice matched (Gowar, 1984) but for other applications this is not always the case (e.g. for MQW lasers (Dagli, 1999) where it is more advantageous to achieve compressive or compressive and tensile strain (through lattice mismatch), for GaAs or InGaAsP material systems, respectively, with typical values being ~1% (Chen *et al.*, 1998))

As was seen in earlier chapters, some of the first GaAs-based devices were the GaAs homojunction p-n devices (Yariv and Leite, 1963); however, electro-optic modulation was first observed for GaP p-n junctions (Nelson and Reinhart, 1964), followed by the GaAs/Al<sub>x</sub>Ga<sub>1-x</sub>As heterojunction p-n modulator (Reinhart and Miller, 1972) (which consisted of the higher refractive index GaAs waveguiding layer sandwiched by the lower refractive index Al<sub>x</sub>Ga<sub>1-x</sub>As layers). GaAs directional coupler-based modulators (Campbell *et al.*, 1975) were then later fabricated and studied. These early devices were operated only on the basis of the linear electrooptic effect. The growth of the larger width intrinsic layer between the two thin p and n doped regions was incorporated into this type of device at a later date. The reason for this is to achieve a higher response to the incoming lightwave, with the depletion region extending through this intrinsic layer for only a few volts (due to the high resistivity of the intrinsic layer). Soon after it was also recognised that these p-n or p-i-n semiconductor junction devices, when working near the bandedge of the device, were not only controlled by the linear electro-optic effect but more so by the electroabsorption effect. Hence, they were called

electroabsorption (EA) modulators. However, it was during the late 80s and early 90s that an understanding of the operation and modelling of semiconductor p-i-n was developed (Mendoza-Alvarez *et al.*, 1988; Faist and Reinhart, 1990a; Lee *et al.*, 1991). This was at the same time that the understanding and development of multiple quantum well (MQW) devices was taking place (Wood *et al.*, 1984; Miller *et al.*, 1984; Miller *et al.*, 1985). Since these EA devices operate best in the region of the bandgap of GaAs, although with less loss if the operation is slightly detuned (Dagli, 1999). The structure of most EA waveguide modulators is that of the simple phase modulator, the simplest of modulator structures (Alferness, 1988), unless used in a push-pull fashion in which case a Y-junction modulator structure is mostly used (see Chapter 5). Directional couplers are mostly in the form of vertical couplers as these have been found to be much more compact (Cho *et al.*, 2001).

The interest in bandwidth for modulators indicate the need for a travelling wave (TW) type electrode since it is with these that the highest bandwidths have been achieved, as lumped device performance appears to be saturated at the 50GHz bandwidth (Dagli, 1999). Although there is a developing interest in TW EA modulators, these devices suffer from high losses and high device capacitance as a consequence of the doped layers, which limits the size of the device and leads to a characteristic impedance of  $25\Omega$  (Dagli, 1999). However, designing the device as part of a  $25\Omega$  transmission line makes longer devices possible. Bandwidths for these travelling wave devices have been shown to reach no higher than around 50-60GHz (Kawano *et al.*, 1997; Irmscher *et al.*, 2002). However, drive voltages are considerably lower (at  $\sim 2V$ ) than for similar electro-optic devices (typically at  $\sim 5V$  or higher). For low loss operation it is common to use unintentionally doped GaAs/ Al<sub>x</sub>Ga<sub>1-x</sub>As layers, which behave very similar to low-loss dielectric materials (Dagli, 1999) and this results in both low optical and microwave losses. For this reason these GaAs based devices operate using the linear electro-optic effect. The terms ‘unintentionally doped GaAs’ or ‘unintentionally doped Al<sub>x</sub>Ga<sub>1-x</sub>As’ indicate that the material is left undoped but that residual doping occurs during the growth process. Typically figures for either positive or negative residual doping are of the order of  $10^{14} \text{ cm}^{-3}$ . Also, Fermi level pinning at the semi-insulating substrate interface and at the surface of the upper Al<sub>x</sub>Ga<sub>1-x</sub>As layer causes depletion of carriers which extends throughout the device, and hence this device then behaves very similar to those fabricated from low-loss dielectric materials. However, since the electro-optic

coefficient is small compared with dielectric crystals such as LiNbO<sub>3</sub>, this leads to longer devices. Nevertheless, because the refractive index is higher for GaAs than for LiNbO<sub>3</sub>, the net index change is comparable to that of LiNbO<sub>3</sub>. Moreover, the wavelength of operation extends over a wider range than the narrowband EA devices, which are restricted to the region around the bandedge of the waveguiding semiconductor material (Lee *et al.*, 1991; Glingener *et al.*, 1995). Travelling-wave modulators made from unintentionally doped semiconductor materials are typically used at wavelengths far away from the absorption edge and this results in low loss, chirp free operation (Spickermann *et al.*, 1996a). The structure of these devices tends to be in the Mach-Zehnder interferometric (MZI) format, which as discussed earlier in Chapter 5 gives much more readily to higher bandwidth and lower drive voltage devices than either the directional coupler format or the simple phase modulator format, and for this reason is used as a basis for a majority of components in optical systems (Wooten *et al.*, 2000; Yim and Shin, 1998).

Hence, the electro-optic GaAs/ Al<sub>x</sub>Ga<sub>1-x</sub>As modulator with an interferometric-based structure is realistic and is entirely satisfactory for the introductory phase of this part of the study.

## **6.2 Structure of the Electro-optic GaAs/ Al<sub>x</sub>Ga<sub>1-x</sub>As MZI modulator**

### **6.2.1 Introduction**

The structure for the unintentionally doped electro-optic GaAs/ Al<sub>x</sub>Ga<sub>1-x</sub>As Mach Zehnder interferometer based modulator (Sakamoto *et al.*, 1999) is that shown below in Fig. 6.1. The input and output sections of the device are in the form of 1x2 multimode interferometric (MMI) couplers: splitters and recombiners, respectively. As was mentioned in Chapter 5 the principle of operation is through the interference between the modes the device can support which leads to well defined images of the input field at certain points along the central multimoded waveguide. It is this efficient imaging of the input field to the outputs that leads to low-loss devices. A more detailed

mathematical understanding of the interference patterns can be found in a number of texts (Soldano and Pennings, 1995; Maat, 2001; Themistos and Rahman, 2002).

There are two types of MMI device: those that follow general interference mechanisms and those that follow restricted interference mechanisms (which comprises paired interference and symmetric interference). Although both types of MMI devices result in a more compact size when compared with directional couplers (Rajarajan *et al.*, 1999)

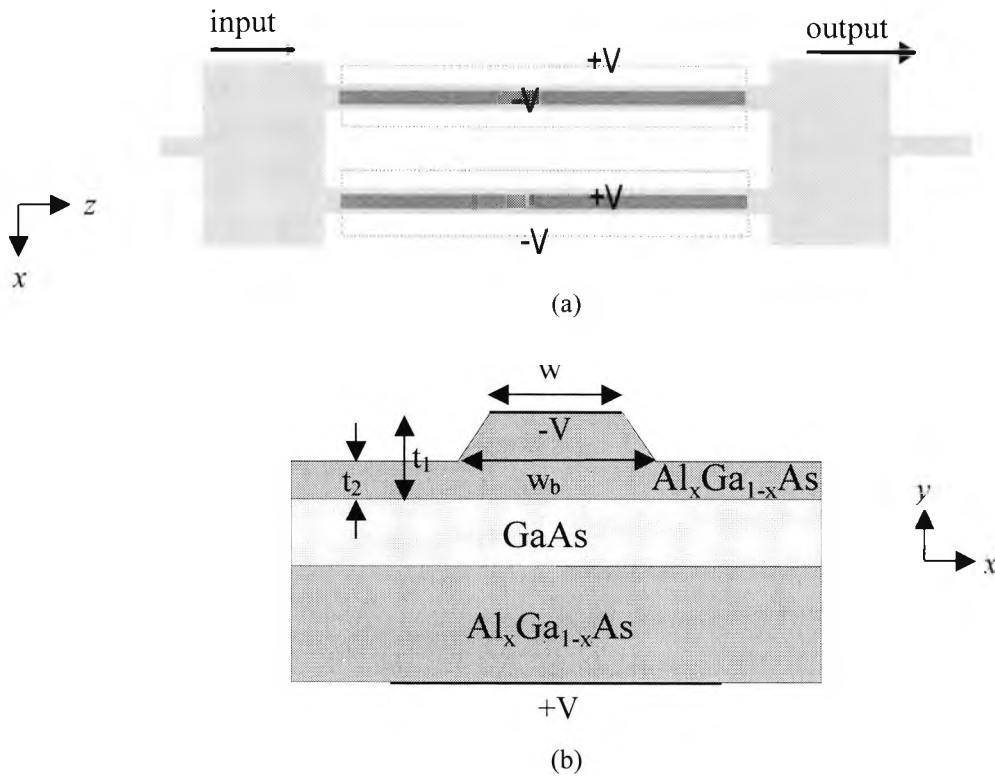


**Fig. 6.1** (a) The layout and (b) a single arm of the Mach-Zehnder Interferometer structure.

or Y-junctions, it is the restricted interference type of device that tends to be three times shorter when compared with the MMI devices that follow general interference mechanisms (Soldano and Pennings, 1995). Of these the MMI devices based on symmetric interference are 25% shorter than those which follow paired interference mechanisms. The length of the device is controlled by the beat length,  $L_\pi$ , of the two lowest order modes where

$$L_\pi = \frac{\pi}{\beta_0 - \beta_1} \quad (6.1)$$

where  $\beta_0$  and  $\beta_1$  are the first and second modes of the MMI coupler.

For the 1x2 3dB MMI coupler shown in Fig. 6.1 it was found that when this device (Soldano and Pennings, 1995) followed restricted resonance mechanisms of paired interference or symmetric interference, device lengths could be  $L_{\pi}/2$  or  $3L_{\pi}/8$ , respectively. The 1x2 3dB MMI coupler is the simplest form of the range of MMI devices, as is the Y-junction when compared with the 3dB directional coupler.

From equations (4.48) and (4.49) it can be seen that the output of the directional coupler follows a cosine relationship with the coupling length. Therefore if the 3dB coupler is in the form of a directional coupler any inaccuracies in the length of that part of the device over which the coupling occurs can lead to an imbalance in the two outputs of the coupler. This imbalance directly translates into a deterioration of the extinction ratio and crosstalk of the Mach-Zehnder device shown in Fig. 6.1. Another reason for this is that transmission sensitivity to any variations in length are maximum at the 3dB point and of opposite sign for each output (Soldano and Pennings, 1995), for the directional coupler. If the 1x2 3dB MMI coupler shown in Fig. 6.1 is used any inaccuracies in the length of the device are no longer so considerable as each single image of the two-fold image is a local maximum and so the sensitivity is minimum for the optimum length as well as the fact that both output powers decrease similarly for any deviations from this length. Hence, there is a very good balancing for the MMI coupler and therefore the extinction ratios should remain favourable for Mach Zehnder interferometric based device. However, any misplacement of the two access waveguides at the output of the 3dB MMI splitter or the input of the 3dB MMI recombiner will be responsible for increasing the extinction ratio (Maat, 2001). Furthermore, inaccuracies in the width or etch depth of the multimode waveguide causes imbalance between the two outputs of the 3dB MMI splitter shown in Fig. 6.1, and likewise for the 3dB MMI recombiner. Any significance of fabrication variations in the access guides has not been mentioned. However, any mismatch of the widths of the access guides should lead to even less unwanted coupling between the guides and this will obviously affect power transmission in the device.

The operation of the overall interferometric device has already been explained in Chapter 5 and therefore there is no need for it to be repeated here.

### 6.2.2 Calculation of the Refractive Indices

GaAs is a cubic crystal of  $\bar{4}3m$  symmetry (zinc-blende group). These crystals are optically isotropic. Hence, the refractive index is same for all direction without any material birefringence. The calculation of the refractive indices for both GaAs and Al<sub>x</sub>Ga<sub>1-x</sub>As has been studied in detail in a number of papers (Adachi, 1988; Jenkins, 1990; Blakemore, 1982). However, it was found that the model proposed by Jenkins (1990) was closer to experimental data for the refractive indices for both GaAs and Al<sub>x</sub>Ga<sub>1-x</sub>As over a larger range of wavelengths than the model proposed by Adachi (1988), which tends to overestimate the refractive indices for a number of wavelengths. Moreover, the values calculated for both GaAs (3.37037) and Al<sub>0.38</sub>Ga<sub>0.62</sub>As (3.19457) at the operating wavelength of 1.55 $\mu\text{m}$ , using the model proposed by Jenkins (1990), are in agreement with the values obtained by Pikhtin and Yas'kov (1980) with only a  $\pm 0.5\%$  difference between the values obtained from these two models. The Jenkins model is also in agreement with the data obtained by Blakemore (1982) for GaAs. From this it is evident that the value of the refractive index obtained from the Jenkins (1990) model for the Al<sub>x</sub>Ga<sub>1-x</sub>As (where  $x=0.3$ ) material used in this study (3.23174) must also be in agreement with the data from other sources and therefore a realistic value.

### 6.2.3 Structure of the Rib Waveguide

In this section two types of rib structures will be studied: a shallow etched slanted rib waveguide and a slightly deeper etched 90° vertical rib waveguide. The cross-section of these waveguides is shown in Fig. 6.2. The lower Al<sub>x</sub>Ga<sub>1-x</sub>As layer is taken to be 2 $\mu\text{m}$  thick and the GaAs layer is taken to be 0.73 $\mu\text{m}$  thick (Sakamoto *et al.*, 1999), with  $t_2=0.32\mu\text{m}$  and  $t_1=0.82\mu\text{m}$  (implying a rib height of 0.5 $\mu\text{m}$ ). The width of the rib,  $w$ , for both the vertical and slanted rib structures is taken to be 4 $\mu\text{m}$ . The method to obtain the shallow slanted rib is by purely chemical (wet) etching (Sakamoto *et al.*, 1998) and typically yields an angle of 52° to the horizontal for the upper layer of Al<sub>0.3</sub>Ga<sub>0.7</sub>As, whereas a vertical rib or higher tilts are achieved by a dry (ion assisted) etching method. Moreover, for much deeper vertical ribs reactive ion etching (RIE) can be used (Heaton *et al.*, 1995). However, for such a structure sidewall loss becomes very important (Maat, 2001), as the optical mode comes into contact with the rough sidewalls; although

devices can become more compact as a consequence of the light from the guides not coupling even when placed closer together.

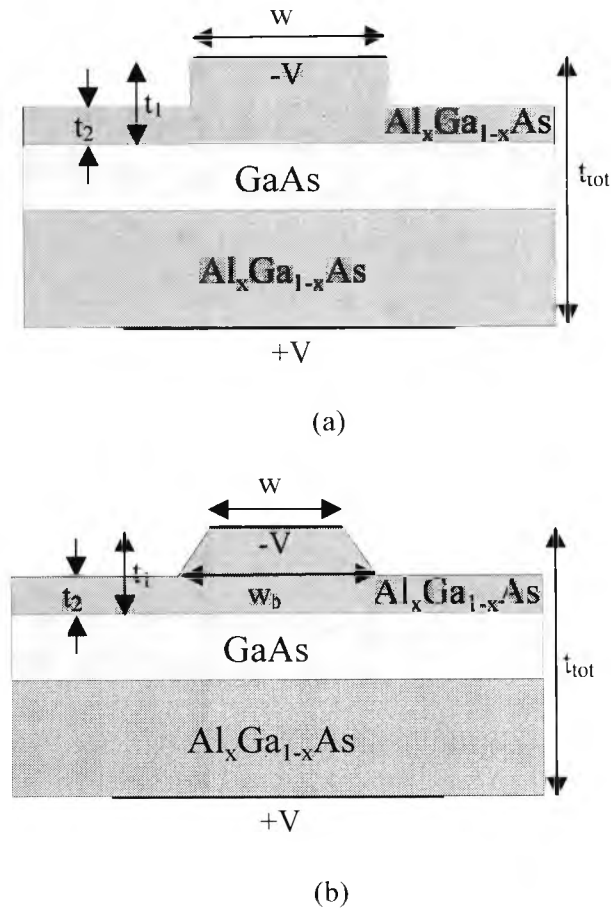


**Fig. 6.2** Cross-section of a (a) vertical rib waveguide (b) slanted rib waveguide.

The use of substrate removal techniques (Sakamoto *et al.*, 1998) have allowed for a much thinner device which subsequently yields a much smaller distance between the electrodes placed at the top and bottom of the device than could otherwise have been achieved with standard device processing techniques. Hence, a much smaller drive voltage,  $V_{\pi}$ , is expected (Sakamoto *et al.*, 1999) than was previously obtained for these unintentionally doped GaAs-Al<sub>x</sub>Ga<sub>1-x</sub>As modulators (Spickermann *et al.*, 1996b).

The vector H-field finite element method (HFEM) has, as for the devices detailed in previous chapters, been used to numerically model these two types of devices. At first a single guide was taken for the vertical rib waveguide and it was observed (see Fig. 6.3) how  $\beta$  varied with the mesh size for both the fundamental mode quasi-TE and TM type

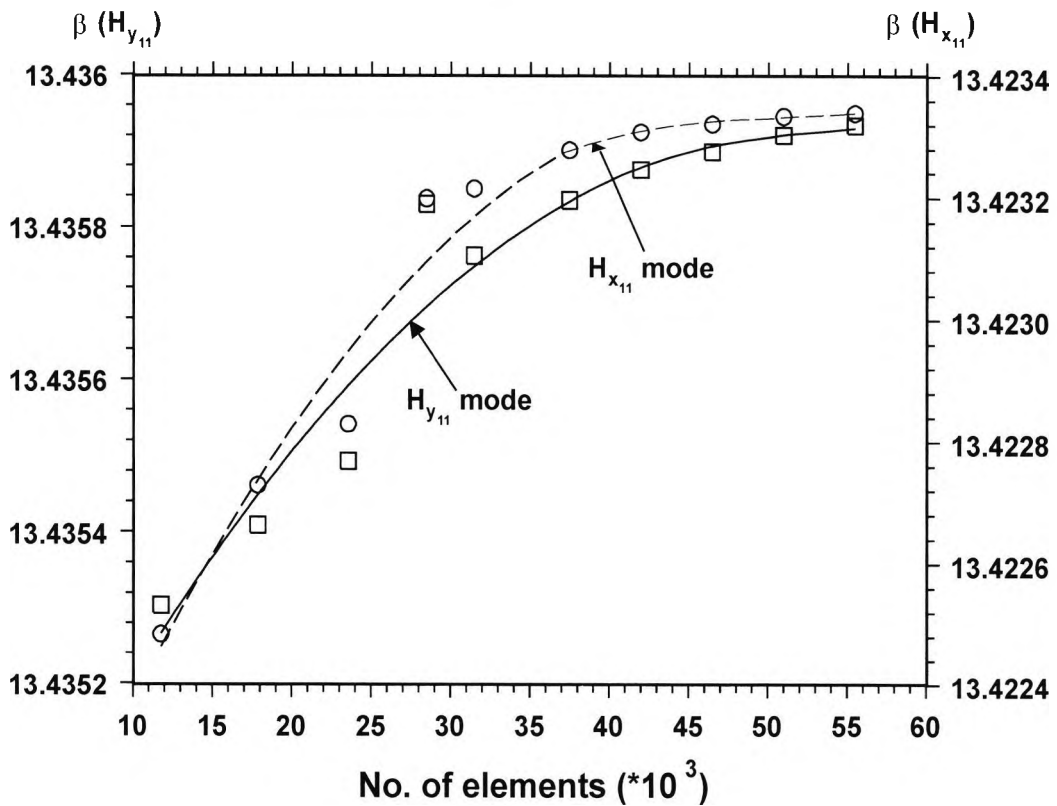
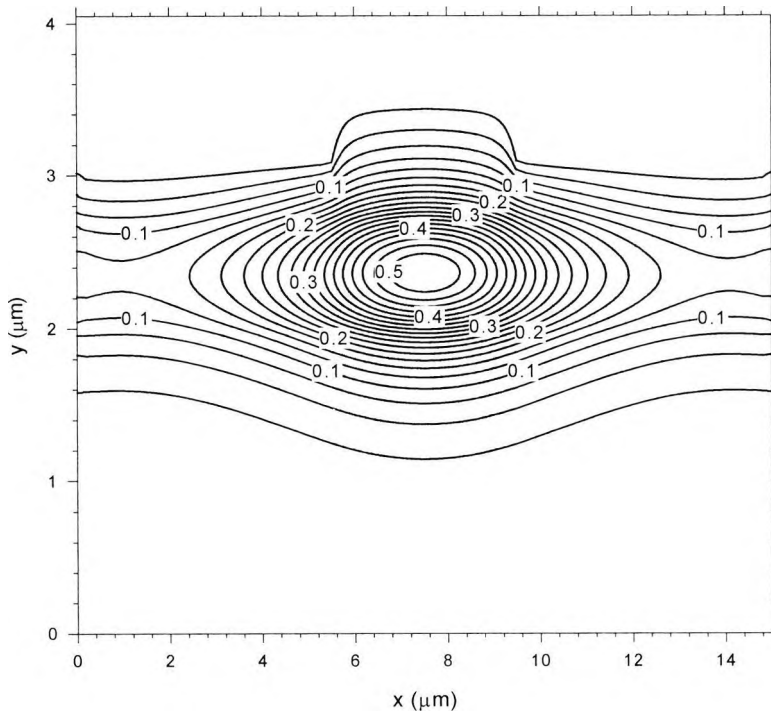


Fig. 6.3  $\beta$  vs mesh size for both the fundamental quasi-TE and TM modes at  $V=0$  for the vertical rib waveguide.

modes. Hence, a mesh of  $150 \times 140$  ( $=42,000$  elements) was considered to be reasonable since there is a minute ( $4 \times 10^{-4} \%$ ) difference in  $\beta$  between this and the larger mesh size of  $55,500$  elements. A similar but larger mesh of  $208 \times 140$  ( $=58,240$  elements) was used for the slanted rib waveguide structure in order to correctly incorporate the slanted section of the structure, yielding a comparable propagation constant of  $13.4367354$ .

First to be considered was the condition when electric field is not applied to the device. In this case the two waveguides of the Mach-Zehnder remain identical. Stronger transverse waveguiding occurs in the planar GaAs layer whereas weaker lateral waveguiding occurs due to the loading of the  $\text{Al}_{0.3}\text{Ga}_{0.7}\text{As}$  rib. Both structures shown in Fig. 6.2 are able to support a number of modes in both quasi-TE and quasi-TM type, depending on the width of the rib in the upper  $\text{Al}_{0.3}\text{Ga}_{0.7}\text{As}$  layer and the thickness of the waveguiding GaAs layer. However, for the structures in Fig. 6.2, for which the dimensions have been given earlier, only the fundamental mode is able to propagate light in the guide for both the quasi-TE and quasi-TM modes. For rib widths of  $4.25 \mu\text{m}$  and above only the fundamental quasi-TE mode is able to propagate light in the guide, whereas for the quasi-TM modes higher order modes are also supported by the

waveguide structure. However, if the thickness of the guiding GaAs layer is increased to 0.9 μm or more higher order modes (for both the quasi-TE and quasi-TM modes) are also supported by the waveguide structure. Additionally, as will be shown in a later section of this chapter, the quasi-TM mode is not modulated by the electric field produced by the voltage applied to the electrodes for the structure shown in Fig. 6.1, and therefore the  $H_x^{mn}$  (quasi-TM) modes are not of interest to this study. Hence, the rib waveguides are understood to be single moded structures (Sakamoto *et al.*, 1999). However, even for the original dimensions (given above) it was also observed that these waveguide structures may appear to be multimoded (for the quasi-TE modes) when either infinite elements are not used or through improper use of parameters for the infinite elements. When used with the correct decay parameters these ‘modes’ then iterated to the nearest quasi-TE mode (the fundamental mode in this case). The reason for this is because the optical mode extends to the right and left hand edges of the structure and so the field can in theory extend over all the open space (even though the device is spatially bounded). With the correct use of infinite elements at the edges of the structure the mode is transformed at the edges of the structure to take this aspect of the mode into account. The fundamental quasi-TE mode,  $H_y^{11}$ , obtained for the vertical rib waveguide and the slanted rib waveguide, shown in Figs. 6.4 and 6.5, are obtained by



**Fig. 6.4** Optical field profile of the fundamental  $H_y^{11}$  mode at  $V=0$  for a vertical rib waveguide.

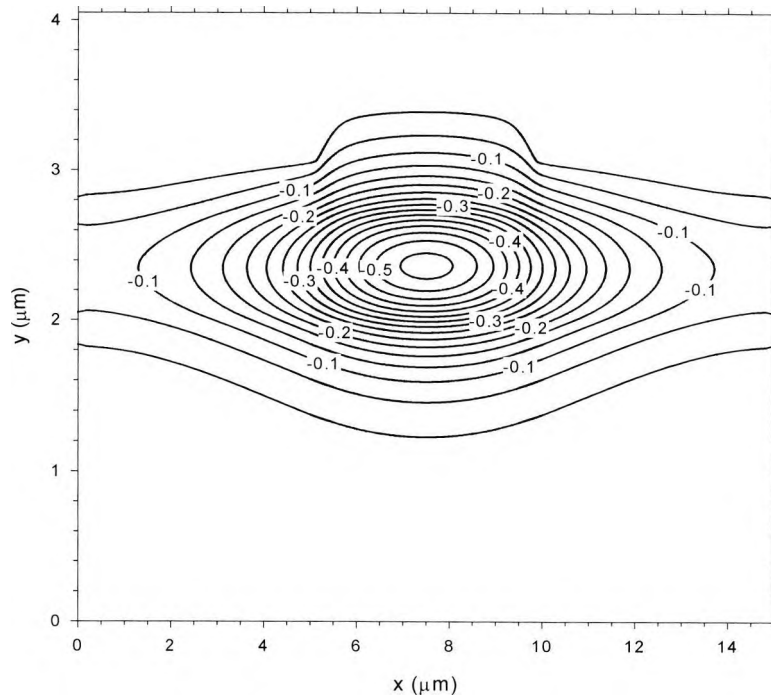


**Fig. 6.5** Optical field profile of the fundamental  $H_y^{11}$  mode at  $V=0$  for a slanted rib waveguide.

using the HFEM to solve the wave equation, where the propagation constant,  $\beta$ , was found to be 13.4367354 and 13.4359191, respectively. The weaker effect of the lateral waveguiding can be seen from these modes in the way the field contours extend towards the right and left walls of the structure but the majority of contours are, and therefore light energy is, concentrated in the centre of the waveguide area. This can be confirmed by calculating the spotsize area of the mode, where the spot size area of the optical field is defined as that area over which the power density of the light beam is greater than half of the maximum power density. For the vertical rib waveguide this is  $2.016\mu\text{m}^2$  centred in the waveguide, which has a guiding area of  $10.95\mu\text{m}^2$ . Furthermore, approximately 83% of the light is confined in this waveguide area: most of that remaining leaking into the surrounding  $\text{Al}_{0.3}\text{Ga}_{0.7}\text{As}$  layers. Similarly, the slanted rib waveguide has a spotsize area of  $2.157\mu\text{m}^2$  centred in the waveguide, which again has a core area of  $10.95\mu\text{m}^2$ , with more than about 83% of the light being confined to this waveguide area. There is only a slight difference of 1.22% in the spotsize area between the slanted rib and vertical rib waveguides. This is most likely because the base of the slanted rib,  $w_b$ , is approximately  $4.78\mu\text{m}$ . Hence, it is clear that a vertical or slanted rib do not affect the spot size area of the optical mode.

The optical modes for the structures presented throughout this work (and indeed for most optical waveguides) are to some extent all hybrid. For the fundamental quasi-TE ( $H_{11}^y$ ) mode  $H_y$  and  $E_x$  are the dominant field components. However, there are minimal  $H_x$  and  $H_z$  (as well as  $E_y$  and  $E_z$ ) components. Likewise, for the fundamental quasi-TM ( $H_{11}^x$ ) mode  $H_x$  and  $E_y$  are the dominant field components with minimal  $H_y$  and  $H_z$  (as well as  $E_x$  and  $E_z$ ) components. It has been reported (Somasiri *et al.*, 2002) that for slanted wall structures, the dominant component no longer remains so and both the  $H_y$  and  $H_x$  components for each mode are comparable and for certain parameters (see Somasiri *et al.*, 2002) can have equal strength. This phenomenon is termed hybridism. No hybridness was observed for either of the structures presented in this chapter. This could be because of a number of reasons including that (Somasiri *et al.*, 2002):

- a) neither structure has a deeply etched rib with the rib extending into the guiding (core) of the structure
- b) the rib width is much greater than  $1.5\mu\text{m}$
- c) both structures are symmetrical about the central vertical plane of the structure (parallel to the  $y$  axis (in Cartesian co-ordinates)) and therefore enhanced field hybridness does not occur since the symmetry of the structure has not been destroyed.

In Chapter 1 it was mentioned that for any waveguide  $k_0 n_s < \beta < k_0 n_g$ , where  $n_s$  and  $n_g$  are the substrate and guide refractive indices, respectively, and  $k_0$  is the freespace wave number. Not only are the values of  $\beta$  less than  $k_0 n_{\text{GaAs}}$  and more than  $k_0 n_{\text{AlGaAs}}$  as is the normal case for guided modes, it is can be seen from Table 6.1 that  $\beta$  also lies in

**Table 6.1**  $\beta$  values for four different modes in two planar waveguides of thickness  $t_2$  and  $t_1$ , as well as those for a vertical rib waveguide and a slanted rib waveguide structure with similar dimensions.

Mode	$\beta$			
	Planar waveguide ( $t_{\text{AlGaAs}} = t_2$ )	Planar waveguide ( $t_{\text{AlGaAs}} = t_1$ )	Vertical rib waveguide	Slanted rib waveguide
$H_y^{11}$	13.4281047	13.4419004	13.4359191	13.4367354
$H_y^{21}$	13.4263579	13.4401577	-	-
$H_x^{11}$	13.4103164	13.4290055	13.4228151	13.4240094

between the  $\beta$  values obtained for a planar waveguide when the thickness of the upper Al<sub>x</sub>Ga<sub>1-x</sub>As layer,  $t_{u-AlGaAs}$ , is equal to  $t_1$  and for a planar waveguide when the upper Al<sub>x</sub>Ga<sub>1-x</sub>As layer is of a thickness  $t_2$  (where  $t_1$  and  $t_2$  are as shown in the Fig. 6.1). This is not surprising as the modes are similar to those obtained from the planar waveguides because of the weak lateral waveguiding. Deeper etched ribs, where the guiding layer is in the rib, would have a much different behaviour (Maat, 2001) because of the tightly confined modes for such a structure but, as mentioned above, this leads to sidewall losses becoming a highly significant contribution to the overall losses of the device. As mentioned in Chapter 3, it is important (as is for any optical device) to keep insertion loss of the modulator low and a shallow etched rib waveguide modulator is therefore much better suited for this purpose as is evident by the fact that there are no reports of deep etched rib waveguide GaAs/AlGaAs electro-optic modulators (where the unintentionally doped semiconductor behaves as a dielectric) found in the relevant literature (Dagli, 1999). This is because the loss for single waveguide phase modulators with upper and lower electrodes (as for the substrate removed electro-optic modulator simulated in this study) is already 5dB/cm (Bek *et al.*, 1999); with the guiding layer in the rib section and even closer to the electrodes, the optical loss and, therefore, the total loss is likely to be greater. Coupled with sidewall losses these losses would be even larger: hence the use of shallow etched rib waveguides, where the rib is etched only into the upper cladding layer.

### 6.3 Electro-Optical Characteristics of the GaAs/Al<sub>x</sub>Ga<sub>1-x</sub>As MZI Modulator

As mentioned in the introductory section of this chapter, unintentionally doped GaAs/Al<sub>x</sub>Ga<sub>1-x</sub>As material behaves much like dielectric material and therefore the Laplace equation can be used to determine the nature of the electric field across the structure rather than the Poisson equation as would have to be the case for doped GaAs/Al<sub>x</sub>Ga<sub>1-x</sub>As devices. Moreover, only the linear electro-optic effect is responsible for the change in refractive index with electric field for a device fabricated using unintentionally undoped GaAs/Al<sub>x</sub>Ga<sub>1-x</sub>As material.

### 6.3.1 Calculation of the Electric Field

As shown in Chapter 5, the electric field, for any general material, can be found by using

the Poisson equation

$$\nabla \cdot (\epsilon E) = \rho \quad (6.2)$$

However, in the case of a dielectric material such as LiNbO<sub>3</sub> there are no free carriers/charge and so  $\rho$  is zero in value with equation (6.2) becoming the Laplace equation

$$\nabla \cdot (\epsilon E) = 0 \quad (6.3)$$

Since unintentionally doped GaAs/Al<sub>x</sub>Ga<sub>1-x</sub>As also behaves as a dielectric material, it is therefore feasible to use this equation for a modulator fabricated from this material.

Further, as the electric fields which were studied are those due to the application of dc voltage to the electrodes (shown in Fig. 6.1), the dielectric constant used here will be the static dielectric constant, given by (Goldberg, 1997)

$$\epsilon(x) = 12.90 - 2.84x \quad (6.4)$$

for Al<sub>x</sub>Ga<sub>1-x</sub>As. So for the GaAs waveguide the static dielectric constant is taken to be 12.9 and for the Al<sub>0.3</sub>Ga<sub>0.7</sub>As cladding the static dielectric constant is taken to be 12.048. Hence, there is no need for a permittivity tensor as for LiNbO<sub>3</sub> as both GaAs and Al<sub>x</sub>Ga<sub>1-x</sub>As are isotropic in nature.

Therefore, the finite element scalar formulation for the Laplace equation is (Davies, 1989) is now

$$\epsilon \int (\nabla \psi)^* (\nabla \psi) d\Omega = 0 \quad (6.5)$$

where  $\psi$  is the scalar modulating potential, and the modulating electric field can be obtained by the knowledge that (as shown in equation (4.28))

$$E_x = -\frac{d\psi}{dx} \quad \text{and} \quad E_y = -\frac{d\psi}{dy} \quad (6.6)$$

A 3-d plot of  $E_y(x,y)$ , the vertical or  $y$ -component of the applied electric field  $\mathbf{E}(E_x, E_y)$  is shown in Fig. 6.6 for  $V=10V$ . The cross-section of the slanted rib waveguide of the MZI modulator (shown in Fig. 6.1) is symmetrical about  $x=7.5\mu\text{m}$ , with the edges of the

upper electrode occurring at  $x=5.5\mu\text{m}$  and  $x=9.5\mu\text{m}$  and hence the applied electric field  $E_y$  is symmetric about  $x=7.5\mu\text{m}$ . The reason for the symmetry is that variation in

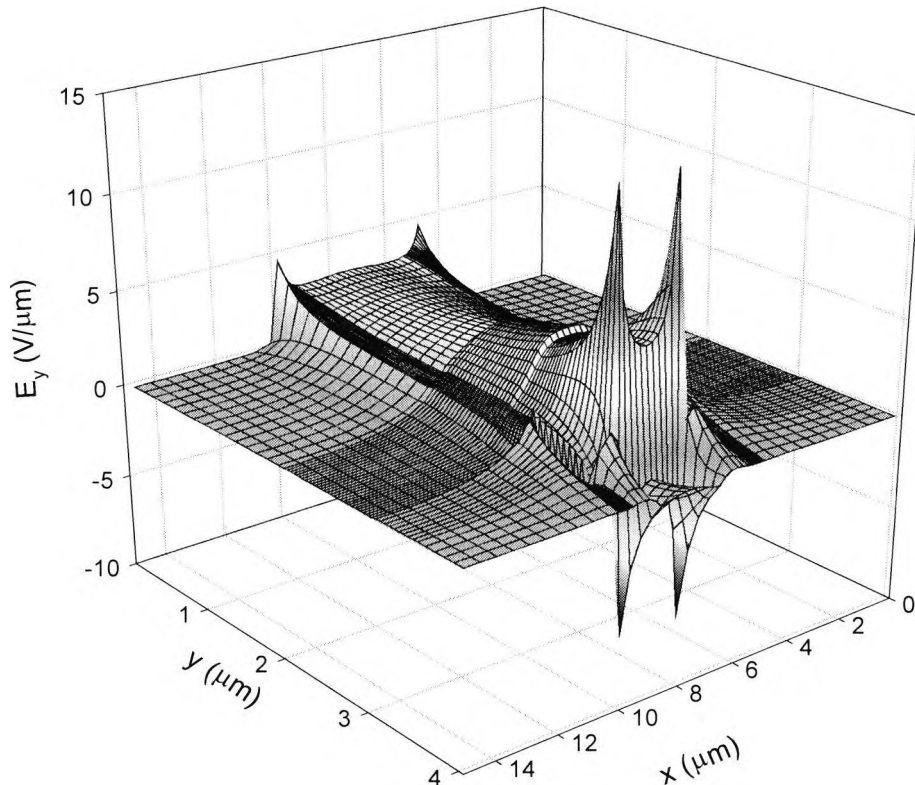


**Fig. 6.6** A 3-d plot of the magnitude of the  $E_y$  component of the applied electric field across the device at 10V.

the modulating potential,  $\psi$ , in the direction of  $y$  is always negative across the whole waveguide structure and so  $E_y$  is positive throughout the waveguide structure (see Equation (6.6)). Furthermore, the sharp peaks in  $E_y$  occur at the edges of this upper electrode (Marcuse, 1982) and smaller peaks are present at the edges of the lower electrode. There is also a sharp change in  $E_y$  at the Al<sub>x</sub>Ga<sub>1-x</sub>As-air interface at  $y=3.55\mu\text{m}$ .

$E_x(x,y)$  is shown in Fig. 6.7 and it can be clearly seen that the field  $E_x$  is anti-symmetric about  $x=7.5\mu\text{m}$ . The reason for the anti-symmetry is that variation in the modulating potential,  $\psi$ , in the direction of  $x$  is negative across the whole waveguide structure up to the line of symmetry of the waveguide ( $x=7.5\mu\text{m}$ ) and then becomes positive for  $x$

greater than  $7.5\mu\text{m}$ . Hence,  $E_x$  is positive throughout the waveguide structure up to  $x=7.5\mu\text{m}$  and then becomes negative for  $x$  greater than  $7.5\mu\text{m}$  (see equation (6.6)). The

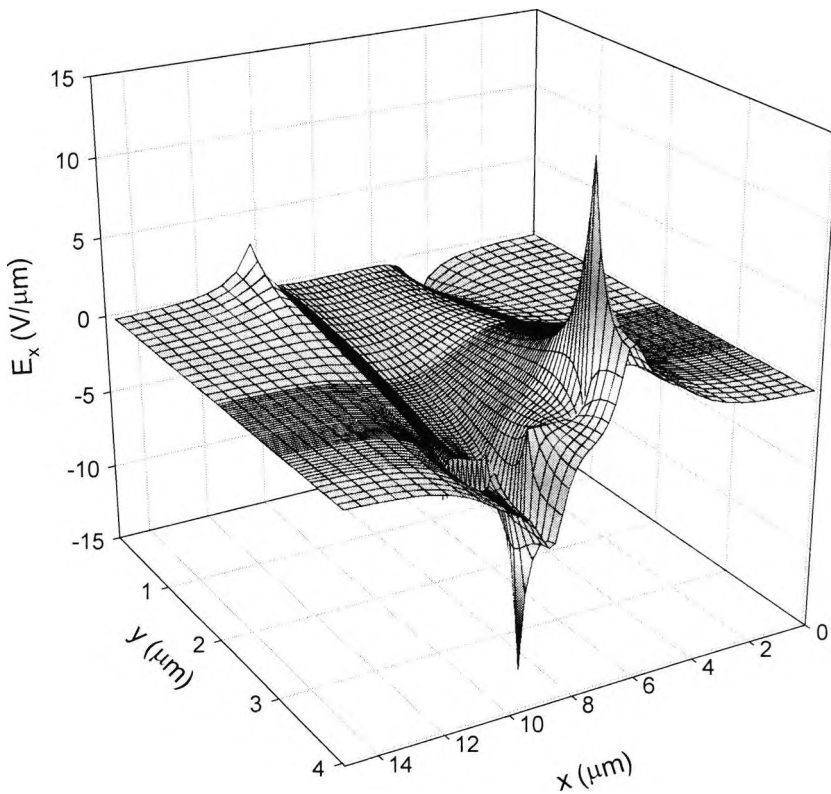


**Fig. 6.7** A 3-d view of the magnitude of the  $E_x$  component of the applied electric field across the device at  $10V$ .

effect of such an applied electric field acting on the rib waveguide would give a zero average refractive index change with applied electric field and for that reason this component of the applied electric field can therefore be ignored.

As can be seen neither  $E_x$  nor, more importantly,  $E_y$  is not constant over the structure, as assumed in some of the previously published work (Dagli, 1999). This can be seen more clearly in Fig. 6.8 where  $E_y$  is taken along the line of symmetry of the waveguide ( $x=7.5\mu\text{m}$ ) and along  $y$  at one of the peak centres ( $x=5.5\mu\text{m}$ ). For the latter profile of  $E_y$  along  $y$  at  $x=5.5\mu\text{m}$ , the electric field is not constant over  $y$ . Hence for rigorous analysis

and optimisation of the device performance it is important to consider the spatial variation of the electric field,  $E_y(x,y)$ , rather than just the very simple approximation of  $V/t$  (where  $V$  is the applied voltage and  $t$  is the distance between the upper and lower electrodes of the device), in order to obtain the overlap integral with the optical field. Although the peak value of  $E_y$  could be as high as  $16\text{V}/\mu\text{m}$  (due to the sharp change in value which occurs at the Al<sub>x</sub>Ga<sub>1-x</sub>As-air interface at  $y=3.55\mu\text{m}$ ), however over the waveguide core its average value is approximately  $2.5\text{V}/\mu\text{m}$ .

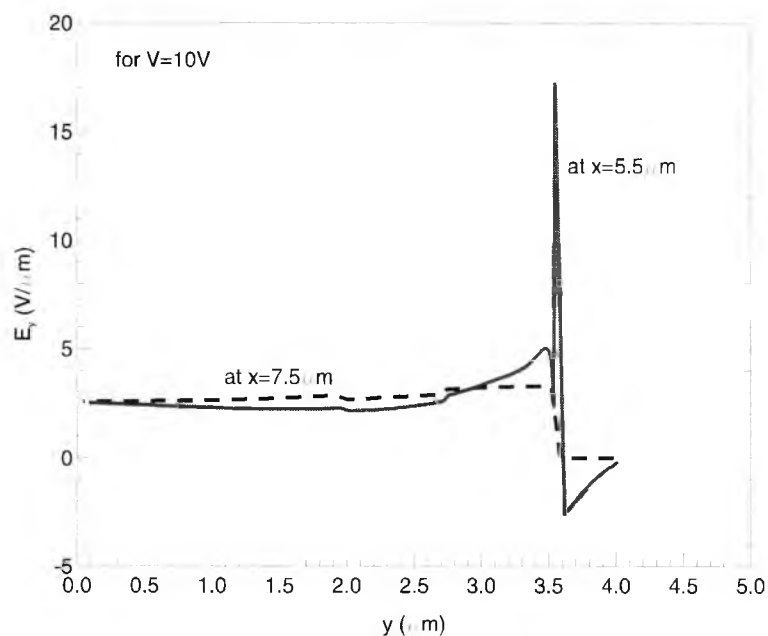


**Fig. 6.8** A view of the magnitude of the  $E_y$  component of the applied electric field at two cross-sections in the device.

### 6.3.2 Calculation of the Refractive Index Profile under the Influence of an Applied Field

The refractive index profile of any semiconductor device typically changes with field effects or carrier effects (Glingener *et al.*, 1995). However, for unintentionally doped GaAs or Al<sub>x</sub>Ga<sub>1-x</sub>As it is understood that the only change in refractive index profile is linear with applied electric field. Therefore, in order to calculate the change in refractive index profile,  $\Delta n$ , the equation for the linear electro-optic effect is used,

$$\Delta\left(\frac{1}{n^2}\right)_i = \sum_{j=1}^3 r_{ij} E_j \quad (6.7)$$

where  $i=1,\dots,6$  and  $E_1=E_x$ ,  $E_2=E_y$ ,  $E_3=E_z$  (the components of the electric field  $\mathbf{E}(E_x, E_y, E_z)$ ). Since GaAs and Al<sub>x</sub>Ga<sub>1-x</sub>As have a Zinc Blende or  $\overline{43m}$  crystal structure,  $r_{41}$  is the only electro-optic coefficient (Yariv, 1991) as shown by the electro-optic tensor

$$r_{ij} = \begin{bmatrix} r_{11} & r_{12} & r_{13} \\ r_{21} & r_{22} & r_{23} \\ r_{31} & r_{32} & r_{33} \\ r_{41} & r_{42} & r_{43} \\ r_{51} & r_{52} & r_{53} \\ r_{61} & r_{62} & r_{63} \end{bmatrix} = \begin{bmatrix} 0 & 0 & 0 \\ 0 & 0 & 0 \\ 0 & 0 & 0 \\ r_{41} & 0 & 0 \\ 0 & r_{41} & 0 \\ 0 & 0 & r_{41} \end{bmatrix} \quad (6.8)$$

where

$$r_{41} = 1.4 \times 10^{-12} \text{ m/V at a wavelength of } 1.55 \mu\text{m (Sakamoto et al., 1999).}$$

In a crystal the phase velocity of a wave propagating along a given direction depends on the direction of its polarisation. The direction of the polarisation of the electric field of the optical wave is determined using the index ellipsoid

$$\frac{X^2}{n_x^2} + \frac{Y^2}{n_y^2} + \frac{Z^2}{n_z^2} = 1 \quad (6.9)$$

where  $X$ ,  $Y$  and  $Z$  are the principal dielectric axes (of the crystal), which are those directions in the crystal along which  $\mathbf{D}$ , the electric flux density, and  $\mathbf{E}$ , the applied electric field are parallel.

If  $n_x = n_y = n_z$ , then the material is isotropic and the direction of the polarisation is independent of the field direction, and hence the phase velocity is independent of the direction of polarisation. However, for an anisotropic medium the phase velocity of the wave will be  $c_0/n_{dir}$ , where  $dir$  indicates the direction along which the electric field of the optical wave is acting and  $c_0$  is the phase velocity in a vacuum given by  $(\mu_0 \epsilon_0)^{-1/2}$ .

However, the index ellipsoid in the presence of an applied electric field changes to (Yariv, 1991)

$$\frac{1}{n_x^2} X^2 + \frac{1}{n_y^2} Y^2 + \frac{1}{n_z^2} Z^2 + 2 \left( \frac{1}{n^2} \right)_4 YZ + 2 \left( \frac{1}{n^2} \right)_5 XZ + 2 \left( \frac{1}{n^2} \right)_6 XY = 1 \quad (6.10)$$

So substituting (6.7) and (6.8) into (6.10) gives

$$\frac{1}{n^2} X^2 + \frac{1}{n^2} Y^2 + \frac{1}{n^2} Z^2 + 2r_{41} E_x YZ + 2r_{41} E_y XZ + 2r_{41} E_z XY = 1 \quad (6.11)$$

the index ellipsoid for GaAs and Al<sub>x</sub>Ga<sub>1-x</sub>As in the presence of an electric field, and where  $n_x = n_y = n_z = n$  for GaAs and Al<sub>x</sub>Ga<sub>1-x</sub>As.

The most commonly used crystal orientation is a (001) substrate (Dagli, 1999). See Appendix C for a brief guide on the notation for crystal cuts and crystal directions. As mentioned in the previous section, due to the position of the electrodes  $E_y$  is the main component of  $\mathbf{E}$  to be acting on the optical field. This is  $E_y$  in terms of Cartesian co-ordinates but is  $E_z$  in terms of the principal dielectric axes  $X, Y, Z$ . However, the principal dielectric axes  $X$  and  $Y$  are not equivalent with the Cartesian co-ordinates  $x$  and  $z$ , respectively, but each is equivalent to a different combination of  $x$  and  $z$ . Hence, the applied electric field is acting along  $Z$  (in the [001] direction) and so equation (6.11) becomes

$$\frac{1}{n^2}X^2 + \frac{1}{n^2}Y^2 + \frac{1}{n^2}Z^2 + 2r_{41}E_zXY = 1 \quad (6.12)$$

Now consider the index ellipsoid to be written in terms of a new co-ordinate system  $X', Y', Z'$ , where the equation of the ellipsoid contains no mixed terms. Using a general matrix-based solution, as shown in Appendix B, the new ellipsoid equation becomes

$$\left(\frac{1}{n^2} - r_{41}E_z\right)X'^2 + \left(\frac{1}{n^2} + r_{41}E_z\right)Y'^2 + \frac{1}{n^2}Z'^2 = 1 \quad (6.13)$$

or in terms of Cartesian co-ordinates as in Appendix B

$$\left(\frac{1}{n^2} - rE_y\right)x^2 + \frac{y^2}{n^2} + \left(\frac{1}{n^2} + rE_y\right)z^2 = 1 \quad (6.14)$$

where  $x=X'$ ,  $y=Z'$ ,  $z=Y'$ .

From Appendix B it can be seen that a vertically applied electric field in the [001] direction increases the index of refraction by  $\Delta n$  in the  $[1\bar{1}0]$  direction and it decreases by  $\Delta n$  in the  $[110]$  direction. It is very easy to cleave the crystal along either of these directions. Therefore, it is taken that the waveguide is [001] cut and [110] propagating. No index change is observed in the [001] direction.

As was seen in Section 6.2.3, both the shallow vertical rib waveguide device and the shallow slanted rib waveguide device support both quasi-TE and quasi-TM modes. However, since there is no change in refractive index in the [001] direction (the direction of the  $Z$  principal dielectric axis which is in the  $y$  direction when considering

Cartesian co-ordinates), there will be no modulation for the quasi-TM modes, which have their main electric field component in the [001] direction. Hence, this implies that a vertically applied electric field to an (001)-oriented crystal will only modulate the TE mode of the optical waveguide, which can have its dominant electric field component in either the  $[1\bar{1}0]$  or  $[110]$  directions. However, since the waveguide has been taken to be  $[110]$  propagating, the dominant electric field component of the optical mode should act in the  $[1\bar{1}0]$  direction. Therefore, the expression for the change in refractive index with applied modulation voltage,  $V$  is

$$\Delta n(x, y, V) = \pm \frac{n^3}{2} r_{41} E_y(x, y) \quad (6.15)$$

for the  $[1\bar{1}0]$  direction, where  $E_y(x, y)$ , the spatial variation of the vertically modulating field is obtained via the Laplace equation.

The change in  $\Delta n(x, y)$  for an application of 10V is shown in Fig. 6.9. This shows a similar profile to the electric field, as is expected from equation (6.15), but it only extends in the region containing electro-optic materials, however with strong spatial variations, rather than constant values, as has often been considered in simpler approaches. The maximum value of  $\Delta n(x, y)$  is 0.000176. The phase difference,  $\Delta\phi$ , in the two arms of the MZI, due to the change in refractive index due to applied voltage, is shown in Fig. 6.10. The phase difference in the propagation constants between the two arms of the MZI linearly increases with increasing voltage. This would be expected as the strength in the overlap between the optical field and the applied electric field

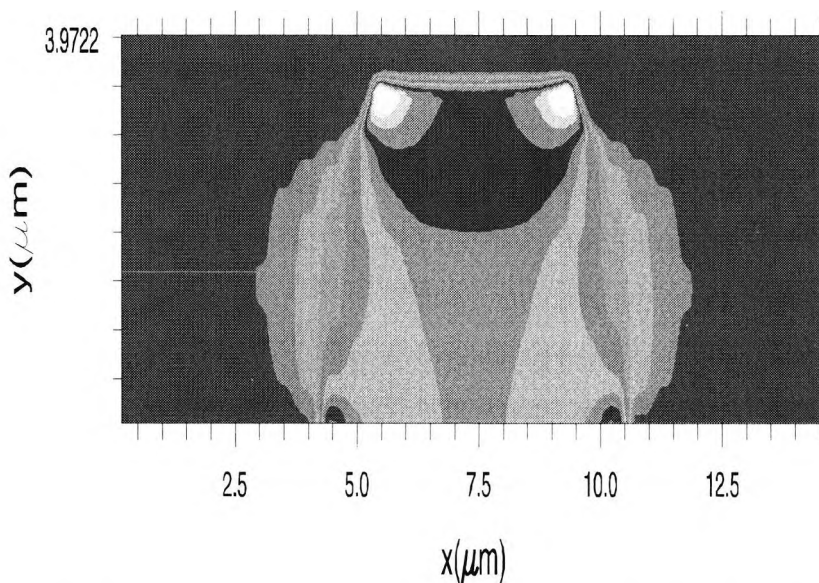


**Fig. 6.9** The contour profile  $\Delta n(x, y)$  for an applied voltage of 10V for the slanted rib device.

increases leading to a greater change in refractive index and hence a greater change in  $\Delta\beta$ , which leads to an increasing phase difference,  $\Delta\phi$ . This shows that  $V_{\pi}L$  is 7.726 Vcm (using the spatial variation,  $E_y(x,y)$ ) or  $V_{\pi}L$  is 5.24 Vcm (using a constant field given by  $V/t_{tot}$ ), which is in close agreement with both the expected and experimental results for this type of structure (Sakamoto *et al.*, 1999). The length of the electrodes,  $L$ , was taken to be 1 cm.

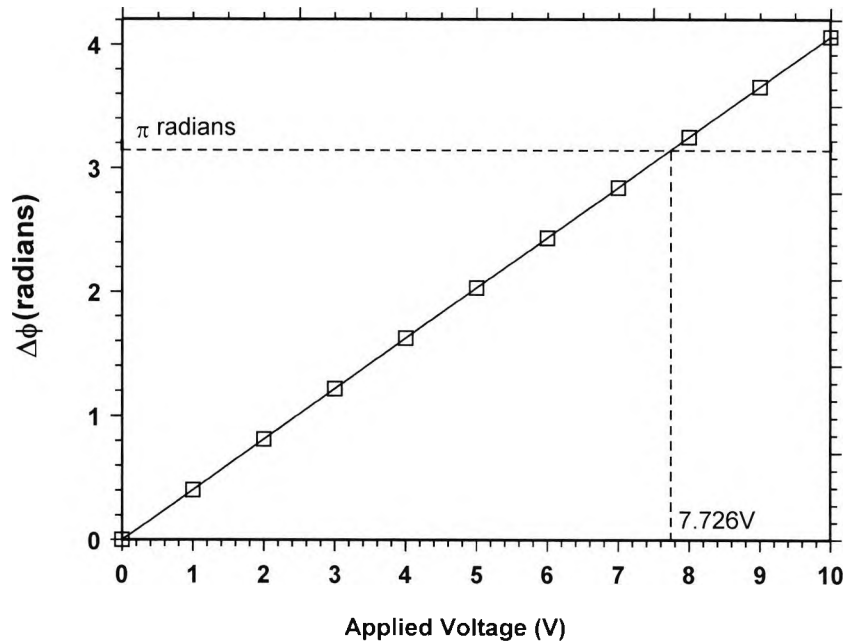


**Fig. 6.10** The variation of  $\Delta\beta$  with the applied voltage.

Finally, Figs. 6.11 and 6.12 shows the fundamental quasi-TE ( $H_y^{11}$ ) in a single arm of a slanted rib waveguide MZI and vertical rib waveguide MZI, respectively, as a consequence of the application of a 10V modulating signal. The optical field shape does not significantly change from that for 0V. This is because there is no significant change in the effective index,  $n_{eff}$ , with application of voltage away from the waveguiding area (where  $\beta = k_0 n_{eff}$ ). As before, the reason for the shape of the mode is that the weak lateral confinement only occurs through the upper AlGaAs rib structure, whereas if there was strong lateral confinement in the GaAs layer the mode would be much more confined and no lateral spreading would occur. Also, the optical field when an electric field is applied to the device yields no significant change when compared to the optical field in the case of no applied voltage to the MZI device. Moreover, there is very little difference between the optical fields for the slanted and vertical rib waveguides even

under the influence of an applied voltage, as is shown in the next section.

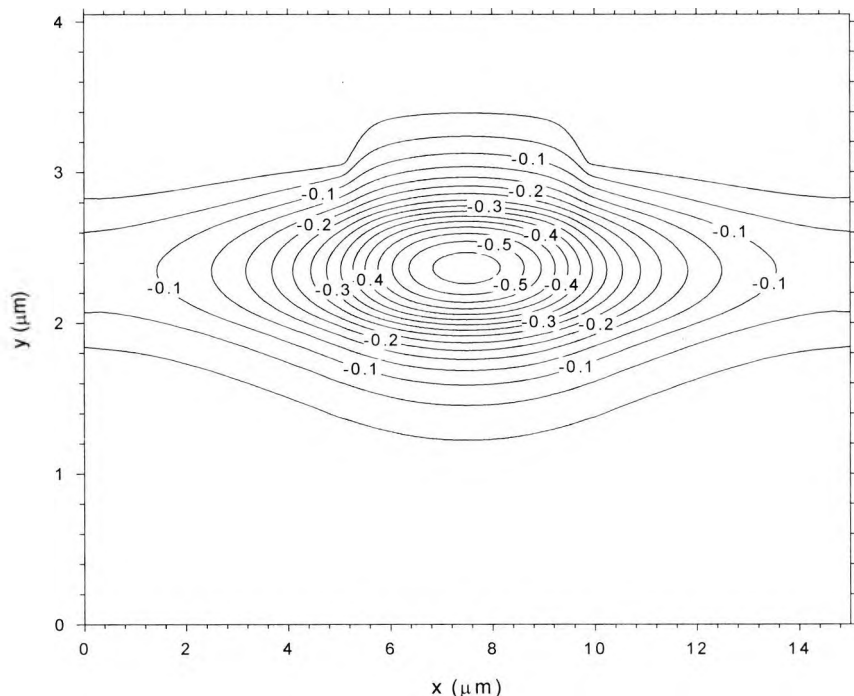


**Fig. 6.11** The fundamental quasi-TE optical mode for an applied voltage of 10V for the slanted rib device.

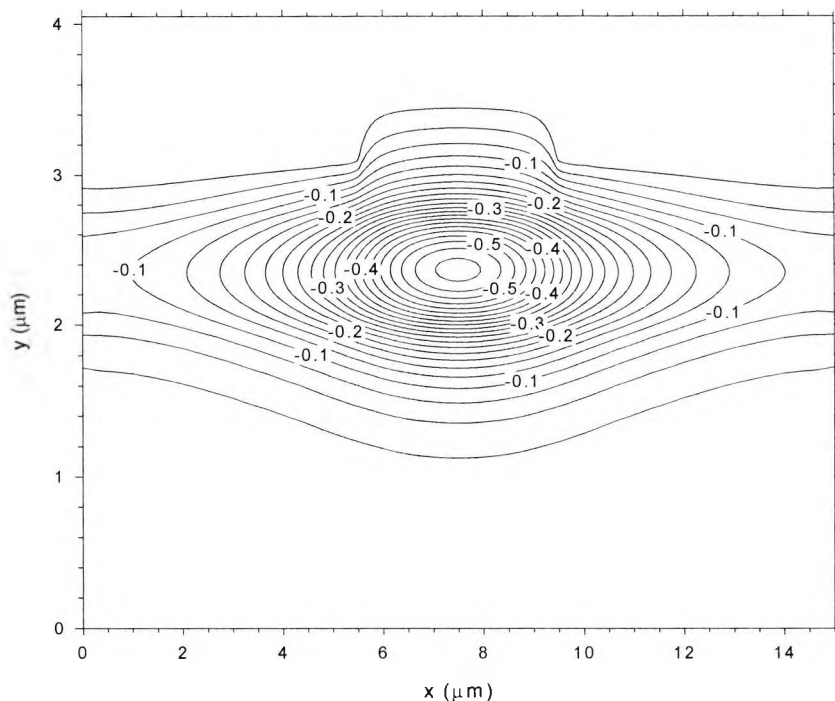


**Fig. 6.12** The fundamental quasi-TE optical mode for an applied voltage of 10V for the vertical rib device.

### 6.3.3 Calculation and Relevance of the Spot Size Area of the Optical Field

The spot size area of the optical field has been previously defined (in Section 6.2.3) as that area over which the power density of the light beam is greater than half of the maximum power density. It is essentially identical to the full width half maximum of the optical mode that was encountered in Chapters 4 and 5. As indicated in those chapters, it is a useful measure for determining the coupling losses into and out of the waveguides of the modulator devices.

**Table 6.2** The change in spot size ( $H_y^{11}$  mode) with applied voltage.

Applied voltage (V)	Vertical rib waveguide	Slanted rib waveguide
0	2.0161273	2.1570681
1	2.0148000	2.1552724
3	2.0121455	2.1511932
5	2.0094909	2.1456861
7	2.0068363	2.1430303
10	2.0028545	2.1348704

As can be seen from Table 6.2, the spot size does not significantly change with applied voltage for both the vertical rib waveguide or slanted rib waveguide MZI. The results for the spot size are only given for the  $H_y^{11}$  mode since the quasi TE modes are the only ones affected by application of voltage, as indicated in the previous section. In fact, the slight reduction in spot size area with increasing voltage is due to the slight increase in refractive index with applied field (see equation 6.15). Moreover it can be seen that the spot size for the slanted rib waveguide device is greater (by 6.53% at 0V and 6.18% at 10V) than that for the vertical rib waveguide device, and so a slanted rib waveguide is likely to suffer a small amount of less coupling loss (when coupled to other waveguides or fibres) than its vertical rib waveguide equivalent. One further point to note is that the large amount of power confined to the waveguide area remains in the region of  $80 \pm 5.52\%$ , even in the event of changing voltage or of fabrication parameters. This is because of the much greater difference in refractive index between GaAs and Al<sub>0.3</sub>Ga<sub>0.7</sub>As compared with that for Ti:LiNbO<sub>3</sub>, and hence much better vertical confinement in the GaAs guiding layer.

## 6.4 Changes in Characteristics with Fabrication Parameters

Although there are a number of parameters that are important to modulators, these have been detailed in the previous two chapters but it is necessary to repeat them as the material and structure of the waveguide devices is different, and the procedures outlined in the previous chapters are needed again in order to study the device structure. The two parameters considered to be unique to the device(s) detailed in this chapter are the rib height of the shallow etched waveguide and the slant angle of the rib. How both vary with the drive voltage,  $V_\pi$ , and the spot size will be detailed below. The spot size area given in this part of the study is that for no applied electric field because, as seen in Table 6.2, there is insignificant variation in spot size area with applied voltage.

### 6.4.1 Rib Height

Although a shallow rib is employed, for both the slanted and vertical rib waveguides, it is nevertheless responsible for a weak 2-d confinement of the optical field. The extent to which the height of this rib,  $h$ , affects the spot size and the voltage for which a  $\pi$  phase change is achieved between the light propagating in the two arms of the MZI,  $V_\pi$ , is given in Table 6.3. The results are given for the  $H_y^{11}$  mode since is this mode that is of interest in this study, as mentioned in the previous section. It can be seen that there is an insignificant reduction of 2.72% in spot size area between 0.5 $\mu\text{m}$  and 1.0 $\mu\text{m}$ , whereas there is a 15.89% increase in  $V_\pi$ . The latter is to be expected because with increasing rib height (while keeping all other dimensions as given in Section 6.2.3.) there is a consequential increase in the distance between the upper and lower electrodes; and so

**Table 6.3** Variation in spot size area and  $V_\pi$  with height of AlGaAs rib.

Height of the slanted rib, $h$ . ( $\mu\text{m}$ )	Spot size area ( $\mu\text{m}^2$ )	$V_\pi$ (V)
0.5	2.1570681	7.726
0.625	2.1272416	7.990
0.75	2.1206413	8.294
0.875	2.1145595	8.621
1.0	2.1145384	8.961

the voltage needed to change the refractive index, and hence the phase in both arms, for the push-pull operation of the device, also increases with increasing rib height in a near linear manner.

A better alternative might be to change the rib height but maintain the original overall height of the device structure (the distance between the upper and lower electrodes) at 4.05 $\mu\text{m}$ . This is possible to realise in two ways:

- (i) by decreasing the thickness of the lower (substrate) AlGaAs layer by the same amount by which the rib height has been increased while keeping all other dimensions fixed (to those given in Section 6.2.3.)
- (ii) by decreasing the thickness of  $t_2$  (see Fig. 6.2), the upper unetched AlGaAs layer, by the same amount by which the rib height has been increased while keeping all other dimensions fixed (to those given in Section 6.2.3.).

The results for a rib height of 0.75 $\mu\text{m}$  complying with the two scenarios, (i) and (ii), given in the previous paragraph have been presented in Table 6.4. However, even when retaining the overall device height at the original value of 4.05 $\mu\text{m}$  by reducing the lower AlGaAs layer (see row (i) of Table 6.4) there is no change in the spot size area with only an insignificant decrease in  $V_\pi$  of 2.67% when compared with the results in Table 6.3 (where the rib height was varied while all other dimensions are fixed) for a rib height of 0.75 $\mu\text{m}$ . This is to be expected since the thickness of the substrate should have little impact on the working of the device. It is the distance between the upper electrode

**Table 6.4** Variation in spot size area and  $V_\pi$  with height of AlGaAs rib for the two scenarios given above.

Height of the slanted rib, $h$ ( $\mu\text{m}$ )	Spot size area( $\mu\text{m}^2$ )	$V_\pi$ (V)
(i) 0.75 (lower AlGaAs layer reduced by 0.25 $\mu\text{m}$ )	2.1206413	8.072
(ii) 0.75(upper AlGaAs layer, $t_2$ , reduced by 0.25 $\mu\text{m}$ )	1.5347889	6.177

(to which voltage is applied) and the GaAs waveguiding layer as well as the distance between the base of the rib (loading the GaAs waveguiding layer) and the GaAs waveguiding layer that should make an impact on device operation. This is indeed the

case for scenario (ii) with a rib height of 0.75 $\mu\text{m}$ , the results for which are presented in row (ii) of Table 6.4, where the distance between the upper electrode and the GaAs waveguiding layer,  $t_1$  (see Fig. 6.2), is kept the same as for the original structure but where  $t_2$  is decreased by 0.25 $\mu\text{m}$  since the rib height has been increased by 0.25 $\mu\text{m}$  from the rib height of 0.5 $\mu\text{m}$  (for the original structure). There is a marked reduction in the spot size area of the optical mode (compared with that for the original structure) because  $t_2$  has decreased to 0.07 $\mu\text{m}$  and so the rib has a much greater influence in confining the optical mode as it is nearer the waveguiding layer. There is a reduction in  $V_\pi$  (compared with the original structure) due to the optical mode becoming better confined and smaller. It has been previously reported that  $V_\pi$  decreases for smaller optical modes (Veselka and Korotky, 1986). However, a very small value of  $t_2$  infers that the device operation could be affected by any fabrication defects – particularly with regard to surface states, but any increase in  $t_2$  would again lead to linear increases in  $V_\pi$ .

#### 6.4.2 Slant Angle

A slanted rib with an angle,  $\theta_r$ , of about 52° is realised when the rib is fabricated using wet etch techniques. With reactive ion etching it is possible to achieve vertical ribs ( $\theta=90^\circ$ ). However, a varied set of angles from about  $\sim 75^\circ$  to 90° is more generally achieved with a variety of dry etching techniques (Franz *et al.*, 1996). Hence the relationship of  $V_\pi$  and spot size with slant angle,  $\theta_r$ , for the fundamental quasi-TE mode, can be seen in Table 6.5.

**Table 6.5** Variation in spot size area and  $V_\pi$  with slant angle of the AlGaAs rib.

Angle of the slanted rib, $\theta_r$	Spot size area( $\mu\text{m}^2$ )	$V_\pi$ (V)
52°	2.1570681	7.726
62°	2.1108099	7.700
72°	2.0728610	7.692
82°	2.0400182	7.689
90°	2.0161273	7.692

Only a reduction of spot size area of 6.53% and a 0.36% reduction in  $V_\pi$  occurred in changing from a 52° slanted rib to a vertical rib. This reduction in spot size may be because the width at the base of the rib,  $w_b$ , decreases with increasing rib angle and so the loading of the AlGaAs rib is slightly smaller. The vertical rib, represented by 90° in Table 6.5, has a width of 4μm. If the width of the vertical rib is taken to match  $w_b$  for the 52° slanted rib ( $\approx 4.78\mu\text{m}$ ), then the spot size area is  $2.1750504\mu\text{m}^2$ , showing that the spot size is insignificantly dependent on  $w_b$  as well as the shape of the rib. However, the overlap between the optical and electric fields has negligible variation and hence this is reflected in the 0.36% variation in  $V_\pi$  with the angle of the slanted rib. However, for cases where the guiding area of the waveguide is located in the rib (Llobera *et al.*, 2002; Rahman *et al.*, 2001), the slant angle of the rib has more significant effects on waveguide properties. This is also mostly true for any other fabrication parameters when the waveguide is located in the rib (Byun *et al.* 1996). However, even when the rib (with reasonable dimensions) is directly above the guiding layer, for a planar-type waveguide, the optical mode was found to be very well confined (Lohmeyer, 1997).

#### 6.4.3 Other Fabrication Parameters

There are other variations in fabrication parameters which are more likely to affect spot size and/ or  $V_\pi$ , and these are the thickness of the GaAs guiding layer ( $d_g$ ), the thickness of the upper AlGaAs layer, ( $t_2$ ), and the width of the AlGaAs rib,  $w_r$ . The results again for the fundamental quasi-TE mode are given in Tables 6.6 – 6.8. The values that have been used throughout this study for these three parameters were 0.73μm, 0.32μm and 4.0μm, respectively. From Table 6.6 it can be seen that there were significant changes

**Table 6.6** Variation in spot size area and  $V_\pi$  with thickness of the GaAs guiding layer,  $d_g$ .

Thickness of GaAs guiding layer, $d_g$ (μm)	Spot size area(μm <sup>2</sup> )	$V_\pi$ (V)
0.23	1.2440795 (-42.33%)	5.514 (-28.63%)
0.43	1.3769394 (-36.17%)	6.035 (-21.89%)
0.73	2.1570681 (0.00%)	7.726 (0.00%)
1.03	3.4705062 (60.89%)	10.578 (36.91%)

in the spot size area with changing  $d_g$ . The increase in spot size area was much larger than the corresponding increase of 41% in the guide area when  $d_g$  was increased to 1.03 $\mu\text{m}$ . However, the decrease in spot size area was comparable with the corresponding decrease (of 41%) in the guide area when  $d_g$  was decreased to 0.43 $\mu\text{m}$ . Moreover, when  $d_g$  was increased by 0.3 $\mu\text{m}$  to 1.03 $\mu\text{m}$ , the corresponding increase in  $V_\pi$  was comparable with 41% in the guide area but when  $d_g$  was increased by the same amount, to 0.43 $\mu\text{m}$ , the corresponding decrease in  $V_\pi$  was 28.63% (much smaller than 41%). These unequal changes in  $V_\pi$  may mirror the unequal changes in spot size area/ mode size as it is well known that  $V_\pi$  increases for larger optical modes (Veselka and Korotky, 1986).

Table 6.7 shows that as  $t_2$ , the thickness of the upper Al<sub>0.3</sub>Ga<sub>0.7</sub>As layer, was decreased this corresponded to a linear decrease in  $V_\pi$ . However, for an increase in  $t_2$  changes in  $V_\pi$  are no longer linear. This is because for a large value of  $t_2$  (0.44 $\mu\text{m}$ ) the rib no longer

**Table 6.7** Variation in spot size area and  $V_\pi$  with the thickness of the upper Al<sub>x</sub>Ga<sub>1-x</sub>As layer,  $t_2$ .

Thickness of upper AlGaAs layer, $t_2$ ( $\mu\text{m}$ )	Spot size area( $\mu\text{m}^2$ )	$V_\pi$ (V)
0.02	1.4785818 (-31.45%)	5.241 (-32.16%)
0.20	1.7851818 (-17.24%)	6.324 (-18.15%)
0.32	2.1570681 (0.00%)	7.726 (0.00%)
0.44	2.8442103 (31.86%)	10.403 (34.65%)

influences the lateral waveguiding of the optical mode and so the mode increases quickly to become very close to that for a planar waveguide. Otherwise, when the waveguide is influenced by the Al<sub>0.3</sub>Ga<sub>0.7</sub>As rib loading then both the spot size area and  $V_\pi$  remain linear with changes in  $t_2$ .

**Table 6.8** Variation in spot size area and  $V_\pi$  with the width of the rib,  $w_r$ .

Width of slanted rib, $w_r$ ( $\mu\text{m}$ )	Spot size area( $\mu\text{m}^2$ )	$V_\pi$ (V)
3.0	1.960028 (-9.13%)	8.109 (4.95%)
4.0	2.1570681 (0.00%)	7.726 (0.00%)
5.0	2.3773667 (10.21%)	7.722 (-0.05%)

The spotsize area varies linearly with  $w_r$ , the width of the rib, as shown in Table 6.8, but there is very little difference in  $V_\pi$  when the width of the Al<sub>x</sub>Ga<sub>1-x</sub>As rib is increased. This is because there is virtually no change in the overlap of the electric and optical field as a consequence of increasing the width of the rib and the corresponding increase in the spot size area of the optical field. However, when the width of the rib is decreased by 1  $\mu\text{m}$ , the overlap between the optical and electric field decreases by a small amount and hence  $V_\pi$  increases by approximately 5%. This is because the width of the base electrode is controlling the spatial electric field  $E_v(x,y)$  – see Fig. 6.6.

With the increase in percentage of aluminium (Al) to 0.32 and 0.38 in Al<sub>x</sub>Ga<sub>1-x</sub>As, the refractive index of Al<sub>x</sub>Ga<sub>1-x</sub>As reduces to 3.22241 and 3.19457, respectively, and for a decrease in  $x$  to 0.22 and 0.28 the refractive index increases to 3.26891 and 3.24105, respectively. From this it can be seen that for larger percentage of Al, the contrast between the refractive index of the GaAs guiding layer and the surrounding Al<sub>x</sub>Ga<sub>1-x</sub>As layers is larger. As the refractive index of the Al<sub>x</sub>Ga<sub>1-x</sub>As layers surrounding the GaAs guiding layer decreases (with increasing Al percentage), then the propagation constant of the fundamental quasi-TE mode ( $H_y^{II}$ ) also decreases leading to lower effective index,  $n_{eff}$ , of the optical mode (for a definition of  $n_{eff}$ , see Section 6.2.3). From Table 6.9 it can be seen that this leads to larger voltages, to produce a  $\pi$  phase shift between the light in the two arms of the MZI-based modulator,  $V_\pi$ .

**Table 6.9** Variation in spot size area and  $V_\pi$  with percentage of Al in the Al<sub>x</sub>Ga<sub>1-x</sub>As layers,  $x$ .

Percentage of Al, $x$ ( $\mu\text{m}$ )	Refractive Index for Al <sub>x</sub> Ga <sub>1-x</sub> As, $n$	Spot size area( $\mu\text{m}^2$ )	$V_\pi$ (V)
0.22	3.26891 (1.15%)	2.1361000 (-0.97%)	7.076 (-8.41%)
0.28	3.24105 (0.29%)	2.1444150 (-0.59%)	7.537 (-2.45%)
0.30	3.23174 (0.00%)	2.1570681 (0.00%)	7.726 (0.00%)
0.32	3.22241 (-0.29%)	2.1690353 (0.55%)	7.921 (2.52%)
0.38	3.19457 (-1.15%)	2.2595495 (4.75%)	8.607 (11.04%)

For small changes (positive and negative) in Al percentage,  $x$ , the changes in  $V_\pi$  are linear. This is also true for the spot size area. However, as the Al percentage change becomes larger (positive and negative) the change in  $V_\pi$  and spot size area becomes slightly nonlinear such that a negative change leads to a slightly lower increase (in both

$V_\pi$  and spot size area) than that which would be obtained for a linear increase and a positive change leads to a greater increase (in both  $V_\pi$  and spot size area) than that which would be obtained for a linear increase.

In order to gain some understanding of the reason for these results, look at the following equation (Sakamoto *et al.*, 1999)

$$V_\pi = \frac{\lambda}{2L} \frac{t_{tot}}{n^3 r_{41}} \frac{1}{\Gamma} \quad (6.16)$$

(where  $\lambda$ =wavelength of operation,  $L$ =length of electrode,  $n$ =refractive index of the Al<sub>x</sub>Ga<sub>1-x</sub>As material and  $\Gamma$ =the overlap between the applied electric and optical fields.  $t_{tot}$  and  $r_{41}$  have already been defined). From equation (6.16) it is clear that  $V_\pi$  is dependent on  $(n_{\text{AlGaAs}})^{-3}$  and  $\Gamma^{-1}$ , as all other variables are constant. The spot size area is inversely dependent on  $\Gamma$ , and so should also contribute to  $V_\pi$  (If the spot size area increases, the size of the applied electric field remains unchanged, and therefore the overlap between the optical and applied electric fields,  $\Gamma$ , will decrease). However, as seen in Table 6.9, that there is a small variation in spot size area with  $x$ . Hence, it is clear that spot size area,  $1/\Gamma$  and  $V_\pi$  all follow a similar trend, although not necessarily in a linearly with changes in  $n_{\text{AlGaAs}}$ .

## 6.5 Summary

It is well known that the MMI device is superior with respect to both Y junctions and 3dB directional couplers, as mentioned in Chapter 5 and also in this chapter. Moreover, no detrimental coupling losses will affect the waveguides of the MMI coupler as there is no need to bring the waveguides closer together as for the 3dB directional coupler.

In summary the following observations were made from the results:

- The modulator only supported single-mode TE polarised light (in agreement with Sakamoto *et al.*, (1999))
- Sharp peaks occur in the modulating electric field at the edges of the electrodes – less so for the ground electrode (in agreement with Marcuse (1982))

- Simulated results from programs designed for the work in this thesis gave  $V_{\pi}L$  of 7.726Vcm which is slightly lower than 8.7Vcm found by published experimental work (Sakamoto *et al.*, 1999)
- The rib serves to only weakly control the planar optical mode in a lateral manner, likewise variations in the rib fabrication parameters only weakly affect the characteristics of the GaAs/Al<sub>x</sub>Ga<sub>1-x</sub>As MZI modulator. Hence, there is a minimal variation between the characteristics of a slanted waveguide device and its vertical rib waveguide equivalent

The fabrication parameters that greatly affect this device are those associated with the design of the planar nature of the device. However, it can be seen that the main variation in  $\Delta n(x,y)$  due to the applied electric field occurs not only in the guide area but in the upper cladding area and rib as well: hence, the reason for significant changes in  $V_{\pi}$  when both the thickness of the upper Al<sub>x</sub>Ga<sub>1-x</sub>As cladding layer and height of the rib were varied. Yet, in decreasing these two properties of the device the metal electrode becomes nearer the guiding GaAs layer and so the optical loss due to the upper metal electrode can increase. This and a number of other studies need to be done to obtain a complete model for the device. However, this approach has already been covered in previous chapters.



# 7

## *Discussion and Suggestions for Further Work*

---

---

### **7.1. General Conclusions**

In this part of the thesis it is important to evaluate the study as a whole. This will be done in a number of ways: (a) to determine whether and how the aims of project have been achieved, (b) to determine the validity of the results, (c) to determine the directions in which this study can be continued and, (d) to determine the relevance of this study to the research and development of optical modulator devices.

Section 1.3 of this thesis gave the aims of the project.

**1:**The initial aims of the study were to determine the more popular device and material configurations for electro-optic modulators and then to determine the best method with which to model these devices. Both were covered in the introductory parts of this thesis (i.e. Sections 1.3 and 1.4, respectively). When considering the numerical method that is the most powerful and versatile (see Section 1.4) it is evident that for an anisotropic, inhomogeneous waveguide (as is the Ti-indiffused LiNbO<sub>3</sub> waveguide), which for single-mode operation works near to the cutoff for the waveguide, the full vectorial **H**-

field finite element method is the only numerical method with which accurate results can be obtained with relative ease (even when compared with the corresponding full vectorial  $\mathbf{E}$ -field approach). Moreover, it was also determined that of the three main device configurations (i.e. single waveguide phase modulator structures, directional coupler based structures and Mach-Zehnder interferometer based structures) that for high speed Ti:LiNbO<sub>3</sub> modulator devices Mach-Zehnder interferometer based structures were mainly used. Directional coupler based structures are used for Ti:LiNbO<sub>3</sub> lower speed switching applications. For semiconductor based electro-optic devices high-speed switching devices can also take the form of Mach-Zehnder interferometer based structures with a multimode interference based device input and output – see Chapter 6. In fact the greater flexibility (by way of better fabrication control – e.g. epitaxial growth, greater device integration – e.g. EMLs) achievable with semiconductor materials when compared with electrooptic dielectric materials such as Ti:LiNbO<sub>3</sub> (see Chapter 1) has led to much more interest in semiconductor electrooptic (or electroabsorption) modulator devices. However, LiNbO<sub>3</sub> is the dielectric crystal material in which most interest has been shown, because of its low transmission loss, large electro-optical, piezo-electrical and elasto-optical coefficients, high second order nonlinearity, as well as low chirp and high bandwidth. Moreover, as mentioned in Chapter 1 a market study has shown that electro-optic modulators (of which LiNbO<sub>3</sub> is the most widely used material) still dominate the optical modulator market with over 60% consumption and it will not be until 2008 that electroabsorption modulators are expected to have a leading share of the market. Also, future generation wavelength-agile networks are expected to move away from the current wavelength range of operation (i.e. 1530-1565nm) and encompass the range between 1570-1610nm. Lithium niobate modulators have been designed to have low loss and constant switching voltages over the total wavelength range from 1530-1610nm, where the present InP-based semiconductor devices may have a problem with moving towards longer wavelengths. In the meantime, new and better semiconductor materials can be found which can work efficiently over these longer wavelengths. Hence, LiNbO<sub>3</sub> is still a market force, and research work in this area should only serve to improve the function of electro-optic modulator devices fabricated from this material and therefore show the relevance of this study to the research and development of electro-optic modulator devices. LiNbO<sub>3</sub> has shown to have the potential for achieving high bandwidth (in excess of 70GHz) modulator devices with acceptable insertion losses and extinction ratio. However, the

drive voltage for these smaller devices is considered to be high compared to semiconductor modulators, and it is this which remains an area for improvement for these LiNbO<sub>3</sub> devices. However, before any novel improvements can be made or suggested to the device design, a fully working model is needed to be realised, and it is expected that the work carried out in this project will make a significant contribution to this end.

**2:** The next aim was to develop programs to model the refractive index of LiNbO<sub>3</sub> (a uniaxially birefringent material) together with the change in refractive index due to the indiffusion of Ti and to observe how this change is affected by fabrication parameters. The diffusion process is given by Fick's second law of diffusion (see equation (3.1)), a second order partial differential equation, the solution for which depends on the concentration of the Ti on the surface of the LiNbO<sub>3</sub> crystal, the depth of the diffusion and any symmetry involved (as explained in chapter 3). It is obvious that the refractive index profile also follows the diffusion profile (compare equations (4.14) and (3.3)). Several models have been published in order to find the maximum change in refractive index (which occurs on the surface of the LiNbO<sub>3</sub>),  $\Delta n$ , with Ti indiffusion. These were examined in order to assess how these matched with real values and how they could realistically include the main fabrication parameters while still giving realistic values for the ordinary and, more importantly, the extraordinary indices of Ti:LiNbO<sub>3</sub>. Only one of the methods included all the diffusion parameters in the expression for  $\Delta n_e$ , the peak change in the extraordinary refractive index with Ti indiffusion, and it is for this reason that the expression given by Korotky and Alferness (1987) was used in Chapter 4, as by using all the diffusion parameters the expression therefore appeared to be more realistic. However, it was later found to give low values for  $\Delta n_e$  and there was no corresponding expression for  $\Delta n_o$ . To calculate  $\Delta n_o$  a second method (Fouchet *et al.*, 1987) was used. In Chapter 5, four methods were compared, and it was found that the third method (Strake *et al.*, 1988) gave discrepancies for any Ti concentrations over  $0.5 \times 10^{21}$  atoms/cm<sup>3</sup>. For present day Ti:LiNbO<sub>3</sub> devices (typically operating at wavelengths of 1.55  $\mu\text{m}$ ) that use diffusion parameters which seek to maximise  $\Delta n_e$  (without any adverse outcomes), Ti concentration are typically higher than  $0.5 \times 10^{21}$  atoms/cm<sup>3</sup> (see structure in Chapter 5) and so the third method is not a viable option for today's Ti:LiNbO<sub>3</sub> devices.

An **H**-field full vectorial finite element method modal solver package was then developed for an anisotropic, inhomogeneous (e.g. Ti:LiNbO<sub>3</sub>) electro-optic modulator – for both the directional coupler and Mach-Zehnder interferometer structures. The refractive index values were input to this package. The package at this stage would only have been capable of noting modal properties of the device without application of voltage.

**3:**As mentioned throughout this thesis for electrooptic modulators there is no resultant charge with applied voltage and so the Laplace equation is used to examine the variation in modulating potential and electric field throughout the cross-section of the device. Hence, a Laplace solver was developed for these electrooptic structures studied in this work. Using the equations for the linear electrooptic effect, a program was then developed to find the change in the refractive index throughout the device for any applied voltage. This change in refractive index was added to the original refractive index profile.

**4:**The **H**-field full vectorial finite element method modal solver package was then adapted to take this changed refractive index profile as a file input. The basis for the study was established in the form of these computer programs.

**5:**In fact it is the development, testing and verification of the numerical algorithm used in this work, for the modelling of electrooptic modulators, that forms the majority of the work in this thesis. However, the work described up till now in this chapter can be used to find only the half-wave voltage,  $V_{\pi}$ , for the Mach-Zehnder interferometer-based modulator (see Chapters 5 and 6), or  $V_{\pi}L$  for the directional coupler (see Chapter 4). It was also determined how  $V_{\pi}$  varied with fabrication parameters and which parameters were significant to the functioning of these devices. Although a central figure of merit for the functioning of a modulator device,  $V_{\pi}$  (or  $V_{\pi}L$ ) is one of many important characteristics.

$V_{\pi}$  is a very important characteristic and this feature of the device should be as low as possible. However, since the phase change occurring along the device is dependent on the interaction length of the device (for the directional coupler modulator– see equation (4.1) and for the Mach-Zehnder interferometric (MZI) modulator – see equation (5.1))

or essentially the electrode length, if the voltage applied to the electrodes is low, then the interaction length of the device has to be much longer in order to obtain a phase change of  $\pi$  at the output of the device. Hence, it is expected that the device should be long. However, the interaction length of the directional coupler device modelled in Chapter 4 is dependent on the coupling length of the device before voltage is applied. So one of the first trade-offs that is encountered in the design of these devices is that between device length and half-wave (or drive) voltage. Hence it is essential to design for the purpose for which the device is to be used. For example if a small voltage is needed for the device design, then a longer device should be expected. However, if a smaller device is needed in order to have a higher (3dB electrical) bandwidth then a higher drive voltage should be anticipated. As mentioned earlier in this chapter, the drive voltage for these electro-optic modulator devices is considered to be high (from Chapter 4: 7.682V for a 1.5cm Ti:LiNbO<sub>3</sub> directional coupler device; or from Chapter 5: 4.015V for a 2cm Ti:LiNbO<sub>3</sub> MZI-based modulator; or from Chapter 6: 7.726V for a 1cm GaAs/ Al<sub>0.3</sub>Ga<sub>0.7</sub>As MZI-based modulator) when compared with semiconductor electroabsorption modulators (which are also much shorter than Ti:LiNbO<sub>3</sub> electrooptic modulators, typically 1mm or less – even for devices designed to be packaged) and this is one of the major disadvantages of Ti:LiNbO<sub>3</sub> electrooptic modulators.

**6:** It can be clearly seen that  $V_{\pi}L$  is very similar for both Ti:LiNbO<sub>3</sub> ( $V_{\pi}L=8.03\text{V}\cdot\text{cm}$ ) and GaAs/ Al<sub>0.3</sub>Ga<sub>0.7</sub>As ( $V_{\pi}L=7.726\text{V}\cdot\text{cm}$ ) rib waveguide electro-optic modulators, and so are very similar in operation. Moreover, the GaAs/ Al<sub>0.3</sub>Ga<sub>0.7</sub>As electro-optic modulator had an back etched substrate (Sakamoto *et al.*, 1999) and so it would be difficult to integrate a laser and a photodetector onto the same substrate. Therefore, there is no real benefit of using semiconductor electro-optic material compared with Ti:LiNbO<sub>3</sub> for electro-optic modulators.

**7:** Related to the trade-off between  $V_{\pi}$  and  $L$  is the trade-off between  $V_{\pi}$  and bandwidth since if  $L$  is long  $V_{\pi}$  is small but the bandwidth is also small (due to increased capacitance of the electrodes – see Sections 3.3.3 and 5.6.2). The calculation of the bandwidth was obtained through the development of the Laplace solver to include the RF properties of the electrodes of the Ti:LiNbO<sub>3</sub> MZI-based modulator. The equations used to calculate the microwave effective index,  $n_m$ , and the characteristic impedance of the electrode,  $Z_c$ , are those used in standard texts. The calculation of the conductor loss

of the electrode was also based on the same principles for the calculation of any power (loss or gain) calculation – see equations (3.37)-(3.39). However, it is hard to consider that equation (3.36), in the case of both impedance and velocity matching, would give a realistic value for bandwidth even when the conductor loss calculations,  $\alpha_c$ , were found to be close to those of Noguchi *et al.* (1998).

The half-wave voltage and the bandwidth are not the only important characteristics of an electrooptic modulator: insertion loss is also an important facet of these devices. It was mentioned in Chapter 3 that there are four main components of insertion loss (i.e. coupling loss (between a laser and the modulator device); propagation loss of the material, optical propagation loss due to the electrodes; optical loss due to the bends in the waveguide at the input and output of device), and of these propagation loss of a dielectric material is the smallest. The component mentioned first is mainly due to the difference in the size of the optical modes of the light source and the waveguides of the modulator. Dielectric devices up till recently have been in the form of channel waveguides, and especially for Ti:LiNbO<sub>3</sub> this would not be a problem since the mode size of a laser would probably be encompassed by that of a larger mode of the Ti:LiNbO<sub>3</sub> channel waveguides. However, with etched ridge devices this may be a problem but not insurmountable as much research work has been done in this area (particularly by the Numerical Modelling Group at City University). Bends in most waveguide devices (S-bends being the more widely used) are somewhat circular in their structure. It is the change in direction of the waveguide which leads to the optical power leaking from the guide into the substrate (there is a sharper increase in power loss at the start of the bend than further on– see Fig 5.15). These circular bends were modelled using a conformal transformation method in conjunction with a SVFEBPM. The program was adapted to take a diffused refractive index profile.

The larger the angle of the bend, the more power is leaked (although linearly – see Fig 5.15) into the substrate. Also, the smaller the bend radius the more power is lost. This was also expected. However, the power lost decreased with increasing the height of the rib,  $h$ , for the etched ridge waveguides. This reached a minimum for heights of 4.5 $\mu\text{m}$  and greater. Hence, it was reasoned that there was no need to give results in Figs. 5.15-5.16 for  $h$  greater than 4.5 $\mu\text{m}$ .

In this way, it was possible to attain shorter input/output (I/O) bend sections by using etched waveguides with  $h=4.5\mu\text{m}$  as well as shorter interaction lengths, causing a significant overall reduction of the device size. In fact the reason that a minimum is reached for both  $V_{\pi}L$  and radiation loss due to the  $90^\circ$  circular bend is that the mode is totally contained in the ridge for  $h\geq 4.5\mu\text{m}$ .

The optical loss due to the metal electrodes was obtained by incorporating a perturbation theory component into the **H**-field full vectorial finite element method modal solver package. These were then adapted to include a diffused refractive index profile. It was shown Chapters 4 and 5 that this optical loss decreases exponentially with increasing buffer layer thickness,  $d$ , as expected for both unetched and etched ridge structures. However, this loss increases for an etched device ( $\alpha=0.2\text{dB/cm}$  for  $d=0.2\text{mm}$  and  $e=0.15\text{mm}$ ) when compared with an unetched device ( $\alpha=0.12\text{dB/cm}$  for  $d=0.2\text{mm}$  and  $e=0.15\text{mm}$ ). This is because the optical mode although well-confined in the ridge is now more concentrated under the electrodes than for an unetched waveguide device.

The results for the circular bends given by the SVFEBPM program, gave low losses for these sections. However, real devices have S-bends. This can be done by using different conformal transformation equations – similar to that given in equation (3.18). The optical loss due to the metal electrodes may have given realistic values: however, there was not enough data to compare. It was therefore essential to incorporate all the losses into the program to calculate a total value of insertion losses for the device and then compare this with published experimental data. These are the more obvious suggestions for further work.

Most importantly, it can be clearly seen in Chapters 4 to 6 that when several real structures (from experiments reported in other author's published work) were tested using these programs, the results obtained were in good agreement with those from the published work regarding these structures.

## 7.2 Suggestions For Future Work

There are, in fact, several ways that this work can be carried forward.

The most obvious may be to add more features (such as extinction ratio, chirp – both important to high speed devices) to the present model, as separate program modules, may be more viable at this stage, as the model for electro-optic modulators will become more complete. In this way it will be possible to design devices which have high extinction ratios and very low chirp. This will also involve adding further realistic imperfections to the device structure, (e.g. inconsistencies in waveguide width). Another way in which the model for the electro-optic modulator can be enhanced is to use full-wave equation instead of quasi-TEM equations in order to obtain the RF properties of the device, as it has been shown in published literature that the quasi-TEM equations overestimate the bandwidth of the device (as mentioned in this work – see Section 5.6.2).

As there is more interest today in semiconductor modulator devices than for their electro-optic equivalents, it could also be equally worthwhile to proceed straight to GaAs/Al<sub>x</sub>Ga<sub>1-x</sub>As doped electroabsorption modulators. However, this would involve the development of new core programs since the way these devices function is quite different from the electro-optic modulator, as evidenced by the free carriers and consequent charge flow in these devices. However, bulk electroabsorption semiconductor modulators should be modelled before progressing to the more complicated semiconductor MQW electroabsorption modulators.

Even more relevant would be to develop the present model to include electro-optic polymer modulators, as the core programs could easily be adapted and developed for these modulators.

The device model could also be easily extended to include other devices, as the interest for today's optoelectronic devices is to have integrated multifunctional devices. In each case, as for the electro-optic modulator model, the device first modelled should be simple, any complexities can be added later.

So it can be seen that the vector **H**-field finite element method when used alone or in conjunction with other methods can indeed create a very powerful waveguide electro-optic modulator device model, and by using these methods again it should be possible to simulate other modulator devices as well as other electro-optic devices.

## Appendix A1: Maxwell's Equations

---

These equations can be used to describe any electromagnetic field solutions, and so are used in the analysis of optical waveguides. In differential form Maxwell's equations for time dependent fields are given below:

$$\nabla \times \mathbf{E} = -\frac{\partial \mathbf{B}}{\partial t} \quad (\text{A1.1})$$

$$\nabla \times \mathbf{H} = \frac{\partial \mathbf{D}}{\partial t} + \mathbf{J} \quad (\text{A1.2})$$

$$\nabla \cdot \mathbf{D} = \rho \quad (\text{A1.3})$$

$$\nabla \cdot \mathbf{B} = 0 \quad (\text{A1.4})$$

where  $\nabla$  is the del operator ( $= \partial/\partial x, \partial/\partial y, \partial/\partial z$ ),  $\mathbf{E}$  is the electric field vector (V/m),  $\mathbf{H}$  is the magnetic field vector (A/m),  $\mathbf{J}$  is the conduction or convection current density (A/m<sup>2</sup>),  $\rho$  is the charge density (C/m<sup>3</sup>) and

$$\mathbf{B} = \mu \mathbf{H} \quad (\text{A1.5})$$

$$\mathbf{D} = \varepsilon \mathbf{E} + \mathbf{P} \quad (\text{A1.6})$$

where  $\mathbf{B}$  is the magnetic flux density (T),  $\mathbf{D}$  is the electric flux density (C/m<sup>2</sup>),  $\mathbf{P}$  is the electric polarisation (C/m<sup>2</sup>) and

$$\mathbf{P} = \varepsilon_0 \chi_e \mathbf{E} \quad (\text{A1.7})$$

$$\mu = \mu_0 \mu_r \quad (\text{A1.8})$$

$$\varepsilon = \varepsilon_0 \varepsilon_r \quad (\text{A1.9})$$

where  $\chi_e$  is the electric susceptibility ( $= \varepsilon_r - 1$ ),  $\varepsilon_0$  and  $\mu_0$  are permittivity and permeability of a vacuum, respectively, and are given by  $8.854 \cdot 10^{-12}$  F/m and  $4\pi \cdot 10^{-7}$  H/m,  $\varepsilon_r$  and  $\mu_r$  are the relative permittivity and relative permeability of the medium, respectively. For optical waveguides,  $\mu_r$  typically has the value of unity. Also, another term for  $\varepsilon_r$  is the dielectric constant. For anisotropic guides, there is no longer a simple dielectric constant but a dielectric tensor, where  $\varepsilon_r$  would take different values along the three co-ordinate axes.

Two important and related equations are the continuity equation and the Poynting vector for energy flow. The continuity equation is given by:

$$\nabla \cdot \mathbf{J} = -\frac{\partial \rho}{\partial t} \quad (\text{A1.10})$$

It is associated with the current flow and the conservation of charge, and this together with equation (A1.3), is particularly important to the modelling and characterisation of semiconductor devices.

The Poynting vector is given by:

$$\mathbf{P} = \mathbf{E} \times \mathbf{H} \quad (\text{A1.11})$$

It is a measure of the rate of energy flow out of an enclosing surface, and is therefore important in calculating power variations along the waveguide, say, of a directional coupler or even along waveguide bends.

Taking the curl of equation (A1.1)

$$\nabla \times \nabla \times \mathbf{E} = -\frac{\partial}{\partial t}(\nabla \times \mathbf{B}) \quad (\text{A1.12})$$

using a number of vector identities and relations, and the source free time (i.e.  $\rho=0$ ,  $\mathbf{J}=0$ ) versions of equations (A1.1)-(A1.6) with  $\mathbf{P}=0$ , the above expression becomes

$$\nabla^2 \mathbf{E} + \nabla(\mathbf{E} \cdot \nabla \ln \varepsilon) + \varepsilon \mu_0 \frac{\partial^2 \mathbf{E}}{\partial t^2} = 0 \quad (\text{A1.13})$$

This is the wave equation for  $\mathbf{E}$ , with a spatial variation of the permittivity,  $\varepsilon$ .

Similarly, the wave equation for  $\mathbf{H}$  is

$$\nabla^2 \mathbf{H} + (\nabla \ln \varepsilon) \times (\nabla \times \mathbf{H}) + \varepsilon \mu_0 \frac{\partial^2 \mathbf{H}}{\partial t^2} = 0 \quad (\text{A1.14})$$

For waveguides where the material is an isotropic, homogeneous and source-free dielectric, the wave equation becomes the Helmholtz equation, which for  $\mathbf{E}$  is

$$\nabla^2 \mathbf{E} = \varepsilon \mu_0 \frac{\partial^2 \mathbf{E}}{\partial t^2} \quad (\text{A1.15})$$

and for  $\mathbf{H}$  is

$$\nabla^2 \mathbf{H} = \varepsilon \mu_0 \frac{\partial^2 \mathbf{H}}{\partial t^2} \quad (\text{A1.16})$$

## *Appendix A2: Modal Solutions for Symmetric Domains*

---

---

The rectangular waveguide structure shown in Fig. A2.1, is to be used as an example for a rectangular channel waveguide throughout this section. The waveguide has horizontal

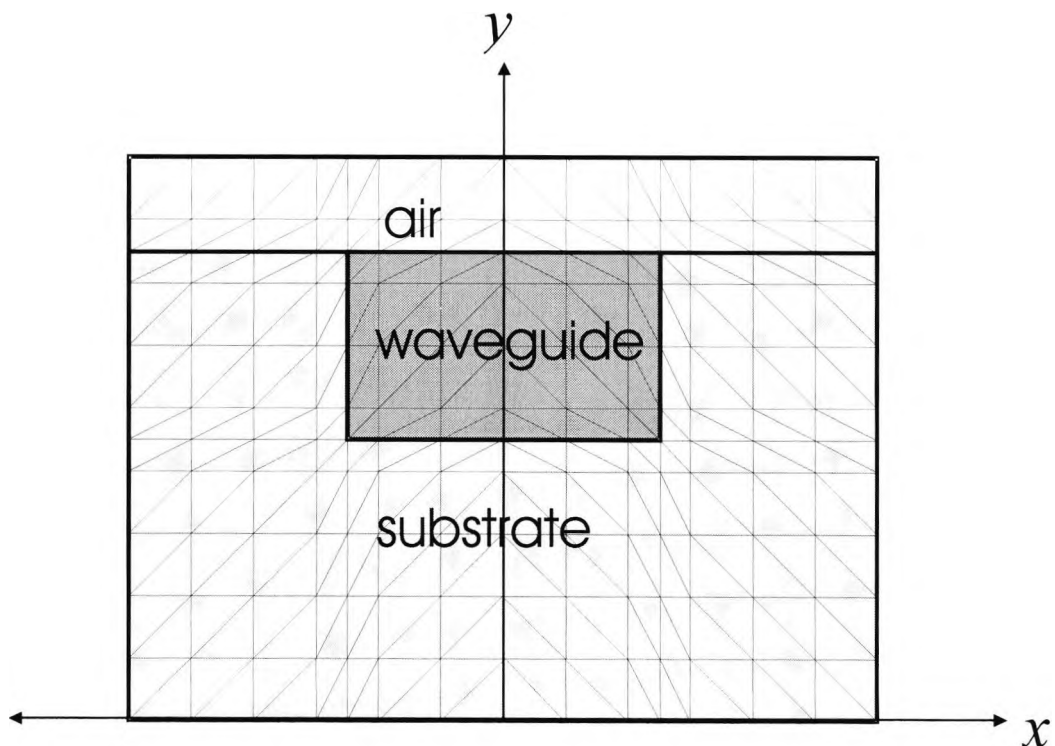


*Fig. A2.1. A rectangular channel dielectric waveguide showing symmetry in the  $y$ -axis.*

reflection symmetry with the  $y$ -axis ( $x=0$ ) as the line of symmetry. It is possible to exploit the symmetry by only examining half the waveguide (either in the region of positive  $x$  or of negative  $x$ ) in order to model the whole waveguide. In order to achieve this an appropriate boundary condition is required along the line of symmetry ( $x=0$ ).

In Section 1.4.2.1 it was mentioned that there are only two types of boundary condition possible when there is abrupt change in material (as would be the case if only the positive half of the above dielectric waveguide in Fig. A2.1 were considered) but when continuity in the electromagnetic field is necessary. These are:

- (i) the magnetic wall boundary condition, represented by

$$\hat{\mathbf{n}} \times \mathbf{H} = 0 \quad (\text{A2.1})$$

- in which case there is continuity of the magnetic field at the boundary

(ii) the electric wall boundary condition, represented by

$$\hat{\mathbf{n}} \cdot \mathbf{H} = 0 \quad (\text{A2.2})$$

- in which case there is no magnetic field at the boundary

For the waveguide structure shown in Fig. A2.1, where the boundary will be taken along the line of symmetry  $x = 0$ ,  $\hat{\mathbf{n}} = \hat{\mathbf{x}}$ .

(i) Taking the case of the magnetic wall boundary condition,  $\hat{\mathbf{n}} \times \mathbf{H} = 0$ , for the waveguide structure in Fig A2.1 gives

$$\hat{\mathbf{x}} \times \mathbf{H} = 0$$

or rather

$$\begin{vmatrix} \hat{\mathbf{x}} & \hat{\mathbf{y}} & \hat{\mathbf{z}} \\ 1 & 0 & 0 \\ H_x & H_y & H_z \end{vmatrix} = 0$$

which gives

$$H_z \hat{\mathbf{y}} + H_y \hat{\mathbf{z}} = 0$$

$\therefore H_y$  &  $H_z$  are both zero.

(ii) Taking the case of the electric wall boundary condition,  $\hat{\mathbf{n}} \cdot \mathbf{H} = 0$ , for the waveguide structure in Fig A2.1 gives

$$\hat{\mathbf{x}} \cdot \mathbf{H} = 0$$

or rather

$$\hat{\mathbf{x}} \cdot (H_x \hat{\mathbf{x}} + H_y \hat{\mathbf{y}} + H_z \hat{\mathbf{z}}) = 0$$

which gives

$$H_x = 0$$

When the whole structure is modelled using the FEM then all modes can be observed if a full modal analysis is implemented. As  $\beta$ , the propagation constant for the waveguide, is decreased from  $k_0 n_{\text{waveguide}}$  the fundamental modes, both TE and TM, are first identified by the model and these are followed by higher order TE and TM modes for

this type of multimode waveguide. However, if only half the structure is modelled (due to use of symmetry) the modes that are observed in the modal analysis are dependent on which boundary condition is used (magnetic wall or electric wall) along the line of symmetry. Half of the modes are observed if a magnetic wall boundary condition is used and the other half are observed if the electric wall boundary condition is used. This will be explained in more detail below.

From the FEM analysis for the whole waveguide structure, the mode for the fundamental TM solution ( $H_x^{11}$  mode) or the fundamental TE solution ( $H_y^{11}$  mode), both very similar in shape and size with  $\beta$  values that are very close together, are first obtained. The next allowed modes are typically  $H_x^{21}$ ,  $H_y^{21}$ ,  $H_x^{12}$  or  $H_x^{31}$  and  $H_y^{12}$  or  $H_y^{31}$ . The order in which the modes are generated, with increasing  $\beta$  is dependent on a number of properties including the dimensions of the waveguide, the operating wavelength, permittivity of the waveguiding section of the waveguide structure as well as the difference between the permittivity of the waveguiding section and that of the substrate of the waveguide structure.

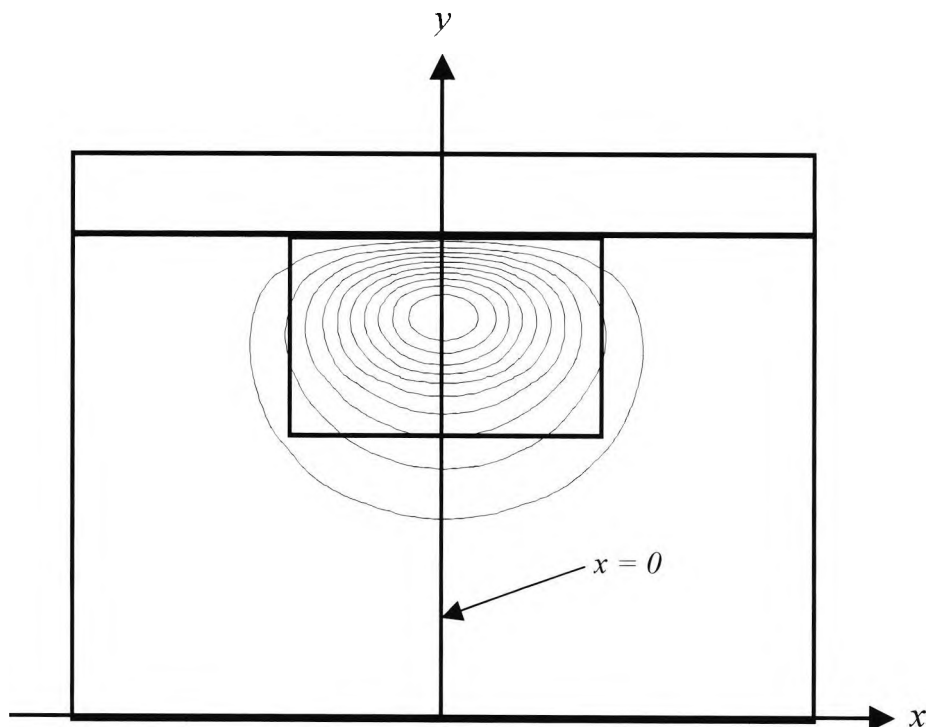


**Fig. A2.2.** The  $H_x^{11}$  mode for a rectangular channel dielectric waveguide, showing symmetry in the  $y$ -axis.

The mode for the fundamental TM solution ( $H_x^{11}$  mode) is shown in Fig. A2.2. It is clearly symmetrical in the line  $x=0$  (the  $y$ -axis) and therefore it would be effective to only analyse half (either for  $x \geq 0$  or  $x \leq 0$ ) of the symmetrical waveguide structure using the FEM such that the modal solutions for the whole waveguide are obtained (as in Fig. A2.2). This can be realised by imposing boundary conditions along the line of symmetry (the line  $x=0$  in this case). From Fig. A2.2 it can be clearly observed that  $H_x^{11}$  is non-zero at  $x=0$ , and  $H_x^{11}$  can only be non-zero for the magnetic wall boundary condition when  $\hat{\mathbf{n}} \times \mathbf{H} = 0$ , or rather  $\hat{\mathbf{x}} \times \mathbf{H} = 0$ .

In order to attain the fundamental TE solution ( $H_y^{11}$  mode) for the waveguide structure, the appearance of which will be very much like that of the  $H_x^{11}$  mode in Fig. A2.2., the symmetry of the waveguide can again be used to advantage by imposing boundary conditions along the line of symmetry (the line  $x=0$ ). However, now it will be  $H_y^{11}$  that is non-zero at  $x=0$ , and  $H_y^{11}$  can only be non-zero for the electric wall boundary condition when  $\hat{\mathbf{n}} \cdot \mathbf{H} = 0$ , or rather  $\hat{\mathbf{x}} \cdot \mathbf{H} = 0$ .

Either of these boundary conditions is then used throughout the extent of the modal analysis performed for the waveguide structure. The first allowed mode to be generated in the half-waveguide structure was the fundamental TE( $H_y^{11}$ ) or TM( $H_x^{11}$ ) mode – depending on the boundary.

If a magnetic wall boundary condition was imposed along the line of symmetry ( $x=0$ ), both  $H_y$  and  $H_z$  are required to be zero and only  $H_x$  can be non-zero at the boundary ( $x=0$ ). Hence, as shown above,  $H_x^{11}$  is the first mode observed for this half-waveguide structure. For the mode  $H_y^{11}$ ,  $H_y$  has to be non-zero but the requirement for a magnetic wall boundary condition is contrary to this and so  $H_y^{11}$  will not be observed for this case.

For the mode  $H_x^{21}$ ,  $H_x$  is zero at the boundary ( $x=0$ ), which is contrary to the requirement for a magnetic wall boundary condition, and so  $H_x^{21}$  will not be observed for this half-waveguide structure. For the mode  $H_y^{21}$ ,  $H_y$  is zero at the boundary, which satisfies the requirement for a magnetic wall boundary condition, and so  $H_y^{21}$  will be observed for this half-waveguide structure.

For the mode  $H_x^{31}$ ,  $H_x$  is non-zero at the boundary ( $x=0$ ), which satisfies to the requirement for a magnetic wall boundary condition, and so  $H_x^{31}$  will be observed for this half-waveguide structure. For the mode  $H_y^{31}$ ,  $H_y$  is non-zero at the boundary, which is contrary to the requirement for a magnetic wall boundary condition, and so  $H_y^{31}$  will not be observed for this half-waveguide structure.

It can therefore be seen that  $H_x^{51}, H_x^{71}, H_x^{91}, \dots, H_x^{n1}$  (where  $n$  is an odd integer) – for the original whole waveguide structure – would also be observed for a half-waveguide structure when a magnetic wall boundary condition was imposed along the line of symmetry ( $x=0$ ). Following this procedure it can be seen that  $H_x^{12}, H_x^{32}, H_x^{52}, \dots, H_x^{n2}$  (where  $n$  is an odd integer) – for the original whole waveguide structure – would also be observed for the half-waveguide when a magnetic wall boundary condition was imposed along the line of symmetry ( $x=0$ ). Hence, the modes  $H_x^{nm}$  (where  $m$  is an integer and  $n$  is only an odd integer) – for the original whole waveguide structure – can only be observed in the half-waveguide when a magnetic wall boundary condition was imposed along the line of symmetry ( $x=0$ ). Similarly, the modes  $H_y^{nm}$  (where  $m$  is an integer and  $n$  is only an even integer) – for the original whole waveguide structure – can only be observed in the half-waveguide when a magnetic wall boundary condition was imposed along the line of symmetry ( $x=0$ ).

Following this procedure it also can be seen that modes  $H_y^{nm}$  (where  $m$  is an integer and  $n$  is only an odd integer) – for the original whole waveguide structure – can only be observed in the half-waveguide when an electric wall boundary condition was imposed along the line of symmetry ( $x=0$ ). Similarly, the modes  $H_x^{nm}$  (where  $m$  is an integer and  $n$  is only an even integer) – for the original whole waveguide structure – can only be observed in the half-waveguide when an electric wall boundary condition was imposed along the line of symmetry ( $x=0$ ).

A similar analysis can also be done for a waveguide with line of symmetry along  $y=0$ .

For a waveguide with two-fold symmetry, e.g. an optical fibre waveguide (which although has infinite rotational symmetry, as can be seen from Fig. A2.3, can be easily analysed by using two-fold symmetry), two boundary conditions will have to be

imposed – typically along the positive sections of the  $x$  and  $y$  axes (i.e. in first quadrant of the Cartesian co-ordinate axes which has been shaded in Fig. A2.3).

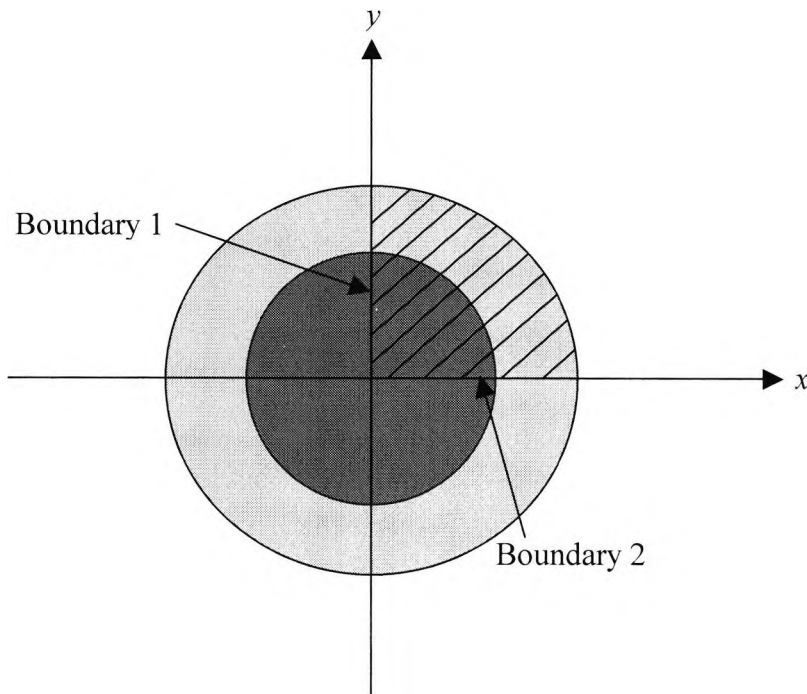


**Fig. A2.3.** An optical fibre waveguide, showing two-fold symmetry such that the shaded region need only be modelled/ analysed.

The fundamental TE or TM mode will naturally follow the shape of the circular waveguide. Considering the fundamental TE mode ( $H_y^{11}$ ) for the whole structure but when only a quarter of the optical fibre waveguide is analysed,  $H_y^{11}$  needs to be continuous at boundary 1 and boundary 2. The normal vector  $\hat{\mathbf{n}}$  for boundary 1 is  $\hat{\mathbf{x}}$  and for boundary 2 it is  $\hat{\mathbf{y}}$ .

(i) Taking the case of the magnetic wall boundary condition,  $\hat{\mathbf{n}} \times \mathbf{H} = 0$ , at both boundaries for the waveguide structure in Fig A2.3 gives for

Boundary 1:

$$\hat{\mathbf{x}} \times \mathbf{H} = 0$$

or rather

$$\begin{vmatrix} \hat{\mathbf{x}} & \hat{\mathbf{y}} & \hat{\mathbf{z}} \\ 1 & 0 & 0 \\ H_x & H_y & H_z \end{vmatrix} = 0$$

which gives

$$H_z \hat{\mathbf{y}} + H_y \hat{\mathbf{z}} = 0$$

$\therefore H_y$  &  $H_z$  are both zero.

and

Boundary 2:

$$\hat{\mathbf{y}} \times \mathbf{H} = 0$$

or rather

$$\begin{vmatrix} \hat{\mathbf{x}} & \hat{\mathbf{y}} & \hat{\mathbf{z}} \\ 0 & 1 & 0 \\ H_x & H_y & H_z \end{vmatrix} = 0$$

which gives

$$H_z \hat{\mathbf{x}} - H_x \hat{\mathbf{z}} = 0$$

$\therefore H_x$  &  $H_z$  are both zero.

(ii) Taking the case of the electric wall boundary condition,  $\hat{\mathbf{n}} \cdot \mathbf{H} = 0$ , at both boundaries for the waveguide structure in Fig A2.3 gives

Boundary 1:

$$\hat{\mathbf{x}} \cdot \mathbf{H} = 0$$

or rather

$$\hat{\mathbf{x}} \cdot (H_x \hat{\mathbf{x}} + H_y \hat{\mathbf{y}} + H_z \hat{\mathbf{z}}) = 0$$

which gives

$$H_x = 0$$

and

Boundary 2:

$$\hat{\mathbf{y}} \cdot \mathbf{H} = 0$$

or rather

$$\hat{\mathbf{y}} \cdot (H_x \hat{\mathbf{x}} + H_y \hat{\mathbf{y}} + H_z \hat{\mathbf{z}}) = 0$$

which gives

$$H_y = 0$$

Since  $H_y^{11}$  is continuous at boundary 1 a magnetic wall boundary condition (which requires both  $H_y$  &  $H_z$  to be zero) cannot be imposed but an electric wall boundary condition (which only requires  $H_x$  to be zero) can be imposed at this boundary. Similarly, since  $H_y^{11}$  is also continuous at boundary 2 an electric wall boundary condition (which requires  $H_y$  to be zero) cannot be imposed but a magnetic wall boundary condition (which only requires  $H_x$  &  $H_z$  to be zero) can be imposed at this boundary.

Hence, in order to observe  $H_y^{11}$  for the quarter-waveguide structure, an electric wall boundary condition is forced on boundary 1 and a magnetic wall boundary condition forced on boundary 2. Similarly, it can be seen that in order to observe  $H_x^{11}$  for the quarter-waveguide structure, a magnetic wall boundary condition is forced on boundary 1 and an electric wall boundary condition forced on boundary 2. It can also be shown that in order to observe  $H_y^{21}$  for the quarter-waveguide structure, a magnetic wall boundary condition is forced on both boundary 1 and boundary 2. Thus, a similar process as was demonstrated for the horizontally symmetric rectangular channel waveguide in Fig. A2.1 can be repeated for this two-fold symmetric waveguide in Fig. A2.3 in order to determine which modes are observed when certain boundary conditions are imposed at the two boundaries (1 & 2).

## *Appendix A3: Assembly of Element Matrices*

---



---

In Section 2.2 it was mentioned that equation (2.7) is the standard eigenvalue equation, and from the detailed account of the full-vector  $\mathbf{H}$ -field formulation it was seen that the eigenvalue equation can be rewritten as

$$[A]\{\mathbf{H}\} - \omega^2 [B]\{\mathbf{H}\} = 0 \quad (\text{A3.1})$$

where  $\omega^2$  is the eigenvalue and more importantly  $[A]$  and  $[B]$  are global matrices that have been formed by summing the contributions of the triangular elements of the discretised waveguide domain. In this section it will be shown how the element matrices are formed.

When the cross-section of the waveguide, or the domain  $\Omega$ , is discretised into a number of elements, the scalar magnetic field (the unknown solution), in the linear triangular element,  $e$ , can be approximated by

$$H_e = \sum_{i=1}^3 N_i H_i^e \quad (\text{A3.2})$$

This can also be expressed in matrix notation as

$$H_e = [N]\{H\}_e \quad (\text{A3.3})$$

where  $[N]$ , the shape function matrix

$$[N] = [N_1 \quad N_2 \quad N_3] \quad (\text{A3.4})$$

and

$$\{H\}_e = \begin{Bmatrix} H_1 \\ H_2 \\ H_3 \end{Bmatrix} \quad (\text{A3.5})$$

However, a vector  $\mathbf{H}$ -field with components  $H_x$ ,  $H_y$  and  $H_z$  can be represented in the matrix form as

$$\mathbf{H}_e = [\mathbf{N}]^T \{H\}_e \quad (\text{A3.6})$$

where

$$[\mathbf{N}] = \begin{bmatrix} \{N\} & \{0\} & \{0\} \\ \{0\} & \{N\} & \{0\} \\ \{0\} & \{0\} & j\{N\} \end{bmatrix} \quad (\text{A3.7})$$

and

$$\{H\}_e = \begin{Bmatrix} \{H_x\}_e \\ \{H_y\}_e \\ \{H_z\}_e \end{Bmatrix} \quad (\text{A3.8})$$

and where

$$\{N\} = [N_1 \quad N_2 \quad N_3]^T \quad (\text{A3.9})$$

and

$$\{H_x\}_e = \begin{Bmatrix} H_{x1} \\ H_{x2} \\ H_{x3} \end{Bmatrix} \quad (\text{A3.10})$$

with similar expressions for  $\{H_y\}_e$  and  $\{H_z\}_e$ .

The  $j (= \sqrt{-1})$  in the shape function matrix  $[\mathbf{N}]$  signifies that the  $H_z$  component is  $90^\circ$  out of phase with the transverse components (or plane).

So

$$\mathbf{H}_e = \begin{bmatrix} N_1 & N_2 & N_3 & 0 & 0 & 0 & 0 & 0 & 0 \\ 0 & 0 & 0 & N_1 & N_2 & N_3 & 0 & 0 & 0 \\ 0 & 0 & 0 & 0 & 0 & 0 & jN_1 & jN_2 & jN_3 \end{bmatrix} \begin{Bmatrix} H_{x1} \\ H_{x2} \\ H_{x3} \\ H_{y1} \\ H_{y2} \\ H_{y3} \\ H_{z1} \\ H_{z2} \\ H_{z3} \end{Bmatrix} \quad (\text{A3.11})$$

Now

$$(\nabla \times \mathbf{H})_e = \begin{Bmatrix} \partial H_z / \partial y - \partial H_y / \partial z \\ \partial H_x / \partial z - \partial H_z / \partial x \\ \partial H_y / \partial x - \partial H_x / \partial y \end{Bmatrix} \quad (\text{A3.12})$$

but because  $H_x$ ,  $H_y$  and  $H_z$  are all functions of  $e^{-j\beta z}$ , which implies  $z$ -dependence.

$$(\nabla \times \mathbf{H})_e = \begin{bmatrix} \frac{\partial H_z}{\partial y} + j\beta H_y \\ -j\beta H_x - \frac{\partial H_z}{\partial x} \\ \frac{\partial H_y}{\partial x} - \frac{\partial H_x}{\partial y} \end{bmatrix} \quad (\text{A3.13})$$

and in matrix form this can be represented as

$$(\nabla \times \mathbf{H})_e = \begin{bmatrix} 0 & j\beta & \frac{\partial}{\partial y} \\ -j\beta & 0 & -\frac{\partial}{\partial x} \\ -\frac{\partial}{\partial y} & \frac{\partial}{\partial x} & 0 \end{bmatrix} \begin{bmatrix} H_x \\ H_y \\ H_z \end{bmatrix} \quad (\text{A3.14})$$

However,

$$\mathbf{H}_e = \begin{bmatrix} H_x \\ H_y \\ H_z \end{bmatrix} = [\mathbf{N}]^T \{H\}_e \quad (\text{A3.15})$$

$$\mathbf{H}_e = \begin{bmatrix} [N] & [0] & [0] \\ [0] & [N] & [0] \\ [0] & [0] & j[N] \end{bmatrix} \{H\}_e \quad (\text{A3.16})$$

where

$$[N] = \{N\}^T = [N_1 \quad N_2 \quad N_3] \quad (\text{A3.17})$$

and

$$[0] = \{0\}^T = [0 \quad 0 \quad 0] \quad (\text{A3.18})$$

$$\therefore (\nabla \times \mathbf{H})_e = \begin{bmatrix} 0 & j\beta & \frac{\partial}{\partial y} \\ -j\beta & 0 & -\frac{\partial}{\partial x} \\ -\frac{\partial}{\partial y} & \frac{\partial}{\partial x} & 0 \end{bmatrix} \begin{bmatrix} [N] & [0] & [0] \\ [0] & [N] & [0] \\ [0] & [0] & j[N] \end{bmatrix} \{H\}_e \quad (\text{A3.19})$$

$$(\nabla \times \mathbf{H})_e = \begin{bmatrix} [0] & j\beta[N] & j\frac{\partial[N]}{\partial y} \\ -j\beta[N] & [0] & -j\frac{\partial[N]}{\partial x} \\ -\frac{\partial[N]}{\partial y} & \frac{\partial[N]}{\partial x} & [0] \end{bmatrix} \{H\}_e \quad (\text{A3.20})$$

This can be written as

$$(\nabla \times \mathbf{H})_e = [\mathbf{Q}]^T \{H\}_e \quad (\text{A3.21})$$

where

$$[\mathbf{Q}] = \begin{bmatrix} \{0\} & -j\beta\{N\} & -\partial\{N\}/\partial y \\ j\beta\{N\} & \{0\} & \partial\{N\}/\partial x \\ j\partial\{N\}/\partial y & -j\partial\{N\}/\partial x & \{0\} \end{bmatrix} \quad (\text{A3.22})$$

By substituting equations (A3.15) and (A3.21) into the variational expression given in equation (2.10), the following is obtained

$$\iint_{\Omega} (\{H\}_e^\dagger [\mathbf{Q}]^* \hat{\varepsilon}^{-1} [\mathbf{Q}]^T \{H\}_e) d\Omega - \omega^2 \iint_{\Omega} \mu \{H\}_e^\dagger [\mathbf{N}]^* [\mathbf{N}]^T \{H\}_e d\Omega = 0 \quad (\text{A3.23})$$

where

† represents the conjugate transpose of the column matrix  $\{H\}_e$

\* represents the conjugate of the matrices  $[\mathbf{Q}]$  and  $[\mathbf{N}]$

T represents the transpose of the matrices  $[\mathbf{Q}]$  and  $[\mathbf{N}]$

By summing over all the elements in  $\Omega$ , the following eigenvalue equation is obtained

$$[\mathbf{A}]\{\mathbf{H}\} - \omega^2 [\mathbf{B}]\{\mathbf{H}\} = 0 \quad (\text{A3.24})$$

where

$$[\mathbf{A}] = \sum_e [\mathbf{A}]_e = \sum_e \iint [\mathbf{Q}]^* \hat{\varepsilon}^{-1} [\mathbf{Q}]^T dxdy \quad (\text{A3.25})$$

$$[\mathbf{B}] = \sum_e [\mathbf{B}]_e = \sum_e \iint [\mathbf{N}]^* [\mathbf{N}]^T dxdy \quad (\text{A3.26})$$

$[\mathbf{A}]$  and  $[\mathbf{B}]$  are the global matrices of the eigenvalue equation and  $[\mathbf{A}]_e$  and  $[\mathbf{B}]_e$  are the element matrices that are summated for all elements  $e$  to obtain  $[\mathbf{A}]$  and  $[\mathbf{B}]$ .

If

$$\hat{\varepsilon} = \begin{bmatrix} \varepsilon_{11} & \varepsilon_{12} & \varepsilon_{13} \\ \varepsilon_{21} & \varepsilon_{22} & \varepsilon_{23} \\ \varepsilon_{31} & \varepsilon_{32} & \varepsilon_{33} \end{bmatrix} = [\mathbf{P}_{mv}] \quad (\text{A3.27})$$

then

$$\hat{\varepsilon}^{-1} = \begin{bmatrix} \varepsilon_{11} & \varepsilon_{12} & \varepsilon_{13} \\ \varepsilon_{21} & \varepsilon_{22} & \varepsilon_{23} \\ \varepsilon_{31} & \varepsilon_{32} & \varepsilon_{33} \end{bmatrix}^{-1} = [\mathbf{P}_{mv}]^{-1} = [\mathbf{P}] = \begin{bmatrix} P_{11} & P_{12} & P_{13} \\ P_{21} & P_{22} & P_{23} \\ P_{31} & P_{32} & P_{33} \end{bmatrix} \quad (\text{A3.28})$$

Although for generality some of the terms of the  $\hat{\epsilon}$  permittivity tensor matrix are sometimes complex (Katsriku, 2000); for the materials to be studied in this work, although anisotropic, the elements of the permittivity tensor matrix are not complex. So throughout this work  $\hat{\epsilon}$  and therefore  $\hat{\epsilon}^{-1}$  are considered as real. (Appendix A4 shows the calculation of  $\hat{\epsilon}^{-1}$ .)

So

$$[\mathbf{A}]_e = \iint [\mathbf{Q}]^* [\mathbf{P}][\mathbf{Q}]^T dx dy \quad (\text{A3.29})$$

where

$$[\mathbf{Q}]^* [\mathbf{P}][\mathbf{Q}]^T = \begin{bmatrix} \{0\} & j\beta\{N\} & -\partial\{N\}/\partial y \\ -j\beta\{N\} & \{0\} & \partial\{N\}/\partial x \\ -j\partial\{N\}/\partial y & j\partial\{N\}/\partial x & \{0\} \end{bmatrix} \begin{bmatrix} p_{11} & p_{12} & p_{13} \\ p_{21} & p_{22} & p_{23} \\ p_{31} & p_{32} & p_{33} \end{bmatrix} \begin{bmatrix} [0] & j\beta[N] & j\partial[N]/\partial y \\ -j\beta[N] & [0] & -j\partial[N]/\partial x \\ -\partial[N]/\partial y & \partial[N]/\partial x & [0] \end{bmatrix} \quad (\text{A3.30})$$

The shape function equation given in equation (2.20), is written again

$$N_1(x, y) = \{(x_2 y_3 - x_3 y_2) + (y_2 - y_3)x + (x_3 - x_2)y\} / \det \quad (\text{A3.31})$$

and  $N_2(x, y)$  and  $N_3(x, y)$  are given by

$$N_2(x, y) = \{(x_3 y_1 - x_1 y_3) + (y_3 - y_1)x + (x_1 - x_3)y\} / \det \quad (\text{A3.32})$$

$$N_3(x, y) = \{(x_1 y_2 - x_2 y_1) + (y_1 - y_2)x + (x_2 - x_1)y\} / \det \quad (\text{A3.33})$$

These equations can be rewritten as

$$N_1 = a_1 + b_1 x + c_1 y$$

$$N_2 = a_2 + b_2 x + c_2 y \quad (\text{A3.34})$$

$$N_3 = a_3 + b_3 x + c_3 y$$

Therefore,

$$\begin{aligned} \frac{\partial\{N\}}{\partial x} &= \left[ \frac{\partial N_1}{\partial x} \quad \frac{\partial N_2}{\partial x} \quad \frac{\partial N_3}{\partial x} \right]^T \\ &= [b_1 \quad b_2 \quad b_3]^T = [b]^T = \{b\} \end{aligned} \quad (\text{A3.35})$$

Similarly,

$$\frac{\partial\{N\}}{\partial y} = [c_1 \quad c_2 \quad c_3]^T = [c]^T = \{c\} \quad (\text{A3.36})$$

which implies that

$$\begin{aligned}
 & [\mathbf{Q}][\mathbf{P}][\mathbf{Q}]^T \\
 &= \begin{bmatrix} \{0\} & j\beta\{N\} & -\{c\} \\ -j\beta\{N\} & \{0\} & \{b\} \\ -j\{c\} & j\{b\} & \{0\} \end{bmatrix} \begin{bmatrix} p_{11} & p_{12} & p_{13} \\ p_{21} & p_{22} & p_{23} \\ p_{31} & p_{32} & p_{33} \end{bmatrix} \begin{bmatrix} [0] & j\beta[N] & j[c] \\ -j\beta[N] & [0] & -j[b] \\ -[c] & [b] & [0] \end{bmatrix} \\
 &= \begin{bmatrix} j\beta p_{21}\{N\} - p_{31}\{c\} & j\beta p_{22}\{N\} - p_{32}\{c\} & j\beta p_{23}\{N\} - p_{33}\{c\} \\ -j\beta p_{11}\{N\} + p_{31}\{b\} & -j\beta p_{12}\{N\} + p_{32}\{b\} & -j\beta p_{13}\{N\} + p_{33}\{b\} \\ -j p_{11}\{c\} + j p_{21}\{b\} & -j p_{12}\{c\} + j p_{22}\{b\} & -j p_{13}\{c\} + j p_{23}\{b\} \end{bmatrix} \begin{bmatrix} [0] & j\beta[N] & j[c] \\ -j\beta[N] & [0] & -j[b] \\ -[c] & [b] & [0] \end{bmatrix}
 \end{aligned} \tag{A3.37}$$

$[\mathbf{A}]_e$  is a 9x9 matrix where elements  $Ae_{11}$  and  $Ae_{99}$  are given by

$$\begin{aligned}
 Ae_{11} &= \iint [-j\beta N_1(j\beta p_{22}N_1 - p_{32}c_1) - c_1(j\beta p_{23}N_1 - p_{33}c_1)] dx dy \\
 &= \iint (\beta^2 p_{22}N_1^2 - j\beta p_{23}c_1N_1 + j\beta p_{32}c_1N_1 + p_{33}c_1^2) dx dy
 \end{aligned} \tag{A3.38}$$

and

$$\begin{aligned}
 Ae_{99} &= \iint [j c_3(-j p_{11}c_3 + j p_{21}b_3) - j b_3(-j p_{12}c_3 + j p_{22}b_3)] dx dy \\
 &= \iint (p_{11}c_3^2 - p_{12}b_3c_3 - p_{21}b_3c_3 + p_{22}b_3^2) dx dy
 \end{aligned} \tag{A3.39}$$

Using the integration formula for shape function coefficients (Koshiha, 1992)

$$\iint N_1^i N_2^j N_3^k = \frac{i!j!k!}{(i+j+k+2)!} \cdot 2A \tag{A3.40}$$

where A is the area of the triangular elements.

$Ae_{11}$  and  $Ae_{99}$  are then shown to be

$$Ae_{11} = \beta^2 p_{22} \frac{A}{6} - j\beta p_{23} c_1 \frac{A}{3} + j\beta p_{32} c_1 \frac{A}{3} + p_{33} c_1^2 A \tag{A3.41}$$

$$Ae_{99} = p_{11} c_3^2 A - p_{12} b_3 c_3 A - p_{21} b_3 c_3 A + p_{22} b_3^2 A \tag{A3.42}$$

Similarly

$$[\mathbf{B}]_e = \iint [\mathbf{N}]^* [\mathbf{N}]^T dx dy \tag{A3.43}$$

$$[\mathbf{N}]^* [\mathbf{N}]^T = \begin{bmatrix} \{N\} & \{0\} & \{0\} \\ \{0\} & \{N\} & \{0\} \\ \{0\} & \{0\} & -j\{N\} \end{bmatrix} \begin{bmatrix} \{N\}^T & \{0\}^T & \{0\}^T \\ \{0\}^T & \{N\}^T & \{0\}^T \\ \{0\}^T & \{0\}^T & j\{N\}^T \end{bmatrix} \tag{A3.44}$$

$$[\mathbf{B}]_e = \iint \begin{bmatrix} \{N\}\{N\}^T & \{0\}\{0\}^T & \{0\}\{0\}^T \\ \{0\}\{0\}^T & \{N\}\{N\}^T & \{0\}\{0\}^T \\ \{0\}\{0\}^T & \{0\}\{0\}^T & \{N\}\{N\}^T \end{bmatrix} dx dy \quad (\text{A3.45})$$

Using the integration formula in equation (A3.40)

$$[\mathbf{B}]_e = \begin{bmatrix} A/6 & A/12 & A/12 & 0 & 0 & 0 & 0 & 0 & 0 \\ A/12 & A/6 & A/12 & 0 & 0 & 0 & 0 & 0 & 0 \\ A/12 & A/12 & A/6 & 0 & 0 & 0 & 0 & 0 & 0 \\ 0 & 0 & 0 & A/6 & A/12 & A/12 & 0 & 0 & 0 \\ 0 & 0 & 0 & A/12 & A/6 & A/12 & 0 & 0 & 0 \\ 0 & 0 & 0 & A/12 & A/12 & A/6 & 0 & 0 & 0 \\ 0 & 0 & 0 & 0 & 0 & 0 & A/6 & A/12 & A/12 \\ 0 & 0 & 0 & 0 & 0 & 0 & A/12 & A/6 & A/12 \\ 0 & 0 & 0 & 0 & 0 & 0 & A/12 & A/12 & A/6 \end{bmatrix} \quad (\text{A3.46})$$

## Appendix A4: The calculation of $\hat{\epsilon}^{-1}$

---

The permittivity tensor matrix,  $\hat{\epsilon}$ , is represented as

$$\hat{\epsilon} = \begin{bmatrix} \epsilon_{11} & \epsilon_{12} & \epsilon_{13} \\ \epsilon_{21} & \epsilon_{22} & \epsilon_{23} \\ \epsilon_{31} & \epsilon_{32} & \epsilon_{33} \end{bmatrix} = [\mathbf{P}_{inv}]$$

The inverse of the matrix is obtained by first finding the transpose of the matrix, replacing each element by its cofactor and then dividing by the determinant of the original matrix, as shown below.

$$[\mathbf{P}_{inv}]^T = \begin{bmatrix} \epsilon_{11} & \epsilon_{21} & \epsilon_{31} \\ \epsilon_{12} & \epsilon_{22} & \epsilon_{32} \\ \epsilon_{13} & \epsilon_{23} & \epsilon_{33} \end{bmatrix}$$

$$[\mathbf{P}_{inv}]^{T'} = \begin{bmatrix} (\epsilon_{22}\epsilon_{33} - \epsilon_{32}\epsilon_{23}) & -(\epsilon_{12}\epsilon_{33} - \epsilon_{32}\epsilon_{13}) & (\epsilon_{12}\epsilon_{23} - \epsilon_{22}\epsilon_{13}) \\ -(\epsilon_{21}\epsilon_{33} - \epsilon_{31}\epsilon_{23}) & (\epsilon_{11}\epsilon_{33} - \epsilon_{31}\epsilon_{13}) & -(\epsilon_{11}\epsilon_{23} - \epsilon_{21}\epsilon_{13}) \\ (\epsilon_{21}\epsilon_{32} - \epsilon_{31}\epsilon_{22}) & -(\epsilon_{11}\epsilon_{32} - \epsilon_{31}\epsilon_{12}) & (\epsilon_{11}\epsilon_{22} - \epsilon_{21}\epsilon_{12}) \end{bmatrix}$$

where T' indicates the cofactor of the matrix

$$\det[\mathbf{P}_{inv}] = \epsilon_{11}(\epsilon_{22}\epsilon_{33} - \epsilon_{23}\epsilon_{32}) - \epsilon_{12}(\epsilon_{21}\epsilon_{33} - \epsilon_{23}\epsilon_{31}) + \epsilon_{13}(\epsilon_{21}\epsilon_{32} - \epsilon_{22}\epsilon_{31})$$

$$[\mathbf{P}_{inv}]^{-1} = [\mathbf{P}] = \begin{bmatrix} p_{11} & p_{12} & p_{13} \\ p_{21} & p_{22} & p_{23} \\ p_{31} & p_{32} & p_{33} \end{bmatrix}$$

$$= \frac{1}{\det[\mathbf{P}_{inv}]} \begin{bmatrix} (\epsilon_{22}\epsilon_{33} - \epsilon_{32}\epsilon_{23}) & -(\epsilon_{12}\epsilon_{33} - \epsilon_{32}\epsilon_{13}) & (\epsilon_{12}\epsilon_{23} - \epsilon_{22}\epsilon_{13}) \\ -(\epsilon_{21}\epsilon_{33} - \epsilon_{31}\epsilon_{23}) & (\epsilon_{11}\epsilon_{33} - \epsilon_{31}\epsilon_{13}) & -(\epsilon_{11}\epsilon_{23} - \epsilon_{21}\epsilon_{13}) \\ (\epsilon_{21}\epsilon_{32} - \epsilon_{31}\epsilon_{22}) & -(\epsilon_{11}\epsilon_{32} - \epsilon_{31}\epsilon_{12}) & (\epsilon_{11}\epsilon_{22} - \epsilon_{21}\epsilon_{12}) \end{bmatrix}$$

## *Appendix B: Calculation of the General Solution of the Problem of Optical Propagation in a Crystal in the Presence of an External Field along an Arbitrary Direction*

---

The equation of the index ellipsoid in the presence of an applied electric field is (Yariv, 1991)

$$\left(\frac{1}{n^2}\right)_1 X^2 + \left(\frac{1}{n^2}\right)_2 Y^2 + \left(\frac{1}{n^2}\right)_3 Z^2 + 2\left(\frac{1}{n^2}\right)_4 YZ + 2\left(\frac{1}{n^2}\right)_5 XZ + 2\left(\frac{1}{n^2}\right)_6 XY = 1 \quad (\text{B.1})$$

In the case of  $E=0$

$$\begin{aligned} \left(\frac{1}{n^2}\right)_1 &= \left(\frac{1}{n_x^2}\right) \\ \left(\frac{1}{n^2}\right)_2 &= \left(\frac{1}{n_y^2}\right) \\ \left(\frac{1}{n^2}\right)_3 &= \left(\frac{1}{n_z^2}\right) \\ \left(\frac{1}{n^2}\right)_4 &= \left(\frac{1}{n^2}\right)_5 = \left(\frac{1}{n^2}\right)_6 = 0 \end{aligned} \quad (\text{B.2})$$

The linear change in refractive index due to the applied electric field  $\mathbf{E}(E_x, E_y, E_z)$  is given by

$$\Delta\left(\frac{1}{n^2}\right)_i = \sum_{j=1}^3 r_{ij} E_j \quad \text{for } i=1,6 \quad (\text{B.3})$$

In general form equation (B.1) can be expressed in the quadratic form (Yariv, 1991)

$$S_{ij} x_i x_j = 1 \quad (\text{B.4})$$

where

$$\begin{aligned} S_{11} &= \left(\frac{1}{n^2}\right)_1 & S_{22} &= \left(\frac{1}{n^2}\right)_2 \\ S_{33} &= \left(\frac{1}{n^2}\right)_3 & S_{12} &= S_{21} = \left(\frac{1}{n^2}\right)_6 \\ S_{13} &= S_{31} = \left(\frac{1}{n^2}\right)_5 & S_{23} &= S_{32} = \left(\frac{1}{n^2}\right)_4 \end{aligned} \quad (\text{B.5})$$

(Here the convention of summation over repeated indices has been used)

The solution to the problem (expressed in equation (B.4) and ultimately equation (B.1)) consists of finding the direction and magnitude of the new principal axes for the ellipsoid given in equation (B.1).

Basic vector calculus can be used to determine the direction and magnitudes of the principal axes of the ellipsoid given in equation (B.1). This is that if a vector from the origin to point  $(x_1, x_2, x_3)$  on the ellipsoid (in form of equation (B.4)) is denoted by  $\mathbf{R}(x_1, x_2, x_3)$  then vector  $\mathbf{N}$  defined by

$$N_i = S_{ij}x_j \quad (\text{B.6})$$

is normal to the ellipsoid at  $\mathbf{R}$ .

Since the principal axes will be normal to the surface of the ellipsoid, their point of intersection with the ellipsoid  $(x_1, x_2, x_3)$  can be found by the above requirement that at such points the radius vector  $\mathbf{R}$  should be parallel to the normal

$$\text{i.e.} \quad S_{ij}x_j = Sx_i \quad (\text{B.7})$$

or

$$S_{ij}x_j - Sx_i = 0$$

where  $S$  is a constant independent of  $i$

This can be written as

$$\begin{aligned} (S_{11} - S)x_1 + S_{12}x_2 + S_{13}x_3 &= 0 \\ S_{21}x_1 + (S_{22} - S)x_2 + S_{23}x_3 &= 0 \\ S_{31}x_1 + S_{32}x_2 + (S_{33} - S)x_3 &= 0 \end{aligned} \quad (\text{B.8})$$

which is a system of 3 homogeneous equations for the unknowns  $x_1, x_2, x_3$

or

$$\begin{bmatrix} S_{11} - S & S_{12} & S_{13} \\ S_{21} & S_{22} - S & S_{23} \\ S_{31} & S_{32} & S_{33} - S \end{bmatrix} \begin{bmatrix} x_1 \\ x_2 \\ x_3 \end{bmatrix} = 0$$

The condition for a nontrivial solution for (B.8) is that the determinants of the coefficients vanish

$$\text{i.e.} \quad \det[S_{ij} - S\delta_{ij}] = 0 \quad (\text{B.9})$$

$S'$ ,  $S''$  and  $S'''$  are the roots of the determinant, or rather the eigenvalues of the equation (B.8) since (B.9) is an eigenvalue equation, and the corresponding radius vectors found using the above eigenvalues are

$$\begin{aligned} \mathbf{X}'(x_1', x_2', x_3') \\ \mathbf{X}''(x_1'', x_2'', x_3'') \\ \mathbf{X}'''(x_1''', x_2''', x_3''') \end{aligned} \quad (\text{B.10})$$

where eigenvectors  $\mathbf{X}'$ ,  $\mathbf{X}''$  and  $\mathbf{X}'''$  are mutually orthogonal.

Since the vectors satisfy (B.7), the following are also true

$$\begin{aligned} S_{ij}x_j' &= S'x_i' \\ S_{ij}x_j'' &= S''x_i'' \\ S_{ij}x_j''' &= S'''x_i''' \end{aligned} \quad (\text{B.11})$$

Thus the directions of the principal axes have been solved.

Now, the magnitudes are to be obtained.

If the first equation of (B.11) is multiplied by  $x_1'$  it becomes

$$S_{ij}x_j'x_i' = S'(x_i')^2 = S'|\mathbf{X}'|^2 \quad (\text{B.12})$$

but from equation (B.4)

$$S_{ij}x_i'x_j' = 1$$

since  $(x_1', x_2', x_3')$  is on the ellipsoid described by equation (B.4).

Therefore,

$$\begin{aligned} |\mathbf{X}'| &= \frac{1}{\sqrt{S'}} \\ |\mathbf{X}''| &= \frac{1}{\sqrt{S''}} \\ |\mathbf{X}'''| &= \frac{1}{\sqrt{S'''}} \end{aligned} \quad (\text{B.13})$$

So, the lengths of the principal axes of the ellipsoid are  $2/\sqrt{S'}$ ,  $2/\sqrt{S''}$  and  $2/\sqrt{S'''}$ .

If the index ellipsoid equation (B.4) is written in terms of a Cartesian co-ordinate system, the axes for which are parallel to  $\mathbf{X}'$ ,  $\mathbf{X}''$  and  $\mathbf{X}'''$  it becomes

$$S'x'^2 + S''y'^2 + S'''z'^2 = 1 \quad (\text{B.14})$$

where  $\mathbf{x}$ ,  $\mathbf{y}$  and  $\mathbf{z}$  are vectors parallel to  $\mathbf{X}'$ ,  $\mathbf{X}''$  and  $\mathbf{X}'''$ , respectively.

Since it is of interest in thesis only to find the new principal axes (transformed under the influence of the applied electric field) for the GaAs/ $\text{Al}_x\text{Ga}_{1-x}\text{As}$  modulator, the next section is dedicated only for this modulator (hence, equation labelling was only for the previous section).

Now equation (B.3) is of the form

$$\begin{bmatrix} \Delta(1/n^2)_1 \\ \Delta(1/n^2)_2 \\ \Delta(1/n^2)_3 \\ \Delta(1/n^2)_4 \\ \Delta(1/n^2)_5 \\ \Delta(1/n^2)_6 \end{bmatrix} = \begin{bmatrix} 0 & 0 & 0 \\ 0 & 0 & 0 \\ 0 & 0 & 0 \\ r_{41} & 0 & 0 \\ 0 & r_{41} & 0 \\ 0 & 0 & r_{41} \end{bmatrix} \begin{bmatrix} E_x \\ E_y \\ E_z \end{bmatrix}$$

So,

$$\Delta(1/n^2)_1 = \Delta(1/n^2)_2 = \Delta(1/n^2)_3 = 0$$

$$\Delta(1/n^2)_4 = r_{41}E_x$$

$$\Delta(1/n^2)_5 = r_{41}E_y$$

$$\Delta(1/n^2)_6 = r_{41}E_z$$

where  $r_{41} = 1.4 \times 10^{-12} \text{ m/V}$  (at the wavelength of operation –  $1.55 \mu\text{m}$ ).

Hence the ellipsoid equation (B.1) becomes

$$\frac{1}{n_x^2} X^2 + \frac{1}{n_y^2} Y^2 + \frac{1}{n_z^2} Z^2 + 2r_{41}E_xYZ + 2r_{41}E_yXZ + 2r_{41}E_zXY = 1$$

but GaAs (likewise  $\text{Al}_x\text{Ga}_{1-x}\text{As}$ ) is isotropic for  $\mathbf{E}=0$  (i.e. no applied electric field), therefore,

$$\frac{1}{n_x^2} = \frac{1}{n_y^2} = \frac{1}{n_z^2} = \frac{1}{n^2}$$

and so the ellipsoid equation can be written as

$$\frac{1}{n^2}(X^2 + Y^2 + Z^2) + 2r_{41}(E_X YZ + E_Y XZ + E_Z XY) = 1$$

So the  $S_{ij}$  matrix is

$$S_{ij} = \begin{bmatrix} 1/n^2 & r_{41}E_Z & r_{41}E_Y \\ r_{41}E_Z & 1/n^2 & r_{41}E_X \\ r_{41}E_Y & r_{41}E_X & 1/n^2 \end{bmatrix}$$

The eigenvectors are obtained from

$$\det[S_{ij} - S\delta_{ij}] = 0 \quad (\text{B.9})$$

with  $\delta_{ij}=1$  only for  $i=j$

$$\text{i.e.} \quad \begin{vmatrix} 1/n^2 - S & r_{41}E_Z & r_{41}E_Y \\ r_{41}E_Z & 1/n^2 - S & r_{41}E_X \\ r_{41}E_Y & r_{41}E_X & 1/n^2 - S \end{vmatrix} = 0$$

which becomes

$$(1/n^2 - S) \begin{vmatrix} 1/n^2 - S & r_{41}E_X \\ r_{41}E_X & 1/n^2 - S \end{vmatrix} - r_{41}E_Z \begin{vmatrix} r_{41}E_Z & r_{41}E_X \\ r_{41}E_Y & 1/n^2 - S \end{vmatrix} + r_{41}E_Y \begin{vmatrix} r_{41}E_Z & 1/n^2 - S \\ r_{41}E_Y & r_{41}E_X \end{vmatrix} = 0$$

and again this simplifies to

$$(1/n^2 - S) \left[ (1/n^2 - S)^2 - r_{41}^2 E_X^2 - r_{41}^2 E_Z^2 - r_{41}^2 E_Y^2 \right] + 2r_{41}^3 E_X E_Y E_Z = 0$$

or

$$(1/n^2 - S) \left[ (1/n^2 - S)^2 - r_{41}^2 |\mathbf{E}|^2 \right] + 2r_{41}^3 E_X E_Y E_Z = 0$$

where  $|\mathbf{E}|^2 = E_X^2 + E_Y^2 + E_Z^2$

However, as mentioned in Chapter 6, only the  $y$  (Cartesian co-ordinates) component of the electric field  $\mathbf{E}(x,y) - Z$  component in terms of the crystal axes used in this appendix section – gives an overall change in refractive index and therefore, this is only of interest.

Hence  $\mathbf{E} = E_Z$ .

So the above discrimination equation now simplifies to

$$(1/n^2 - S) \left[ (1/n^2 - S)^2 - r_{41}^2 E_Z^2 \right] = 0$$

Therefore,

$$S' = 1/n^2$$

$$S'' = 1/n^2 - r_{41}E_Z$$

$$S''' = 1/n^2 + r_{41}E_Z$$

As mentioned above the magnitudes of the principal axes are  $2/\sqrt{S'}$ ,  $2/\sqrt{S''}$  and  $2/\sqrt{S'''}$ . So in this case, the magnitudes of the principal axes are  $2n$ ,  $2/\sqrt{1/n^2 - r_{41}E_Z}$  and  $2/\sqrt{1/n^2 + r_{41}E_Z}$ .

Next, it is necessary to find the directions of these principal axes, or the eigenvectors  $\mathbf{X}'$ ,  $\mathbf{X}''$  and  $\mathbf{X}'''$ .

$\mathbf{X}'$ :

From equation (B.11)

$$S_{ij}x'_j = S'x'_i$$

or

$$\begin{bmatrix} 1/n^2 - S' & r_{41}E_Z & r_{41}E_Y \\ r_{41}E_Z & 1/n^2 - S' & r_{41}E_X \\ r_{41}E_Y & r_{41}E_X & 1/n^2 - S' \end{bmatrix} \begin{bmatrix} x'_1 \\ x'_2 \\ x'_3 \end{bmatrix} = 0$$

but  $S' = 1/n^2$  and  $E_X = E_Y = 0$

$$\begin{bmatrix} 0 & r_{41}E_Z & 0 \\ r_{41}E_Z & 0 & 0 \\ 0 & 0 & 0 \end{bmatrix} \begin{bmatrix} x'_1 \\ x'_2 \\ x'_3 \end{bmatrix} = 0$$

From this system of equation it can be seen that

$$r_{41}E_Z x'_2 = 0$$

$$r_{41}E_Z x'_1 = 0$$

since  $E_Z$  is nonzero it means

$$x'_1 = x'_2 = 0$$

$x'_3$  can have any value for the above set if equation to hold true.

This implies that  $\mathbf{X}'$  is parallel to the Z (crystal) axis.

$\mathbf{X}''$ :

Again,

$$S_{ij}x_j'' = S''x_i''$$

or

$$\begin{bmatrix} 1/n^2 - S'' & r_{41}E_Z & r_{41}E_Y \\ r_{41}E_Z & 1/n^2 - S'' & r_{41}E_X \\ r_{41}E_Y & r_{41}E_X & 1/n^2 - S'' \end{bmatrix} \begin{bmatrix} x_1'' \\ x_2'' \\ x_3'' \end{bmatrix} = 0$$

but  $S'' = 1/n^2 - r_{41}E_Z$  and  $E_X = E_Y = 0$

$$\begin{bmatrix} r_{41}E_Z & r_{41}E_Z & 0 \\ r_{41}E_Z & r_{41}E_Z & 0 \\ 0 & 0 & r_{41}E_Z \end{bmatrix} \begin{bmatrix} x_1'' \\ x_2'' \\ x_3'' \end{bmatrix} = 0$$

From this set of equations it can be seen that

$$x_2'' = -x_1''$$

and since  $E_Z$  is nonzero

$$x_3'' = 0$$

This implies that  $\mathbf{X}''$  is parallel to  $X\cos 45^\circ - Y\sin 45^\circ$  (in terms of crystal axes) or  $[1\bar{1}0]$  using Miller indices (see Appendix C).

$\mathbf{X}'''$ :

Again,

$$S_{ij}x_j''' = S'''x_i'''$$

or

$$\begin{bmatrix} 1/n^2 - S''' & r_{41}E_Z & r_{41}E_Y \\ r_{41}E_Z & 1/n^2 - S''' & r_{41}E_X \\ r_{41}E_Y & r_{41}E_X & 1/n^2 - S''' \end{bmatrix} \begin{bmatrix} x_1''' \\ x_2''' \\ x_3''' \end{bmatrix} = 0$$

but  $S''' = 1/n^2 + r_{41}E_Z$  and  $E_X = E_Y = 0$

$$\begin{bmatrix} -r_{41}E_Z & r_{41}E_Z & 0 \\ r_{41}E_Z & -r_{41}E_Z & 0 \\ 0 & 0 & -r_{41}E_Z \end{bmatrix} \begin{bmatrix} x_1''' \\ x_2''' \\ x_3''' \end{bmatrix} = 0$$

From this set of equations it can be seen that

$$x_2''' = x_1'''$$

and since  $E_Z$  is nonzero

$$x_3''' = 0$$

This implies that  $\mathbf{X}'''$  is parallel to  $X\cos 45^\circ + Y\sin 45^\circ$  (in terms of crystal axes) or  $[110]$  using Miller indices.

The index ellipsoid can now be written in terms of a Cartesian co-ordinate system, the axes for which are parallel to  $\mathbf{X}'$ ,  $\mathbf{X}''$  and  $\mathbf{X}'''$  it becomes

$$S''x^2 + S'y^2 + S'''z^2 = 1$$

where  $\mathbf{x}$ ,  $\mathbf{y}$  and  $\mathbf{z}$  are vectors parallel to  $\mathbf{X}''$ ,  $\mathbf{X}'$  and  $\mathbf{X}'''$ , respectively, or rather

$$\left(\frac{1}{n^2} - rE_y\right)x^2 + \frac{y^2}{n^2} + \left(\frac{1}{n^2} + rE_y\right)z^2 = 1$$

where  $r = r_{41}$

However, this equation can be written as

$$\frac{x^2}{n_x^2} + \frac{y^2}{n_y^2} + \frac{z^2}{n_z^2} = 1$$

where

$$\frac{1}{n_x^2} = \frac{1}{n^2} - rE_y$$

$$\frac{1}{n_y^2} = \frac{1}{n^2}$$

$$\frac{1}{n_z^2} = \frac{1}{n^2} + rE_y$$

Using the relationship

$$d\left(\frac{1}{n_{x,y,z}^2}\right) = -2n_{x,y,z}^{-3} dn_{x,y,z} \approx -2n^{-3} dn_{x,y,z}$$

as  $1/n^2 \gg rE_y$ .

This can be rewritten as

$$dn_{x,y,z} = -\frac{n_{x,y,z}^3}{2} d\left(\frac{1}{n_{x,y,z}^2}\right)$$

and it can be seen that

$$dn_x = \frac{n^3}{2} rE_y$$

$$dn_y = 0$$

$$dn_z = -\frac{n^3}{2} rE_y$$

since  $d\left(\frac{1}{n_x^2}\right) = -rE_y$  ,  $d\left(\frac{1}{n_y^2}\right) = 0$  ,  $d\left(\frac{1}{n_z^2}\right) = rE_y$ .

Therefore,

$$n_x = n + \frac{n^3}{2} rE_y$$

$$n_y = n$$

$$n_z = n - \frac{n^3}{2} rE_y$$

## Appendix C: Miller Indices

This section is just a reminder of the terminology used to describe crystal planes and directions. A convenient way to do this is by using Miller indices. A number of important planes in a cubic crystal are shown in Fig. C.1; however, Miller indices are used to describe the planes of any type of lattice.

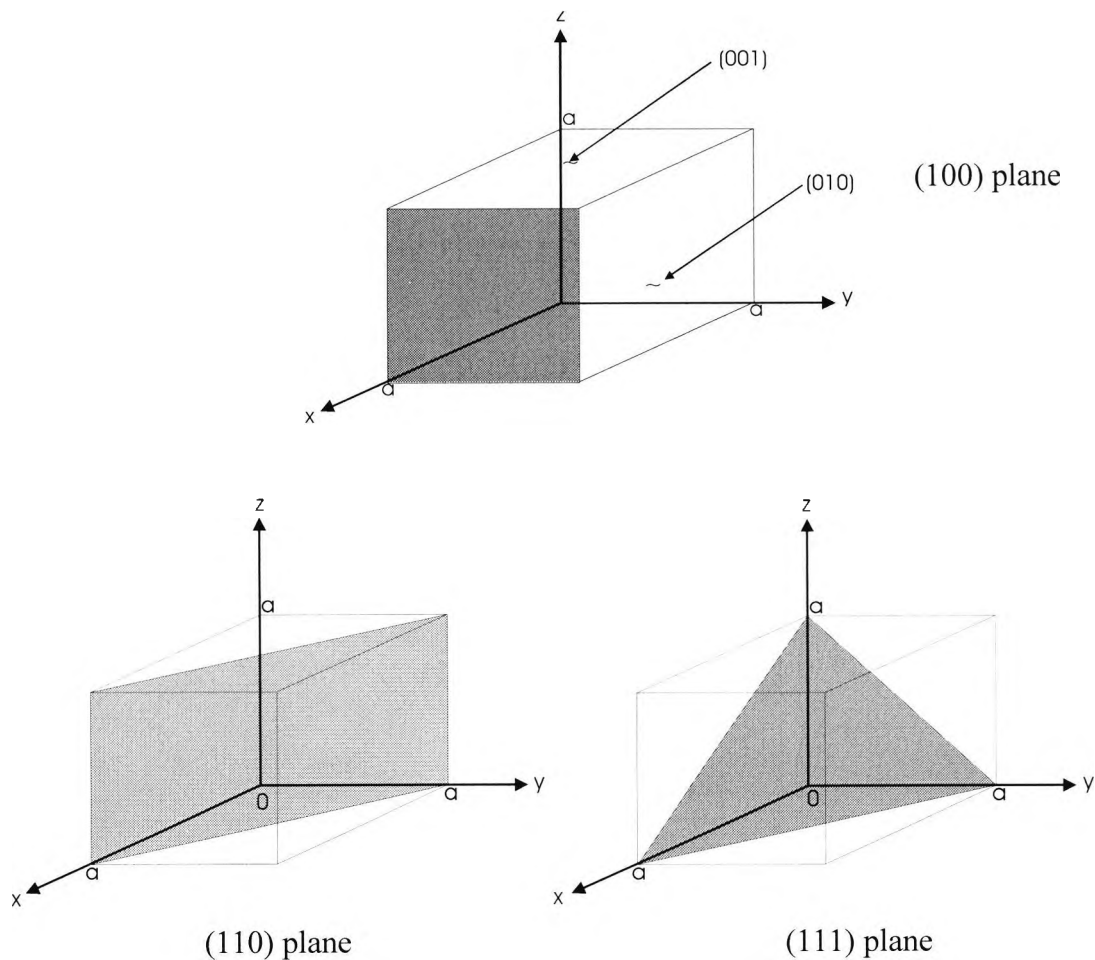


Fig. C.1 The Miller indices of the simpler, more important planes of a cubic crystal.

GaAs and  $\text{Al}_x\text{Ga}_{1-x}\text{As}$ , both  $\bar{4}3m$  (zinc-blende) cubic crystal structures, and  $\text{LiNbO}_3$ , a  $3m$  trigonal crystal structure, are used in this thesis in the form of  $\langle 100 \rangle$ -cut,  $\langle 110 \rangle$ -propagating GaAs/ $\text{Al}_x\text{Ga}_{1-x}\text{As}$  material and  $\langle 100 \rangle$ -cut  $\text{LiNbO}_3$  material, respectively.

However, a general form should be given here to have a greater understanding of the rules outlining the format for the Miller indices.

In general, these planes are thought to be of the form  $(hkl)$  where  $h$ ,  $k$  and  $l$  are integers related to the general reciprocal lattice vector, which is defined by (Sze, 1981)

$$\mathbf{G} = h\mathbf{a}^* + k\mathbf{b}^* + l\mathbf{c}^* \quad (\text{C.1})$$

where  $\mathbf{a}^*$ ,  $\mathbf{b}^*$  and  $\mathbf{c}^*$  are the reciprocal lattice basis vectors.

Further conventions include:

$(h\bar{k}l)$  for a plane that intercepts the  $y$  axis on the negative side of the origin

$\{hkl\}$  for a full set of planes of equivalent symmetry, e.g.  $\{100\}$  for  $(100)$ ,  $(010)$ ,  $(001)$ ,

$(\bar{1}00)$ ,  $(0\bar{1}0)$  and  $(00\bar{1})$  in cubic symmetry

$[hkl]$  for the directions of a crystal, e.g.  $[100]$  for the  $x$ -axis

$\langle hkl \rangle$  for a full set of directions.

In order to obtain the Miller indices, it is necessary to:

1. Determine the intercepts of the face along the crystallographic axes, in terms of unit cell dimensions ( $a$  in Fig. C.1). If a plane is parallel to an axis, its intercept is at infinity and its Miller index is zero.
2. Take the reciprocals of the points of intercept
3. Multiply by the lowest common denominator of the fractions in order to clear them
4. Again make sure the indices are given in the lowest possible terms

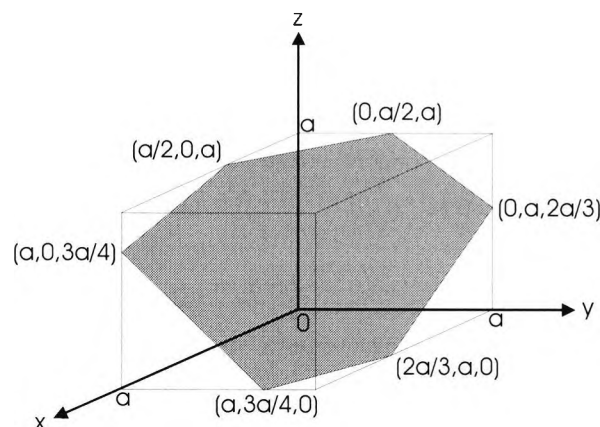


Fig. C.2 A  $(346)$  plane in a cubic crystal.

In Fig. C2, the  $x$ -intercept of this crystallographic plane (used by way of example) is 4 (in terms of the unit cell dimensions,  $a$ ), the  $y$ -intercept is 3 and the  $z$ -intercept is 2.

Taking the reciprocals gives  $1/4$ ,  $1/3$ ,  $1/2$ .

Multiply these fractions by the lowest common denominator (i.e. by 12) to give 3, 4, 6.

Check that the lowest terms possible are used.

Thus, the Miller indices are 3,4,6.

## *Appendix D: List of Publications by the Author Relevant to the Thesis*

---

---

1. **Anwar N, Wongcharoen T, Katsriku FA, Rahman BMA, Grattan KTV.** (1996). An accurate model for a LiNbO<sub>3</sub> electro-optic modulator. In: High Performance Electron Devices for Microwave and Optoelectronic Applications Workshop – EDMO: Leeds, UK; Nov 25-26, 1996. Proceedings (Cat. No.96TH8155): ISBN 0780331303. New York, NY, USA: IEEE, pp.56-61.
2. **Anwar N, Rahman BMA, Grattan KTV.** (1998). The effect of diffusion parameters on a Ti:LiNbO<sub>3</sub> electro-optic directional coupler modulator. In: APPLIED OPTICS AND OPTOELECTRONICS (Applied Optics Divisional Conference of the Institute of Physics); Brighton, UK; Mar 16-19, 1998. Proceedings: ISBN 0750304561. Bristol, UK: IOP Publishing Ltd., pp. 199-204.
3. **Anwar N, Themistos C, Rahman BMA, Grattan KTV.** (1999). Design considerations for an electrooptic directional coupler modulator. IEEE/OSA Journal of Lightwave Technology 17(4): 598-605.
4. **Rahman BMA, Anwar N, Meyer M, Rajarajan M, Themistos C, Wongcharoen T, Grattan KTV.** (1999). Finite element modelling of photonic devices. In: Photonics, Devices And Systems (3rd Photonic Prague Conference on Photonics, Devices, and Systems); Prague, Czech Republic; Jun 21-23, 1999. Proceedings of the Society of Photo-optical Instrumentation Engineers (SPIE), vol. 4016; Hrabovsky M, Tomanek P, Miler M (Eds); ISBN 0819436410. Bellingham, WA 98227-0010 USA: SPIE Press, pp. 198-203.
5. **Anwar N, Rahman BMA, Grattan KTV.** (1999). The effect of electrode design on an integrated-optic Mach-Zehnder interferometer-based high-voltage sensor. In: Sensors and their Applications X (The Tenth Conference on Sensors and their Applications); Cardiff, UK; Sep 5-8, 1999. Proceedings, White NM and Augousti AT (Eds); ISBN 0750306629. Bristol, UK: IOP Publishing Ltd., pp.207-12.
6. **Anwar N, Rahman BMA, Grattan KTV.** (2001). Design of compact LiNbO<sub>3</sub> electrooptic modulators. In: ACTIVE AND PASSIVE OPTICAL COMPONENTS FOR WDM COMMUNICATION; Denver, CO, USA; Aug 21-24, 2001. Proceedings of the Society of Photo-optical Instrumentation Engineers (SPIE), vol. 4532; Dutta AK, Awwal AAS, Dutta NK, Okamoto K (Eds); ISBN 0819442569. Bellingham, WA 98227-0010 USA: SPIE Press, pp. 4-15.
7. **Anwar N, Obayya SSA, Rahman BMA, Grattan KTV.** (2001). Compact Ti:LiNbO<sub>3</sub> Mach-Zehnder Interferometric Modulator using Etched Waveguides. In: Sensors and their Applications XI (The Eleventh Conference on Sensors and their Applications); London, UK; Sep 3-6, 2001. Proceedings, Grattan KTV and Khan SH (Eds); ISBN 0750308214. Bristol, UK: IOP Publishing Ltd., pp.?-?.

8. **Anwar N, Rahman BMA, Grattan KTV.** (2001). Numerical modeling and design of a compact Ti:LiNbO<sub>3</sub> Mach-Zehnder interferometric modulator using etched waveguides. In: *ADVANCED PHOTONIC SENSORS AND APPLICATIONS II*; Singapore; Nov 27-30, 2001. Proceedings of the Society of Photo-optical Instrumentation Engineers (SPIE), vol. 4596; Asundi AK, Osten W, Varadan VK (Eds); ISBN 0819443263. Bellingham, WA 98227-0010 USA: SPIE Press, pp. 334-342.
  
9. **Anwar N, Obayya SSA, Haxha S, Themistos C, Rahman BMA, Grattan KTV.** (2002). The effect of fabrication parameters on a ridge Mach-Zehnder interferometric (MZI) modulator. IEEE/OSA Journal of Lightwave Technology 20(5): 826-833.

## References

---

---

- ACKERMAN, E.I. (1999). Broad-band linearization of a Mach-Zehnder electrooptic modulator. IEEE Transactions on Microwave Theory and Techniques 47(12): 2271-2279.
- ADACHI, S. (1988). Optical properties of  $\text{Al}_x\text{Ga}_{1-x}\text{As}$  alloys. Physical Review B 38: 12345-12352.
- AHMED, S. and DALY, P. (1969). Finite-element methods for inhomogeneous waveguides. IEE Proceedings 116(10): 1661-1664.
- AITCHISON, J.S., VILLENEUVE, A. and STEGEMAN, G.I. (1995). All-optical switching in two cascaded nonlinear directional couplers. Optics Letters 20(7): 698-700.
- ALFERNESS, R.C. and SCHMIDT, R.V. (1978). Tunable optical waveguide directional coupler filter. Applied Physics Letters 33(2): 161-163.
- ALFERNESS, R.C. (1979a). Efficient waveguide electrooptic  $\text{TE} \leftrightarrow \text{TM}$  mode converter/ wavelength filter. Applied Physics Letters 36(7): 513-515.
- ALFERNESS, R.C. (1979b). Polarization-independent optical directional coupler switch using weighted coupling. Applied Physics Letters 35(10): 748-750.
- ALFERNESS, R.C., SCHMIDT, R.V. and TURNER, E.H. (1979). Characteristics of Ti-diffused lithium niobate optical directional couplers. Applied Optics 18(23): 4012-4016.
- ALFERNESS, R.C. (1981). Guided-wave devices for optical communication. IEEE Journal of Quantum Electronics 17(6): 946-959.
- ALFERNESS, R.C. (1982). Waveguide electrooptic modulators. Invited paper. IEEE Transactions on Microwave Theory and Techniques 30(8): 1121-1137.
- ALFERNESS, R.C. (1988) Titanium-diffused lithium niobate waveguide devices. In: Guided wave optoelectronics, ed. by T. Tamir. (Berlin: Springer-Verlag).
- ALFERNESS, R.C., KOGELNIK, H. and WOOD, T.H. (2000). The evolution of optical systems: Optics everywhere. Bell Labs Technical Journal 5(1): 188-202.
- ALPING, A., WU, X.S., HAUSKEN, T.R. and COLDREN, L.A. (1986). Highly efficient wave-guide phase modulator for integrated optoelectronics. Applied Physics Letters 48(19): 1243-1245.
- AN, D., SHI, Z., SUN, L., TABOADA, J.M., ZHOU, Q., LU, X., CHEN, R.T., TANG, S., ZHANG, H., STEIER, W.H., REN, A. and DALTON, L.R. (2000). Polymeric electro-optic modulator based on 1x2 Y-fed directional coupler. Applied Physics Letters 76(15): 1972-1974.

ANGKAEW, T., MATSUHARA, M. and KUMAGAI, N. (1987). Finite-element analysis of waveguide modes: A novel approach that eliminates spurious modes. IEEE Transactions on Microwave Theory and Techniques 35(2): 117-123.

ARGYRIS, J.H. (1954). Energy theorems and structural analysis, Part 1. Aircraft Engineering 26: 383.

ARIZMENDI, L. (2004). Photonic applications of lithium niobate crystals. Physica Status Solidi 201(2): 253-383.

ASHKIN, A. and GERSHENZON, M. (1963). Reflection and guiding of light at p-n junction. Journal of Applied Physics 34: 2116-2119.

ASHLEY, P.R., CHANG W.S.C., BUCHAL, C.J. and THOMAS, D.K. (1989). Guided wave modulators in Ti ion planted LiNbO<sub>3</sub> waveguides. Journal of Lightwave Technology 7(5): 855-862.

ASPNES, D.E. (1966). Electric-field effects on optical absorption near threshold in solids. Physical Review 147(2): 554-566.

AURACHER, F. and KEIL, R. (1980). Method for measuring the RF modulation characteristics of Mach-Zehnder-type modulators. Applied Physics Letters 36(8): 626-629.

AURACHER, F., SCHICKETANZ, D. and ZEITLER, K.-H. (1984). High-speed  $\Delta\beta$ -reversal directional coupler modulator with low insertion loss for 1.3 $\mu\text{m}$  in LiNbO<sub>3</sub>. Journal of Optical Communications 5(1): 7-9.

AUSTIN, M.W. (1984). Theoretical and experimental investigation of GaAs/AlGaAs and n/n+ GaAs rib waveguides. Journal of Lightwave Technology 2(5): 688-694.

BALLMAN, A.A. (1965). The growth of piezoelectric and ferroelectric materials by the Czochralski technique. Journal of the American Ceramic Society 48: 112-113.

BANDYOPADHYAY, A and DEEN, M.J. (2001). Photodetectors for optical fiber communications. In: Photodetectors and fiber optics, ed. by H. S. Nalwa. (Academic Press).

BARRY, I.E., ROSS, G.W., SMITH, P.G.R. and EASON, R.W. (1999). Ridge waveguides in lithium niobate fabricated by differential etching following spatially selective domain inversion. Applied Physics Letters 74(10): 1487-1488.

BATHE, K.J. and WILSON, E.L. (1976). Numerical methods in finite element analysis. (Englewood Cliffs, NJ: Prentice Hall).

BAUMANN, I., BRINKMANN, R., DINAND, M., SOHLER, W. and WESTWENHÖFER, S. (1996). Ti:Er:LiNbO<sub>3</sub> waveguide laser of optimised efficiency. IEEE Journal of Quantum Electronics 32(9): 1695-1706.

- BECHTEL, J.H., MENDERS, J. and ZANG, D.Y. (2003). Electro-optic polymer integrated optic devices and future applications. Fiber and Integrated Optics 22(4): 211-224.
- BECKER, R.A. (1983). Comparison of guided-wave interferometric modulator fabricated on LiNbO<sub>3</sub> via Ti: indiffusion and proton exchange. Applied Physics Letters 43(2): 131-133.
- BEK, A., AYDINLI, A., CHAMPLAIN, J.G. and NAONE, R. (1999). A study of wet oxidized Al(x)Ga(1-x)As for integrated optics. IEEE Photonics Technology Letters 11(4): 436-438.
- BENSON, T.M., BOZEAT, R.J. and KENDALL, P.C. (1994). Complex finite difference method applied to the analysis of semiconductor lasers. IEE Proceedings—Optoelectronics 141(2): 97-101.
- BERK, A.D. (1956). Variational principles for electromagnetic resonators and waveguides. IRE Transactions on Antennas Propagation AP-4: 104-111.
- BERTOLLOTTI, M., MASCIULLI, P. and SIBILIA, C. (1994). Mol numerical analysis of nonlinear planar waveguide. Journal of Lightwave Technology 12(5): 784-789.
- BETTS, G.E., O'DONNELL, F.J. and RAY, K.G. (1994). Effect of annealing photorefractive damage in titanium indiffused LiNbO<sub>3</sub> modulators. IEEE Photonics Technology Letters 6(2): 211-213.
- BETTS, G.E. (1995). Optical link for cellular-telephone microcells. In: Conference on Optical Fiber Communication, 1995. Technical Digest Series vol. 8., pp. 243-244.
- BINDAL, P. and SHARMA, A. (1992). Modeling of Ti:LiNbO<sub>3</sub> waveguide directional couplers. IEEE Photonics Technology Letters 4(7): 728-731.
- BLAKEMORE, J.S. (1982). Semiconducting and other major properties of gallium-arsenide. Journal Of Applied Physics 53(10): R123-R181
- BLOEMBERGEN, N, PERSHAN, P.S. and WILCOX, L.R. (1960). Microwave modulation of light in paramagnetic crystals. Physical Review 120: 2014-2023.
- BLUMENTHAL, R.M. (1962). Design of a microwave-frequency light modulator. IEEE Proceedings 50: 452-456.
- BRINKMAN, W.F., KOCH, T.L., LANG, D.V. and WILT, D.P. (2000). The lasers behind the communications revolution. Bell Labs Technical Journal 5(1): 150-167.
- BUAH, P.A., RAHMAN, B.M.A., GRATTAN, K.T.V. (1994). Study of transverse effects in optical bistable ring resonators using the finite-element method. Journal Of Modern Optics 41(6): 1135-1139.
- BULMER, C.H., SHEEM, S.K., MOELLER, R.P. and BURNS, W.K. (1980). High efficiency flip-chip coupling between single-mode fibers and LiNbO<sub>3</sub> channel waveguides. Applied Physics Letters 37(4): 351-353.

BULMER, C.H. and BURNS, W.K. (1984). Linear Interferometric Modulators in Ti:LiNbO<sub>3</sub>. Journal of Lightwave Technology 2(4): 512-521.

BULTHUIS, H.F. (1998). Generation of titanium indiffused LiNbO<sub>3</sub> index profiles. Alcatel Optronics Application Notes: A1998006, Netherlands, 12 June 1998.

BURKE, S.V. (1990a). Spectral index method applied to rib and strip-loaded directional couplers. IEE Proceedings—Optoelectronics 137(1): 7-10.

BURKE S.V. (1990b) Spectral index method applied to 2 nonidentical closely separated rib wave-guides. IEE Proceedings—Optoelectronics 137(5): 289-292.

BURNS, W.K., LEE, A.B. and MILTON, A.F. (1976). Active branching waveguide modulator. Applied Physics Letters 29(12): 790-792.

BURNS, W.K. and MILTON, A.F. (1988). Waveguide transitions and junctions. In: *Guided wave optoelectronics*, ed. by T. Tamir. (Berlin: Springer-Verlag).

BURNS, W.K. (1992). Shaping the digital switch. IEEE Photonics Technology Letters 4(8): 861-863.

BURNS, W.K., HOWERTON, M.M., MOELLER, R.P., KRÄHENBÜHL, R., McELHANON, R.W. and GREENBLATT, A.S. (1999). Low drive voltage, broad-band LiNbO<sub>3</sub> modulators with and without etched ridges. Journal of Lightwave Technology 17(12): 2551-2555.

BYUN, Y.T., PARK, K.H., KIM, S.H., CHOI, S.S. and LIM, T.K. (1996). Single-mode GaAs/AlGaAs W waveguides with a low propagation loss. Applied Optics 35(6): 928-933.

CAMPBELL, J.C., BLUM, F.A., SHAW, D.W. and LAWLEY, K.C. (1975). GaAs electro-optic directional-coupler switch. Applied Physics Letters 27(4): 202-205.

CAO, X.F., RAMASWAMY, R.V. and SRIVASTAVA. (1992). Characterization of annealed proton exchanged LiNbO<sub>3</sub> waveguides for nonlinear frequency conversion. Journal of Lightwave Technology 10(9): 1302-1313.

CASEY, H.C. and PANISH, M.B. (1978). *Heterostructure lasers, Part A: Fundamental principles*. (New York: Academic Press).

CHANG, C.Y. and KAI, F. (1994). *GaAs high-speed devices : physics, technology, and circuit applications*. (New York ; Chichester : Wiley).

CHANG, W.-C. (2000). Measurement of coupling characteristics of an Ni:LiNbO<sub>3</sub> directional coupler with a combinational-type waveguide structure. Microwave and Optical Technology Letters 24(1): 60-63.

CHANG, S.-J., TSAI, C.-L., LIN, Y.-B., LIU, J.-F. and WANG, W.-S. (1999). Improved electrooptic modulator with ridge structure in X-cut LiNbO<sub>3</sub>. Journal of Lightwave Technology 17(5): 843-847.

- CHANNIN, D.J. (1971). Voltage-induced optical waveguide. Applied Physics Letters 2(?): 128-130.
- CHARCZENKO, W., JANUAR, I. and MICKELSON, A.R. (1993). Modeling of proton-exchanged and annealed channel waveguides and directional couplers. Journal of Applied Physics 73(7): 3139-3148.
- CHEN, B. and MEIJER, C.M. (1978). Bragg switch for optical channel waveguides. Applied Physics Letters 33(1): 33-35.
- CHEN, C.H. and LIEN, C. (1980). The variational principle for non-self-adjoint electromagnetic problems. IEEE Transactions on Microwave Theory and Techniques 28(8): 878-886.
- CHEN, F.-S. (1969). Optically induced change of refractive indices in LiNbO<sub>3</sub> and LiTaO<sub>3</sub>. Journal of Applied Physics 40(8): 3389-3396.
- CHEN, F.-S. (1970). Modulators for optical communications. Proceedings of the IEEE 58(10): 1440-1457.
- CHEN, H., FEENSTRA, R.M., GOLDMAN, R.S., SILFVENIUS, C. and LANDGREN, G. (1998). Strain variations in InGaAsP/InGaP superlattices studied by scanning probe microscopy. Applied Physics Letters 72(14): 1727-1729.
- CHEW, W.C. and NASIR, M.A. (1989). A variational analysis of anisotropic, inhomogeneous dielectric waveguides. IEEE Transactions on Microwave Theory and Techniques 37(4): 661-668.
- CHIANG, K.S. (1985). Finite element analysis of optical fibres with iterative treatment of the infinite 2-D space. Optical and Quantum Electronics 17(6): 381-391.
- CHIANG, K.S. (1986a). Analysis of optical fibers by the effective-index method. Applied Optics 25(3): 348-354.
- CHIANG, K.S. (1986b). Analysis of fused couplers by the effective-index method. Electronics Letters 22(23): 1221-1222.
- CHIANG, K.S. (1989). Stress-induced birefringence fibers designed for single-polarization single-mode operation. Journal of Lightwave Technology 7(2): 436-441.
- CHIANG, K.S. (1992). Analysis of rectangular dielectric wave-guides - effective-index method with built-in perturbation. Electronics Letters 28(4): 388-390.
- CHIANG, K.S. (1994). Review of numerical and approximate methods for the modal analysis of general optical dielectric waveguides. Invited paper. Optical and Quantum Electronics 26: S113-S134.
- CHIN, M.K. (1993). Design considerations for vertical  $\Delta k$  directional coupler. Journal of Lightwave Technology 11(8): 1331-1336.

CHMIELOWSKI, M. and LANGER D.W. (1989). Multiple-quantum-well vertical light guide switch. Journal of Applied Physics 65(3): 927-934.

CHO, S.-C., KIM, B.-G. and SHAKOURI, A. (2001). Ultra short two-section vertical directional coupler switches with high extinction ratios. Japanese Journal Of Applied Physics Part 1-Regular Papers Short Notes & Review Papers 40(6A): 4045-4050.

CHOY, W.C.H., WEISS, B.L. and LI, E.H. (1997). The effect of interdiffusion on the realization of polarization insensitive quantum well. In: PROGRESS IN ELECTROMAGNETICS RESEARCH SYMPOSIUM, 1997. Proceedings: p. 718.

CHUANG, S.-L. (1987). Application of the strongly coupled-mode theory to integrated optical devices. IEEE Journal of Quantum Electronics 23(5): 499-509.

CLOUGH, R.W. (1960). The finite element method in plane stress analysis. In: ACSE Conference on Electronic Computation, 2<sup>nd</sup>, Pittsburgh, PA 1960. Proceedings.

COURANT, R. (1943). Variational methods for the solution of problems of equilibrium and vibrations. Bulletin of the American Mathematical Society 49: 1-23.

CRANK, J. (1975). The mathematics of diffusion. 2<sup>nd</sup> Ed. (Oxford: Clarendon Press).

CWIK, T., JAMNEJAD, V., ZUFFADA, C. and CHAN, C. (1997). Application of the element residual method for adaptive refinement in finite element design. In: PROGRESS IN ELECTROMAGNETICS RESEARCH SYMPOSIUM, 1997. Proceedings: p. 41.

DAGLI, N.(1999). Wide-bandwidth lasers and modulators for RF photonics. Invited paper. IEEE Transactions on Microwave Theory and Techniques 47(7):1151-1171.

DALTON, L.R. (2003). Rational design of organic electro-optic materials. Journal of Physics-Condensed Matter 15(20): R897-R934.

DAS, B.K., RICKEN, R. and SOHLER, W. (2003). Integrated optical distributed feedback laser with Ti:Fe:Er:LiNbO<sub>3</sub> waveguide. Applied Physics Letters 82(10): 1515-1517.

DAVIES, A.J. (1980). The finite element method: A first approach. Oxford Applied Mathematics and Computing Science Series. (Oxford: Clarendon Press).

DAVIES, J.B. (1972). Review methods for the numerical solution of the hollow waveguide problem. IEE Proceedings 119(1): 33-37.

DAVIES, J.B. (1989). The finite element method. In: Numerical techniques for microwave and millimeter-wave passive structures, ed. by T. Itoh. (New York: Wiley-Interscience).

DAVIES, J.B. (1993). Finite element analysis of waveguides and cavities – a review. IEEE Transactions on Magnetics 29(2): 1578-1583.

- DE MICHELI, M., BOTINEAU, J., NEVEU, S., SIBILLOT, P., OSTROWSKY, D.B. and PAPUCHON, M. (1983). Independent control of index and profiles in proton-exchanged lithium niobate guides. Optics Letters 8(2): 114-115.
- DENTON, R.T., SHEN, F.S. and BALLMAN, A.A. (1967). Lithium tantalate light modulators. Journal of Applied Physics 38(4): 1611-1617.
- DOLFI, D.W. and RANGANATH, T.R. (1992). 50GHz velocity-matched broad wavelength LiNbO<sub>3</sub> modulator with multimode active section. Electronics Letters 28(13): 1197-1198.
- DONNELLY, J.P., DE MAYO, N.L., FERRANTE, G.A., NICHOLS, K.B. and O'DONNELL, F.J. (1984). Optical guided-wave gallium arsenide monolithic interferometer. Applied Physics Letters 45(4): 360-362.
- DONNELLY, J.P., DEMEO, N.L., LEONBERGER, F.J., GROVES, S.H., VOHL, P.H. and O'DONNELL, F.J. (1985). Single-mode optical wave-guides and phase modulators in the InP material system. IEEE Journal of Quantum Electronics 21(8): 1147-1151.
- D'ORAZIO, A., DE SARIO, M., FICARELLA, G., PETRUZZELLI, V. and PRUDENZANO, F. (1997). Design of active switches using an In<sub>x</sub>Ga<sub>1-x</sub>As<sub>y</sub>P<sub>1-y</sub>/InP heterostructure. International Journal of Optoelectronics 11(1): 19-27.
- DUTHIE, P.J. and EDGE, C. (1991). A polarization independent guided-wave LiNbO<sub>3</sub> electrooptic switch employing polarization diversity. IEEE Photonics Technology Letters 3(2): 136-137.
- ENGLISH, W.J. (1971). Vector variational solutions of inhomogeneously loaded waveguide structures. IEEE Transactions on Microwave Theory and Techniques 19(1): 9-18.
- ENGLISH, W.J. and YOUNG, F.J. (1971). An E vector variational formulation of the Maxwells equations for cylindrical waveguide problems. IEEE Transactions on Microwave Theory and Techniques 19(1): 40-46.
- ESAKI, L. (1986). A birds-eye-view on the evolution of semiconductor superlattices and quantum-wells. IEEE Journal Of Quantum Electronics 22(9): 1611-1624.
- FAIST, J. and REINHART, F.-K. (1990a). Phase modulation in GaAs/AlGaAs double heterostructures. I. Theory. Journal of Applied Physics 67(11): 6998-7005.
- FEIT, M.D., FLECK, Jr, J.A. (1978). Light propagation in graded-index optical fibers. Applied Optics 17: 3990-3998.
- FEIT, M.D., FLECK, Jr, J.A. (1980). Computation of mode properties in optical fiber waveguides by a propagating beam method. Applied Optics 19(7): 1154-1164.
- FENG, H., MAKINO, T., OGITA, S., MARUYAMA, H. and KONDO, M. (2002). 40Gb/s electro-absorption-modulator-integrated DFB laser with optimised design. In: Optical Fiber Communication Conference, San Jose, USA, 2002. Proceedings.

FERNÁNDEZ, F.A. and LU, Y. (1991). A variational finite element formulation for dielectric waveguides in terms of transverse magnetic fields. IEEE Transactions on Magnetism 27(5): 3864-3867.

FERNÁNDEZ, F.A., DAVIES, J.B., ZHU, S. and LU, Y. (1991). Sparse matrix eigenvalue solver for finite element solution of dielectric waveguides. Electronics Letters 27(20): 1824-1826.

FERNÁNDEZ, F.A. and LU, Y. (1996). Microwave and optical waveguide analysis by the finite element method. (Somerset: Research Studies Press Ltd., J. Wiley & Sons Inc).

FETTERMAN, M., CHAO, C.-P. and FORREST, S.R. (1996). Fabrication and analysis of high-contrast InGaAsP-InP Mach-Zehnder modulators for use at 1.55- $\mu\text{m}$  wavelength. IEEE Photonics Technology Letters 8(1): 69-71.

FIBER-OPTICS INFO. (2003). Dense Wavelength-division Multiplexing. [Online]. URL: <http://www.fiber-optics.info/articles/dwdm.htm>. [Accessed date: 31 October 2003].

FORESI, J.S., VILLENEUVE, P.R., FERRERA, J., THOEN, E.R., STEINMEYER, G., FAN, S., JOANNOPOULOS, J.D., KIMERLING, L.C., SMITH, H.I. and IPPEN, E.P. (1997). Photonic-bandgap microcavities in optical waveguides. Nature 390: 143-145.

FOUCHET, S., CARENCO, A., DAGUET, C., GUGLIELMI, R. and RIVIERE, L. (1987). Wavelength dispersion of Ti induced refractive index change in  $\text{LiNbO}_3$  as a function of diffusion parameters. Journal of Lightwave Technology 5(5): 700-708.

FRANZ, G., HOYLER, C. and KAINDL, J. (1996). Reactive ion etching GaAs and AlAs: Kinetics and process monitoring. Journal of Vacuum Science and Technology B 14(1): 126-131.

FRASER, M. (1989a). Czochralski growth of lithium niobate. In: Properties of lithium niobate. (London and New York: INSPEC, The Institution of Electrical Engineers).

FRASER, M. (1989b). Poling of lithium niobate. In: Properties of lithium niobate. (London and New York: INSPEC, The Institution of Electrical Engineers).

FRASER, M. (1989c). Cutting and polishing of lithium niobate. In: Properties of lithium niobate. (London and New York: INSPEC, The Institution of Electrical Engineers).

FUJII, Y. (1991). High-isolation polarization-independent optical circulator coupled with single-mode fibers. Journal of Lightwave Technology 9(4): 456-460.

FUKUMA, M. and NODA, J. (1980). Optical properties of titanium-diffused  $\text{LiNbO}_3$  strip waveguides and their coupling-to-a-fiber characteristics. Applied Optics 19(4): 591-597.

FUSHEN, C. (1997). LB-film-deposited optical channel waveguides with sensing functions. Microwave and Optical Technology Letters 15(2): 116-120.

GALICK, A.T., KERKHOVEN, T. and RAVAIOLI, U. (1992). Iterative solution of the eigenvalue problem for a dielectric wave-guide. IEEE Transactions on Microwave Theory and Techniques 40(4): 699-705.

GANGULY, P., BISWAS, J.C. and LAHIRI, S.K. (1998). Modelling of titanium indiffused lithium niobate channel waveguide bends: a matrix approach. Optics Communications 155: 125-134.

GERDES, J. and PREGLA, R. (1991). Beam-propagation method based on the method of lines. Journal of the Optical Society of America B 8(2): 389-394.

GERDES, J., HELF, K.H. and PREGLA, R. (1991). Full-wave analysis of travelling-wave electrodes with finite thickness for electro-optic modulators by the method of lines. Journal of Lightwave Technology 9(4): 461-467.

GHEORMA, I.L., SAVI, P., OSGOOD, R.M. (2000). Thin layer design of X-cut LiNbO<sub>3</sub> modulators. IEEE Photonics Technology Letters 12(12): 1618-1620.

GILL, D.M., JACOBSON, D., WHITE, C.A., JONES, C.D.W., SHI, Y., MINFORD, W.J. and HARRIS, A. (2004). Ridged LiNbO<sub>3</sub> modulators fabricated by a novel oxygen-ionimplant wet-etch technique. Journal of Lightwave Technology 22(3): 887-894.

GLINGENER, C., SCHULZ, D. and VOGES, E. (1995). Modeling of optical waveguide modulators on III-V semiconductors. IEEE Journal of Quantum Electronics 31(1): 101-112.

GOELL, J.E. (1969). A circular-harmonic computer analysis of rectangular dielectric waveguides. Bell Systems Technical Journal 48(9): 2133-2160.

GOLDBERG, YU. A. (1997). Aluminium Gallium Arsenide (Al<sub>x</sub>Ga<sub>1-x</sub>As). In: Handbook Series on Semiconductor Parameters, vol. 2: Ternary and Quaternary III-V Compounds, ed. by M. Levinstein, S. Rumyantsev and M. Shur. (London: World Scientific Pub. Co.).

GOMATAM, B.N. (1992). The distributed feedback waveguide modulator. IEEE Photonics Technology Letters 4(11): 1227-1230.

GOWAR, J. (1984). Optical communication systems. (London: Prentice-Hall International, Inc.).

GOYAL, I.C., GALLAWA, R.L. and GHATAK, A.K. (1993). Improved variational analysis of inhomogeneous optical waveguides using Airy functions. Journal of Lightwave Technology 11(10): 1575-1578.

GRANT, I.R. (1995). LEC growth of GaAs. In: Properties of Gallium Arsenide, ed. by M. R. Brozel and G.E. Stillman. 3<sup>rd</sup> Ed. (London and New York: INSPEC, The Institution of Electrical Engineers).

- GREENBLATT, A.S., BULMER, C.H., MOELLER, R.P. and BURNS, W.K. (1995). Thermal stability of bias point of packaged linear modulators in lithium niobate. Journal of Lightwave Technology 13(12): 2314-2319.
- GU, D., EKNOYAN, O. and TAYLOR, H.F. (2002). Polarization dependence in Ti-diffused LiNbO<sub>3</sub> directional couplers. Applied Optics 41(1): 74-77.
- GU, J.-S., BESSE, P.-A. and MELCHIOR, H. (1991). Method of lines for the analysis of the propagation characteristics of curved optical rib waveguides. IEEE Journal of Quantum Electronics 27(3): 531-537.
- GUDIKNEN, M. S., LAUHON, L. J., WANG, J., SMITH, D. C. & LIEBER, C. M. (2002). Growth of nanowire superlattice structures for nanoscale photonics and electronics. Nature 415: 617-620.
- GUO, C.L., SUN, C.Z., HAO, Z.B., LUO, Y. (2000). Theoretical analysis of polarization insensitive InGaAsP multiple-quantum-wells electroabsorption modulators with negative chirp. Japanese Journal Of Applied Physics Part 1-Regular Papers Short Notes & Review Papers 39(11): 6166-6169.
- HADLEY, G.R. (1992). Wide-angle beam propagation using Padé approximation operators. Optics Letters 17(20): 1426-1428.
- HAEGEL, N.M. (2001). Semiconductor photoconductors for visible to far-infrared detection. In: Photodetectors and fiber optics, ed. by H. S. Nalwa. (Academic Press).
- HAGA, H., IZUTSU, M. and SUETA, T. (1986). LiNbO<sub>3</sub> travelling-wave length modulator/switch with an etched groove. IEEE Journal of Quantum Electronics 22(6): 902-906.
- HALL, R.N., FENNER, G.E., KINGSLEY, J.D., SOLTYS, T.J. and CARISON, R.O. (1962). Coherent light emission from GaAs junctions. Physical Review Letters 9(9): 366-368.
- HAN, S.-K., RAMASWAMY, R.V., LI, W.-Q. and BHATTACHARYA, P.K. (1993). Efficient electrooptic modulator in InGaAlAs/InP optical waveguides. . IEEE Photonics Technology Letters 5(1): 46-54.
- HANO, M. (1984). Finite-element analysis of dielectric-loaded waveguides. IEEE Transactions on Microwave Theory and Techniques 32(10): 1275-1279.
- HARDY, A. and STREIFER, W. (1985). Coupled mode theory of parallel waveguides. Journal of Lightwave Technology 3(5): 1135-1146.
- HASENBERG, T.C., KOEHLER, S.D., YAP, D., KOST, A., and GARMIRE, E.M. (1994). All-binary InAs/GaAs optical waveguide phase modulator at 1.06µm. IEEE Photonics Technology Letters 6(10): 1210-1212.
- HAYATA, K., EGUCHI, M. and KOSHIBA, M. (1988). Self-consistent finite infinite element scheme for unbounded guided wave problems. IEEE Transactions on Microwave Theory and Techniques 36(3): 614-616.

HEATON, J.M., JONES, S.B., BOURKE, M.M., HILTON, K.P., BIRBECK, J.C.H. and D.R. WIGHT. (1995). MMIC compatible GaAs/AlGaAs electro-optic waveguide modulators and switches for microwave applications. Invited paper. International Journal of Optoelectronics 10(6): 479-488.

HECHT, J. (1999a). A short history of fiber optics. Reproduced from Fiber optics technician's handbook, by Jim Hayes (Albany, NY: Delmar Publishers). [Online]. URL: <http://www.sff.net/people/Jeff.Hecht/history.html>. [Accessed date: 30 October 2003].

HECHT, J. (1999b). A fiber-optic chronology. An early version of the one that appears in the book City of Light: The Story of Fiber Optics (Oxford: Oxford University Press), part of the Sloan Technology Series. [Online]. URL: <http://www.sff.net/people/Jeff.Hecht/Chron.html>. [Accessed date: 30 October 2003].

HEIBLUM, M. and HARRIS, J.H. (1975). Analysis of curved optical waveguides by conformal transformation. IEEE Journal of Quantum Electronics 11(2): 75-83.

HEISMANN, F., KOROTKY, S.K. and VESELKA, J.J. (1997). Lithium niobate integrated optics: Selected contemporary devices and system applications. In: Optical fiber telecommunications IIIB, ed. by I.P. Kaminow and T.L.Koch. (New York: Academic Press.).

HIGUMA, K., HASHIMOTO, Y., YATSUKI, M. and NAGATA, H. (2000). Electrode design to suppress thermal drift in lithium niobate modulators. Electronics Letters 36(24): 2013-2014.

HIRAYAMA, K. and KOSHIBA, M. (1993). Rigorous analysis of coupling between laser and passive waveguide in multilayer slab waveguide. Journal of Lightwave Technology 11(8): 1353-1359.

HOBDEN, M.V. and WARNER, J. (1966). The temperature dependence of the refractive indices of pure lithium niobate. Physics Letters 22: 243-244.

HOCKER, G.B. and BURNS, W.K. (1977). Mode dispersion in diffused channel waveguides by the effective index method. Applied Optics 16(1):113-118.

HOLONYAK, N. and BEVACQUA, S.F. (1962). Coherent (visible) light emission from Ga(As<sub>1-x</sub>P<sub>x</sub>) junctions. Applied Physics Letters 1(4): 82-83.

HOU, H.Q. and CHANG, T.Y. (1995). Nearly chirp-free electroabsorption modulation using InGaAs-InGaAlAs-InAlAs coupled quantum wells. IEEE Photonics Technology Letters 7(2): 167-169.

HSIA, C.C.W., CHUONG, C.J.C. and JOHNSON, Jr, R.L. (1997). Red cell distortion and conceptual basis of diffusing capacity estimates: finite element analysis. Journal of Applied Physiology 83(4): 1397-1404.

HUANG, T.-C., CHUNG, Y., COLDREN, L.A. and DAGLI, N. (1993). Field-induced waveguides and their application to modulators. IEEE Journal of Quantum Electronics 29(4): 1131-1143.

- IDO, T., SANO, H., MOSS, D.J., TANAKA, S. and TAKAI, A. (1994). Strained InGaAs/InAlAs MQW electroabsorption modulators with large bandwidth and low driving voltage. IEEE Photonics Technology Letters 6(10): 1207-1209.
- IDO, T, SANO, H., SUZUKI, M., TANAKA, S. and INOUE, H. (1995). High-speed MQW electroabsorption optical modulators integrated with low-loss waveguides. IEEE Photonics Technology Letters 7(2): 170-172.
- IDO, T., TANAKA, S., SUZUKI, M., KOIZUMI, M., SANO, H., and INOUE, H. (1996). Ultra high-speed multiple quantum well electroabsorption optical modulators with integrated waveguides. Journal of Lightwave Technology 14(9): 2026-2034.
- IKEGAMI, T. and SUEMATSU, Y. (1967). Resonance-like characteristics of the direct modulation of a junction laser. IEEE Proceedings 55: 122.
- IRMSCHER, S, LEWEN, R. and ERIKSSON, U. (2002). InP-InGaAsP high-speed traveling-wave electroabsorption modulators with integrated termination resistors. IEEE Photonics Technology Letters 14(7): 923-925.
- ITO, H., FURUTA, T., KODAMA, S., WATANABE, N. and ISHIBASHI, T. (1999). InP/InGaAs uni-travelling photodiode with 220GHz bandwidth. Electronics Letters 35(18):1556-1557.
- ITOH, T. (1989). Introduction. In: Numerical techniques for microwave and millimeter-wave passive structures, ed. by T. Itoh. (New York: Wiley-Interscience).
- JACKEL, J.L., RAMASWAMY, V and LYMAN, S. (1981). Elimination of out-diffused surface guiding in titanium-diffused LiNbO<sub>3</sub>. Applied Physics Letters 38(7): 509-511.
- JAEGER, N.A.F. and YOUNG, L. (1989). High-voltage sensor employing an integrated optics Mach-Zehnder interferometer in conjunction with a capacitive divider. Journal of Lightwave Technology 7(2): 229-235.
- JANUAR, I, FEUERSTEIN, R.J., MICKELSON, A.R. and SAUER, J.R. (1992). Wavelength sensitivity in directional couplers. Journal of Lightwave Technology 10(9): 1202-1209.
- JENKINS, D.W. (1990). Optical constants of Al<sub>x</sub>Ga<sub>1-x</sub>As. Journal of Applied Physics 68(4): 1848-1853.
- JGKB PHOTONICS INC. (2004). 40Gb/s mode converter electro-optic amplitude modulator[Online]. URL: [http://www.jgkb.com/pdf/jgkb\\_product\\_brochure.pdf](http://www.jgkb.com/pdf/jgkb_product_brochure.pdf). [Accessed date: 20 September 2004].
- JIANG, C., MURANAKA, T. and HASEGAWA, H. (2001). Improvement of growth process to achieve high geometrical uniformity in InGaAs ridge quantum wires grown by selective MBE on patterned InP substrate. Japanese Journal Of Applied Physics Part 1-Regular Papers Short Notes & Review Papers 40(4B): 3003-3008.

JIANG, P and O'DONNELL, A.C. (1996). LiNbO<sub>3</sub> Mach-Zehnder modulators with fixed negative chirp. IEEE Photonics Technology Letters 8(10): 1319-1321.

JOHNSON, D.A. (2001). Handbook of through the air communications. [Online]. URL: <http://www.imagineeringezine.com/air-bk2.html>. [Accessed date: 30 October 2003].

JOHNSON, J.E., TANBUN-EK, T., CHEN, Y.K., FISHMAN, D.A, LOGAN, R.A., MORTON, P.A., CHU, S.N.G., TATE, A., SARGENT, A.M., SCIORTINO, Jr, P.F. and WECHT, K.W. (1994). Low-chirp integrated EA modulator/ DFB laser grown by selective-area MOVPE. In: IEEE International Semiconductor Laser Conference, Maui, Hawaii, 1994. Proceedings. pp. 41-42.

JOHNSON, L.M., LEONBERGER, F.J. and PRATT, Jr, G.W. (1982). Integrated optical temperature sensor. Applied Physics Letters 41(2): 134-136.

KAMAN, V., CHIU, Y.-J., LILJEBERG, T., ZHANG, S.Z. and BOWERS, J.E. (2000). Integrated tandem traveling-wave electroabsorption modulators for >100 Gbit/s OTDM applications. IEEE Photonics Technology Letters 12(11): 1471-1473.

KAMINOW, I.P. (1963). Splitting of Fabry-Perot rings by microwave modulation of light. Applied Physics Letters 2(2): 41-42.

KAMINOW, I.P. (1965). Barium titanate light phase modulator. Applied Physics Letters 7(5): 123-125.

KAMINOW, I.P. (1966). Barium titanate light phase modulator II. Applied Physics Letters 8(11): 305-306.

KAMINOW, I.P. and TURNER, E.H. (1966). Electrooptic light modulators. Applied Optics 5(10): 1612-1628.

KAMINOW, I.P. and SHARPLESS, W.M. (1967). Performance of LiTaO<sub>3</sub> and LiNbO<sub>3</sub> light modulators at 4GHz. Applied Optics 6(2): 351-352.

KAMINOW, I.P. and CARRUTHERS, J.R. (1973). Optical waveguiding layers in LiNbO<sub>3</sub> and LiTaO<sub>3</sub>. Applied Physics Letters 22(7): 326-328.

KAMINOW, I.P., CARRUTHERS, J.R., TURNER, E.H. and STULZ, L.W. (1973). Thin-film LiNbO<sub>3</sub> electro-optic light modulator. Applied Physics Letters 22(10): 540-542.

KAMINOW, I.P. (1974). An introduction to electrooptic devices. (New York and London: Academic Press).

KAMINOW, I.P. and STULZ, L.W. (1978). Loss in cleaved Ti-diffused LiNbO<sub>3</sub> waveguides. Applied Physics Letters 33(1): 62-64.

KANEKO, S.-I., NODA, M., MIYAZAKI, Y., WATANABE, H., KASAHARA, K. and TAJIME, T. (1999). An electroabsorption modulator module for digital and analog applications. Journal of Lightwave Technology 17(4): 669-676.

KAO, K.C and HOCKHAM, G.A. (1966). Dielectric-fibre surface waveguides for optical frequencies. Proceedings IEE 113(7): 1151-1158.

KAPANY, N.S. (1967). Fiber optics : principles and applications. (Academic Press).

KAPLAN, A. and RUSCHIN, S. (2000). Layout for polarization insensitive modulation in LiNbO<sub>3</sub> waveguides. IEEE Journal of Selected Topics in Quantum Electronics 6(1): 83-87.

KATSRIKU, F.A., RAHMAN, B.M.A., GRATTAN, K.T.V. (1997). Numerical modeling of second harmonic generation in optical waveguides using the finite element method. IEEE Journal Of Quantum Electronics 33(10): 1727-1733.

KATSRIKU, F.A. (2000). Finite element study of the second order ( $\chi^2$ ) non-linear process of second harmonic generation in optical waveguides. PhD thesis: City University, Department of Electrical, Electronic and Information Engineering.

KATZ, J. (1982). Novel solution of 2-D waveguides using the finite element method. Applied Optics 21(15): 22747-2750.

KAWAGUCHI, H. (1978). GaAs rib-waveguide directional-coupler switch with Schottky barriers. Electronics Letters 14(13): 387-388.

KAWANISHI, H., YAMAUCHI, Y., MINEO, N., SHIBUYA, Y., MURAI, H., YAMADA, K. and WADA, H. (2001) EAM-integrated DFB laser modules with more than 40-GHz bandwidth. IEEE Photonics Technology Letters 13(9): 954-956.

KAWANO, K., KITOH, T., JUMONJI, H., NOZAWA, T., and YANAGIBASHI, M. (1989). New travelling-wave electrode Mach-Zehnder optical modulator with 20GHz bandwidth and 4.7V driving voltage at 1.52 $\mu$ m wavelength. Electronics Letters 25(20): 1382-1383.

KAWANO, K., KOHTOKU, M., UEKI, M., ITO, T., KONDOH, S., NOGUCHI, Y. and HASUMI, Y. (1997). Polarisation-insensitive travelling-wave electrode electroabsorption (TW-EA) modulator with bandwidth over 50GHz and driving voltage less than 2V. Electronics Letters 33(18): 1580-1581.

KENDALL, P.C., McILROY, P.W.A. and STERN, M.S. (1989). Spectral index method for rib waveguide analysis. Electronics Letters 25(2): 107-108.

KEYS, R.W., LONI, A. and DE LA RUE, R.M. (1990). Measurement of the increase in the SHG coefficient of proton exchanged LiNbO<sub>3</sub> after annealing using a grating diffraction technique. Electronics Letters 26(10): 624-626.

KILLEY, R.I., LIU, C.P., WHITEHEAD, M., STAVRINOU, P., SONG, J.B., CHADHA, J.S., WAKE, D., BUTTON, C.C., PARRY, G., SEEDS, A.J. (2001). Multiple-quantum-well asymmetric Fabry-Perot modulators for microwave photonic applications. IEEE Transactions On Microwave Theory And Techniques 49(10), Part 2: 1888-1893.

- KIM, T.W., LEE, D.U., CHOO, C., KIM, J.H., JUNG, M., KIM, M.D., JEONG, H.D., YOO, K.H., KIM, J.Y., LIM, H.J. (2001). 1.55 $\mu$ m wavelength strain-compensated In<sub>x</sub>Ga<sub>1-x</sub>As/In<sub>y</sub>Al<sub>1-y</sub>As electroabsorption modulators with high extinction ratio and low polarization-dependent loss. Japanese Journal Of Applied Physics Part 1-Regular Papers Short Notes & Review Papers 40(5A): 3120-3123.
- KINGSLEY, S.A. and SRIRAM, S. (1995). Parallel-plate integrated optic high-voltage sensor. Electronics Letters 31(13): 1096-1097.
- KISHI, N. and OKOSHI, T. (1989) Vectorial wave analysis of uniform-core optical fibers using a novel boundary integral method. IEEE Transactions on Microwave Theory and Techniques 37(3): 526-533.
- KNOX R.M. and TOULIOS P.P. (1970). In: Proceedings of MRI symposium on submillimeter waves, ed. by J. Fox. (Brooklyn, NY: Polytechnic Press).
- KOAI, K.T. and LIU, P.-L. (1989a). Modeling of Ti:LiNbO<sub>3</sub> waveguide devices: Part I—Directional couplers. Journal of Lightwave Technology 7(3): 533-539.
- KOCH, T.L. and KOREN, U. (1991). Semiconductor photonic integrated circuits. IEEE Journal of Quantum Electronics 27(3): 641-653.
- KOGELNIK, H. and SCHMIDT, R.V. (1976). Switched directional couplers with alternating  $\Delta\beta$ . IEEE Journal of Quantum Electronics 12(7): 396-401.
- KOGELNIK, H. (1988). Theory of optical waveguides. In: Guided wave optoelectronics, ed. by T. Tamir. (Berlin: Springer-Verlag).
- KOMATSU, K., KONDO, M. and OHTA, Y. (1986). Titanium magnesium double diffusion method for efficient fiber-LiNbO<sub>3</sub> waveguide coupling. Electronics Letters 22(17): 881-882.
- KONDO, M. (1993). LiNbO<sub>3</sub> waveguide devices. Journal of the Ceramic Society of Japan, Int. Edition 101(1): 36-39.
- KOREN, U., MILLER, B.I., KOCH, T.L., EISENSTEIN, G., TUCKER, R.S., BARJOSEPH, I., CHEMLA, D.S. (1987). Low-loss InGaAs / InP multiple quantum well optical electroabsorption waveguide modulator. Applied Physics Letters 51(15): 1132-1134.
- KOREN, U., BEN MICHAEL, R., MILLER, B.I., YOUNG, M.G., CHIEN, M., YAFFE, H.H., RAYBON, G. and DREYER, K. (1994). Electroabsorption modulator with passive waveguide spotsize converters. Electronics Letters 30(22): 1852-1853.
- KOROTKY, S.K. and McCAUGHAN, L. (1986). Control of section-asymmetry crosstalk in  $\Delta\beta$ -reversal directional coupler switches. Electronics Letters 22(23): 1222-1224.
- KOROTKY, S.K., and ALFERNESS, R.C. (1987). Ti:LiNbO<sub>3</sub> integrated optic technology: Considerations, and capabilities fundamentals, design. In: Integrated optical

circuits and components: Design and Applications, ed. by L.D. Hutcheson. (New York: Marcel Dekker, Inc.).

KOROTKY, S.K., and ALFERNESS, R.C. (1988). Waveguide electrooptic devices for optical fiber communication. In: *Optical fiber telecommunications II*, ed. by S.E Miller and I.P. Kaminow. (Boston: Academic Press.).

KOROTKY, S.K. and VESELKA, J.J. (1990). Efficient switching in a 72Gb/s Ti:LiNbO<sub>3</sub> binary multiplexer/demultiplexer. In: *Conference on Optical Fiber Communication, San Francisco, 1990. Technical Digest*. Washington, DC: Optical Society of America, paper TuH2.

KOROTKY, S.K. and VESELKA, J.J. (1996). An RC network analysis of long term Ti:LiNbO<sub>3</sub> bias stability. *Journal of Lightwave Technology* 14(12): 2687-2697.

KOSHIBA M., HAYATA, K. and SUZUKI, M. (1982). Approximate scalar finite-element analysis of anisotropic optical waveguides. *Electronics Letters* 18(10): 411-413.

KOSHIBA M., HAYATA, K. and SUZUKI, M. (1984). Approximate scalar finite-element analysis of anisotropic optical waveguides with off-diagonal elements in a permittivity tensor. *IEEE Transactions on Microwave Theory and Techniques* 32(6): 587-593.

KOSHIBA M., HAYATA, K. and SUZUKI, M. (1985). Finite-element formulation in terms of the electric-field vector for electromagnetic waveguide problems. *IEEE Transactions on Microwave Theory and Techniques* 33(10): 900-905.

KOSHIBA M. (1992). *Optical waveguide theory by the finite element method*. Advances in Optoelectronics series. (Tokyo: KTK Scientific Publishers).

KOSHIBA, M. and TSUJI, Y. (1998). Design and modelling of microwave photonic devices. *Optical and Quantum Electronics* 30: 995-1003.

KOSHIBA, M., TSUJI, Y. and NISHIO, M. (1999). Finite-element modeling of broadband travelling-wave optical modulators. *IEEE Transactions on Microwave Theory and Techniques* 47(9): 1627-1633.

KOYAMA F. and IGA, K. (1988). Frequency chirping in external modulators. *Journal of Lightwave Technology* 6(1): 87-93.

KRÄHENBÜHL, R. and HOWERTON, M.M. (2001). Investigations on short-path-length high-speed optical modulators in LiNbO<sub>3</sub> with resonant-type electrodes. *Journal of Lightwave Technology* 19(9): 1287-1297.

KUBOTA, K., NODA, J. and MIKAMI, O. (1980). Travelling-wave optical modulator using directional coupler LiNbO<sub>3</sub> waveguide. *IEEE Journal of Quantum Electronics* 16(?): 754-760.

KUMAR, A., THYAGARAJAN, K. and GHATAK, A.K. (1983). Analysis of rectangular-core waveguides: An accurate perturbation approach. *Optics Letters* 8(1): 63-65.

LAI, Q and HUNZIKER, W. (1997). Design of Y-junction, free-space and MMI couplers in silica on Si. [Online]. URL: [https://www.rdb.ethz.ch/projects/project.php?proj\\_id=7863&type=search&z\\_detailed=1&z\\_popular=1&z\\_keywords=1](https://www.rdb.ethz.ch/projects/project.php?proj_id=7863&type=search&z_detailed=1&z_popular=1&z_keywords=1). [Accessed date: 10 February 2005].

LASER FOCUS WORLD. (2004). Optical modulator market growth forecast. [Online]. URL: [http://cgw.pennnet.com/Articles/Article\\_Display.cfm?Section=OnlineArticles&SubSection=Display&PUBLICATION\\_ID=12&ARTICLE\\_ID=198062](http://cgw.pennnet.com/Articles/Article_Display.cfm?Section=OnlineArticles&SubSection=Display&PUBLICATION_ID=12&ARTICLE_ID=198062). [Accessed date: 20 September 2004].

LAURELL, F., WEBJÖRN, J., ARVIDSSON, G. and HOLMBERG, J. (1992). Wet etching of proton-exchanged lithium niobate – A novel processing technique. Journal of Lightwave Technology 10(11): 1606-1609.

LEE, S.-S., RAMASWAMY, R.V. and SUNDARAM, V.S. (1991). Analysis and design of high-speed high-efficiency GaAs-AlGaAs double-heterostructure waveguide phase modulator. IEEE Journal of Quantum Electronics 27(3): 726-736.

LEE, H.-J., SHIN, S.-Y. and KIM, B.-G. (1993). Fabrication-tolerant  $\Delta\kappa$  directional coupler switch using annealing in proton exchange. Optics Communications 102: 221-224.

LEE, J.-S. and SHIN, S.-Y. (1993). On the validity of the effective-index method for rectangular dielectric waveguides. Journal of Lightwave Technology 11(8): 1320-1324.

LEE, J.F. (1994). Finite element analysis of lossy dielectric waveguides. IEEE Transactions on Microwave Theory and Techniques 42(6): 1025-1031.

LEE, K.-Y., CHANG, G.-D., WANG, H.-T. AND LIN, Y.-J. (2000). Beam propagation analysis of ridge-type Ti:LiNbO<sub>3</sub> Y-junction waveguides. Journal of Optical Communications 21(4): 125-130.

LEIGH, W.B. (1996). Devices for optoelectronics. (New York: Marcel Dekker, Inc.).

LEONBERGER, F.J. (1980). High-speed operation of LiNbO<sub>3</sub> electrooptic interferometric waveguide modulators. Optics Letters 5(7): 312-314.

LEONBERGER, F.J. and DONNELLY, J.P. (1988). Semiconductor integrated optic devices. In: Guided wave optoelectronics, ed. by T. Tamir. (Berlin: Springer-Verlag).

LEVY, M., OSGOOD, Jr., R.M., HEGDE, H., CADIEU, F.J., WOLFE, R. and FRATELLO, V.J. (1996). Integrated optical isolators with sputter-deposited thin-film magnets. IEEE Photonics Technology Letters 8(7): 903-905.

LEWÉN, R., IRMSCHER, S., WESTERGREN, U., THYLÉN, L. and ERIKSSON, U. (2004). Segmented transmission-line electroabsorption modulators. Journal of Lightwave Technology 22(1): 172-180.

- LI, G.L., PAPPERT, S.A., MAGES, P., SUN, C.K., CHANG, W.S.C., YU, P.K.L. (2001). High-saturation high-speed traveling-wave InGaAsP-InP electroabsorption modulator. IEEE Photonics Technology Letters 13(10): 1076-1078.
- LIN, S.H., WANG, S.Y. and HUONG, Y.M. (1986). GaAs PIN electrooptic traveling-wave modulator at 1.3  $\mu\text{m}$ . Electronics Letters 22(18): 934-935.
- LIU, B., SHIM, J., CHIU, Y.-J., KEATING, A., PIPREK, J. and BOWERS, J. (2003). Analog characterization of low-voltage MQW traveling-wave electroabsorption modulators. Journal of Lightwave Technology 21(12): 3011-3019.
- LIU, J.-F., LIN, Y.-B. and WANG, W.-S. (2001). Fine adjustment of the coupling length of a Ti-diffused LiNbO<sub>3</sub> directional coupler with a groove structure. Microwave and Optical Technology Letters 29(5): 301-303.
- LLOBERA, A., SALINAS, I., GARCÉS, I., MERLOS, A. and DOMÍNGUEZ, C. (2002). Effect of wall tilt on the optical properties of integrated optical directional couplers. Optics Letters 27(8): 601-603.
- LOHMEYER, M. (1997). Wave-matching method for mode analysis of dielectric waveguides. Optical and Quantum Electronics 29(9): 907-922.
- LU, M. and FEJER, M.M. (1993). Anisotropic dielectric wave-guides. Journal of the Optical Society of America A-Optics Image Science and Vision 10(2): 246-261.
- LUCENT TECHNOLOGIES. (2000). Bell Laboratories. Physical Sciences Research – Timeline. [Online].  
URL: <http://www.bell-labs.com/org/physicalsciences/timeline/index.html>. [Accessed date: 30 October 2003].
- LUFF, B.J., HARRIS, R.D., WILKINSON, J.S., WILSON, R. and SCHIFFRIN, D.J. (1996). Integrated-optical directional coupler biosensor. Optics Letters 21(8): 618-620.
- LUO, J.D., HALLER, M., LI, H.X., TANG, H.Z., JEN, A.K.Y., JAKKA, K., CHOU, C.H., SHU, C.F. (2004). A side-chain dendronized nonlinear optical polyimide with large and thermally stable electrooptic activity. Macromolecules 37(2): 248-250.
- MA, H., LIU, S., LUO, J.D., SURESH, S., LIU, L., KANG, S.H., HALLER, M., SASSA, T., DALTON, L.R., JEN, A.K.Y. (2002). Highly efficient and thermally stable electro-optical dendrimers for photonics. Advanced Functional Materials 12(9): 565-574.
- MAAT, P. (2001). InP-based integrated MZI switches for optical communication. PhD thesis: Delft University of Technology, Department of Applied Physics.
- MABAYA, N., LAGASSE, P.E. and VANDENBULCKE, P. (1981). Finite element analysis of optical waveguides. IEEE Transactions on Microwave Theory and Techniques 29(6): 600-605.

- MAHMOOD, N., RAHMAN, B.M.A., GRATTAN, K.T.V. (1998). Accurate three-dimensional modal solutions for optical resonators with periodic layered structure by using the finite element method. Journal Of Lightwave Technology 16(1): 156-161.
- MAK, G., ROLLAND, C., FOX, K.E. and BLAAUW, C. (1990). High-speed bulk InGaAsP-InP electroabsorption modulators with bandwidth in excess of 20GHz. IEEE Photonics Technology Letters 2(10): 730-733.
- MAK, H.-M. and YANAGAWA, H. (1994). High-extinction directional coupler switches by compensation and elimination methods. Journal of Lightwave Technology 12(5): 899-908.
- MAO, Z.M. and HUANG, W.P. (1994). Analysis of polarization rotation in periodically loaded rib waveguides by transfer matrix method. Journal of Lightwave Technology 12(5): 768-773.
- MARCATILI, E.A.J. (1969a). Dielectric rectangular waveguide and directional coupler for integrated optics. Bell Systems Technical Journal 48(9): 2071-2102.
- MARCATILI, E.A.J. (1969b). Bends in optical dielectric guides. Bell Systems Technical Journal 48(9): 2103-2132.
- MARCUSE, D. (1971). The coupling of degenerate modes in two parallel dielectric waveguides. Bell Systems Technical Journal 50(6): 1791-1816.
- MARCUSE, D. (1982). Optimal electrode design for integrated optics modulators. IEEE Journal of Quantum Electronics 18(3): 393-398.
- MARCUSE, D. (1991). Theory of dielectric waveguides. (Boston: Academic Press Inc., Harcourt Brace Jovanovich Publishers).
- MARTIN, W.E. (1975). A new waveguide switch/ modulator for integrated optics. Applied Physics Letters 26(10): 562-563.
- MARUYAMA, H., HARUNA, M. and NISHIHARA, H. (1995). TE-TM mode splitter using directional coupling between heterogeneous waveguides in LiNbO<sub>3</sub>. Journal of Lightwave Technology 13(7): 1550-1554.
- MASON, B., OUGAZZADEN, A., LENTZ, C.W., GLOGOVSKY, K.G., REYNOLDS, C.L., PRZYBYLEK, G.J., LEIBENGUTH, R.E., KERCHER, T.L., BOARDMAN, J.W., RADER, M.T., GEARY, J.M., WALTERS, F.S., PETICOLAS, L.J., FREUND, J.M., CHU, S.N.G., SIRENKO, A., JURCHENKO, R.J., HYBERTSEN, M.S., KETELSEN, L.J.P. and RAYBON, G. (2002). 40-Gb/s tandem electroabsorption modulator. IEEE Photonics Technology Letters 14(1): 27-29.
- McCAUGHAN, L. and KOROTKY, S.K. (1986). Three-electrode Ti:LiNbO<sub>3</sub> optical switch. Journal of Lightwave Technology 4(9): 1324-1327.
- McGILLIS, D.A. (1983). Lithography. In: VLSI Technology, ed. by S.M. Sze. (McGraw-Hill International).

McKENNA, J. and REINHART, F.K. (1976). Double-heterostructure GaAsAl<sub>x</sub>Ga<sub>1-x</sub>As 110 p-n-junction-diode modulator. Journal of Applied Physics 47(5): 2069-2078.

MELCHIOR, H. (2003). 2x2 optical InP/InGaAsP waveguide space switches with high performances. [Online]. URL: [https://www.rdb.ethz.ch/projects/project.php?proj\\_id=7864&type=search&z\\_detailed=1&z\\_popular=1&z\\_keywords=1](https://www.rdb.ethz.ch/projects/project.php?proj_id=7864&type=search&z_detailed=1&z_popular=1&z_keywords=1). [Accessed date: 10 February 2005].

MENDOZA-ALVAREZ, J.G., COLDREN, L.A., ALPING, A., YAN, R.H., HAUSKEN, T., LEE, K. and PEDROTTI, K. (1988). Analysis of depletion edge translation lightwave modulators. Journal of Lightwave Technology 6(6): 793-807.

MENIGAUX, L., CARENCO, A. and LIN, N.T. (1982). InP electrooptic directional coupler switch. In: Topical Meeting on Integrated and Guided-Wave Optics, Asilomar (CA, USA), 1982, Proceedings. Paper TLD5.

MICKELSON, A.R. (1993). Guided wave optics. (New York: Van Nostrand Reinhold).

MIKAMI, O. (1980). LiNbO<sub>3</sub> coupled-waveguided TE/TM mode splitter. Applied Physics Letters 36(7): 491-493.

MILLER, D.A.B., CHEMLA, D.S., DAMEN, T.C., GOSSARD, A.C., WIEGMANN, W., WOOD, T.H. and BURRUS, C.A. (1984) Band-edge electroabsorption in quantum well structures - The quantum-confined stark-effect. Physical Review Letters 53(22): 2173-2176

MILLER, D.A.B., CHEMLA, D.S., DAMEN, T.C., GOSSARD, A.C., WIEGMANN, W., WOOD, T.H. and BURRUS, C.A. (1985). Electric-field dependence of optical-absorption near the band-gap of quantum-well structures. Physical Review B32(2): 1043-1060

MILLER, D.A.B. (1995). Quantum Well Optical Switching Devices. In: Confined Electronics and Photons Book Chapter, edited by E. Burstein and C. Weisbuch, (New York: Plenum Press).

MILLER, S.E. (1969). Integrated optics: An introduction. Bell Systems Technical Journal 48(9): 2059-2069.

MINAKATA, M. (2001). Recent Progress of 40 GHz high-speed LiNbO<sub>3</sub> optical modulator. [Online]. URL: <http://www.rie.shizuoka.ac.jp/~hsdhome/list/SPIE/SPIE2001.html>. [Accessed date: 14 August 2005].

MINFORD, W.J., KOROTKY, S.K. and ALFERNESS, R.C. (1982). Low-loss Ti:LiNbO<sub>3</sub> waveguide bends at  $\lambda = 1.3 \mu\text{m}$ . IEEE Journal of Quantum Electronics 18(10): 1802-1806.

MIRSHEKAR-SYAHKAL, D. and DAVIES, J.B. (1982). Accurate analysis of coupled strip-finline structure for phase constant, characteristic impedance, dielectric and conductor losses. IEEE Transactions On Microwave Theory And Techniques 30(6): 906-910

MITOMI, O., NOGUCHI, K. and MIYAZWA, H. (1995). Design of ultra-broad-band LiNbO<sub>3</sub> optical modulators with ridge structure. IEEE Transactions on Microwave Theory and Techniques 43(9): 2203-2207.

MITOMI, O., NOGUCHI, K. and MIYAZWA, H. (1998). Broadband and low driving-voltage LiNbO<sub>3</sub> optical modulators. IEE Proceedings – Optoelectronics 145(6): 360-364.

MITRA, P. P., and STARK, J. B. (2001). Nonlinear limits to the information capacity of optical fibre communications. Nature 411, 1027-1030.

MITSUGI, N., NAGATA, H., SHIMA, K. and TAMAI, M. (1998). Challenges in electron cyclotron resonance plasma etching of LiNbO<sub>3</sub> surface for fabrication of ridge optical waveguides. Journal of Vacuum Science and Technology A16(4): 2245-2251.

MOLL, N.J. and DOLFI, D. (1983) Thermo-optic coupler: a controllable multimode optical directional coupler. Applied Optics 22(19): 2944-2945.

MORISHITA, K. and KUMAGAI, N. (1977). Unified approach to the derivation of variational expression for electromagnetic fields. IEEE Transactions on Microwave Theory and Techniques 25(1): 34-40.

MOSS, D.J., IDO, T. and SANO, H. (1994). Photogenerated carrier sweep-out times in strained In<sub>x</sub>Ga<sub>1-x</sub>As/In<sub>y</sub>Al<sub>1-y</sub>As quantum well modulators. Electronics Letters 30(5): 405-406.

MROZOWSKI, M. (1991). Comments on finite-element analysis of wave-guide modes - A novel-approach that eliminates spurious modes. IEEE Transactions On Microwave Theory And Techniques 39(3): 611.

NAKAMURA, K., ANDO, H. AND SHIMIZU, H. (1987). Ferroelectric Domain Inversion Caused in LiNbO<sub>3</sub> Plates by Heat Treatment. Applied Physics Letters 50(20): 1413-1414.

NATHAN, M.I., DUMKE, W.P., BURNS, G., DILL, Jr, F.H. and LASHER, G. (1962). Stimulated emission of radiation from GaAs p-n junctions. Applied Physics Letters 1(3): 62-64.

NAYYER, J. and NAGATA, H. (1994). Suppression of thermal drifts of high speed Ti:LiNbO<sub>3</sub> optical modulators. IEEE Photonics Technology Letters 6(8): 952-955.

NELSON, D.F. and REINHART, F.K. (1964). Light modulation by the electrooptic effect in reverse-biased GaP p-n junctions. Applied Physics Letters 5(7): 148-150.

NEWS. (2004). Bright future for solid state lighting. IEE Review: September 2004.

NEYER, A. and SOHLER, W. (1979). High-speed cutoff modulator using a Ti-diffused LiNbO<sub>3</sub> channel waveguide. Applied Physics Letters 35(3): 256-258.

- NOGUCHI, K., MITOMI, O., KAWANO, K. and YANAGIBASHI, Y. (1993). Highly efficient 40-GHz bandwidth Ti:LiNbO<sub>3</sub> optical modulator employing ridge structure. IEEE Photonics Technology Letters 5(1): 52-54.
- NOGUCHI, K., MITOMI, O., MIYAZAWA, H. and SEKI, S. (1995). A broadband Ti:LiNbO<sub>3</sub> optical modulator with a ridge structure. Journal of Lightwave Technology 13(6): 1164-1168.
- NOGUCHI, K., MITOMI, O. and MIYAZAWA, H. (1998). Millimeter-wave Ti:LiNbO<sub>3</sub> optical modulators. Journal of Lightwave Technology 16(4): 615-619.
- NIPPON TELEGRAPH AND TELEPHONE CORPORATION (NTT). (2004). Ultrafast EA-modulator monolithically integrated with a DFB laser. [Online]. URL: [http://www.phlab.ecl.ntt.co.jp/eng/theme/2004/e2004\\_01\\_03.pdf](http://www.phlab.ecl.ntt.co.jp/eng/theme/2004/e2004_01_03.pdf). [Accessed date: 10 August 2004].
- OBAYYA, S.S.A. (1999). Vector finite element-based beam propagation analysis of optical guided-wave devices. PhD thesis: Mansoura University, Electrical Communications Engineering Department.
- OBAYYA, S.S.A., RAHMAN, B.M.A. and EL-MIKATI, H. A. (2000a). New full-vectorial numerically efficient propagation algorithm based on the finite element method. Journal of Lightwave Technology 18 (3): 409-415.
- OBAYYA, S.S.A., RAHMAN, B.M.A., EL-MIKATI, H.A. (2000b). Full-vectorial finite-element beam propagation method for nonlinear directional coupler devices. IEEE Journal Of Quantum Electronics 36(5): 556-562.
- OBAYYA, S.S.A., RAHMAN, B.M.A., GRATTAN, K.T.V., EL-MIKATI, H.A. (2001). Beam propagation modeling of polarization rotation in deeply etched semiconductor bent waveguides. IEEE Photonics Technology Letters 13(7): 681-683.
- OKAYAMA, H., MATOBA, A., SHIBUYA, R. and ISHIDA, T. (1987). Optically biased LiNbO<sub>3</sub>  $\Delta\beta$  reversal directional coupler switch. Electronics Letters 23(21): 1145-1147.
- OKAYAMA, H., KAMIJOH, T. and TSURUOKA, T. (2000). Reversed and uniform  $\Delta\beta$  directional coupler optical switch with periodically changing coupling strength. Japanese Journal of Applied Physics, Part 1 39(3B): 1512-1515.
- PANTIĆ, Z. and MITTRA, R. (1986). Quasi-TEM analysis of microwave transmission lines by the finite-element method. IEEE Transactions on Microwave Theory and Techniques 34(11): 1096-1103.
- PAPUCHON, M., COMBEMALE, Y., MATHIEU, X., OSTROWSKY, D.B., REIBER, L., ROY, A.M., SEJOURNE, B. and WERNER, M. (1975). Electrically switched optical directional coupler: Cobra. Applied Physics Letters 27(5): 289-291.
- PARK, C., SHIRALAGI, K.T., DROOPAD, R. and MARACAS, G.N. (1992). A novel optically bistable multiple-quantum-well phase modulator. IEEE Photonics Technology Letters 4(11): 1225-1227.

PATRICK, S.S. and WEBB, K.J. (1992). A variational vector finite-difference analysis for dielectric wave-guides. IEEE Transactions on Microwave Theory and Techniques 40(4): 692-698.

PAVELESCU, I, MÜLLER, R. and MOAGAR-POLADIAN, V. (1997). Analysis and modelling of a silicon micromachined Mach-Zehnder interferometer for pressure sensing. Journal of Micromechanics and Microengineering 7: 214-217.

PENG, S.-T. and OLINER, A.A. (1981). Guidance and leakage properties of a class of open dielectric waveguides: Part I – Mathematical formulations. IEEE Transactions on Microwave Theory and Techniques 29(9): 845-855.

PIKHTIN, A.N. and YAS'KOV, A.D. (1980). Dispersion of the refractive index of semiconducting solid solutions with the sphalerite structure. Soviet Physics – Semiconductors 14(4): 389-392.

PIRES, M.P., DE SOUZA, P.L., YAVICH, B., PEREIRA, R.G., CARVALHO, W. (2000). On the optimization of InGaAs-InAlAs quantum-well structures for electroabsorption modulators. Journal Of Lightwave Technology 18(4): 598-603.

POCKELS, F. (1906). Effects of the electrical and magnetic fields. Reprinted in: An introduction to electrooptic devices. (1974). Kaminow, I.P. (New York and London: Academic Press).

POHLMANN, T., NEYER, A. and VOGES, E. (1991). Polarization independent Ti:LiNbO<sub>3</sub> switches and filters. IEEE Journal of Quantum Electronics 27(3): 602-607.

PREGLA, R. and PASCHER, W. (1989). The method of lines. In: Numerical techniques for microwave and millimeter-wave passive structures, ed. by T. Itoh. (New York: Wiley-Interscience).

PROSYK, K., MOORE, R., BETTY, I., FOSTER, R., GREENSPAN, J., SINGH, P., O'KEEFE, S., OOSTEROM, J. and LANGLOIS, P. (2003). Record unamplified loss 40GHz electroabsorption modulator module. In: Optical Fiber Communication Conference, Atlanta, USA, 2003. Proceedings.

QUIST, T.M., REDIKER, R.H., KEYES, R.J., KRAG, W.E., LAX, B, McWHORTER, A.L. and ZEIGLER, H.J. (1962). Semiconductor maser of GaAs. Applied Physics Letters 1(4): 91-92.

RAGANATH, T.R. and WANG, S. (1977). Ti-diffused LiNbO<sub>3</sub> branched-waveguide modulators performance and design. IEEE Journal of Quantum Electronics 13(4): 290-295.

RAHMAN, B.M.A. and DAVIES, J.B. (1984a). Finite-element analysis of optical and microwave waveguide problems. IEEE Transactions on Microwave Theory and Techniques 32(1): 20-28.

RAHMAN, B.M.A. and DAVIES, J.B. (1984b). Penalty function improvement of waveguide solution by finite elements. IEEE Transactions on Microwave Theory and Techniques 32(8): 922-928.

- RAHMAN, B.M.A. and DAVIES, J.B. (1984c). Finite-element solution of integrated optical waveguides. Journal of Lightwave Technology 2(5): 682-688.
- RAHMAN, B.M.A. and DAVIES, J.B. (1985). Vector-H finite element solution of GaAs/GaAlAs rib waveguides. IEE Proceedings Part J—Optoelectronics 132(6): 349-353.
- RAHMAN, B.M.A. and DAVIES, J.B. (1988). Analysis of optical waveguide discontinuities. Journal of Lightwave Technology 6(1): 52-57.
- RAHMAN, B.M.A., SOUZA, J.R. and DAVIES, J.B. (1990). Numerical analysis of nonlinear bistable optical waveguides. IEEE Photonics Technology Letters 2(4): 265-267.
- RAHMAN, B.M.A., FERNÁNDEZ, F.A. and DAVIES, J.B. (1991). Review of finite element methods for microwave and optical waveguides. Proceedings of the IEEE 79(10): 1442-1448.
- RAHMAN, B.M.A. (1995). Finite element analysis of optical waveguides. In: Progress in Electromagnetics Research, Volume 10: Methods for Modeling and Simulation of Optical Guided-Wave Devices, Part I: Modes and Couplings, edited by W. -P. Huang, (Editor-in-chief: J. A. Kong), EMI Publishing.
- RAHMAN, B.M.A., LIU, Y. and GRATTAN, K.T.V. (1993). Finite-element modelling of one- and two-dimensional MQW semiconductor optical waveguides. IEEE Photonics Technology Letters 5(8): 928-931.
- RAHMAN, B.M.A., RAJARAJAN, M., WONGCHAROEN, T. and GRATTAN, K.T.V. (1996). Improved laser-fiber coupling by using spot-size transformer. IEEE Photonics Technology Letters 8(4): 557-559.
- RAHMAN, B. M. A., GOMOLUCH, J. M., ANWAR, N., AND GRATTAN, K. T. V. (2000). Characterization of Semiconductor Bragg Gratings for Optical Sensor Applications. In: International Conference on Optical Fibre Sensors (OFS2000), 14<sup>th</sup>, Venice 2000. Proceedings.
- RAHMAN, B.M.A., OBAYYA, S.S.A., SOMASIRI, N., RAJARAJAN, M., GRATTAN, K.T.V., EL-MIKATHI, H.A. (2001). Design and characterization of compact single-section passive polarization rotator. Journal Of Lightwave Technology 19 (4): 512-519.
- RAJARAJAN, M., BUAH, P.A., WONGCHAROEN, T., RAHMAN, B.M.A., GRATTAN, K.T.V., SCHULZ, D., GLINGENER, C. and KOPKA, P. (1996). Modelling of multimode interference based power dividers using different numerical approaches. In: Applied Optics Division Conference, Reading, 1996. Proceedings. IOP Publishing Ltd., pp. 429-434.
- RAJARAJAN, M., RAHMAN, B.M.A., GRATTAN, K.T.V. (1999). A rigorous comparison of the performance of directional couplers with multimode interference devices. Journal of Lightwave Technology 17(2): 243-248.

- RAJARAJAN, M., OBAYYA, S.S.A., RAHMAN, B.M.A., GRATTAN, K.T.V. and EL-MIKATI, H.A. (2000). Characterisation of low-loss waveguide bends with offset-optimisation for compact photonic integrated circuits. IEE Proceedings–Optoelectronics 147(6): 382-388.
- RAMASWAMY, V., DIVINO, M.D. and STANDLEY, Balanced bridge modulator switch using Ti-diffused LiNbO<sub>3</sub> strip waveguides. (1978). Applied Physics Letters 32(10): 644-646.
- RAMASWAMY, V. and DIVINO, M.D. (1981). Low-loss bends for integrated optics. In: Conference on Lasers and Electro-Optics, Washington, D.C, 1981. Technical Digest. IEEE, p. 142.
- RAMASWAMY, V., ALFERNESS, R.C. and DIVINO, M.D. (1982). High-efficiency single-mode fiber to Ti:LiNbO<sub>3</sub> waveguide coupling. Electronics Letters 18(1): 30-31.
- RAMER, O. (1982). Integrated optic electrooptic modulator electrode analysis. IEEE Journal of Quantum Electronics 18(3): 386-392.
- RAMO, S., WHINNERY, J. R. AND VANDUZER, T. (1984). Fields and Waves in Communication Electronics, 2<sup>nd</sup> Ed. (New York: John Wiley & Sons).
- REDDY, J.N. (1993). An introduction to the finite element method. (Singapore: McGraw-Hill, Inc.).
- REINHART, F.K. (1968). Reverse-biased gallium phosphide diodes as high-frequency light modulators. Journal of Applied Physics 39(7): 3426-3434.
- REINHART, F.K. (1973). Electroabsorption in Al<sub>y</sub>Ga<sub>1-y</sub>As-Al<sub>x</sub>Ga<sub>1-x</sub>As double heterostructures. Applied Physics Letters 22(8): 372-374.
- REINHART, F.K. and MILLER, B.I. (1972). Efficient GaAs-Al<sub>x</sub>Ga<sub>1-x</sub>As double heterostructure light modulators. Applied Physics Letters 20(1): 36-38.
- RIGBY, P. (2000) Out of the lab: Polymer's progress. [Online newsletter]. URL: [http://www.lightreading.com/document.asp?doc\\_id=2523](http://www.lightreading.com/document.asp?doc_id=2523). [Accessed date: 15 March 2001].
- RIGBY, P. (2001) K2 goes the distance. [Online newsletter]. URL: <http://www.nwfusion.com/newsletters/optical/2001/00916287.html>. [Accessed date: 15 March 2001].
- RIGROD, W.W. and KAMINOW, I.P. (1963). Wide-band microwave light modulation. Proceedings of the IEEE 51: 137-140.
- RODGERS, P.M. (1985). GaAs-GaAlAs Y-branch interferometric modulator. In: Third European Conference on Integrated Optics, Berlin, 1985, Technical Digest. Berlin, Germany: Springer-Verlag (Springer Series in Optical Sciences).
- RODGERS, P.M., ROBERTSON, M.J., CHATERJEE, A.K. and WONG, S.Y. (1986). High-performance InGaAsP/InP phase modulators for integrated optics. In: Topical

Meeting on Integrated and Guided Wave Optics, Atlanta, 1986. Technical Digest. New York: OSA, Paper THAA4. pp. 22-23.

ROLLAND, C., MAK, G., PROSYK, K.L., MARITAN, C.M. and PUETZ, N. (1991). High speed and low loss, bulk electroabsorption waveguide modulators at 1.3 $\mu$ m. IEEE Photonics Technology Letters 3(10): 894-896.

ROLLAND, C., MAK, G., BARDYSZEWSKI, W. and YEVICK, D. (1992). Improved extinction ratio of waveguide electroabsorption optical modulators induced by an InGaAs absorbing layer. Journal of Lightwave Technology 10(12): 1907-1911.

ROTTSCHALK, M., RUSKE, J.-P., HORNIG, K., STEINBERG, S., HAGNER, G. and RASCH, A. (1995). Singlemode channel waveguides and electrooptic modulators in KTiOPO<sub>4</sub> for the short visible wavelength region. Journal of Lightwave Technology 13(10): 2041-2048.

RUSCIO, J.T. (1965). A coherent light modulator. IEEE Journal of Quantum Electronics 1(7): 182-183.

SAAD, S.M. (1985). Review of numerical methods for the analysis of arbitrarily-shaped microwave and optical dielectric waveguides. IEEE Transactions on Microwave Theory and Techniques 33(10): 894-899.

SAHARA, R., MATSUDA, M., SHOJI, H., MORITO, K. and SODA, H. (1996). Proposal for quantum-dot electroabsorption modulator. IEEE Photonics Technology Letters 8(11): 1477-1479.

SAKAMOTO, S.R., OZTURK, C., BYUN, Y.T., KO, J. and DAGLI, N. (1998). Low-loss substrate-removed (SURE) optical waveguides in GaAs-AlGaAs epitaxial layers embedded in organic polymers. IEEE Photonics Technology Letters 10(7): 985-987.

SAKAMOTO, S.R., JACKSON, A. and DAGLI, N. (1999). Substrate removed GaAs-AlGaAs electrooptic modulators. IEEE Photonics Technology Letters 11(10): 1244-1246.

SASAKI, H. and DE LA RUE, R.M. (1976). Electro-optic Y-junction modulator/switch. Electronics Letters 12: 459-460.

SCHIEK, R., FRIEDRICH, L., FANG, H., STEGEMAN, G.I., PARAMESWARAN, K.R., CHOU, M.-H. and FEJER, H.H. (1999). Nonlinear directional coupler in periodically poled lithium niobate. Optics Letters 24(22): 1617-1619.

SCHILLING, O., FORCHEL, A., KOHL, A. and BRITTFNER, S. (1993). Optical analysis of quantum-confined stark-effect in overgrown InGaAs/InP quantum wires. Journal Of Vacuum Science & Technology B 11(6): 2556-2559.

SCHLAAK, H.F. (1984). Modulation behaviour of integrated optical directional couplers. Journal of Optical Communications 5(4): 122-131.

SCHMID, S. (2003). Lithium niobate to rule 40G modulation. Lightwave Europe. [Online newsletter]. URL:

[http://cgw.pennnet.com/Articles/Article\\_Display.cfm?Section=CURRI&ARTICLE\\_ID=1](http://cgw.pennnet.com/Articles/Article_Display.cfm?Section=CURRI&ARTICLE_ID=1). [Accessed date: 01 August 2004].

SCHMIDT, R.V. and KAMINOW, I.P. (1974). Metal-diffused optical waveguides in LiNbO<sub>3</sub>. Applied Physics Letters 25(8): 458-460.

SCHMIDT, R.V. and KAMINOW, I.P. (1975). Acoustic Bragg deflection in LiNbO<sub>3</sub> Ti-diffused waveguides. IEEE Journal of Quantum Electronics 11(1): 57-58.

SCHMIDT, R.V. and KOGELNIK, H. (1976). Electro-optically switched coupler with stepped  $\Delta\beta$  reversal using Ti-diffused LiNbO<sub>3</sub> waveguides. Applied Physics Letters 28(9): 503-506.

SCHMIDT, R.V. and CROSS, P.S. (1978). Efficient optical waveguide switch/modulator. Optics Letters 2(2): 45-57.

SCHMIDT, R.V. and ALFERNESS, R.C. (1979). Directional coupler switches, modulators, and filters using alternating  $\Delta\beta$  techniques. IEEE Transactions on Circuits and Systems 26(12): 1099-1108.

SELLERI, S., VINCETTI, L. and ZOBOLI, M. (2000). Full-vector finite-element beam propagation method for anisotropic optical device analysis. IEEE Journal of Quantum Electronics 36(12): 1392-1401.

SHAH, M.L. (1975) Optical waveguides in LiNbO<sub>3</sub> by ion exchange techniques. Applied Physics Letters 26(11): 652-653.

SHAMES, P., SUN, P.-C., and FAINMAN, Y. (1996). Modeling and Optimization of Electrooptic Phase Modulator. In: SPIE Proceedings: Physics and Simulation of Optoelectronic Devices IV, Vol.2693, 787-96.

SILBERBERG, Y., PERLMUTTER, P. and BARAN, J.E. (1987). Digital optical switch. Applied Physics Letters 51(16): 1230-1232.

SILVESTER, P.P. and FERRARI, R.L. (1990). Finite elements for electrical engineers. 2<sup>nd</sup>. Ed. (Cambridge: Cambridge University Press).

SNITZER, E and OSTERBERG, H. (1961). Observed dielectric waveguide modes in the visible spectrum. Journal of the Optical Society of America 51(5): 499-505.

SNYDER, A.W. and RICHMOND, P. (1972). Effect of anomalous dispersion on visual receptors. Journal of the Optical Society of America 62(11): 1267-1283.

SO, L.C. and LEE, C.A. (1989). A new integrable optical modulator-switch optimised for speed and power consumption. Journal of Applied Physics 66(5): 2200-2205.

SODA, H., FURUTSU, M., SATA, K., MATSUDA, M. and ISHIKAWA, H. (1989). 5Gb/s modulation characteristics of optical intensity modulator monolithically integrated with DFB laser. Electronics Letters 25(5): 334-335.

SOHLER, W. and SUCHE, H. (1999). Erbium-doped lithium niobate waveguide devices. In: *Integrated optical circuits and components: Design and Applications*, ed. by E.J. Murphy. (New York: Marcel Dekker, Inc.).

SOLDANO, L.B. and PENNING, E.C.M. (1995). Optical multimode interference devices based on self-imaging - Principles and applications. Journal of Lightwave Technology 13(4): 615-627.

SOMASIRI, N., RAHMAN, B.M.A. and OBAYYA, S.S.A. (2002). Fabrication tolerance study of a compact passive polarization rotator. Journal of Lightwave Technology 20(4): 751-757.

SOULI, N., DEVAUX, F., RAMDANE, A., KRAUZ, P., OUGAZZADEN A., HUET, F., CARRÉ, M., SOREL, Y., KERDILES, J.F., HENRY, M., AUBIN, G., JEANNEY, E., MONTALLANT, T., MOULU, J., NORTIER, B. and THOMINE, J.B. (1995). 20Gbit/s high-performance integrated MQW TANDEM modulators and amplifier for soliton generation and coding. IEEE Photonics Technology Letters 7(6): 629-631.

SPICKERMANN, R., PETERS, M.G. and DAGLI, N. (1996a). A polarization independent GaAs-AlGaAs electrooptic modulator. IEEE Journal of Quantum Electronics 32(5): 764-769.

SPICKERMANN, R., SAKAMOTO, S.R., PETERS, M.G. and DAGLI, N. (1996b). GaAs/AlGaAs travelling wave electro-optic modulator with an electrical bandwidth >40GHz. Electronics Letters 32(12): 1095-1096.

SPRINGER, A.D. and HENDRICKSON, A.E. (2004). Development of the primate area of high acuity. 1. Use of finite element analysis models to identify mechanical variables affecting pit formation. Visual Neuroscience 21(1): 53-62.

STASA, F.L. (1985) *Applied finite element analysis for engineers*. (New York: Holt, Reinhart and Winston).

STEIER, W.H. (1967). A push-pull optical amplitude modulator. IEEE Journal of Quantum Electronics 3(12): 664-667.

STEINBERG, R.A. and GIALLORENZI, T.G. (1976). Performance limitations imposed on optical waveguide switches and modulators by polarization. Applied Optics 15(10): 2440-2453.

STERN, M.S. (1988). Semivectorial polarized finite-difference method for optical wave-guides with arbitrary index profiles. IEE Proceedings J-Optoelectronics 135(1): 56-63.

STONE, S.M. (1964). A microwave electro-optic modulator which overcomes transit time limitation. *Proceedings of the IEEE*: 409-410.

STRAKE, E., BAVA, G.P. and MONTROSSET, I. (1988). Guided modes of Ti:LiNbO<sub>3</sub> channel waveguides: A novel quasi-analytical technique in comparison with the scalar finite-element method. Journal of Lightwave Technology 6(6): 1126-1135.

- STRANG, G. and FIX, G.J. (1973). An analysis of the finite element method. (Englewood Cliffs, N.J.: Prentice-Hall, Inc).
- SUCHE, H., HAMPEL, B., SEIBERT, H. and SOHLER, W. (1985). Parametric fluorescence, amplification and oscillation in Ti:LiNbO<sub>3</sub> optical waveguides. In: Conference on Integrated Optical Circuit Engineering, Boston, 1985. Proceedings. Bellingham, WA, USA. SPIE. pp. 156-161.
- SUCHOSKI, Jr, P.G. and LEONBERGER, F.J. (1999). Commercialization of lithium niobate modulators. In: Integrated optical circuits and components: Design and Applications, ed. by E.J. Murphy. (New York: Marcel Dekker, Inc.).
- SUDBØ, A.S. (1992). Why are accurate computations of mode fields in rectangular dielectric waveguides difficult? Journal of Lightwave Technology 10(4): 418-419.
- SUEMATSU, Y. and KISHINO, K. (1977). Coupling coefficient in strongly coupled dielectric waveguides. Radio Science 12(4): 587-592.
- SUETA, T. and IZUTSU, M. (1981). High-speed guided-wave optical components. In: IOOC'81, San Francisco (CA, USA), 1981. Proceedings. Paper TUM2.
- SUGII, K., FUKUMA, M. and IWASAKI, H. (1978). A study in titanium diffusion into LiNbO<sub>3</sub> waveguides by electron probe analysis and x-ray diffraction methods. Journal of Material Science 13: 523-533.
- SUHARA, T., TAZAKI, H. and NISHIHARA, H. (1989). Measurement of reduction in SHG coefficient of LiNbO<sub>3</sub> by proton exchanging. Electronics Letters 25(20): 1326-1328.
- SVEDIN, J.A.M. (1989). A numerically efficient finite-element formulation for the general waveguide problem without spurious modes. IEEE Transactions on Microwave Theory and Techniques 37(11): 1708-1715.
- TAKEUCHI, H., KASAYA, K. and OE, K. (1989). Low-switching-voltage InGaAsP/InP waveguide interferometric modulator for integrated optics. IEEE Photonics Technology Letters 1(8): 227-229.
- TAVLYKAEV, R., KÜCKELHAUS, K. and VOGES, E. (1994). Index profile reconstruction of Ti:LiNbO<sub>3</sub> structures and bending loss evaluation from near-field measurements. Journal of Optical Communications 15(2): 71-76.
- TAYLOR, H.F. (1973). Optical switching and modulation in parallel dielectric waveguides. Journal of Applied Physics 44(7): 3257-3262.
- TAYLOR, H.F. (1985). Polarization independent guided-wave optical modulators and switches. Journal of Lightwave Technology 3(6): 1277-1280.
- TAYLOR, H.F. and YARIV, A. (1974). Guided wave optics. Proceedings of the IEEE 62(8): 1044-1060.

THEMISTOS, C., RAHMAN, B.M.A., HADJICHARALAMBOUS, A. and GRATTAN, K.T.V. (1995a). Loss/Gain characterization of optical waveguides. Journal of Lightwave Technology 13(8): 1760-1765.

THEMISTOS, C., RAHMAN, B.M.A., GRATTAN, K.T.V. (1995b). Finite-element analysis of surface-plasmon modes for lossy optical wave-guides by the use of perturbation techniques. Applied Optics 34(33): 7695-7701.

THEMISTOS, C. (1998). Characterization of loss/gain in optical waveguides. PhD thesis: City University, Department of Electrical, Electronic and Information Engineering.

THEMISTOS, C., RAHMAN, B.M.A. and GRATTAN, K.T.V. (1998). Finite-element analysis of lossy TE-TM modes in metal-clad optical waveguides. Applied Optics 37(24): 5747-5754.

THEMISTOS, C. and RAHMAN, B.M.A. (2002). Design issues of a multimode interference-based 3-dB splitter. Applied Optics 41(33): 7037-7044.

THIOULOUSE, P., CARENCO, A. and GUGLIELMI, R. (1981). High-speed modulation of an electrooptic directional coupler. IEEE Journal of Quantum Electronics 17(4): 535-541.

TIEN, P.K. (1971). Light waves in thin films and integrated optics. Applied Optics 10(11): 2395-2413.

TSAI, C.S. and LE, P. (1992). 4x4 nonblocking integrated acousto-optic space switch. Applied Physics Letters 60(4): 431-433.

TSURUMACHI, N., SON, C.S., KIM, T.G., TAKASUKA, Y. and OGURA, M. (2002). Photoluminescence and photoluminescence excitation spectra of strained high-density InGaAs/Al<sub>x</sub>Ga<sub>1-x</sub>As quantum wire structures on submicron grating. Japanese Journal of Applied Physics Part 1-Regular Papers Short Notes & Review Papers 41(4B): 2679-2682.

TURNER, M.J., CLOUGH, R.W., MARTIN, H.C. and TOPP, L.T. (1956). Stiffness and deflection analysis of complex structures. Journal of Aeronautical Science 25: 805-823.

UCHIDA, T. (1965). Direct modulation of gas lasers. IEEE Journal of Quantum Electronics 1(11): 336-343.

U-OPLAZ TECHNOLOGIES, Inc. (1999). U-Oplaz Technologies. Lithium Niobate Crystal Series. [Online]. URL: <http://www.u-oplaz.com/crystals/crystals000.htm>. [Accessed date: 27 June 2004].

Van HEEL, A.C.S. (1954). A new method of transporting optical images without aberration. Nature 173: 39.

VASSALLO, C. (1990). Circular fourier-analysis of full maxwell equations for arbitrarily shaped dielectric wave-guides - Application to gain factors of semiconductor-laser wave-guides. Journal of Lightwave Technology 8(11): 1723-1729.

- VASSALLO, C. (1997). 1993-1995 optical mode solvers. Optical and Quantum Electronics 29(2): 94-114.
- VESELKA, J.J. and KOROTKY, S.K. (1986). Optimization of Ti:LiNbO<sub>3</sub> optical waveguides and directional coupler switches for 1.56 μm wavelength. IEEE Journal of Quantum Electronics 22(6): 933-938.
- WAKITA, K., NOJIMA, S., NAKASHIMA, K. and KAWAGUCHI, Y. (1987). GaInAs/InP wave-guide multiple-quantum-well optical modulator with 9db on/off ratio. Electronics Letters 23(20): 1067-1069.
- WAKITA, K., KOTAKA, I., MITOMI, O., ASAI, H., KAWAMURA, Y. and NAGANUMA, M. (1990). High-speed InGaAlAs/InAlAs multiple quantum well optical modulators. Journal of Lightwave Technology 8(7): 1027-1031.
- WAKITA, K., KOTAKA, I., YOSHINO, K., KONDO, S and NOGUCHI, Y. (1995). Polarization-independent electroabsorption modulators using strain-compensated InGaAs-InAlAs MQW structures. IEEE Photonics Technology Letters 7(12): 1418-1420.
- WALKER, R.G. (1987). High-speed electrooptic modulation in GaAs/AlGaAs waveguide devices. Journal of Lightwave Technology 5(10): 1444-1453.
- WALKER, R.G. (1991). High-speed III-V semiconductor intensity modulators. IEEE Journal of Quantum Electronics 27(3): 654-667.
- WALPITA, L.M. (1985). Solutions for planar optical waveguide equations by selecting zero elements in a characteristic matrix. Journal of the Optical Society of America A – Optics Image Science and Vision 2(4): 595-602.
- WANG, S.Y., LIN, S.H. and HOUNG, Y.M. (1987). GaAs traveling-wave polarization electrooptic wave-guide modulator with bandwidth in excess of 20 GHz at 1.3-μm. Applied Physics Letters 51(2): 83-85.
- WANG, Y.-H. and VASSALLO, C. (1989). Circular fourier-analysis of arbitrarily shaped optical fibers. Optics Letters 14(24): 1377-1379.
- WANG, M.R., XU, G., LIN, F. and JANNSON T. (1995). Single-mode/multimode waveguide electro-optic grating coupler modulator. Applied Physics Letters 66(20): 2628-2630.
- WESSELS, B.W. (1998). Ferroelectric oxide epitaxial thin films: synthesis and non-linear optical properties. Journal of Crystal Growth 195: 706-710.
- WHITE, G. and CHIN, G.M. (1972). Travelling wave electro-optic modulators. Optics Communications 5: 374-379.
- WILLIAMS, R.E (1990). Modern GaAs Processing Methods (Boston: Artech House Publishers).

WILSON, J. and HAWKES, J.F.B. (1989). Optoelectronics. An introduction. 2<sup>nd</sup> Ed. (Hemel Hempstead: Prentice Hall(UK)).

WINNALL, S. and WINDERBAUM, S. (2000). Lithium niobate reactive ion etching. Department of Defence (Australia), Defence Science & Technology Organisation, Report No. DSTO-TN-0291, Australia, July 2000.

WONGCHAROEN, T., RAHMAN, B.M.A. and GRATTAN, K.T.V. (1993). Design and characterization of optical directional couplers using the finite element method. In: Sensors VI, Technology Systems and Applications, Southampton, 1993. Proceedings. Bristol, England. Institute of Physics Publishing. pp. 311-315.

WONGCHAROEN, T. (1995). Computer modelling of directional coupler based optical devices. PhD thesis: City University, Department of Electrical, Electronic and Information Engineering.

WONGCHAROEN, T., RAHMAN, B.M.A. and GRATTAN, K.T.V. (1997). Electro-optic directional coupler switch characterization. Journal of Lightwave Technology 15(2): 377-382.

WONGCHAROEN, T., RAHMAN, B.M.A., RAJARAJAN, M., GRATTAN, K.T.V. (2001). Spot-size conversion using uniform waveguide sections for efficient laser-fiber coupling. Journal Of Lightwave Technology 19(5): 708-716.

WOOD, T.H., BURRUS, C.A., MILLER, D.A.B., CHEMLA, D.S., DAMEN, T.C., GOSSARD, A.C. and WIEGMANN, W. (1984). High-speed optical modulation with GaAs/AlGaAs quantum wells in a p-i-n-diode structure. Applied Physics Letters 44(1): 16-18.

WOOTEN, E.L. and CHANG, W.S.C. (1993). Test structures for characterization of electrooptic waveguide modulators in lithium niobate. IEEE Journal of Quantum Electronics 29(1): 161-170.

WOOTEN, E.L., KISSA, K.M., YI-YAN, A., MURPHY, E.J., LAFAW, D.A., HALLEMEIER, P.F., MAACK, D., ATTANASIO, D.V., FRITZ, D.J., McBRIEN, G.J. and BOSSI, D.E. (2000). A review of lithium niobate modulators for fiber-optic communications systems. IEEE Journal of Selected Topics in Quantum Electronics 6(1): 69-82.

XU, C.-Q., OKAYAMA, H., KAWAHARA, M. (1994). Large Differences In Ti Thermal-Diffusion Caused Domain Inversion Between Undoped And MgO-Doped LinbO<sub>3</sub>, Applied Physics Letters 64(19): 2504-2506.

YAMADA, K., MURAI, H., NAKAMURA, K., MATSUI, Y. and OGAWA, Y. (1995). Low polarisation dependence (<0.3dB) in an EA modulator using a polyimide-buried high-mesa ridge structure with InGaAsP bulk absorption layer. Electronics Letters 31(3): 237-238.

YAMADA, S. and MINAKATA, M. (1981). DC drift phenomena in LiNbO<sub>3</sub> optical-waveguide devices. Japanese Journal of Applied Physics 20(4): 733-737.

- YAP, D., ELLIOTT, K.R., BROWN, Y.K., KOST, A.R., PONTI, E.S. (2001). High-speed integrated optoelectronic modulation circuit. IEEE Photonics Technology Letters 13(6): 626-628.
- YARIV, A. (1973). Coupled mode theory for guided-wave optics. IEEE Journal of Quantum Electronics 9: 919-933.
- YARIV, A. (1991). Optical Electronics. 4<sup>th</sup> Ed. (International: Saunders College Publishing. A Division of Holt, Rinehart and Winston, Inc.).
- YARIV, A. and LEITE, R.C.C. (1963). Dielectric waveguide mode of light propagation in p-n junction. Applied Physics Letters 2: 55-57.
- YEH, C., DONG, S.B. and OLIVER, W. (1975). Arbitrarily shaped inhomogeneous optical fiber or integrated optical waveguides. Journal of Applied Physics 46(5): 2125-2129.
- YEH, C., CASPERSON, L. and SZEJN, B. (1978). Propagation of truncated gaussian beams in multimode fiber guides. Journal of the Optical Society of America 68: 989-993.
- YEH, C., HA, K., DONG, S.B. and BROWN, W.P. (1979). Single-mode optical waveguides. Applied Optics 18(10): 1490-1504.
- YEVICK, D. (1994). A guide to electric field propagation techniques for guided-wave optics. Invited paper. Optical and Quantum Electronics 26: S185-S197.
- YI, J.C., KIM, S.H. and CHOI, S.S. (1990). Finite-element method for the impedance analysis of travelling-wave modulators. Journal of Lightwave Technology 8(6): 817-822.
- YIM, Y.-S. and SHIN, S.-Y. (1998). Lithium niobate integrated-optic voltage sensor with variable sensing ranges. Optics Communications 152: 225-228.
- YU, J., YEVICK, D. and WEIDMAN, D. (1994). A comparison of beam propagation and coupled-mode methods: Application to optical fiber couplers. Journal of Lightwave Technology 12(5): 797-802.
- ZHANG, H., OH, M.C., SZEP, A., STEIER, W.H., ZHANG, C., DALTON, L.R., ERLIG, H., CHANG, Y., CHANG, D.H. and FETTERMAN, H.R. (2001). Push-pull electro-optic polymer modulators with low half-wave voltage and low loss at both 1310 and 1550 nm. Applied Physics Letters 78(20): 3136-3138.
- ZHANG, X. and MIYOSHI, T. (1995). Optimum design of coplanar waveguide for LiNbO<sub>3</sub> optical modulator. IEEE Transactions on Microwave Theory and Techniques 43(3): 523-528.
- ZIENKIEWICZ, O.C. and CHEUNG, Y.K. (1965). Finite elements in the solution of field problems. The Engineer 220: 507-510.
- ZIENKIEWICZ, O.C. (1971). The finite element method in engineering science. (Maidenhead: McGraw-Hill).

ZIENKIEWICZ, O.C. and TAYLOR, R.L. (2000). The finite element method. Volume 1: The basis. (Oxford: Butterworth-Heinemann).

ZUCKER, J.E., JONES, K.L., MILLER, B.I. and KOREN, U. (1990). Miniature Mach-Zehnder InGaAsP quantum well waveguide interferometers for 1.3 $\mu$ m. IEEE Photonics Technology Letters 2(1): 32-34.